ABSTRACT

Title of dissertation: EXPERIMENTAL INVESTIGATIONS AND SCALING ANALYSES OF WHIRLING FLAMES

Sriram Bharath Hariharan
Doctor of Philosophy
2020

Dissertation directed by: Professor Michael J. Gollner
Department of Fire Protection Engineering

Professor Elaine S. Oran
Department of Aerospace Engineering

Swirling flows are ubiquitous in nature, occurring over a large range of length scales − on the order of many tens-of-thousands of kilometers in the case of Saturn's hexagonal polar vortex, to just a few centimeters in dandelion flight. Most instances of swirling flow involve momenta competing in two different directions, axial and azimuthal. Whirling flames (also known as fire whirls) occur at the intersection of vortical flow fields and buoyant, reactive plumes, and they represent a general class of flows that may be considered slender vortices involving axial momentum from heat-release and tangential momentum from air entrainment.

In this work, two previously unexplored characteristics of whirling flames are considered over a wide range of scales, spanning three orders of magnitude in length and four orders in heat-release rate. First, emissions of particulate matter (PM)

from fire whirls (FW) were measured and compared to those from free-buoyant pool fires (PF). For different pool diameters and fuels, FWs showed higher burning rate and fuel-consumption efficiency, but lower PM-emission rate, leading to lower PM-emission factors. The lower PM emissions from FWs is attributed to a feedback cycle between higher oxygen consumption from improved entrainment, higher average temperatures, increased heat feedback to the fuel pool, which in turn increases burning rate and entrainment. A scaling analysis showed that the PM emission factor decreased linearly with the ratio of inverse Rossby number to nondimensional heat-release rate.

Second, the structure of the blue whirl (BW), a soot-free regime, was investigated using dimensional analysis and non-intrusive optical diagnostics. Experimental data of heat-release rates and circulation for BWs and FWs from the literature were used to define the nondimensional equivalents of buoyant and azimuthal momenta. The combinations of these parameters showed that FWs primarily formed in a buoyancy-dominated regime, and that a circulation-dominated regime was required for BW formation, corroborating hypotheses that the transition was caused by the bubble mode of vortex breakdown, resulting in the formation of a recirculation zone. Finally, OH- and PAH-PLIF, OH* and CH* chemiluminescence suggest a triple-flame structure anchored at the blue ring region of the BW, with the rich branch formed by the lower blue cone, and the lean branch by the upper purple haze. These results show that the mixing process occurs upstream of the conical region and that the recirculation zone is comprised of combustion products.

EXPERIMENTAL INVESTIGATIONS AND SCALING ANALYSES OF WHIRLING FLAMES

by

Sriram Bharath Hariharan

Dissertation submitted to the Faculty of the Graduate School of the
University of Maryland, College Park in partial fulfillment
of the requirements for the degree of
Doctor of Philosophy
2020

Advisory Committee:
Professor Michael J. Gollner, Chair & Advisor
Professor Elaine S. Oran, Co-Chair & Co-Advisor
Professor Arnaud Trouvé
Professor Peter B. Sunderland
Professor James H. Duncan
Professor Christopher Cadou
Professor Konstantina Trivisa, Dean's Representative

Acknowledgments

This dissertation was possible primarily because of the people who have supported me during my time in graduate school at the University of Maryland. First and foremost, encouragement from my advisors, Professor Michael J. Gollner and Professor Elaine S. Oran, was the primary reason I chose to pursue doctoral studies. They have stood by me through the ups and downs as a graduate student over the past five years. Michael showed me how to approach a problem meticulously and provided ample room for me to experiment with my own ideas. His rigorous work ethic and enthusiasm for new problems will serve as a personal goal for my career. I cannot emphasize enough Elaine's influence on my development as a researcher. Her encouragement and insights have been crucial to broadening the scope of this work asking the right questions at every stage.

Sincere thanks to Professors Arnaud Trouvé, Peter B. Sunderland, James H. Duncan, Christopher Cadou, and Konstantina Trivisa for serving on the doctoral committee. They were very supportive during early reviews of my research and provided valuable comments to improve the dissertation.

I express my gratitude to my colleagues, Dr. Paul Anderson, who acted as an unofficial mentor, and Dr. Yu Hu, whose experiments on the blue whirl served as a basis for a part of this work.

I would like to acknowledge the Bureau of Safety and Environmental Enforcement (BSEE), U.S. Department of Interior, Washington, D.C. for funding this work under contract No. E17PC00016. Special thanks to Karen Stone, Program Manager,

for her guidance and support throughout the duration of the project. This work was also supported by the National Science Foundation (NSF, CBET-1507623,1554026).

A number of large-scale experiments were conducted at the Fire Protection Engineering Performance Laboratory at the Worcester Polytechnic Institute, thanks to the efforts of Dr. Ali Rangwala and Raymond T. Ranellone.

I would like to thank Drs. Waruna D. Kulatilaka and Yejun Wang at the the Optical Diagnostics and Imaging Laboratory, Texas A&M University, for organizing the optical diagnostics experiments of the blue whirl. Special thanks to Kelsie Thompson, Ryan McDaniel, Department of Aerospace Engineering, for facilitating my visits to College Station, TX.

Much gratitude to Dr. Hamed Farahani, Joseph Dowling, Michael R. Jones, Xingyu Ren and Dr. Ali Tohidi for their important contributions to experiments and analysis in this work. I am grateful to all my fellow lab mates in the Department of Fire Protection Engineering (FPE), University of Maryland − Evan Sluder, Dr. Zhengyang Wang, Dr. Dennis Kim, Dr. Joseph Chung, Dr. Xiao Zhang, Nicholas Chui, Alison Davis, Priya Garg, Lana Benny, Raquel Hakes, Mike Heck and Dushyant Chaudhari. I convey my thanks to the staff at FPE − Brian Sully, Olivia Noble, Olga V. Zeller, Mary Lou Holt, Nicole Hollywood and Christine O'Brien for making administrative formalities easy to navigate.

The past few years have presented many opportunities for collaborative work, including microgravity experiments at the NASA Glenn Research Center. I thank Dr. Paul Ferkul, Dr. Sandra Olson, Vittorio M. Valletta, Luke Ogorzaly and Eric Neumann for arranging them. I also thank the Department of Mechanical

Engineering, University of California, Berkeley for hosting me in the last stage of graduate education.

Finally, my sincere and heartfelt thanks to my family and friends. Their constant and unseen support during this time cannot be overstated.

College Park, Maryland

July 2020

Table of Contents

List of Tables

List of Figures

Nomenclature

Symbols

A	fuel pool area	m^2
C	heat capacity	$J/kg\text{-}K$
d, D	diameter	mm, cm, m
$\mathcal{D}$	diffusion coefficient	m^2/s
f	function	$-$
f	pool-fire puffing frequency	s^{-1}
g	gravitational acceleration	m/s^2
G	intensifier gain value	%
h	height or axial distance	cm, m
H	flame height	cm
Δh	lower heating value	kJ/g
I	chemiluminescence intensity ratio	$-$
$\mathcal{I}$	species chemiluminescence intensity	$-$
L	length scale	m
m	mass	mg, g, kg
$\dot{m}$	burning (mass-loss) rate	g/s
q	heat flux	kW/m^2
$\dot{Q}$	heat-release rate	kW
r	radial distance	mm
R	vortex radius	m
S	enclosure side length	cm
$\mathcal{S}$	Swirl number	$-$
t	time	s, min
T	temperature	K
ΔT	excess temperature	K
u, U	flow velocity	m/s
$\dot{V}$	fuel volumetric flow rate	ml/min
w	flame width	cm
W	enclosure gap size	cm
z	axial distance	mm

Nondimensional numbers

Da	Damköhler number
Fr	Froude number

Gr	Grashof number
Pe	Peclet number
Ra	Rayleigh number
Re	Reynolds number
Ri	Richardson number
Ro	Rossby number
St	Strouhal number
Stk	Stokes number
$\mathcal{W}^*$	whirl number

Greek symbols

β	expansion coefficient	K^{-1}
η	efficiency	$-$
Γ	circulation	m^2/s
ν	kinematic viscosity (momentum diffusivity)	m^2/s
ϕ	equivalence ratio	$-$
κ	thermal conductivity	W/mK
ρ	density	kg/m^3
$\Delta\rho$	density change at the flame sheet	kg/m^3
μ	dynamic viscosity	Ns/m^2
τ	characteristic time scale	s
$\propto$	proportional to	

Abbreviations

ANS	Alaska North Slope crude oil
ASGSR	American Society for Gravitational and Space Research
BSEE	Bureau of Safety and Environmental Enforcement
BW	Blue Whirl
CF	Consumption Factor
DAQ	Data Acquisition

EF	Emission Factor
FE	Forced Entrainment
FID	Flame Ionization Detection
FPS	Frames Per Second
FW	Fire Whirl
HF	Heat Flux
HRR	Heat-Release Rate
ISB	*In-Situ* Burn
LFW	Large Fire Whirl
LII	Laser-Induced Incandescence
LIFS	Laser-Induced Fluorescence Spectroscopy
MCE	Modified Combustion Efficiency
MLR	Mass-Loss Rate
NASA	National Aeronautics and Space Administration
NDIR	Non-Dispersive Infrared
NE	Natural Entrainment
PAH	Polycyclic Aromatic Hydrocarbons
PF	Pool Fire
PIV	Particle Image Velocimetry
PLIF	Planar Laser-Induced Fluorescence
PM	Particulate Matter
RZ	Recirculation Zone
SLPM	Standard Liters Per Minute
TAMU	Texas A&M University, College Station
TBW	Transition Blue Whirl
TC	Thermocouple
TEM	Transmission Electron Microscopy
TPM	Total Particulate Matter
UHC	Unburned Hydro-Carbons

UMD	University of Maryland, College Park
VB	Vortex Breakdown
VOC	Volatile Organic Compounds
WPI	Worcester Polytechnic Institute

Subscripts

0	nominal ambient conditions
b	burning
c	combustion
C	carbon-mass based
cr	critical
f	flame feedback *or* fuel
h	horizontal length scale
H	Hencken burner
p	constant pressure
r	radial component
s	species
θ	azimuthal (tangential) component
z	axial component

Superscripts

$*$	nondimensional quantity *or* excited-state radical species
$''$	per unit area
$\cdot$	per unit time

Chapter 1

Introduction

1.1 Swirling Flows and Whirling Flames

Swirling flows are ubiquitous in nature. They occur at a large range of length scales − on the order of many tens-of-thousands of kilometers in the case of Saturn's hexagonal polar vortex [1] and Jupiter's Great Red Spot [36], a few hundred meters in the case of secondary motions causing river meandering [37–39], to just a few centimeters in dandelion flight [2]. Historically, eddies and vortices have been the topic of academic [40, 41], technical [42], and even artistic interest in the case of Vincent van Gogh's *The Starry Night* [43], which has intrigued turbulence researchers [44–46].

Most instances of swirling flow involve momenta competing in two different directions, primarily axial and azimuthal. Whirling flames (also known as fire whirls) represent a general class of flows that may be considered slender vortices involving axial (buoyant) momentum from heat-release, and azimuthal momentum from air

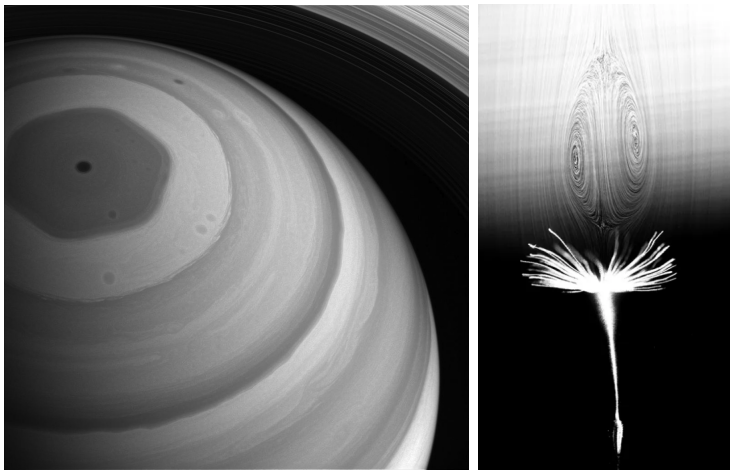

Figure 1.1: Examples of swirling flow in nature at different length scales. (*Left*) Polar vortex within the hexagonal jetstream of Saturn, from [1]. (*Right*) Separated vortex structure in dandelion flight, from Cummins et al. [2].

entrainment. These structures are observed frequently in wildland fires and have been studied for many decades in the context of fire spread and firefighter safety [47–49]. Most recently, four fatalities were reported as the direct result of the formation of a large fire whirl during the 2018 Carr Fire in California [50, 51]. Fire whirls can also accelerate wildland fire spread rates dramatically by increasing buoyancy and helping loft firebrands long distances, causing fires to initiate prior to the arrival of the fire front [52]. Various types of fire whirls can also occur in large urban fires [53].

Many approaches to classify, scale and predict fire whirl formation for the purposes of safety are prevalent [5]. The simplicity of generating *reacting* fire whirls in a laboratory and the complex interaction between combustion and fluid mechanics [8] provides a platform to study phenomena such as turbulence suppression, mixing, vortex stretching and dynamics. Various aspects such as formation methods in the laboratory [5, 47, 48], thermal structure [8], velocity structure [54], scaling [11, 12], flow structure [55, 56], etc. have been reported in the literature. Byram and Martin

[48] listed three essential conditions required for thermally-driven vortex structures such as fire whirls – (i) an eddy generating mechanism, (ii) a fluid sink within the eddy, and (iii) drag (or a boundary layer) at the bottom boundary of the slender eddy.

Swirling flow fields are used in engineering applications to enhance combustion efficiency and reduce emissions [57, 58]. They are typically used in aerospace applications and involve gaseous and liquid fuels, and both premixed and nonpremixed modes of operation [59]. Whirling flames are distinct from swirling flames in the manner that fuel and air interact [60]. In swirl flames, the momentum of fuel injection is comparable with that of the air, both of which have axial and azimuthal components, enabled by mechanical forcing of both to enhance turbulent mixing prior to combustion. The reduced reaction length allows high heat-release rates to be achieved in small burners. In whirling flames, however, momentum of the fuel supply is negligible, as is azimuthal momentum of the entrained air. Turbulence is suppressed in fire whirls [8], causing flame lengths to increase when compared to non-whirling pool flames, even when the burning rate similar. Jet flames under the influence of rotating flow fields posses different boundary conditions at the base of the flame, but show similarity to fire whirls in the vortex structure of the continuous flame region [61–63].

Most fire whirls, irrespective of formation method or fuel (except light, oxygenated fuels such as methanol or ethanol), exhibit a yellow color, which stems from incandescent soot particles in the flame (see Figure 2.3). An aspect of fire whirls that has not been explored in the literature is the quantification of particulate-

matter (soot) emissions. This is investigated in the first part of this dissertation by comparing emissions from fire whirls and free-buoyant pool fires.

1.2 The Blue Whirl

In recent experiments by Xiao et al. [64], the blue whirl was discovered during experiments with liquid-fueled fire whirls formed over a water surface. An abrupt transition from a traditional fire whirl to a completely blue flame was seen at some experimental conditions. The thermal characteristics of this flame structure was the subject of the author's M.S. thesis [65].

The blue whirl is a laminar regime of the fire whirl that burns with negligible soot formation and stabilizes directly over a liquid fuel surface [22,65,66]. The flame (Figure 1.2) has an inverted conical region below, a hazy region above, and a bright blue ring at the edge. This flame regime is of interest since it transitions from the sooty fire whirl regime without any externally-forced air entrainment.

Soot-free flames are preferred in many applications where combustion efficiency and issues like coking are critical to performance. Achieving a soot-free flame typically requires either premixed or lean operation, which may not be possible in many industrial applications due to the safety and control issues associated with premixed flames. Non-premixed (diffusion) flames are the choice for most industrial applications, but are challenged by soot formation. Thus, a burner based on the blue whirl could present opportunities to have control over the combustion process similar to a non-premixed flame, and inherent soot-free operation even when burning liquid fuels.

Swirl stabilization has been used as a technique to extend the lean-side operating range of combustors [59, 67, 68] and to reduce emissions [58, 60, 69]. Since

Figure 1.2: An image of the blue whirl formed with heptane over a water surface. The lower portion of the image is the reflection of the flame over the water surface.

such combustors typically operate at high power output, it is necessary for them to operate in the turbulent regime and use various injection techniques to promote fuel-air mixing. The reduced residence times in combination with lean, low-temperature combustion of light fuels, such as methane or propane, can lead to low emissions [57, 59, 61, 70, 71].

The blue whirl, however, is a laminar whirling flame. In all the experiments, the blue whirl transitions from the fire whirl, and the transition requires buoyancy and circulation to exist in specific ratios, and emits negligible quantities of soot (PM). The thermal structure and experimental conditions required for blue whirl formation were studied in previous work [65], but questions regarding the mechanisms governing its formation and the nature of combustion still remained.

Questions regarding the transition and structure of the blue whirl flame are the second aspect of whirling flames considered in this work. Using recent experimental data on the formation limits of the blue whirl [24], dimensional analysis and scaling

are used to explain the fluid-dynamic factors that govern the transition process from a fire whirl to a blue whirl. Non-intrusive optical diagnostics are used to present preliminary insight into the flame structure. Some of the results presented here have been used as boundary conditions for numerical simulations of the blue whirl [33,72].

1.3 Motivation and Scope

Emissions and near-limit aspects of fire whirls have not been given much consideration in the literature. Emissions such as NO_x, SO_x, CO_2 and particulate matter (PM) from air-breathing engines are regulated since they can impact human health [73]. Emissions from *in-situ* burning (ISB), which are essentially large pool fires, have been characterized in the literature [73–76]. ISBs are a trade-off between marine pollution, caused by oil spreading over the sea water, and airborne particulate-matter (PM) emissions, which can impact human respiratory systems [77,78]. Reducing airborne particulate emissions could reduce the environmental impact of remediating offshore and onshore oil spills.

Reducing soot emissions from ISBs, incinerators and gas flares [79] offer motivation to investigate the differences between the fire whirl and pool fire regimes. In this work, the hypothesis that is tested is that for a burning pool of liquid fuel, fire whirls emit a lower mass of particulate matter. Applicability to ocean environments and practical ISB apparatus may be considered in the future using the fundamental results presented here to design combustion devices.

While emissions from fire whirls in a wildland fire may not be of much practical interest, the intensification in combustion due to a fire whirl and the emissions behavior are still fundamental questions that are a gap in the literature. The addition of swirl to gaseous-fuel burners has been shown to reduce emissions [60]. These results, however, are not immediately applicable to free-burning fires [80] such as pool fires and fire whirls – regimes in which the role of turbulence is quite disparate.

In the first part of this dissertation (Chapters 3 and 4), particulate matter (PM) emissions are measured from pool fires and fire whirls formed using different fuels. Parameters such as fuel and slick diameter are varied to study behavior at different length scales. These emissions are compared for fire whirls and free-buoyant pool fires. If combustion efficiency is higher and emissions from fire whirls are lower than that from pool fires, fire whirls could potentially be used in an engineering device at an appropriate length scale such that it may be utilized for improving incineration of spilled combustible materials.

The second part of this dissertation (Chapters 5 and 6) discusses the blue whirl, the near-limit whirling flame that occurs at very low heat-release rates [24] and is very sensitive to experimental conditions. These factors do not permit their use in practical engineering devices in the near future since sufficient energy-release rates may not be achieved for applications such as propulsion. The flame is, however, of academic interest to identify the characteristics that enable soot-free combustion while directly burning liquid fuels. It could also serve as a model to study reacting vortex breakdown and edge flames under in a rotating flow field.

A scaling analysis is presented to understand the conditions that influence the transition from the fire whirl to the blue whirl. This analysis builds on previous work by Hu et al. [24], and uses flame geometry to determine the characteristic length scales for nondimensionalization of the two parameters that influence whirling flames – circulation and heat-release rate. Buoyancy and momentum dominated regimes are common in many flame and fire problems [81] and these analogies are used here to explain the transition.

Finally, the flame structure of the blue whirl is investigated using optical diagnostics including chemiluminescence and planar laser-induced fluorescence (PLIF). Species such as OH, PAH, OH* and CH* are imaged to identify their locations in the flame and comment on the general structure and relate them to previous work. The results from both of these aspects have been used for numerical modeling of the blue whirl [72, 82]. Scaling results were also used to design preliminary microgravity experiments of fire whirls, conducted in the 5.18 s drop tower at NASA Glenn Research Center in May 2019 [83].

1.4 Outline of the Dissertation

This dissertation explores whirling flames at different length scales from an experimental standpoint. The largest fire whirls were on the order of 5 m in height, while the smallest blue whirls were on the order of 5 cm. A general literature review on fire whirls, the motivation and background on the diagnostic techniques are presented in Chapter 2. The chapters that follow are roughly organized based on the journal articles that compose this dissertation, and each contains a separate introduction and literature review. A comprehensive list of references is provided as a bibliography. Chapter 3 presents the experimental data obtained for pool fires and fire whirls. This raw data is analyzed in detail and the relevant nondimensional relationships influencing PM emissions are presented in Chapter 4. The effect of boilover on the burning characteristics and emissions from large-scale ANS crude oil fires is also discussed. Chapter 5 presents the dimensional analysis used to explain the onset of vortex breakdown and the transition to the blue whirl regime, followed by non-intrusive optical diagnostics measurements in Chapter 6. A summary, conclusion and future research directions are presented in Chapter 7. Additional figures, raw data and preliminary data for future work are included in Appendices A−C. Videos are included in a separate accompanying document as *Supplementary Figures*.

Chapter 2

Review of Fire Whirls and Experimental Methods

2.1 Swirl and Whirl Combustion

Whirling flames, also known as fire whirls, are a class of thermally-driven vortices which can be either reacting or non-reacting flows. A detailed classification is given by Kuwana et al. [11] and Tohidi et al. [5]. Type-I fire whirls are stationary, on-source (formed directly over the fuel source), reacting fire whirls. Reacting fire whirls that are unsteady and shed periodically (Type-II) are typically formed when a line fire is subject to angled crosswind. Type-III fire whirls can be reacting or non-reacting (comprised only of hot combustion products), but are usually formed off source [53]. They typically form close to one or more nearby reacting plumes. The fire whirls investigated in this work are all classified as stationary, on-source, and Type-I.

Whirl flames are distinct from swirl flames, with the definitions depending on the manner in which fuel and air are introduced into the reaction zone [60, 84]. In

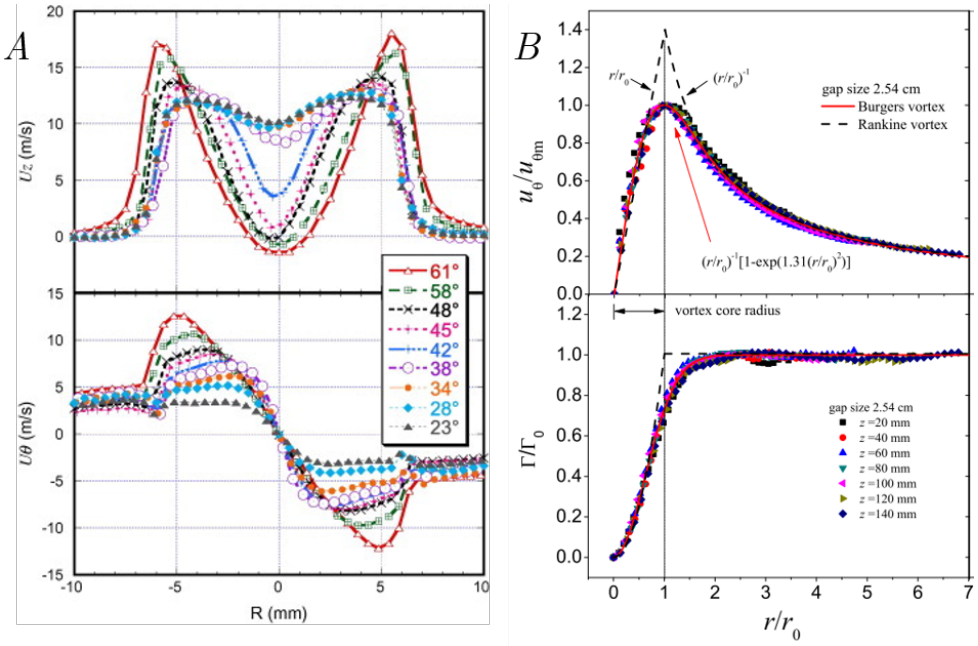

Figure 2.1: Radial variation of azimuthal velocity in (A) a swirl combustor [3], and (B) a fire whirl [4].

whirl combustion, air is introduced with a strong azimuthal component and very low axial component. Fuel is introduced separately and whirl flames are typically nonpremixed flames. In contrast, in swirl combustion, air is introduced with a combination of both axial and azimuthal components, and may be premixed with fuel. The method of flame stabilization between these flames is different. Swirl flames are stabilized by a recirculation zone that acts as a flame holder, and peak azimuthal velocities are found at the edges of the enclosure, and don't show the existence of a free-vortex region due to wall effects.

Whirling flames have a radial distribution of azimuthal velocity that is well described by a Burger's vortex model [12], and have an inner core defined by solid-body rotation and an external free vortex region. The differences are shown in Figure 2.1, adapted from references [3, 4]. The inner core in swirl flames consists of

reactants and products, whereas the inner core in whirling flames consists mostly of fuel vapor [8]. Additionally, swirl flames typically operate in the turbulent regime, even at low swirl numbers [85]; the reaction zone in fire whirls is typically in the laminar or transitional regimes for a very large range of length scales, with the plume being turbulent [86].

2.2 Fire Whirls

One of the necessary conditions for fire whirl formation according to Byram and Martin [48] is the presence of drag along the surface over which the fire whirl is formed (refer to section 1.1). This third condition, essentially a radial boundary layer at the base of the fire whirl, is not expected to be applicable to some laboratory fire whirl apparatus that are referred to as an "Emmons-type rotating mesh" setup [8], where circulation is externally imposed on the flame.

In fire whirls (Figure 2.3), the fluid sink is created by buoyancy that is generated by heat release from combustion. In a laboratory, the eddy is generated either by arrangement of obstacles in the path of the entrained air using vanes or walls, or mechanically swirling air by means of a rotating mesh or fans (Figure 2.2). During wildland fires, concentrated regions of buoyant flow may be created by fires in confined regions and eddy formation is enabled by topographical factors or opposing winds. In a laboratory environment, fire whirls are generated in a multitude of ways, all of which can be classified as either natural air entrainment [9, 12, 56, 87, 88] or forced entrainment.

The design of natural entrainment configurations typically involves a set of walls with multiple openings that permit tangential entrainment. Configurations with two half-cylindrical shells are used for small fire whirls, while the four-walled configuration is the most common [5]. When the number of panels used is above four, they are sometimes referred to as *vanes*, although few studies utilize such configurations [89]. Coenen et al. [23] used twelve vanes for their experimental study

on the blue whirl. Fire whirls can also be formed without the use of physical walls. The shedding of fire whirls from line fires was shown to be dependent on a critical ambient velocity by Zhou et al. [90], and Wang et al. [91] built a configuration using air screens, and may be considered to be a variation of the four-walled apparatus.

The most popular of forced-entrainment apparatus is the Emmons-type rotating mesh [8, 92, 93]. Lee and Garris [94] modified this configuration to include a line burner between two screens moving anti-parallelly, generating multiple equidistant fire whirls. Byram and Martin also suggested the use of a combination of both natural and forced entrainment methods to generate fire whirls by using a combination of vanes and air curtains [48]. The combination of natural and forced entrainment systems are used in some laboratory apparatus for safety purposes. A combination of the four-walled configuration with an exhaust suction system was used to generate the fire whirl photographed in Figure 2.3.

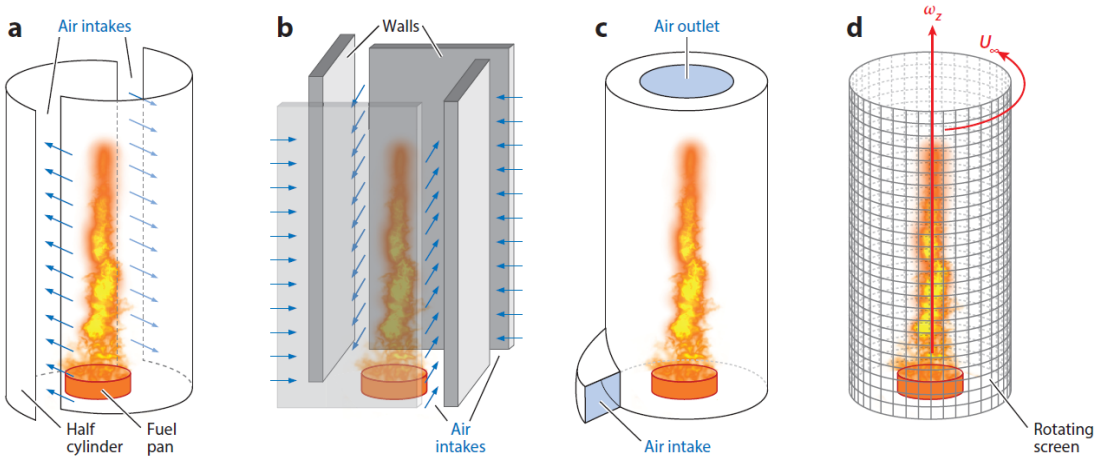

Figure 2.2: Laboratory configurations used to form fire whirls. Figure from Tohidi et al. [5].

Figure 2.3: Photograph of a fire whirl formed in a fixed-frame setup with a combination of natural and forced air entrainment. The pool diameter is 30 cm, placed in an enclosure of dimensions $3.6 \times 3.6 \times 1.5$ m^3. To increase entrainment velocity through the four inlets, a suction system was employed above the fire. In configurations with natural entrainment, buoyancy and air entrainment are coupled. Buoyancy within the enclosure must be capable of drawing sufficient air into the enclosure. This minimum level of circulation required for fire-whirl formation depends on many factors including pool diameter [6], and small pools within large enclosures do not form strong fire whirls without externally-forced entrainment.

Combustion in a fire whirl occurs in a slender cylindrical structure with the reaction occurring mostly at the edge of the vortex core where the shear is highest, promoting mixing. The interior of the fire whirl core contains mostly fuel vapor under solid body rotation [4,12,54]. Peak temperatures are found at the edge of the vortex core (Figure 2.4 A). For the same pool diameter, the height of a fire whirl is larger than that of a pool fire. This elongation and stretching of the fire whirl may be attributed to

1. the increase in burning rate (Figure 2.4), caused by increased heat flux, both convective [88] and radiative [87], feedback to the fuel surface.

2. turbulence suppression in turbulent fire whirls [95]. This is caused by increased temperatures and lower Richardson number (Ri) in the continuous-flame region of the fire whirl, resulting in increased mixing length.

3. an absence of the puffing instability that is prevalent in pool fires (see section 2.3), where the instability is responsible for periodic mixing of fuel and air. The puffing instability is replaced by a helical mode in fire whirls [23], also sometimes associated with the helical mode of vortex breakdown in conical fire whirls which are close to a transitional regime [64].

4. the vortex structure and the concentration of the vortex core through angular momentum conservation and turbulence suppression [95]. Vortex core concentration is balanced by pressure gradients generated by centripetal acceleration [8]. This structure is present even in non-reacting swirling buoyant plumes.

These ensure that in the absence of puffing, a central core of fuel vapor requires a long mixing length (and time), increasing the length of the flame sheet. The increased flame surface area essentially balances the higher burning rate in liquid-fueled flames. The higher temperatures and larger surface area also lead to a ∼40% increase in radiative feedback (see *Fig. 9* in [96]). Even if the burning rate (and thus, heat-release rate) for a pool fire and fire whirl are the same, while the total fire-whirl surface area may be the same, depending on the fuel pool diameter, fire whirls may have a lower flame width and higher flame height owing to the vortex structure. This needs to be verified in the future through systematic experiments of pool fires *and* fire whirls, both formed at the same heat-release rate using gas burners.

Drag at the bottom surface boundary is generated by a boundary layer formed by radial entrainment along the surface over which the fire whirl is formed. When circulation is not externally imposed on the flame, the presence of a radial boundary layer is essential for, or rather a consequence of, fire whirl formation. Dobashi et al. [87] performed preliminary experiments to elucidate the effect of the radial boundary layer on fire whirl formation. If the height of the vertical obstruction to inflow is higher than the radial boundary layer, fire whirl formation does not occur and the flame remains similar to a pool fire regime. For this reason, fire whirl apparatus with natural air entrainment typically have the surface of the burner (for gaseous fuels) or the fuel dish (for liquid fuels) flush with the bottom surface boundary [6, 7, 12, 23, 54, 88, 97].

For both natural and forced entrainment, when this radial boundary layer

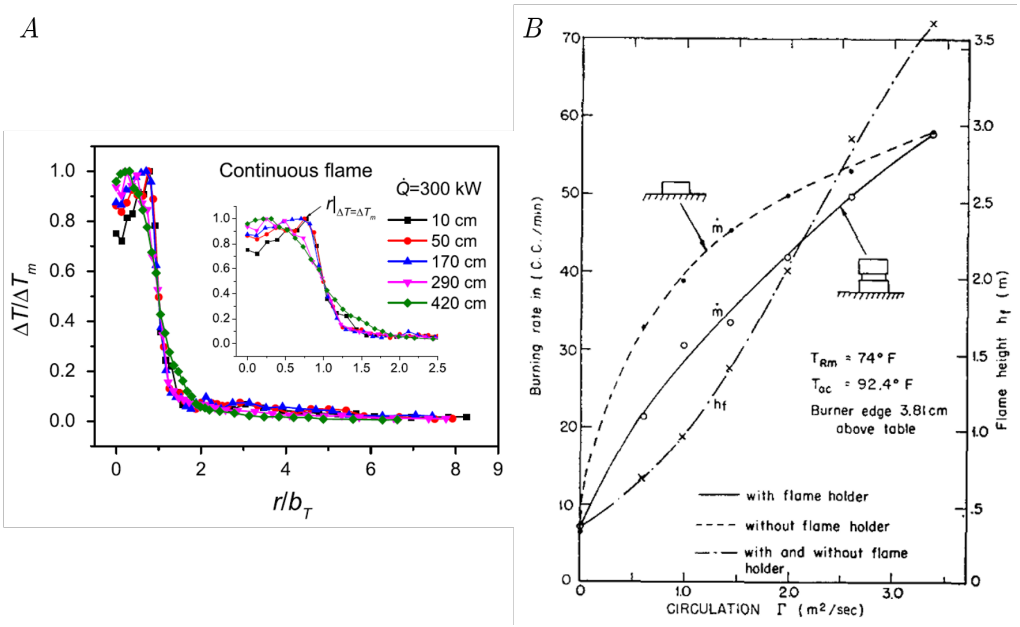

Figure 2.4: (A) Radial variation of temperature in a fire whirl, from [7]. (B) Burning rate of acetone as a function of ambient circulation, from [8]. The difference in burning rate between the cases *with* and *without* the flame holder may be attributed the level of disruption in the Ekman layer by the vertical lip formed by the flame holder.

(Ekman layer) is affected by the presence of disruptions to the incoming flow such as vertical projections formed by fuel pans etc., fire whirl behavior is affected. For instance, the influence of fuel pool height on burning rate is seen in the results of Emmons and Ying (*Fig. 5* in [8], shown in Figure 2.4 B). Experiments by Byram and Martin [48] also noted the effects of such obstructions on fire whirl formation, and noted that when the

> *burning pool of alcohol is flush with the surrounding horizontal surface, the burning rate will be drastically reduced in a strong vortex. The flame will be blown over the liquid surface except in a small, central area where a core of whirling flame a few inches in height remains. This does not happen if the edge of the burner projects a short distance above the liquid.*

These observations are very similar to the sensitivity of the blue whirl to experimental conditions [65,66]. In an apparatus allowing natural entrainment of air, fire whirl formation depends on the strength of the radial boundary layer that causes Ekman layer formation [5, 87]. The radial boundary formed under swirling flow is typically referred to as the Ekman layer in fire whirls, and a graphical representation of the velocity field around a fire whirl is shown in Figure 2.5. For a given fuel pool diameter, when the height of the step is sufficiently large to affect the radial boundary layer, the fire whirl flame shape at the bottom surface is affected (see *Fig. 11* in [87] and *Fig. 8* in [5]). Similar effects are observed even in pool fires, where the height of the lip above the bottom surface boundary affects burning rate [98–100]. For fire whirls formed in a 50 cm fuel pool, Lei et al. [97] show about a 10% difference in burning rate between two different lip heights, although the authors claim that the difference is not significant since only 1 repetition for each was performed.

Apparatus in which swirl is imposed on a jet flame, however, do not necessarily need a boundary layer or drag at the bottom surface boundary to form a concentrated reaction zone. Laboratory experiments on fire whirls do not operate in a regime where radial inflow does not exist at the base, although formation of a flame with swirling characteristics is still possible. In these cases, the concentration mechanism may be expected to be similar to a buoyant plume under ambient circulation that exhibits vortex stretching and concentration [101], and turbulence is actually enhanced by mixing at the edge of the fuel jet and the swirling flow field [62].

Chigier et al. [62] noted that in some jet flames under imposed swirl (where the radial boundary does not exist), the central reacting core does not exhibit ro-

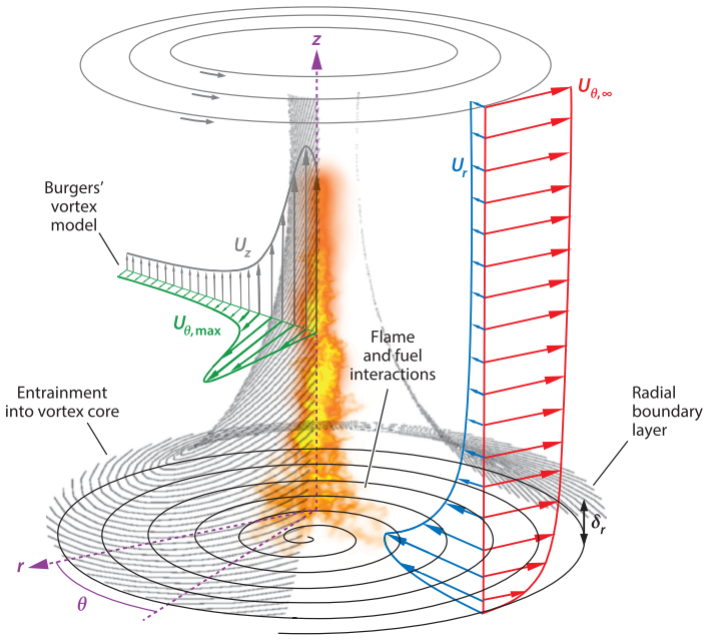

Figure 2.5: A graphical representation of the velocity field around a stationary Type-I fire whirl. Figure adapted from [5].

tation, and the external ambient circulation induces turbulence causing shortening of the flame. This is fundamentally different from a fire whirl, where the central core exhibits solid-body rotation and turbulence is suppressed, reducing mixing and leading to flame lengthening [8, 95]. Thus, in apparatus that use a central gaseous jet and externally imposed circulation to study fire whirls, the surface of the burner is typically flush with the burner exit to promote the formation of a radial boundary layer at the bottom surface boundary [6, 92, 93, 102].

For fire whirls formed with gaseous fuels supplied through a burner, burner diameters typically above 35 mm show fluid dynamic similarity with larger fire whirls. Apparatus with smaller burner diameters tend to form jets, which under imposed rotating flow fields [103] tend to show both turbulence enhancement at the lower region of the flame (similar to Chigier's observations [62]) and suppression

further downstream (similar to fire whirls). This causes jet fires under rotating flow fields to show flame shapes that are different from gas-fueled fire whirls (for ex. [92]), and consequently scale differently from fire whirls [103]. Some of these differences may be attributed to momentum from the fuel jet, which causes lift-off under high swirl [103], an effect typically not seen in liquid-fueled fire whirls. Lift-off from the surface of a liquid fuel can, however, occur when both heat-release rate and the boundary layer conditions are met [24], such as in the case of the blue whirl [23,64].

2.2.1 Scaling Approach and Influential Parameters

Scaling methods on the basis of similarity arguments have been used to predict the formation of fire whirls [11,53] and the geometric attributes of fire whirl structure [9, 12, 13, 56]. The parameters influencing fire whirl structure, as summarized in [5, 104] are

$$(U_r, U_z, \Gamma, H, \dot{m}) = \phi\left(L_h, \dot{Q}, C_p, \Delta\rho, \rho, \Delta T, T, g, \mu, \beta, \kappa, \mathcal{D}_s\right) \tag{2.1}$$

where U_r and U_z are the radial and azimthual velocity components, Γ is the circulation, H is the fire-whirl height, and $\dot{m}$ is the burning rate of fuel (either gaseous or liquid). The horizontal length scale is given by L_h. Experimentally, the heat-release rate ($\dot{Q}$) is determined either from $\dot{m}$ or oxygen-consumption calorimetry. The specific heat capacity (C_p) density change ($\Delta\rho$), excess temperature (ΔT), dynamic viscosity (μ), expansion coefficient (β), thermal conductivity (κ) and molecular species diffusion coefficient ($\mathcal{D}_s$) are determined as a function of flame temperature at the

fire whirl flame sheet. The ambient air density and temperature are given by ρ and T.

This parameter space results in 13 nondimensional groups, of which a few important numbers are mentioned here. The Froude number $\left(Fr = \frac{U_z}{\sqrt{gH}}\right)$ denotes the ratio of tangential velocity to buoyant velocity. The Rossby number $\left(Ro = \frac{U_z H}{\Gamma}\right)$ also relates the buoyant and tangential momenta, and is analogous to the swirl number for swirl combustors [57]. Dimensionally, it is the inverse of Froude number, but is estimated based on Γ, which represents the strength of ambient swirl outside the flame sheet. Chuah et al. [9] showed that the structure of fire whirls could be better described by Ro than by Fr [5]. Other traditional quantities such as Reynolds number $\left(Re = \frac{\rho\Gamma}{\mu}\right)$, Grashof number $\left(Gr = \frac{g\beta\Delta T L_h^3}{\nu^2}\right)$ and Richardson number $\left(Ri = \frac{Gr}{Re^2}\right)$, all defined for the vortex core, have been used to discuss the important role of turbulence suppression in fire whirl height [95]. Finally, the heat-release rate and buoyant momentum from fuel evaporation are given by $\dot{Q}^* = \frac{\dot{Q}}{\rho C_p \Delta T \sqrt{g L_h^5}}$ and the Peclet number $\left(Pe = \frac{\dot{m}}{\rho L_h \mathcal{D}_s}\right)$, respectively. The axial momentum represented by these two quantities is typically applicable only to reacting fire whirls. Klimenko and Williams [10] estimated Pe as $(U_z L_h/\mathcal{D}_s)$, and showed the strong influence of Pe on the nondimensional height of fire whirls under high ambient circulation (Figure 2.6). Chuah et al. [9] also found a similar relationship, and estimated U_z as

$$U_z = \left.\frac{\dot{m}''}{\frac{1}{2}\left(\rho_{fuel} + \rho_{air}\right) L_h^2}\right|_{1300\ K}$$

Apart from the quantities discussed above, parameters derived from experi-

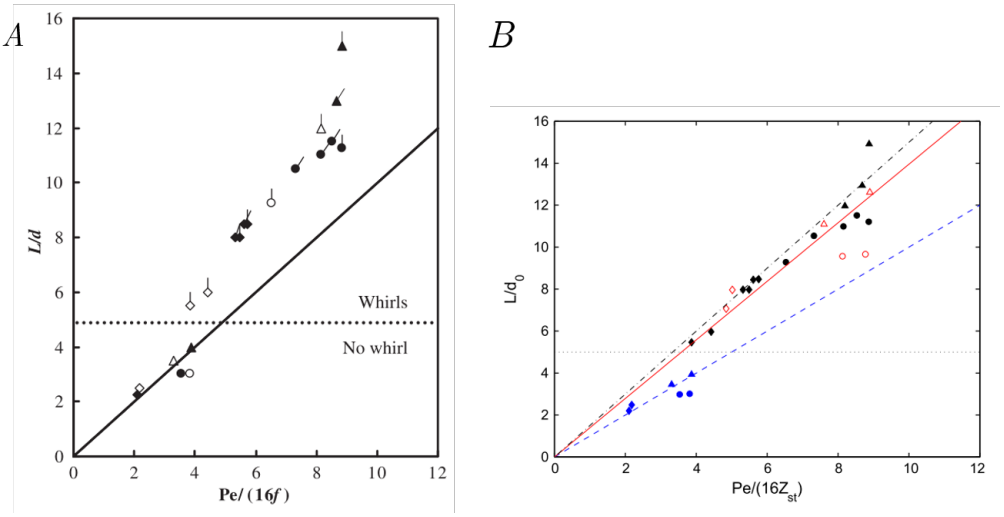

Figure 2.6: Influence of Pe on nondimensional height of fire whirls under high ambient circulation, (A) shown experimentally in [9] using a tilting fire whirl apparatus, and (B) developed analytically in [10].

mental conditions not directly related to the momenta within the vortex core have also been studied. For instance, the critical ambient velocity (U_{cr}) that may result in fire whirl formation, provided an existing fire is not dominated by momentum, varies as $\frac{U_{cr}}{g/L} \sim Fr_f^{0.15}$ [11], where L is the horizontal length scale, and Fr_f is the fuel Froude number (Figure 2.7 A). For small scale fire whirls, fire whirl height depends primarily on circulation, and this is consistent for naturally entrained configurations as well for apparatus where circulation is imposed (Figure 2.7 B). Along the height of a fire whirl that is not fully dominated by buoyancy, the circulation remains relatively constant above the entrainment region at the bottom [4,97]. The peak tangential velocity (and thus, circulation) reduces consistently from a height of $\frac{H}{L_h} = 0.4$, to the bottom surface boundary where viscous effects cause the no-slip condition [12,63].

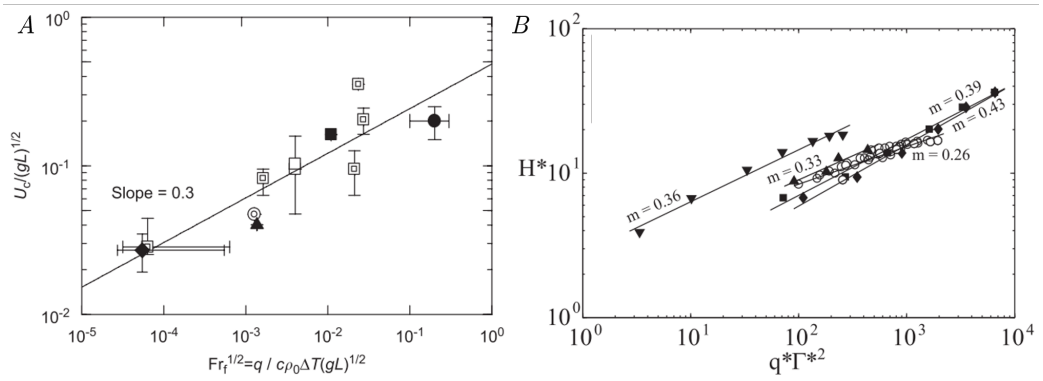

Figure 2.7: (A) Dependence of U_{cr} on Fr_f for buoyancy-dominated fire whirls, adapted from [11]. (B) Variation of nondimensional fire whirl height with nondimensional circulation, adapted from [12].

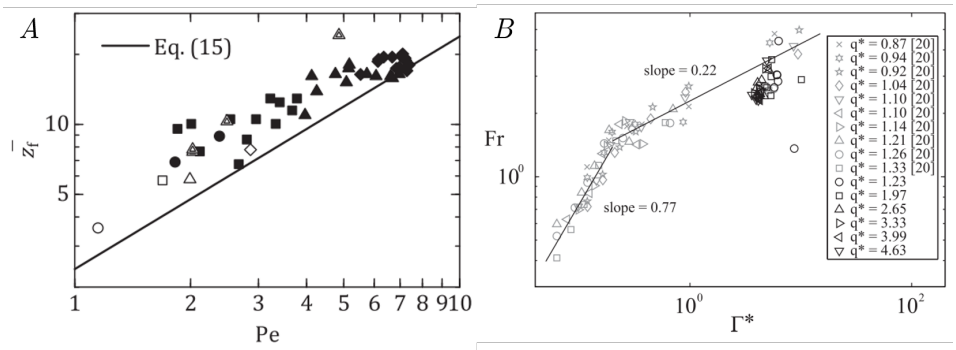

Figure 2.8: (A) Variation of flame height with Pe. The prediction of flame height based on Pe was improved by using a modified axial velocity profile. Figure adapted from [13]. (B) Dependence of Fr on nondimensional circulation, adapted from [12].

The other parameter that influences fire whirl flame height is Pe, derived from the fuel flow velocity (evaporation velocity for liquid pools, exit velocity for gas burners). Pe for fire whirls (Chuah et al. [9]) is similar to the fuel Froude number (Fr_f) defined by Kuwana et al. [11] and the ratio of fuel flow rate to advection rate [5,105]. The effect of Pe on fire whirl height is shown in Figure 2.8A. Pe defined based on fuel mass flux is represented as $\frac{\dot{m}}{\rho L_h D_s}$, where L_h is the horizontal length

scale and D_s is the species diffusivity. Similarly, Fr_f is defined as $\frac{(\dot{m}'')^2}{\rho_0 \, g \, L_h}$. The overall Fr for the fire whirl also depends on nondimensional circulation (Figure 2.8B). Hartl and Smits [12] also noted that fire whirl diameter is the appropriate horizontal reference length scales for fire whirls since fire whirls can form over an infinite fuel pool. Consequently, their experiments using a gas burner did not conform to the scaling between nondimensional circulation and Fr.

2.3 Pool Fires, Emissions and Marine Oil Spills

Pool fires (Figure 2.9) are a standard research problem applicable to a wide range of fire scenarios, and are of interest for both fundamental and practical purposes. Characteristics such as pulsation frequency, burning rate, heat flux feedback, temperature, soot fraction and radiation have been studied for various fuels, and detailed reviews are presented in [106–109]. Additionally, flame structure [98] and scaling behavior [110] are also of interest for predictive purposes, including cases where a free buoyant plume is affected by crosswinds etc. [111].

Entrainment of air towards pool fires causes necking of the flame at the base and causes the initiation of Rayleigh-Taylor instabilities [112]. These instabilities cause the development of the phenomenon known as "puffing," which is a periodic oscillation and fluctuation of the flame height. The puffing frequency, f, decreases with pool diameter as $\mathsf{f} \propto D^{-0.49}$ [14], and the puffing Strouhal number (St), is linearly dependent on the Froude number (Fr) [15] (see Figure 2.10). The onset of puffing is attributed to a critical Rayleigh number (Ra) [113], supported by the development of large-scale toroidal vortex rolls occurring at an axial distance within one burner diameter above the fuel surface [114]. Cetegen et al. [114] also found that the puffing frequency for thermal and isothermal plumes was similar ($\mathsf{f} \propto D^{-0.5}$). Bejan [115] analyzed the phenomenon using the buckling of inviscid streams to explain why the expression $\mathsf{f}^2 \cong \frac{2.7\,[m/s^2]}{D}$ worked well in predicting shedding frequency (f, [s^{-1}]) over a very large range of pool diameters (D, [m]).

Interest in the studies of emissions from pool fires, particularly particulate

Figure 2.9: Photograph of a pool fire formed with n-heptane, $D = 30$ cm.

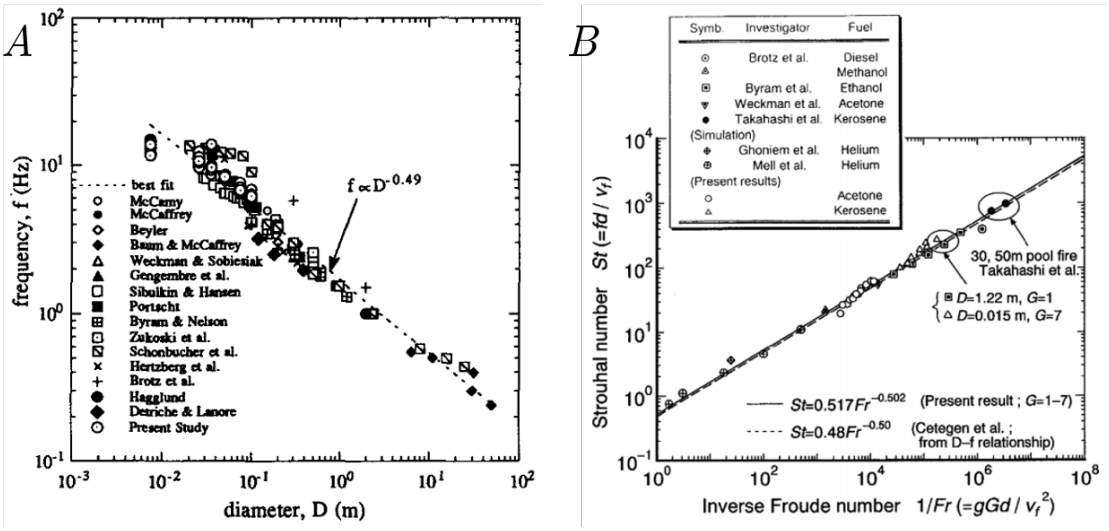

Figure 2.10: (A) Dependence of pool-fire puffing frequency on pool diameter, adapted from [14]. (B) Influence of Fr on puffing St, adapted from [15].

matter, CO, and CO_2 is recent, stemming mostly from the initial work of Aurell et al. [116] on solid waste incineration. Measurements of emissions from pool fires of gaseous and liquid fuels have also been performed [16]. Apart from particulate matter, CO, and CO_2, various PAHs and VOCs were also measured, each with an emission factor in the range of hundreds of milligrams per kilogram of fuel. Experiments involved sampling in the fire plume, and the calculated emission factors and the modified combustion efficiency $\left(MCE = \frac{\Delta CO_2}{\Delta CO_2 + \Delta CO}\right)$ are shown in Figure 2.11.

There have been a number of studies of oil spreading over open water [117,118], and several of these have addressed the problems of burning spilled fuel [119]. Oil spills can have devastating effects on both onshore and offshore ecosystems. Burning spilled oil is a quick response method [76] since their long-term existence can cause toxicity to both wildlife and humans [120]. The work of van Gelderen et al. [121] identified properties such as initial slick thickness, vaporization order, slick diameter, weathering state, heat flux feedback and heat losses to the water layer as factors that influence burning efficiency in an *in-situ* burn (ISB).

During recovery efforts for accidental spills, the dispersed fuel is gathered using booms and ignited once the fuel layer is thick enough. This layer must be thick enough because it must insulate the top layer of fuel from the water. This entire approach is fundamentally different from traditional approaches and studies of pool fires burning lighter fuels over water [122]. Wu et al. [123] performed experiments to determine the ignition, flame spread, and mass burning characteristics of oil spilled on water. Later they expanded to more detailed ignition experiments determining

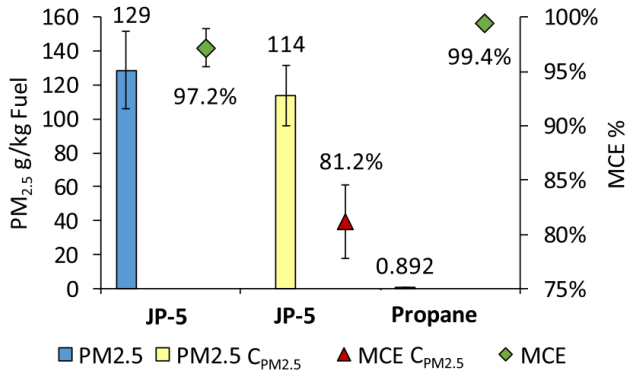

Figure 2.11: Comparison of PM-2.5 emission factor and Modified Combustion Efficiency (MCE) for JP-5 and propane pool fires. Figure adapted from [16].

the effects of weathering on crude oil [124], which is important because, as oil becomes more weathered, it becomes more difficult to ignite, and finally it emulsifies to the point where ignition is no longer possible [125]. Based on these results, phenomenological descriptions have been developed for combustion of oil on a water layer [126, 127].

More recent experiments have extended the experimental capability to measure the properties of crude oil layers and its effects, particularly applied to arctic regions [128]. No prior studies, however, have been conducted to understand and characterize the fundamentals of fire whirl behavior over open water, in particular from small to large scales. More background on this is provided in Chapters 3 and 4.

2.4 Soot Formation and Emission

The study of soot formation and emission from flames has been a challenging problem in combustion science [129]. Soot may be defined as a carbonaceous material containing up to 1% hydrogen by mass, an empirical formula of C_8H, with diameters of aggregates ranging between 100 and 2000 Å [130]. Soot formation and destruction processes occur simultaneously in flames. This was illustrated as early as 1908 in "*The Chemical History of a Candle*" by Michael Faraday [131, 132]. The process may be simplified to the following four processes [17]:

1. Formation of precursor species.
2. Particle inception.
3. Surface growth and particle agglomeration.
4. Particle oxidation.

While both premixed [133–135] and nonpremixed [130, 136] flames can form and emit soot, from an engineering perspective, nonpremixed flames are primarily studied since they are used in most engines (internal combustion such as reciprocating [137] or gas turbine [58]) and industrial burners and flares [79]. The term particulate matter (PM) is more commonly used [58] and is a concern since they can have significant impact on human health [138]. As a consequence, PM emissions from commercial engines and burners are strictly regulated by environmental agencies around the world [139].

The tendency for a flame to emit soot can be represented by an empirically obtained property called the *smoke point*, an experimental condition that results in visible emission of black soot from a flame. Experiments use a diffusion flame and the smoke point is measured in terms of either the maximum flame height or maximum fuel flow rate at which a stream of soot is first visible downstream of the flame. The larger either of these values, the lower the propensity of the fuel to soot [17]. The propensity for the different fuel families to soot, from highest to lowest, is *aromatics*>*alkynes*>*alkenes*>*alkanes* [140].

Although soot may be formed in the flame, it is not necessary that soot is emitted from the flame. Soot typically originates on the fuel side of a diffusion flame and has to pass through the oxidation region at some point during the flow. If the soot if fully oxidized in this region, no soot is emitted. If the soot is not fully oxidized, it is emitted from the flame and may be visible as a streak. Laminar jet diffusion flames typically have a pointed shape when the soot is completely oxidized by the flame. The formation of soot, however, causes "wings" to form, from which a streak of soot emanates (refer to *Fig. 4* in [141]). This is illustrated in Figure 2.12.

The primary factors controlling sooting are the nature of the fuel (number of C–C bonds, C/H ratio etc. which are dependent on the whether the fuel is an aromatic, alkyne etc.), diluents in the fuel stream, equivalence ratio (controlled by mixing), local temperature, flow conditions such as turbulence, ambient pressure, gravitational environment, the flame curvature and strain rate, and acoustic excitations, [130, 142–149]. These factors also affect the structure of soot formed in different regions of the flame [150]. Of course, these factors have multiple interde-

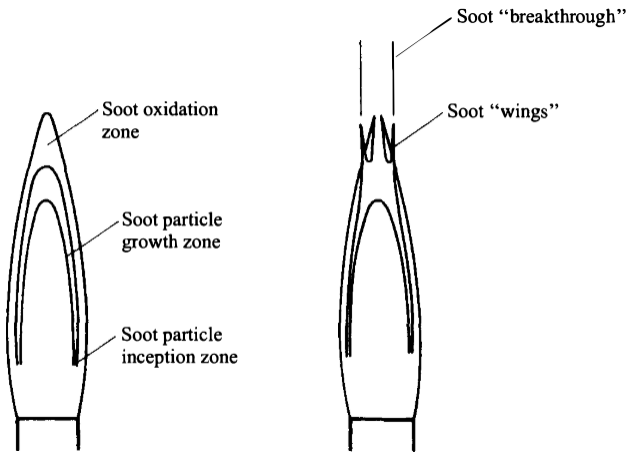

Figure 2.12: Schematic showing soot formation and destruction zones in a laminar jet diffusion flame. Figure from Turns [17].

pendencies. For instance, fuel structure affects sooting tendencies in nonpremixed flames, but has little effect in fully premixed flames since "*in premixed flames there is a competition between the rate of pyrolysis to form the precursors and the rate of oxidative attack; thus, since the oxidation rate increases faster with temperatures than the pyrolysis rate, the higher the flame temperature, the lower is the tendency to soot*" [151]. In nonpremixed flames, however, soot inception begins around 1300–1400 K and soot volume fraction depends on temperature and initial structure of the fuel molecule [130].

Soot inception and growth in flames depends on flame structure [152] and chemical kinetics which control both formation and oxidation [153, 154]. Processes responsible for the conversion of gas-phase species to the condensed phase are controlled by the chemical kinetic behavior of precursor species such as polycyclic aromatic hydrocarbons (PAHs) and aromers [18,155]. A schematic of soot formation in different regions of a flame is shown in Figure 2.13. Johansson et al. further studied

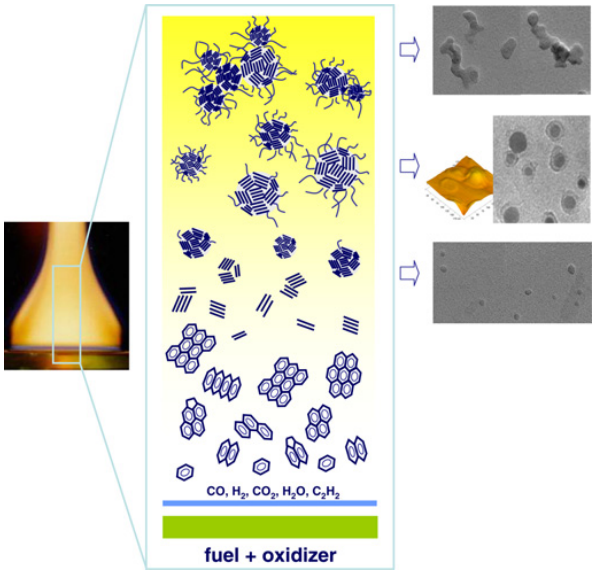

Figure 2.13: Figure showing the evolution of soot structure in different regions of a flame. Figure from [18].

the processes involved in the conversion of gas-phase PAHs to particle formation and growth [19]. The stability of the formed soot was found to be from resonance stabilization of the graphitic layers in the multi-layered structure of soot. The different stages of soot inception, graphitization and growth are shown in Figure 2.14.

2.4.1 Soot Diagnostics

Measuring parameters such as soot number density, volume fraction and size distribution are important to understand kinetics in flames, radiation in fires and emissions. A classification of the different techniques is shown in Figure 2.15, adapted from [20]. *In-situ* experimental techniques to measure such characteristics may involve thermocouples and [156], dilution probes [157], thermophoretic sampling [158–161], and deposition based techniques [20]. Transmission Electron Microscopy (TEM) is used to measure soot-aggregate size distribution from the

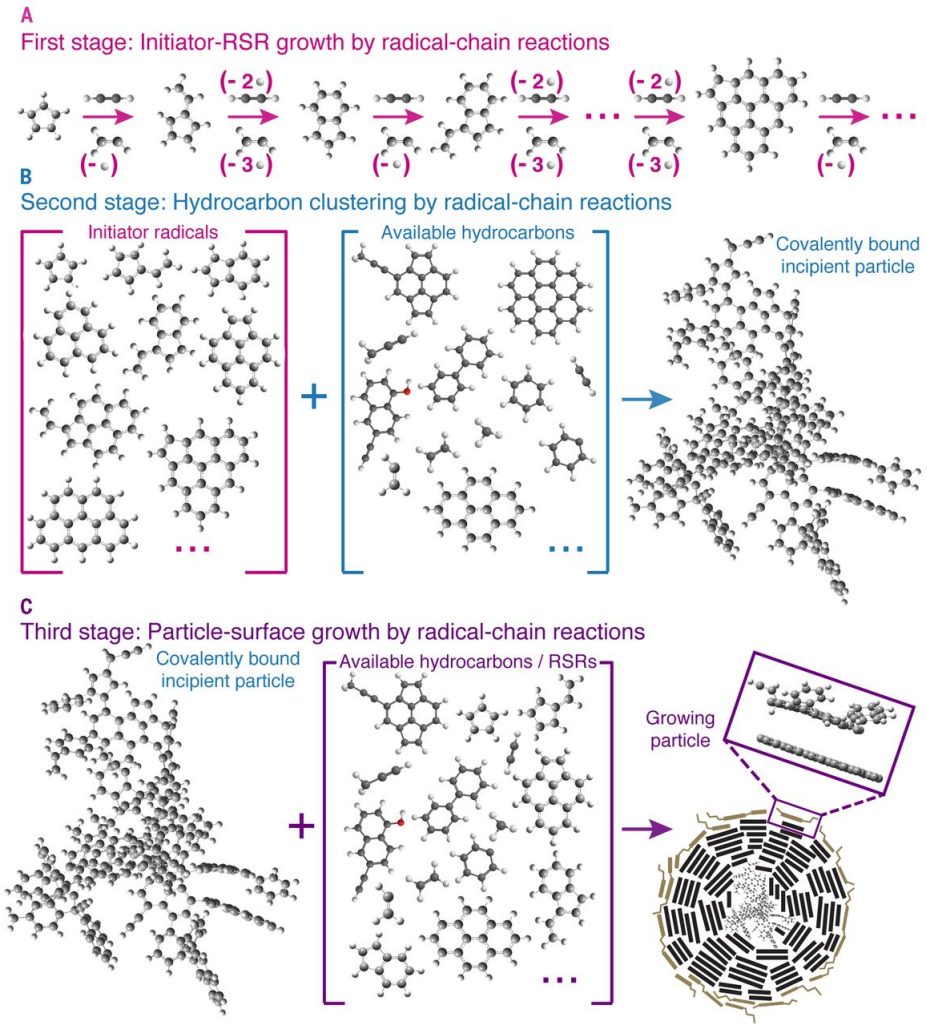

Figure 2.14: Schematic showing the different stages of soot inception and formation, beginning from PAHs to particle growth. Figure from [19].

samples, which may be collected *in-situ* and or in the post-flame regions [162, 163]. Non-intrusive optical techniques involve either digital cameras [164, 165] to perform pyrometry [166, 167], or laser-based diagnostics such as Laser-Induced Incandescence (LII) [168, 169]. Optical diagnostics are more suitable when physical probing can interfere with the physical or chemical processes in the flame. They may be used to measure soot temperature, volume fraction and size distribution and are used in laminar or turbulent flames [170], premixed [171] or nonpremixed flames [172].

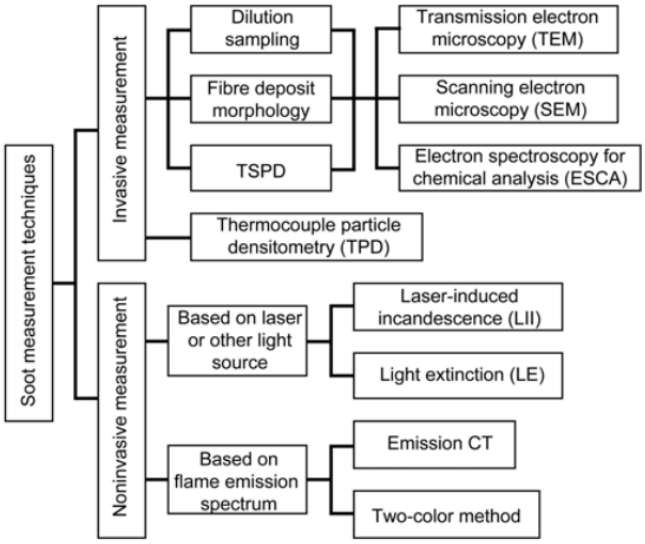

Figure 2.15: Soot measurement techniques, adapted from [20].

The measurement of particulate matter emitted by flames in the post-flame region uses a combination of different techniques including gravimetric approaches, scattering and absorption [173]. A review of the different techniques are presented in [174]. Flame Ionization Detection (FID) is a technique used to detect both soot and unburned hydrocarbons [175]. Atmospheric particulate matter measurements typically use a gravimetric approach to quantify the mass of PM emitted over a stipulated time period and are deployed over large geographic areas [176] and during events such as wildfires [177]. Measurement of PM specific to soot emissions from engines require sensors to be portable and typically use optical techniques such as infrared scattering since understanding size distribution in the exhaust is important [178, 179].

For the work considered in this dissertation, measurement of particulate matter is performed in the post-flame region using a laser scattering technique. Particle size distributions are determined based on Mie theory [180]. The TSI DustTrak

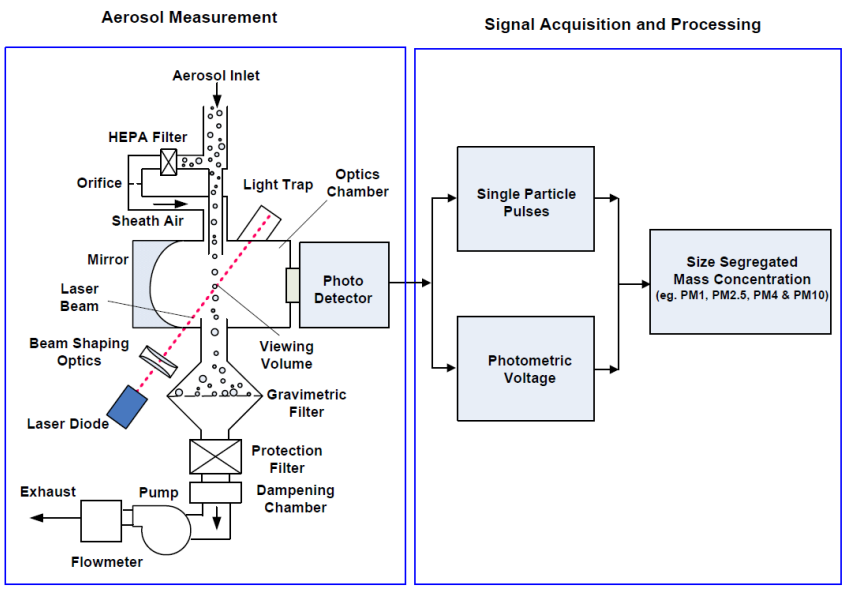

Figure 2.16: Schematic of soot measurement in the TSI DustTrak, adapted from [21].

instrument [27] used in this work measures the mass concentration of PM-2.5 particles and estimates a particle size distribution based on a calibration aerosol mix called Arizona Road Dust [21]. A schematic of the aerosol measurement by the TSI DustTrak is shown in Figure 2.16. A separate gravimetric calibration was performed to convert adjust for the difference in density between the calibration aerosol and soot emitted from the fires. Only Total Particulate Matter (TPM) measurements are reported since measurements of size distributions of the emitted soot are not available.

2.5 Current Understanding of the Blue Whirl

The blue whirl (Figure 2.17) is a flame first observed when studying fire whirls in a fixed-frame setup with natural air entrainment. The blue whirl evolved from fire whirls formed with liquid fuels floating over a water surface, first reported by Xiao et al. [64]. Figure 2.18 is a sequence of images showing intermediate states that are visible in the transition to a blue whirl. Although the blue whirl was discovered to transition from fire whirls formed over a water surface, experiments with other surfaces showed that the "presence of the water itself was not essential, but the presence of a smooth boundary is critical" [66]. This unimpeded surface boundary permits the formation of an Ekman layer, thought to be necessary for transition to the blue whirl.

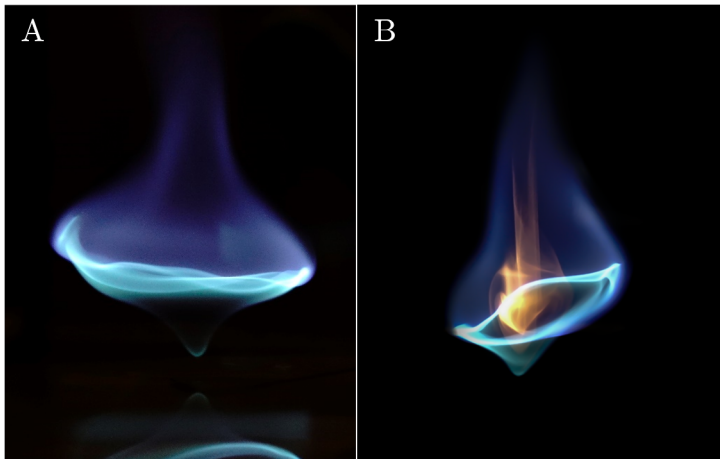

Figure 2.17: (A) Image of a blue whirl formed using iso-octane over a flat metallic plate. (B) The recirculation zone within the blue whirl is visualized by incandescence of soot particles entrapped in the recirculation zone. This image was captured with an exposure time of 1/25 s, allowing sufficient time for steaks to develop in the axial direction. Image from Hariharan et al. [22].

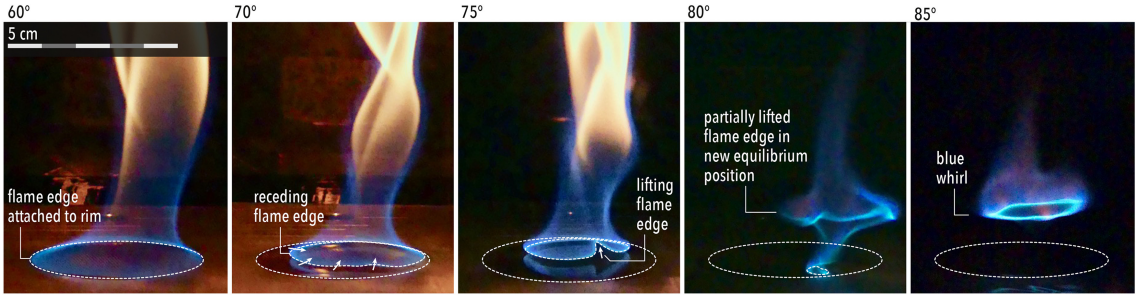

Figure 2.18: Sequence of images showing the region immediately above the fuel pool during different intermediary states before formation of the blue whirl. Figure from Coenen et al. [23].

During the transition from a fire whirl to a blue whirl, the presence of a recirculation zone within the lower blue conical region is visible due to soot incandescence (Figure 2.17 B). This internal flow structure is visible only during the transition due to the temporary presence of soot, but it is expected that the recirculation zone exists after stable blue whirl formation [66]. This recirculation zone was postulated to be the result of the onset of a bubble mode of vortex breakdown in a fire whirl [65, 181]. The transition process from a fire whirl to a blue whirl occurs in this order – onset of vortex breakdown in the fire whirl, appearance of the recirculation bubble, lifting of the base of the flame to form the bright blue ring, formation of the lower blue cone, disappearance of soot in the flame, and finally stable blue whirl formation (see *Fig. 10* in [66]). The bright blue ring was termed as the vortex rim in [22], and it was suggested in [65] that it may be similar to a vortex ring, although these have not yet been confirmed.

Hariharan et al. [22] obtained a thermal map of the blue whirl using thin-filament pyrometry. The map showed a wide region of high temperatures above the bright blue ring, and relatively lower temperatures below it. Peak temperatures,

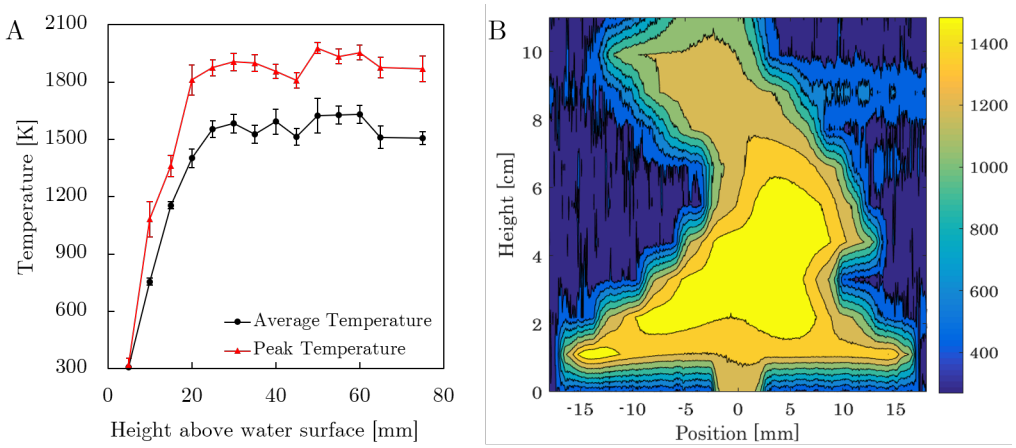

Figure 2.19: (A) Thermocouple measurements in the blue whirl, showing peak temperatures around 2000 K. (B) Temperature map obtained by thin-filament pyroemtry, for a blue whirl formed using iso-octane formed over a water surface. Figures adapted from [22].

obtained from thermocouple measurements, were found to be around 2000 K in the region above the ring, termed the purple haze. The temperature measurements are shown in Figure 2.19. Formation of the blue whirl over surfaces other than water, such as a flat metallic plate and a porous surface was shown in a follow-up study [66], which also showed qualitative similarity in the temperature maps. Further, images of OH* chemiluminescence in the blue whirl (UV, 310 nm) showed significant intensity in the bright blue ring, and minimal intensity in the regions below and above it, which suggested that a significant fraction of the reaction occurred there, which also supports the thermal structure obtained from temperature measurements. Obtaining a map of equivalence ratio distribution in the blue whirl using chemiluminescence measurements is discussed later in Chapter 6.

The relationship between the combination of circulation (Γ), heat-release rate ($\dot{Q}$) and the dimensions of the enclosure within which the blue whirl formed was

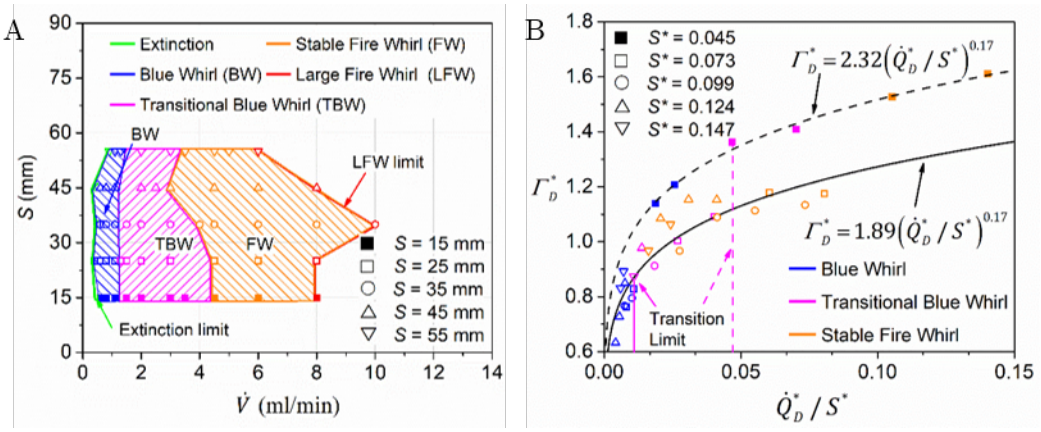

Figure 2.20: (A) The effect of gap size, S, and fuel flow rate, $\dot{V}$, on the fire whirl regime formed. (B) Relationship between nondimensional circulation and heat-release rate showing transition limits to the blue whirl. The subscript 'D' refers to the reference length scale, which was chosen as the enclosure diameter for nondimensionalization. Figures from [24].

explored by Hu et al. [24]. This work showed that the Γ and $\dot{Q}$ resulting in blue whirl formation (Figure 2.20) was close to the extinction limit previously defined for fire whirls by Lei et al. [92]. Although apparatus diameter or gap size are not intrinsic properties affecting fire whirl behavior, these have been used in the literature for experiments on fire whirls formed in both natural and forced air-entrainment configurations [5, 11, 12, 54]. Following this approach, nondimensional circulation (Γ^*_D) and heat-release rate ($\dot{Q}^*_D$) were defined based on the enclosure diameter, D. The relationship between these quantities is shown in Figure 2.20 B, which shows that the blue whirl transition limit depends on the ratio of gap size, S, to D.

2.6 Chemiluminescence and Planar Laser-Induced Fluorescence

The detection and measurement of species important to combustion processes is an important diagnostic method to understand the behavior of flames and combustion devices. A multitude of techniques exist to non-intrusively measure various properties such as temperature, flow and chemistry, in a combustion process. Optical methods are the primary non-intrusive technique, including Raman scattering for major species and temperature [182], and Laser-Induced Fluorescence Spectroscopy (LIFS) for minor species [183]. While Raman spectroscopy and absorption methods are also used for detecting and measuring concentrations of major species [25, 184], techniques related to emission spectroscopy are used in this work. The nature of emission and absorption by the species are governed by quantum mechanics [25], and the kinetics governing the formation and destruction of these radicals in hydrocarbon-air reactions has been studied previously [185–187], and are used in numerical evaluation of local flame properties [188].

The important species for optical characterization of flames are OH, CH, CO_2 and C_2 [189], and the spontaneous emission by de-excitation of these radicals is termed as chemiluminescence. Excited radicals are denoted as OH*, CH*, C_2*, CO_2*, which contribute the most to visible and UV emissions in hydrocarbon-air flames [187,189]. The concentration of these radicals and the corresponding intensity of emission are a function of pressure [190], local equivalence ratio, strain rate [191], nature of the fuel, etc. [32,192]. The relative intensity of chemiluminescence signals may be used to determine local flame properties (in non-sooting flames [182]) by

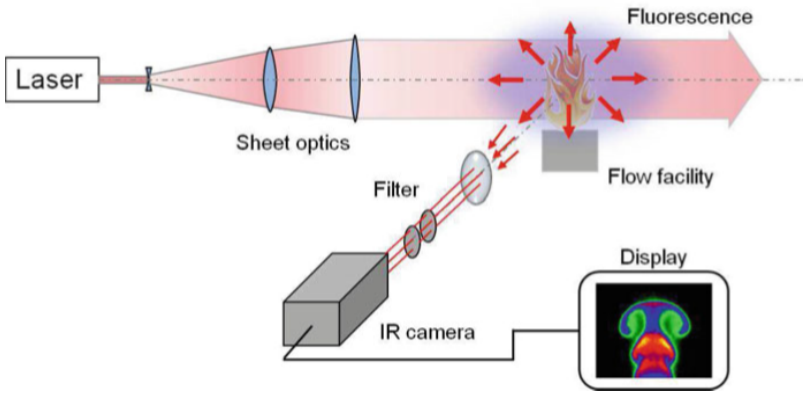

Figure 2.21: Schematic showing an experimental setup to perform PLIF. Figure from Hanson et al. [25].

evaluating the ratio of the relative emission intensities of the different radicals [32, 187, 190, 192–195].

The other important technique is induced fluorescence, of which the most commonly used configuration is Laser Induced Fluorescence (LIF). Here, the radicals are excited by a laser at a particular frequency, and the emission from the excited state is observed using a camera, which is similar to observations of spontaneous chemiluminescence. Compared to Raman scattering, the signal levels are higher in LIF, and species measurement are not affected much by background noise from other species [25]. When a 2-D laser sheet is used to excite the flame, a camera is positioned 90° to the sheet to detect signals, the technique is called Planar LIF (PLIF). Figure 2.21 shows a typical experimental setup to perform PLIF. The pulse (or repetition) rate of the laser can be on the order of kHz, and PLIF is thus used in the diagnostics of complex combustion environments such as high speed flow [196, 197], turbulence [67, 198]. It is often used in engines and turbines since it can often be coupled with other diagnostics such as Particle Image Velocimetry

(PIV) and/or temperature measurements [59, 70, 199–202], along with the ability to image multiple species simultaneously.

Chapter 3

Measurement of Particulate-Matter Emissions from Liquid-Fueled Fires

3.1 Introduction

Marine activities such as oil exploration and extraction can cause accidental oil spills into inshore or offshore waters. Oil spills can pose a serious threat to surrounding populations [78,203], response workers [77], and ecosystems [120,204,205]. Additional effects include substantial disruption to local oil exploration infrastructure, marine transportation, and potentially widespread economic impacts [206]. Rapidly advancing oil recovery technology as well as increased interest in local production continues to increase the probability of oil spills' occurrence [207]. In the case of such a spill, an efficient, effective, and robust treatment technique is crucial to mitigate their impact. In this regard, in situ burning (ISB) is one of the most reliable and effective oil spill treatment techniques [74,125,208], particularly in con-

ditions where remoteness, harshness of the climate, and scale of the incident make it impossible for mechanical recovery or dispersant techniques to be deployed and utilized immediately after the spill.

Decades of laboratory and meso-scale testing of in-situ combustion of oil have shown that the composition and concentration of emitted emissions from ISBs is an acceptable trade-off in relation to inshore and offshore contamination and its environmental consequences and cleanup costs [75, 208]. In fact, efficient ISBs have been shown to effectively eliminate at least 90% of the released liquid oil in some cases [209–211], and is a relatively fast and portable method of treating oil spills. This is especially important since 70% of the untreated, spilled oil can emulsify during the first 24 hours [125].

Despite their effectiveness, ISB techniques are still challenged by the airborne emissions they release (especially near shorelines), the degree of weathering and emulsification which decreases fuel flammability, and the intensity of ambient wind and waves. In general, pool fire burns over water are oxygen-starved [206,212]. This leads to the emission of black soot (particulate matter, PM) that is visible from as dense smoke emanating from ISBs. In fact, one of the major operational limits of current ISB practices is the after-burn emission concentrations, particularly at the downwind locations that may lie close to populated areas. For instance, the maximum 1-hour averaged concentration of PM-10 (PM of ten μm or lower in diameter) must not exceed 150 $\mu g/m^3$, according to ISB guidance from the United States National Response Team, Science and Technology Committee [206]. Reduction of PM emission and high-efficiency burning requires the fire to reach ample

oxygen concentrations, high temperatures over the fuel surface and completeness of combustion [208].

One potential method of enhancing these parameters is to induce swirl to the air entrained to the fire, causing the formation of a fire whirl (FW). FWs are structures which arise when the right conditions of wind and fire interact, and are typically studied in the context of fire safety during wildland and urban fires [5]. The FW structure results in intensification of combustion, imposing significantly higher heat feedback to the fuel surface, increasing the rate of burning, potentially reducing airborne PM, and decreasing post-combustion residuals (on the water surface). It is thought that high efficiency combustion may occur through higher of oxygen availability and increased temperatures within the fire, ultimately reducing the emission of PM from the plume. There are open questions, however regarding this hypothesis. For instance, one important mechanisms of reducing emissions is ensuring sufficient mixing, which is typically achieved by increasing turbulence intensity. Turbulence, however, is suppressed in FWs [8, 95]. Thus, the hypothesis that is tested is: the burning of a pool of liquid hydrocarbon fuel in a FW structure emits lower quantities of PM as compared to burning as a PF.

3.1.1 Outline

This chapter details experimental investigations of emissions from pool fires (PF) and fire whirls (FW) at various scales, conducted at the University of Maryland (UMD) and Worcester Polytechnic Institute (WPI). To demonstrate the ef-

fectiveness of using FWs over pool fires, experiments were conducted using two fuels, n-heptane and Alaska North Slope (ANS) crude oil. For all experiments, laboratory-grade heptane from Aqua Solutions Inc. or Fisher Scientific was used, and ANS crude oil was supplied by the Bureau of Safety and Environmental Enforcement (BSEE). Experiments were performed at four different fuel-pool diameters ($D = [10, 20, 30, 70]$ cm). Experiments at $D = [10, 20, 30]$ cm were performed at UMD, and those at $D = 70$ cm were performed at WPI. PFs and FWs are compared on the basis of burning rate ($\dot{m}$), post-burn residual weight, emissions of PM, CO, CO_2, O_2 consumption, flame temperature and heat feedback ($\dot{q}''$) to the fuel pool.

The general experimental methods used for all experiments at all scales are described in section 3.2. The experimental data are presented in detail in section 3.3. An analysis of the emission factors and preliminary explanation of the factors controlling emissions from the different fires is presented in section 3.4, along with a summary in section 3.5. A detailed analysis of the mechanisms and the role of circulation and buoyancy are discussed in Chapter 4.

3.2 Experimental Methods

3.2.1 General Apparatus

A fixed-frame, four-wall configuration was used to generate FWs at all scales. The four walls were positioned to form an enclosure, and the fuel pool was placed at the center of the enclosure over the bottom surface. This four-walled setup permits natural entrainment of air to the fire through the four gaps (see Figure 3.1), forming an on-source, quasi-steady FW [5]. These are a stable and stationary form of FWs, providing a good platform to compare them with PFs. Four-walled setups are also simple to construct and allow flexibility in choosing the enclosure side (S) and gap width (W). For experiments at all scales, reliable and steady FW formation was observed when the $\frac{W}{S}$ ratio was kept constant at $\frac{1}{4}$. The dimensions of the enclosures used at different scales in this study are tabulated in Table 3.1. To generate PFs, the walls were removed to allow radially-symmetric air entrainment to the fire.

A circular dish made of aluminum was used to contain the fuel pool. The dish was used to hold a water sublayer above which the fuel slick floated, mimicking open-water conditions at a lab scale. This also eliminated any warping in the metal dish due to high temperatures during burning of the fuel pool. The quantity of fuel used for experiments at each scale were determined based on the thickness of the resulting fuel slick. Since a minimum slick thickness around $2 - 2.5$ mm is required to support combustion, a thickness of 5 mm was decided to allow sufficient time for fire whirl development and adequate data from the various measurements. For

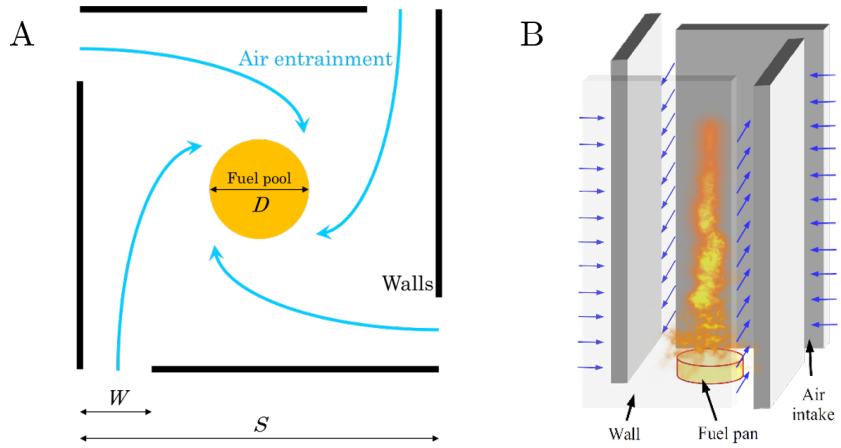

Figure 3.1: Schematics of the experimental configuration used to form FWs at various scales. The ratio of gap width (W) to enclosure side length (S) was maintained at $W/S = 1/4$ for experiments at all scales. Schematic in panel (B) from Tohidi et al. [5].

experiments at the 70 cm scale, some experiments were performed with both 5 and 7 mm slicks of ANS crude oil to study their effect on boilover. This is discussed in detail in section 3.3.3 and Chapter 4.

The depth of the dish was dependent on the pool diameter, D. The values of D, dish depth, fuel volume, fuel-slick thickness for the different experiments are shown in Table 3.1. For a given experimental condition (defined by D, fuel type and flame regime), the slick thicknesses were the same for both fuels to maintain consistency. Similarly, all test conditions were kept consistent for both PF and FW regimes.

Two liquid fuels, n-heptane and ANS crude oil, were used for experiments. Experiments were performed at each scale with both fuels to allow for comparisons and scaling. N-heptane (C_7H_{16}) is a single-component liquid hydrocarbon with a low flash point (-4 °C) and was chosen due to its steady burning rate in both the pool fire and fire whirl regimes. Using this fuel eliminates the effect of time-varying

Table 3.1: Experimental conditions for pool fires and fire whirls formed using heptane and ANS crude oil.

Pool diameter, D [cm]	Gap width, W [cm]	Enclosure side, S [cm]	Enclosure height, H [cm]	Fuel volume [ml]	Slick thickness [mm]	Fuel dish depth [cm]
10	15	60	60	40	5	10
20	25	100	100	160	5	5
30	25	100	100	350	5	20
70	45	175	240	2000	5	70
				3000	7	

fuel composition on the burning rate and aid in identifying general trends to explain the behavior of more complex fuels like crude oil. ANS crude oil was used to mimic a realistic spill. Multi-component fuels such as ANS, with their constituent species having a wide range of flash points, provide an opportunity to study the influence of a fire whirl on complex fuels and their residue after extinction of the fire. Table 3.2 shows important physical properties of the fuels used.

At $D = [10, 20, 30]$ cm, the fuel dish was placed over a load cell, which was used to measure the instantaneous mass of the fuel and determine the burning rate ($\dot{m}$). The heat-release rate (HRR, $\dot{Q}$) is determined by $\dot{m}$. At $D = 70$ cm, however, the excessive weight of the fuel-water container, the use of a load cell was not possible, and thus $\dot{m}$ was not directly measured. Two alternate methods were used instead to measure $\dot{Q}$: (i) peak and instantaneous $\dot{Q}$ was measured using oxygen-consumption calorimetry; and (ii) the average $\dot{Q}$ was measured using the average value of $\dot{m}$,

Table 3.2: Physical properties of the fuels discussed in this work. Data obtained from Material Safety Data Sheet (MSDS) for each fuel. Crude oil properties are a strong function of the level of evaporation and composition, resulting in significant variation in the reported properties.

Fuel	Density [kg/m^3]	Flash point [°C]	Boiling point [°C]
n-Heptane	684	-4	98
ANS Crude Oil	866	$25-35$	>38
West Texas Intermediate	867	32	>35
Diesel	830	50	$120-350$

determined as the ratio of fuel mass consumed by the fire and the burning duration (t_b).

A typical experiment involved the following steps:

(i) addition of water into the glass dish,

(ii) addition of of fuel (n-heptane or ANS) over the water surface,

(iii) beginning data logging using NI LabView, TSI TrakPro and/or BalanceLink,

(iv) ignition of the fuel using a butane torch,

(v) stopping data logging upon extinction. Residue was collected and weighed for experiments with ANS crude oil.

All experiments were performed a minimum of three times to assess variability in the measured quantities.

3.2.2 Exhaust Duct and Emissions Sampling

The exhaust from the fires were channeled through a duct (28 cm in diameter) to facilitate sampling and measurement of the different gas species in the combustion products. The entire fire whirl apparatus was placed under a suction hood as shown in Figure 3.2. A fiberglass curtain was draped along the perimeter of the hood to ensure all combustion products were collected. Gases were sampled from the duct at a downstream location greater than 10 diameters from the entrance to the duct to ensure for sufficient mixing.

The exhaust duct was instrumented with thermocouples (TCs) and a Verabar V100 differential pressure transducer. The volumetric flow rate through the duct was estimated to be 0.114 m^3/s, based on a 0.5 V operating voltage in the differential pressure sensor. A maximum flow rate of 0.8 m^3/s could be achieved at $\sim$3.5 V, with a roughly linear dependence of flow rate on voltage. The TCs were positioned 5 cm, 10 cm and 14 cm from the wall of the duct. During operation, the maximum spread of temperature between the three TCs was less than 2 K, justifying the assumption of constant temperature and well-mixedness across the duct.

Two sampling tubes were used in the suction duct, each with 17 holes, each 2 mm in diameter, along the length of the tube. This ensured sufficient sampling from across the diameter of the exhaust duct. In both sampling tubes, the sampling holes were pointed in the downstream direction of the flow within the duct to avoid clogging of the holes by soot. Combustion products encountered the differential flow meter, thermocouples, the sampling tube for PM, and sampling tube for gases, in

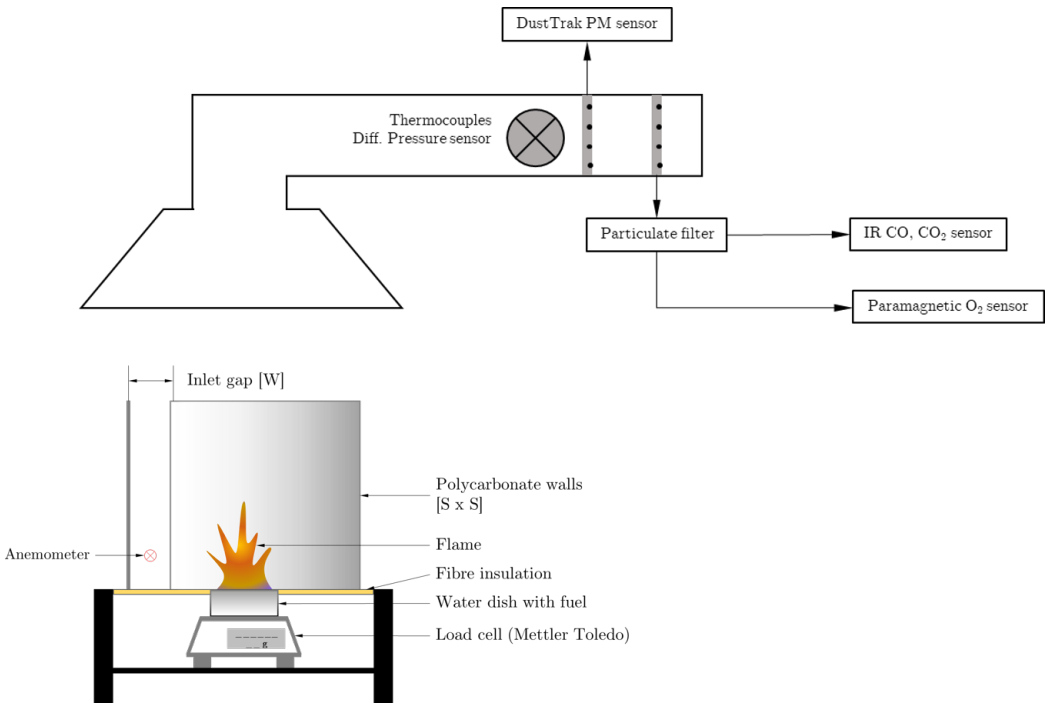

Figure 3.2: Schematic showing suction hood and exhaust duct positioned above the fire whirl apparatus. Flow rate in the duct was determined using temperature measurements and a differential pressure sensor. Two sampling tubes were used, one for gaseous species and one for particulate matter. Inlet velocity into the fire whirl enclosure was measured using either a hot-wire or vane anemometer. Mass of the fuel dish was measured using a Mettler-Toledo load cell.

that order. Due to the close proximity of the the two sampling tubes, they were offset by 45° (around the axis of the duct) to prevent interference in sampling. An image of the cross-section of the exhaust duct showing the described arrangement is shown in Figure 3.3.

The two sampling tubes were used for measuring PM and gas species. The sampling tube for PM was positioned upstream of the other. The upstream sampling tube was connected directly to a DustTrak 8534 with the manufacturer-recommended high-temperature rubber tubing. Exhaust from the duct was sampled at a rate of 3 L/min using the internal pump in the instrument. In order to use

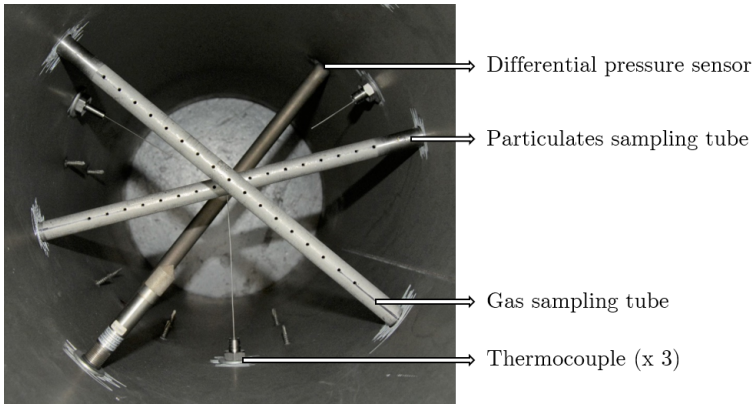

Figure 3.3: Exhaust-gas sampling tubes, pressure and temperature sensors positioned inside the exhaust duct. Exhaust flow direction is towards the reader.

the device on particulate matter (PM) from crude oil and heptane, a gravimetric calibration of the DustTrak was performed.

The downstream sampling tube was connected to a California Instruments CAI ZPA NDIR/O_2 Analyzer. Sampling was enabled by a double-head vacuum pump connected upstream of the gas analyzer to provide the required flow rate. A particulate filter was also connected upstream to the vacuum pump to prevent any clogs in the pump or gas sensor. The instrument contains IR sensors to measure the CO and CO_2 concentrations on one flow channel and a paramagnetic O_2 sensor on a second channel. CO_2, CO and O_2 were measured in the range 0–10%, 0–1%, and 0–25%, respectively. The DustTrak 8534 and CAI ZPA Analyzer used are shown in Figure 3.4. For experiments conducted at WPI, the same arrangement was used, with the DustTrak for measuring particulates and a Spectris Servomex 4200 gas analyzer. The operating range of the Servomex and CAI gas analyzers was the same for each of the gas species (CO_2, CO, O_2).

A two-point reference calibration for CO, CO_2 and O_2 using the gas analyzer

Figure 3.4: Images of (A) CAI ZPA NDIR/O_2 Analyzer [26], and (B) DustTrak DRX Aerosol Monitor 8534 [27].

was performed to determine the response of each sensor before each experiment. Zero calibration was performed by supplying the sensors with 100% N_2 and span calibration was performed by using a gas combination of 1.007% CO, 7.855% CO_2 and 20.01% O_2, with the remainder composed of N_2. The gas sensors were all calibrated with their respective calibration gases on each day that experiments were performed. Experiments conducted at WPI used a similar suite of gas analyzers, while the same DustTrak was used to measure PM.

The measured soot mass and that measured by the DustTrak was compared to determine the appropriate settings for future experiments. The instrument was factory calibrated using Arizona Test Dust [21], and the baseline mass concentrations calculated by the instrument were based on this density. To adjust for the density variation between the test dust and the soot in our experiments, a gravimetric calibration was performed. In parallel to the DustTrak, a separate pump sampling system was operated at the same flow rate, and the exhaust gases were channeled through a fine particulate filter, which collects all the PM greater than 0.8 μm. The

filter elements were weighed on a high-precision mass balance before the experiment, and the DustTrak and parallel pump system operated for the same amount of time. Post experiment, the filter element was again weighed to determine the mass of soot deposited in the test duration. A density adjustment was made according to Equation 3.1 [213]. Once this correction factor is determined, the values were either programmed into the instrument directly or applied during data processing.

$$Concentration\left[\frac{mg}{m^3}\right] = \frac{Filter\ post\text{-}weight - Filter\ pre\text{-}weight\,[mg]}{\frac{2}{3} \times \frac{Sampling\ rate\,[L/s]}{1000\left[L/m^3\right]} \times Sampling\ duration\,[s]} \tag{3.1}$$

The instrument uses an inbuilt photometric calibration that separates the size fractions of soot, classifying them as PM-1, PM-2.5, PM-4, PM-10, and Total PM. The fundamental measurement in the instrument is based on PM-2.5, and the other fractions are determined based on the size distribution in Arizona Road Dust. This photometric calibration of size distribution is not directly applicable to soot since it depends on fuel characteristics. In this work, however, the size calibration had little effect since the fundamental measurement (PM-2.5) and the Total PM (TPM) were nearly identical.

An E-instruments E-8500 multi-gas analyzer was used to try to measure other gaseous species such as NO_x, SO_x and unburned hydrocarbons (UHC or C_xH_y) in experiments with $D = 10$ cm. However, even when the instrument was used to probe directly in the flame, the concentration of these species in the plume was lower than the sensitivity of the instrument, and it was thus difficult to distinguish between

actual signals and electronic noise. These results are not presented in this work, and the measurement of these species is suggested as future work. The emission of SO_x is especially important when burning crude oil. Based on the temperature measurements, substantial emissions of NO_x is not expected.

Regardless, the potential presence of these species in the combustion products does not affect measurements of CO, CO_2 and PM, which were reliably detected and measured.

3.2.3 Temperature Measurements

3.2.3.1 Gas-Phase Temperature

Flame temperature was measured for each fire. For $D = [10, 20, 30]$ cm, five K-type thermocouples (TC, sheathed and grounded, 50 μm bead size) were positioned along the centerline of the fuel pool at different heights (H), such that the ratio $\frac{H}{D}$ varied between 1 and 5 (see Figure 3.5A). For $D = 70$ cm, a tree of 25 K-type TCs was mounted in the middle of the pool. The first five TCs above the fuel surface were spaced 0.5 cm apart, and the remaining were separated by 6 cm along the tree. A schematic of the arrangement is shown in Figure 3.5B. Radiation correction was not performed for any measurements since measured temperatures were generally below 1300 K, and the flames were unsteady. Such flames or fires typically require a two-TC approach to estimate correction [214].

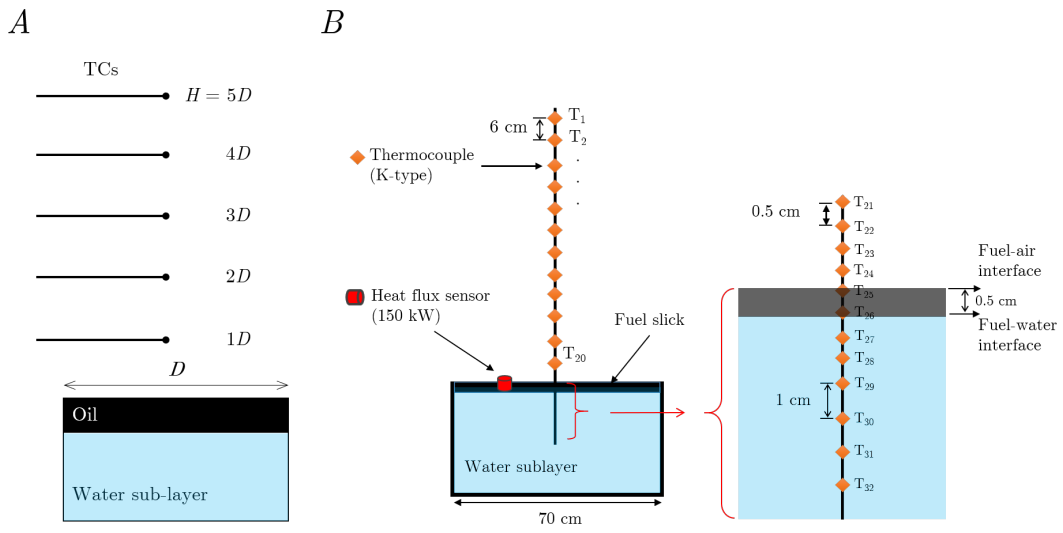

Figure 3.5: (A) Schematic showing locations of TCs above the fuel pool, used for experiments with $D = [10, 20, 30]$ cm. (B) Schematic showing locations of TCs for gas- and liquid-phase temperature measurements for experiments with $D = 70$ cm.

3.2.3.2 Liquid-Phase Temperature

Another important parameter in PFs and FWs is heat-flux feedback to the fuel pool. The fraction of heat release that is fed back from the flame to the fuel surface is a critical parameter influencing energy balance in the fuel layer and is dependent on flame dynamics and geometry. Since a conventional Schmidt-Boelter gauge could not be positioned within the fuel dishes with $D = [10, 20, 30]$ cm, the heat flux was calculated as the average rate of heating of the water sublayer. Prior to each experiment, the amount of water in the fuel dish was measured, and four TCs were positioned in the water sublayer (see Figure 3.19). Data from the TCs in the water layer were used to determine the total heat-flux feedback to the pool.

For experiments at $D = 70$ cm, a water-cooled heat flux gauge was installed at different locations in the fuel pool to measure heat feedback from the flame to

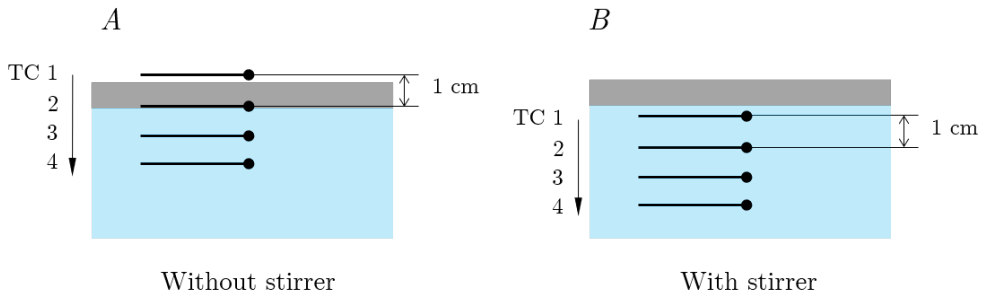

Figure 3.6: TCs for liquid-phase temperature measurements for $D = 10, 20, 30$ cm. (A) TCs to check for boiling at the fuel-water interface, without the stirrer. (B) TCs to check for effect of the stirrer on temperature stratification in the water sublayer.

the fuel.

Small pools with ANS burning were prone to boilover towards the end of the experiments. Based on previous work on boilover [215], this was attributed to temperature stratification in the water sublayer and near-boiling temperatures at the water-fuel interface. To check this, one TC was placed at the fuel-water interface (3.6A). Results from this experiment are shown in Figure 3.19. One method of avoiding boilover is ensuring that the water sublayer heats up uniformly. To do this, a magnetic stirrer was introduced at the bottom of the fuel dish to mix the sublayer and prevent water at the interface from reaching boiling point. To check for stratification after positioning of the TCs, all four TCs were positioned within the sublayer (Figure 3.6B).

A stirrer could not be employed at $D = 70$ cm, and boilover could not be avoided. To delay the onset of boilover, however, a pump was used to recirculate water between the water-fuel interface and the bottom of the dish.

3.3 Results

3.3.1 Physical Characteristics of PFs and FWs

For each experiment, photographs of PFs and FWs were obtained using a digital camera. Images of the fires at difference scales are shown in Figures 3.7 and 3.8. For PFs, the average flame height, $H_f \in [1, 2]D$. At the base of PFs, the flame width, w_f, is equal to the pool diameter, D. PFs have a conical flame shape as w_f reduces with axial distance. Entrainment of air along the boundary layer toward a PF causes necking of the flame at the base and the initiation of Rayleigh-Taylor instabilities [112]. These instabilities cause rolling-up of the flame sheet (see Figure 3.8A) and a periodic fluctuation of the flame height [14], a phenomenon referred to as "puffing". In contrast to PFs, $H_f \in [3, 6]D$ for FWs, which have a cylindrical shape. FWs also show stronger necking at the base of the flame, resulting in reduced average flame width, $w_f \in [0.5, 1)D$. FWs do not show puffing, which is replaced by a helical instability that causes the flame to wrap around a vortex core [23, 102].

3.3.2 Burning Rate

The fuel mass-loss behavior for fires at $D = [10, 20, 30]$ cm is presented in Figures 3.9 and 3.10. For experiments with heptane fuel, the total mass loss was the same for both PFs and FWs as no residue was left behind after extinction. For all conditions considered here, $\dot{m}$ of the FW regime is higher than the PF regime. Generally, mass loss is linear for heptane fires, but the rate declines with time for

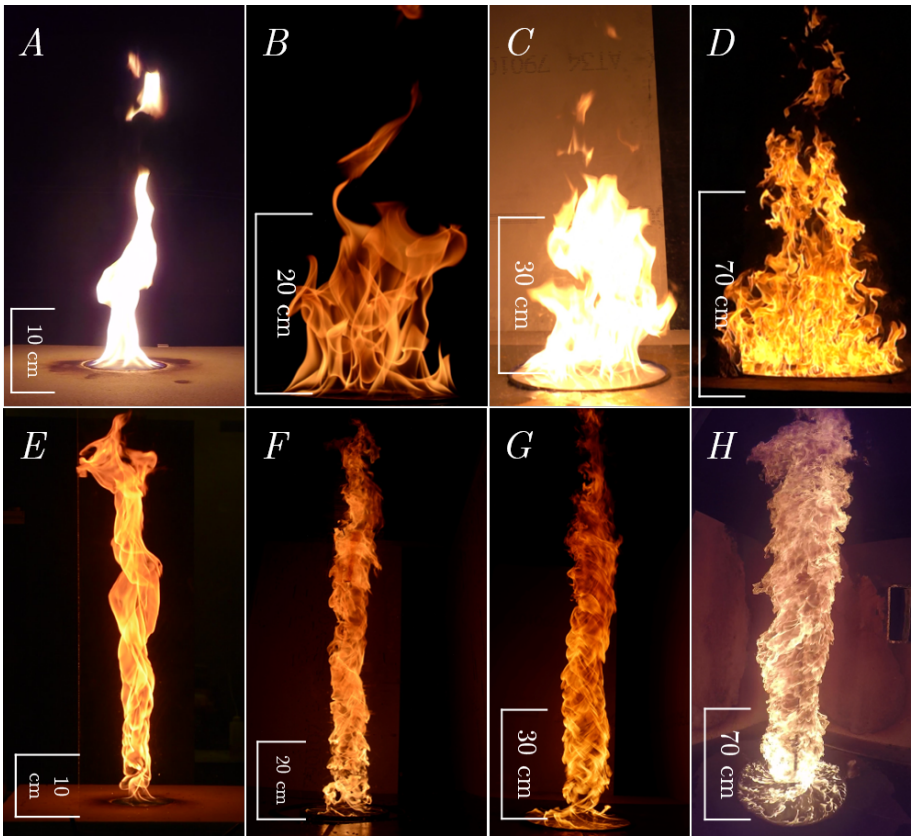

Figure 3.7: Photographs of PFs (panels $A - D$) and FWs (panels $E - H$) formed using heptane at $D = [10, 20, 30, 70]$ cm.

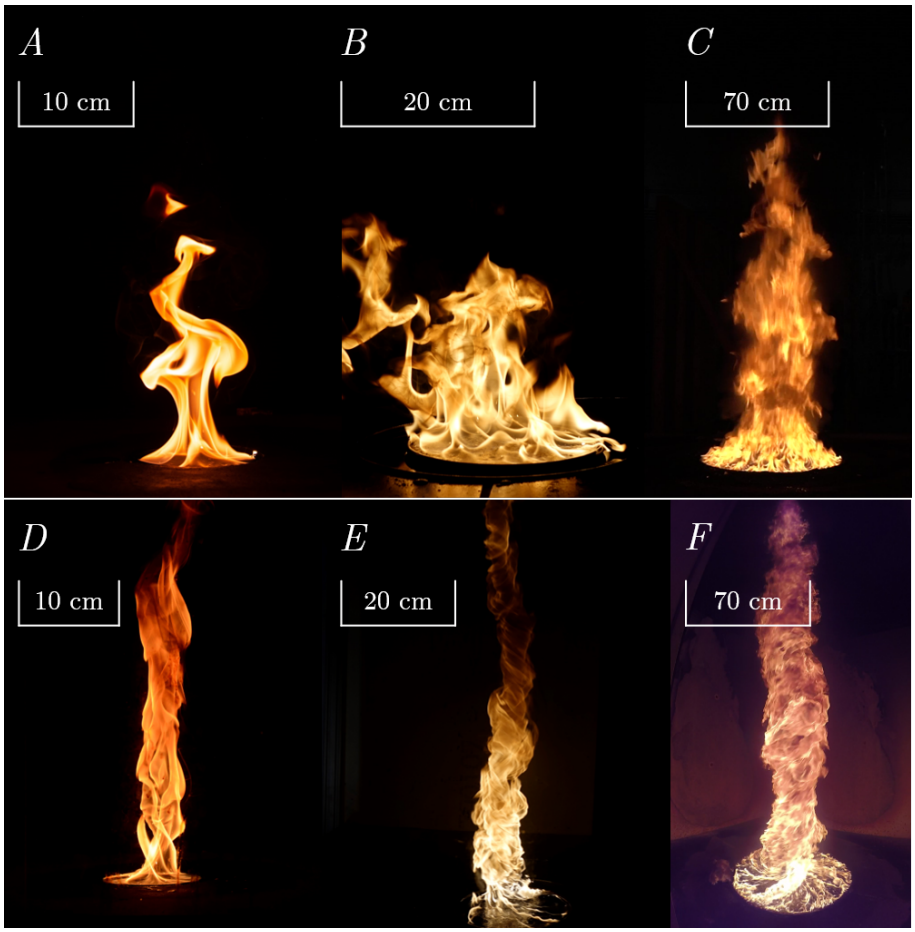

Figure 3.8: Photographs of PFs (panels $A - C$) and FWs (panels $D - F$) formed using ANS crude oil at $D = [10, 20, 70]$ cm.

ANS fires. This non-linear behavior of ANS crude oil is seen at smaller scales (see Figure 3.9). The physical characteristics of the different fires are tabulated in Table 3.3.

A linear fit is used to determine the average $\dot{m}$ (in [g/s]) from the slope of the line. For the purposes of comparison, these are shown in Figure 3.9 D and Figure 3.10 C& F. For both heptane and ANS crude oil, the FW regime consumes fuel at approximately twice the rate of the corresponding PF. For heptane fires, the entire quantity of initial fuel was consumed, while there was a residue left behind after extinction of ANS crude oil fires.

For experiments at $D = 70$ cm, since a load-cell could not be installed beneath the large fuel container, only an overall average of $\dot{m}$ could be determined based on the burn time of each fire and the fuel mass consumed. For a 5 mm slick of fuel, the mass of heptane and ANS for each experiment was $\sim$ 1250 g and $\sim$ 1710 g, respectively. Since boilover was always observed for ANS at this scale, the slick was increased to 7 mm, corresponding to an average fuel mass of 2450 g. The post-burn residual ANS crude oil was collected with adsorbent pads (3M Petroleum Sorbent Static Resistant Pad HP-556). Table 3.3 shows the initial mass, residual weight and average burning rate for the different fires at the 70 cm scale. While boilover was delayed with the 7 mm slick as compared to the 5 mm slick, the intensity was visibly higher, and is evidenced by the higher average mass-loss rate of the 7 mm slick fires.

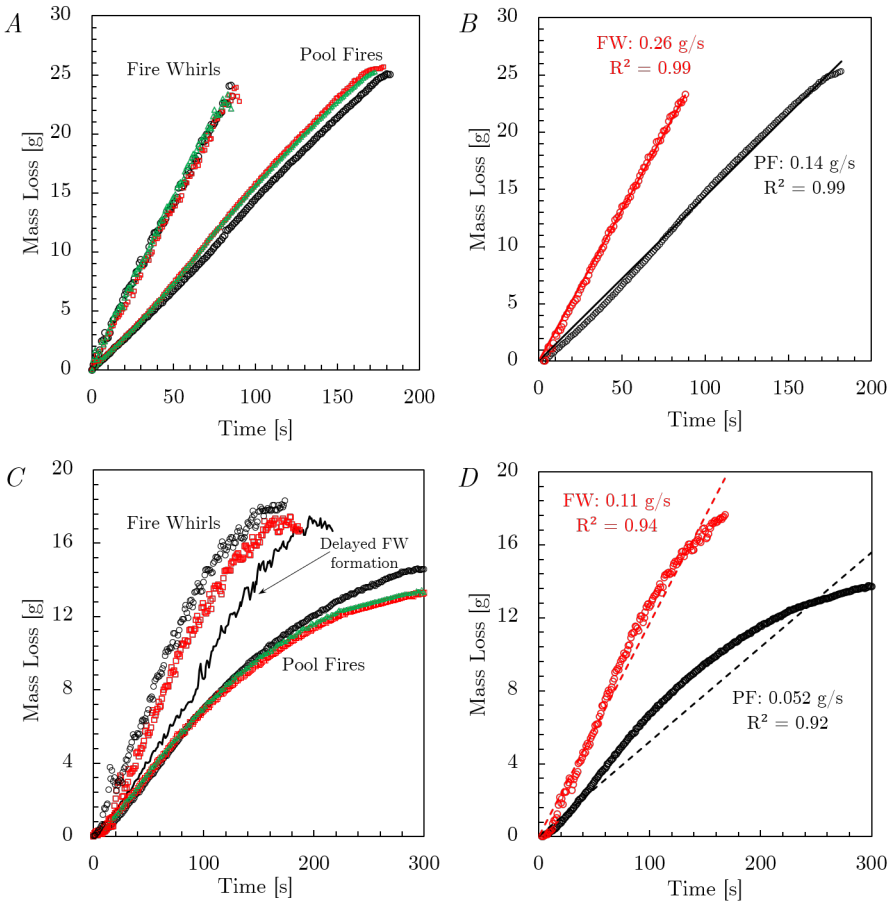

Figure 3.9: Mass loss behavior of PFs and FWs formed at $D = 10$ cm. Data from individual experiments using (A) heptane and (C) ANS crude oil. The marker colors denote individual experiments. Averaged data and linear fits are shown in (B) and (D). The slope of the linear fits represents the average burning rate.

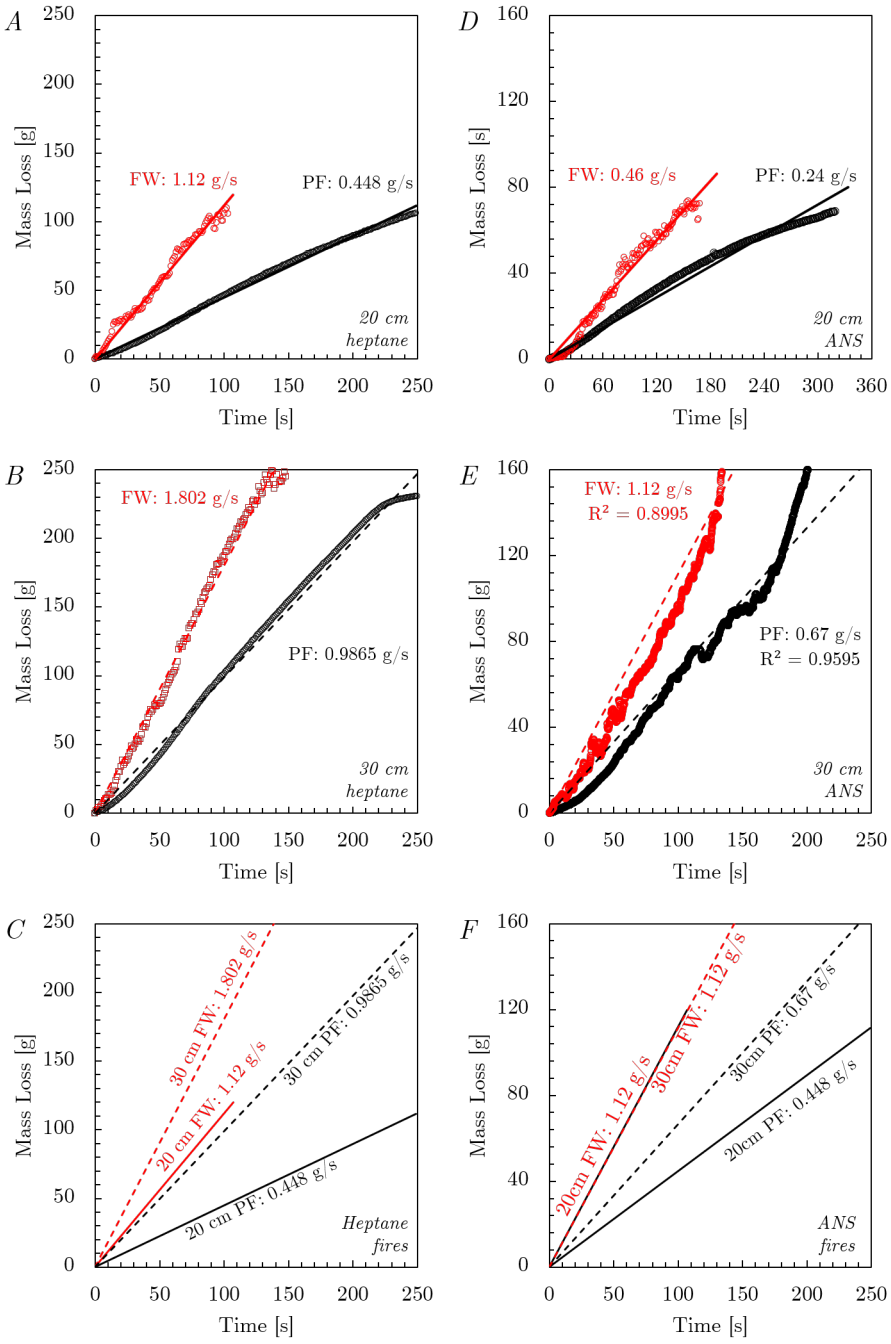

Figure 3.10: Burning rate for PFs and FWs formed with $D = [20, 30]$ cm. The red and black markers in each panel represent the average of three experiments. Overall burning rate is shown in panel (C) for heptane fires and in panel (F) for ANS fires. compared for all medium-scale heptane fires.

Table 3.3: Tabulated data of average values of burning duration, burning rate, and estimations for flame width (w_f) and flame height (H_f) for the different flame regimes and pool diameters. Experimental variability for $\dot{m}$ and residue mass are presented in Appendix B.

Fuel	Flame Regime	D [cm]	t_b [s]	$\dot{m}$ [g/s]	Residue [g]	Approx. w_f	Approx. H_f
Heptane	PF	10	182	0.00015	-	$1D$	(1–1.5)D
		20	249	0.00044			
		30	239	0.001			
		70	165	0.0083			
	FW	10	91	0.0003	-	$\sim 0.5D$	(3.5–6)D
		20	100	0.0011			
		30	133	0.0018			
		70	137	0.01			
ANS	PF	10	291	0.00005	-	$1D$	(1–2)D
		20	278	0.00024			
		30	257	0.00067			
	(5 mm)	70	180	0.0094	301		
	(7 mm)	70	169	0.01	382		
	FW	10	161	0.00011	-	(0.5–1)D	(3–4)D
		20	167	0.00046			
		30	206	0.001			
	(5 mm)	70	161	0.0106	290		
	(7 mm)	70	167	0.013	382		

3.3.3 Emissions: Particulate matter

Time-varying PM concentration was obtained directly from the DustTrak, after calibration using Equation 3.1. This value was then converted to a PM emission rate according to Equation 3.2.

$$\textit{PM emission rate}\left[\frac{mg}{s}\right] = \textit{Measured concentration}\left[\frac{mg}{m^3}\right] \times \textit{Exhaust flow rate}\left[\frac{m^3}{s}\right] \quad (3.2)$$

The variation of PM-emission rate with time for the different fires at $D = [10, 20, 30]$ cm is shown in Figures 3.11−3.13. Consistent with the behavior of $\dot{m}$ for PFs and FWs, the duration of PM emission from FWs is roughly half that of PFs. For $D = 10$ cm, the peak emission rate is similar for PFs and FWs, and the steep spikes in PM-emission rate due to boilover are visible in Figure 3.11 C, D. For $D = 10$ cm, a few experiments are shown with boilover only to show the effectiveness of stirring in the water sublayer. At $D = [10, 20, 30]$ cm, experiments that resulted in boilover were *not* used to calculate emission factors. The PM-emission rate for $D = [20, 30]$ cm is similar to those at the $D = 10$ cm, with some difference in the peak emission rate between PFs and FWs at each scale. Comparing the different fuels, for each experimental condition, the PM-emission rate from ANS fires is an order of magnitude higher than that from heptane fires. Data for $D = 70$ cm is discussed in detail in Chapter 4.

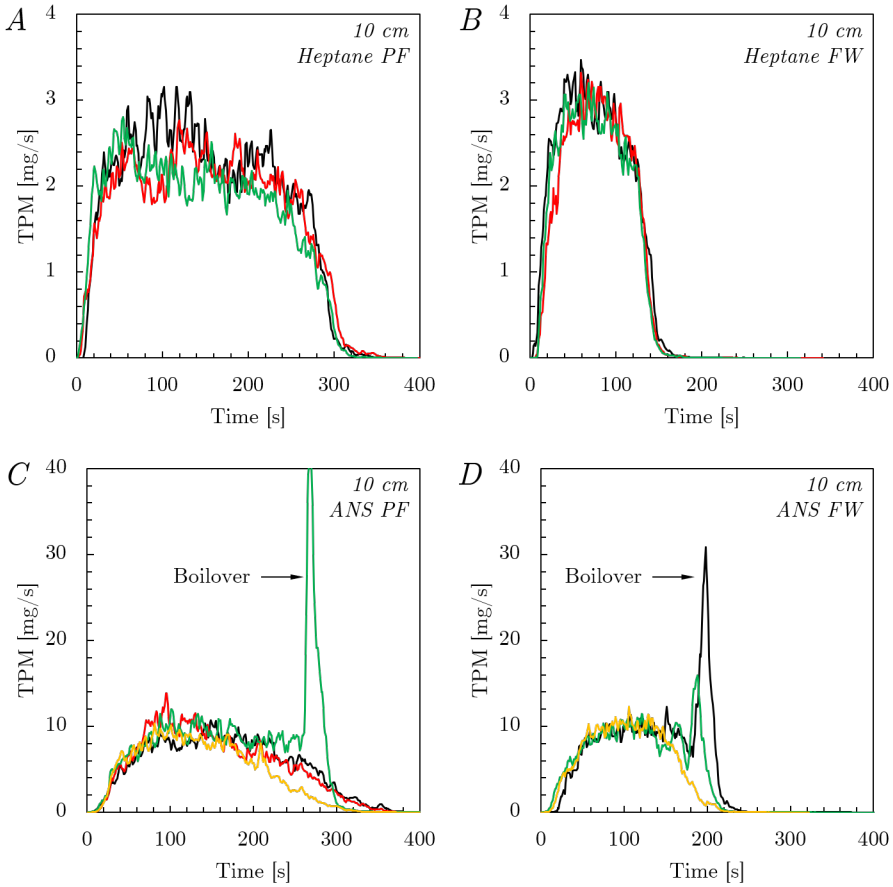

Figure 3.11: Variation of PM-emission rate with time at $D = 10$ cm. The spikes in (C) and (D) are instances of boilover towards the end of the burn.

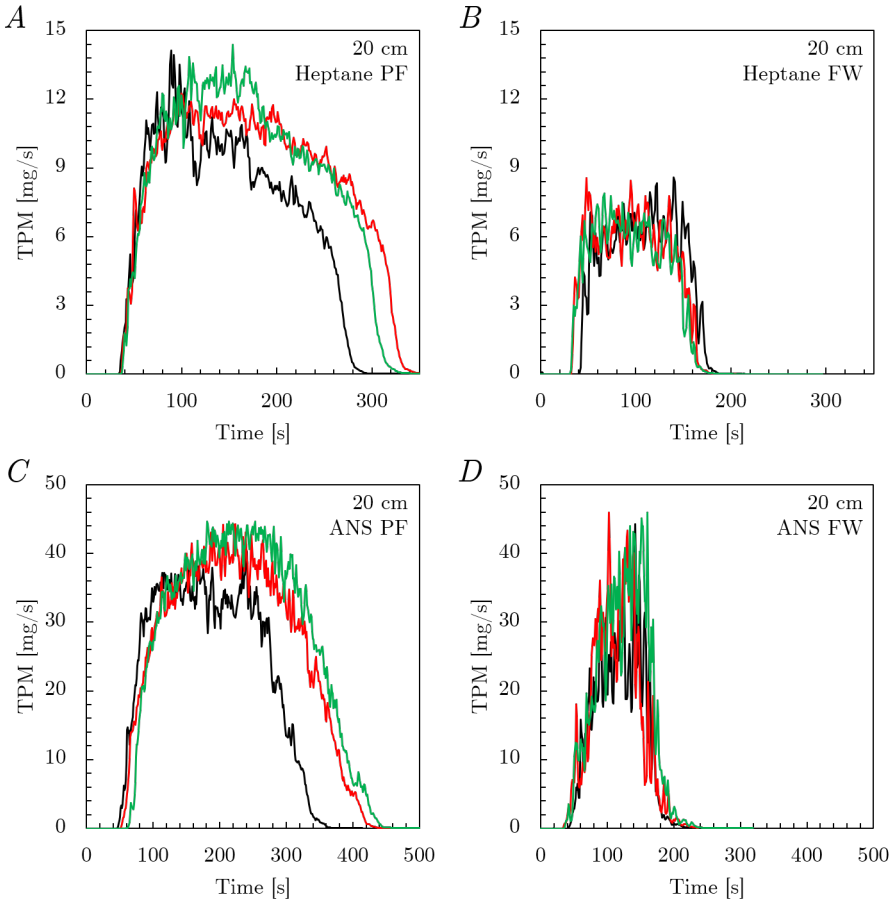

Figure 3.12: Variation of PM-emission rate with time at $D = 20$ cm for PFs and FWs formed using heptane (A, B) and ANS crude oil (C, D). The different colors represent data from individual experiments.

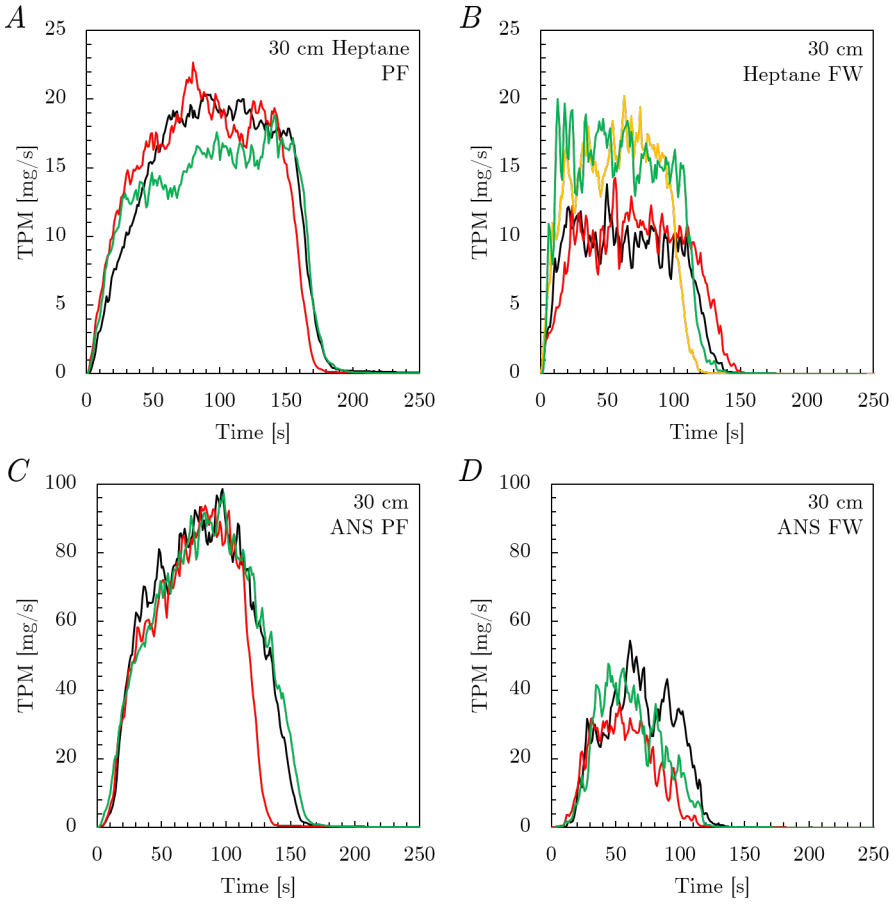

Figure 3.13: Variation of PM emissions rate with time at $D = 30$ cm for PFs and FWs formed using heptane (A, B) and ANS crude oil (C, D).

For the 70 cm scale, the emission rate of fires formed using a 5 mm slick of ANS crude oil are shown in Figure 3.14. For both PFs and FWs, the PM rate increases linearly initially, but a sharp spike occurs after about 85 s in PFs and 70 s in FWs. This rise in PM rate is due to boilover. To delay the onset of boilover, a 7 mm slick of ANS was used. Results for fires formed using the 7 mm ANS slick and 5 mm heptane slick are presented in Chapter 4.

The total mass of PM emitted in each case was calculated according to Equation 3.3. This value is used to calculate an emission factor, described in section 3.4.

$$TPM\left[mg\right] = \dot{V}\left[\frac{m^3}{s}\right]\int_0^{t_b} TPM\left[\frac{mg}{m^3}\right] dt\left[s\right] \tag{3.3}$$

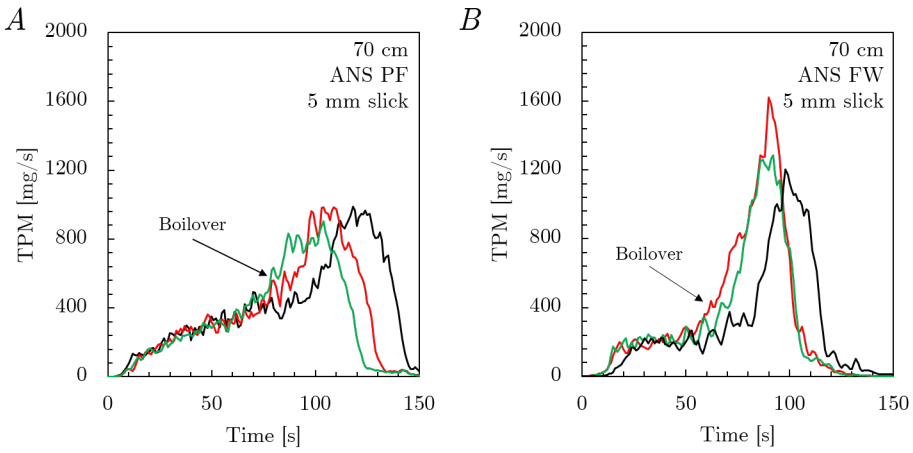

Figure 3.14: PM emissions rate from PFs and FWs formed using a 5 mm slick of ANS crude oil at $D = 70$ cm.

3.3.4 Emissions: Gaseous species

The gaseous species measured were CO, CO_2 and O_2. O_2 measurements were also used to estimate the instantaneous heat-release rate of each fire. Data and figures for $D = 70$ cm are presented in this section for brevity, and the figures for $D = [10, 20, 30]$ cm are included in Appendix B.

The emission of CO_2 is directly proportional to the consumption of O_2. The emission rate of CO_2 and consumption rate of O_2 with time for 70 cm fires are shown in Figure 3.17 and Figure 3.15. For both fuels, peak CO_2 emission and O_2 consumption are higher for the fire whirl. Consequently, the peak $\dot{Q}$ of FWs is also higher than that of PFs (Figure 3.16), which is also evident from the higher $\dot{m}$ of FWs (Table 3.3). By assuming $\Delta h_c = 44.9$ kJ/g for heptane [17], the average $\dot{Q}$ derived from $\dot{m}$ was found to be 0.373 MW for PFs and 0.45 MW for FWs. The peak $\dot{Q}$ obtained from O_2-consumption calorimetry for these fires was around 0.3 MW and 0.45 MW, respectively.

Similarly, using $\Delta h_c = 42$ kJ/g for ANS crude oil [216], the average $\dot{Q}$ calcualted from $\dot{m}$ was 0.42 MW and 0.55 MW for PFs and FWs, and the peak experimental values are in a similar range. The sharp spike in CO_2 production and O_2 consumption denotes the onset of boilover in ANS fires. This also indicates that the instantaneous value of $\dot{m}$ rises significantly during the boilover phase, leading to the higher $\dot{Q}$. This behavior has been observed in previous studies on boilover [215]. The trends in CO emission rate (Figure 3.18) are similar to CO_2 and O_2. The CO emission rate from ANS crude oil fires is an order magnitude higher than that from

heptane fires.

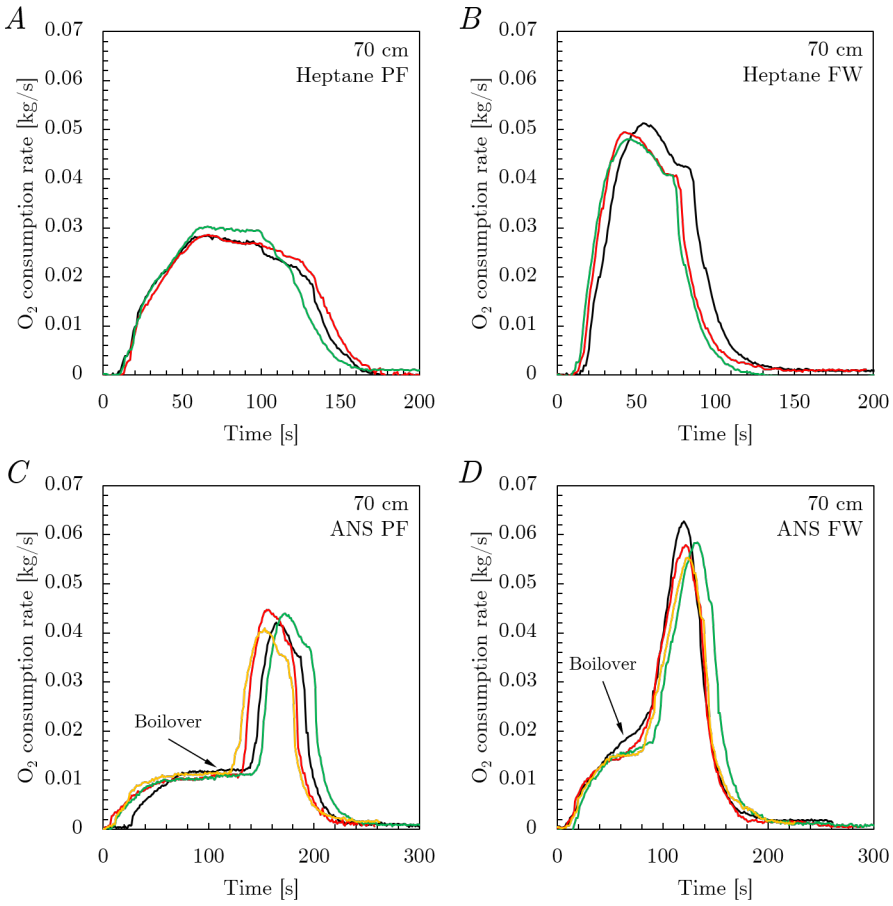

Figure 3.15: Variation of O_2 consumption rate with time for the different fires at $D = 70$ cm.

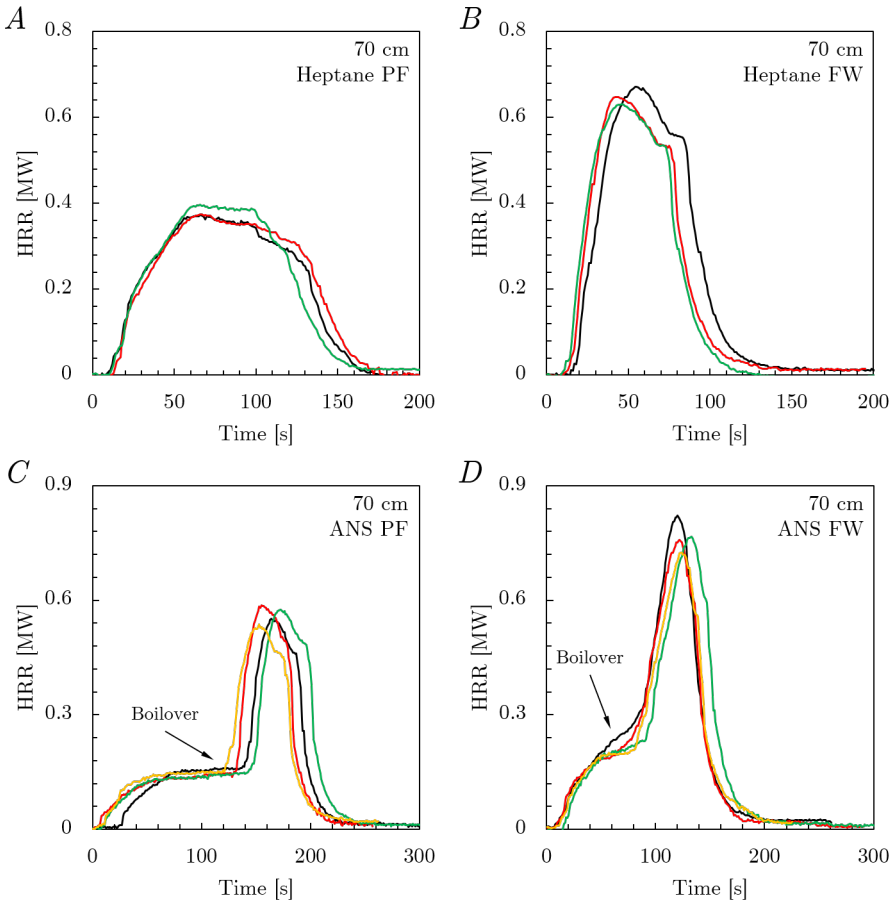

Figure 3.16: Variation of heat-release rate (HRR) with time for the different fires at $D = 70$ cm. HRR was estimated by O_2-consumption calorimetry, assuming a value of 13.1 kJ/g-of-O_2 [28, 29].

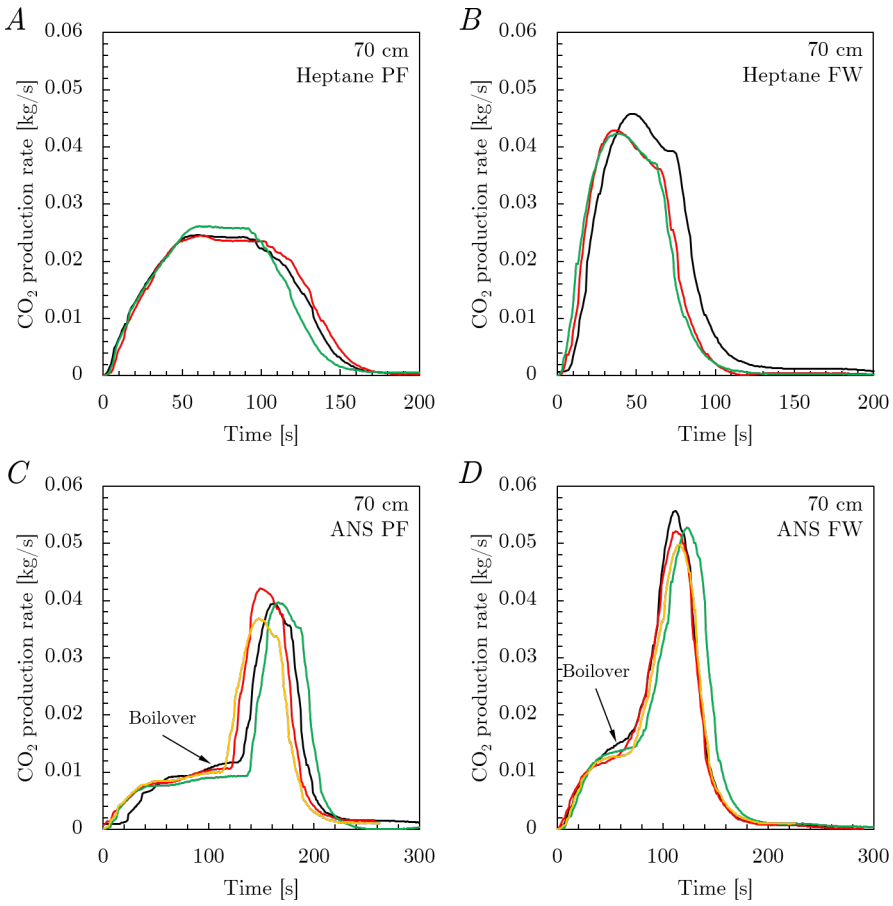

Figure 3.17: Variation of CO_2 emission rate with time for the different fires at the 70 cm scale.

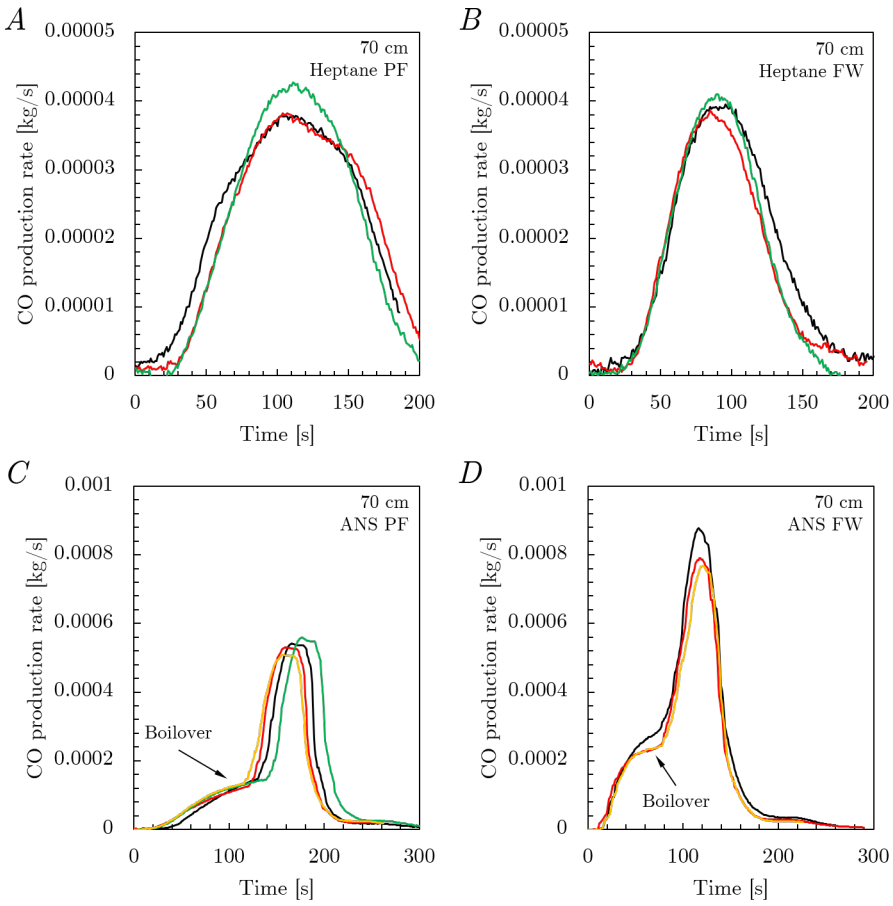

Figure 3.18: Variation of CO emission rate with time for different fires at the 70 cm scale.

3.3.5 Heat Feedback and Temperature

The efficacy of the stirrer in the sublayer was tested by comparing the temperature measurements *with* and *without* the stirrer. When the stirrer was not used, the temperature at the water-fuel interface reached about 400 K, resulting in boilover. This is shown in Figure 3.19A, which also shows that the temperature within the sublayer reduces with depth. This stratification in the sublayer, however, did not exist When the stirrer was used, and the sublayer temperature showed a linear increase with time (Figure 3.19B). This shows that the stirrer was effective in avoiding boilover.

Heat feedback to the fuel pool was obtained in two different ways depending on D. For $[D = 10, 20, 30]$ cm, heat flux was calculated using temperature measurements of the water sublayer since a heat-flux gauge could not be positioned within these pools. Thus, the heat-flux feedback estimated is averaged temporally and spatially at these scales.

The total heat feedback was calculated as $q = m\, C_{p,water}\, \Delta T$, where m is the mass of water in the sublayer, $C_{p,water}$ is the heat capacity of water, and ΔT is the total rise in temperature of the water sublayer. Since the water sublayer was well mixed, the temperature readings from all TCs in the sublayer showed very similar readings. Thus, ΔT represents the rise in bulk temperature. Then, the averaged heat flux is given by

$$\dot{q}'' = \frac{q}{A_{pool}\, t_b}$$

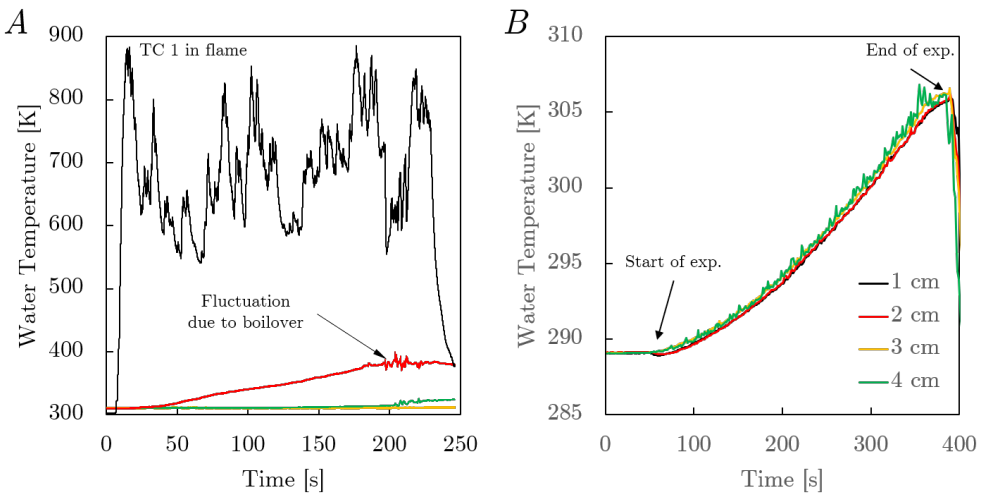

Figure 3.19: Effect of using the magnetic stirrer on temperature in the water sublayer, (A) *with* the stirrer showing a decrease in temperature with depth, and (B) *without* the stirrer, showing minimal stratification and a single bulk temperature for the sublayer.

where t_b is the burn time and A_{pool} is the pool area. The results for this scale are shown in Figure 3.20. $\dot{q}''$ increases wtih D, and at each scale, FWs exhibit higher feedback than PFs. This behavior is consistent for both fuels, and ANS fires have higher feedback than heptane fires. The difference in values at these scales is small, but the averaging causes peaks in heat flux to be smeared.

At the 70 cm scale, heat-flux gauges were installed in the pool and direct measurements from a Schmidt-Boelter gauge are shown in Figure 3.21. The heat flux from heptane PFs tends to peak immediately after ignition, stabilize around 25 kW/m^2, and then spike to about 45 kW/m^2 prior to extinction. Heptane FWs, on the other hand, have a relatively stable heat flux feedback around $60 - 75$ kW/m^2 throughout the burn, peaking around 90 kW/m^2. ANS pool fires show relatively stable heat flux around 40 kW/m^2, and fire whirls peak just below 120 kW/m^2.

Fire temperature was measured above the fuel pool, with axial distances in

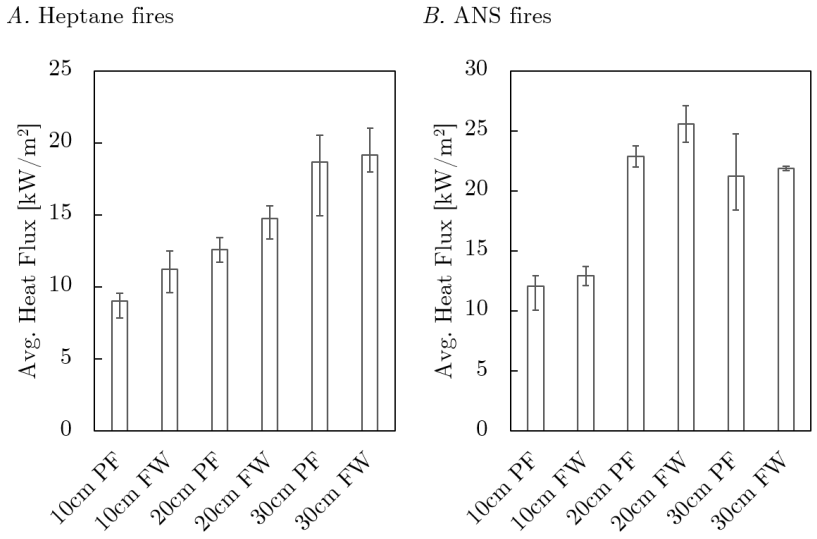

Figure 3.20: Temporally and spatially averaged $\dot{q}''$ for PFs and FWs at $D = [10, 20, 30]$ cm, formed using (A) heptane and (B) ANS crude oil.

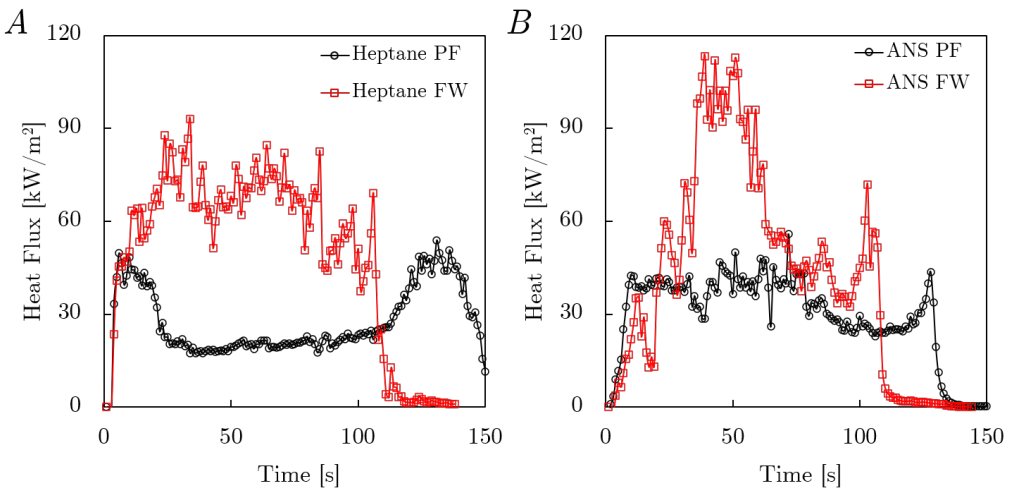

Figure 3.21: Variation of $\dot{q}''$ to the center of a 70 cm pool for PFs and FWs formed using (A) heptane and (B) ANS crude oil.

the range of $H/D \in [1, 5]$ (see Figure 3.5). Measurements along the centerline give an understanding of the qualitative differences in the heat-flux feedback to the fuel pool. The temporal change in temperature at the different axial locations for $D = [10, 20, 30]$ cm is shown in Figures 3.22−3.24.

At $D = 10$ cm, the peak temperatures are similar for both PFs and FWs, however, the temperature drops sharply with height in case of PFs. Temperatures are highest at $H/D = 1$, and the decline in temperature with height is more gradual in the case of fire whirls. For the 20 and 30 cm scales, the peak temperatures of fire whirls is higher by about 200 K, but the decline in temperature with height is still evident in the pool fires. The temperatures measured here cannot be used to directly calculate heat-flux feedback, but they help in explaining the qualitative differences between pool fires and fire whirls. These measurements do not represent temperatures at the flame sheet, and have not been corrected for radiation since the maximum value is below 1300 K.

Temperature data for $D = 70$ cm are shown in Appendix B.

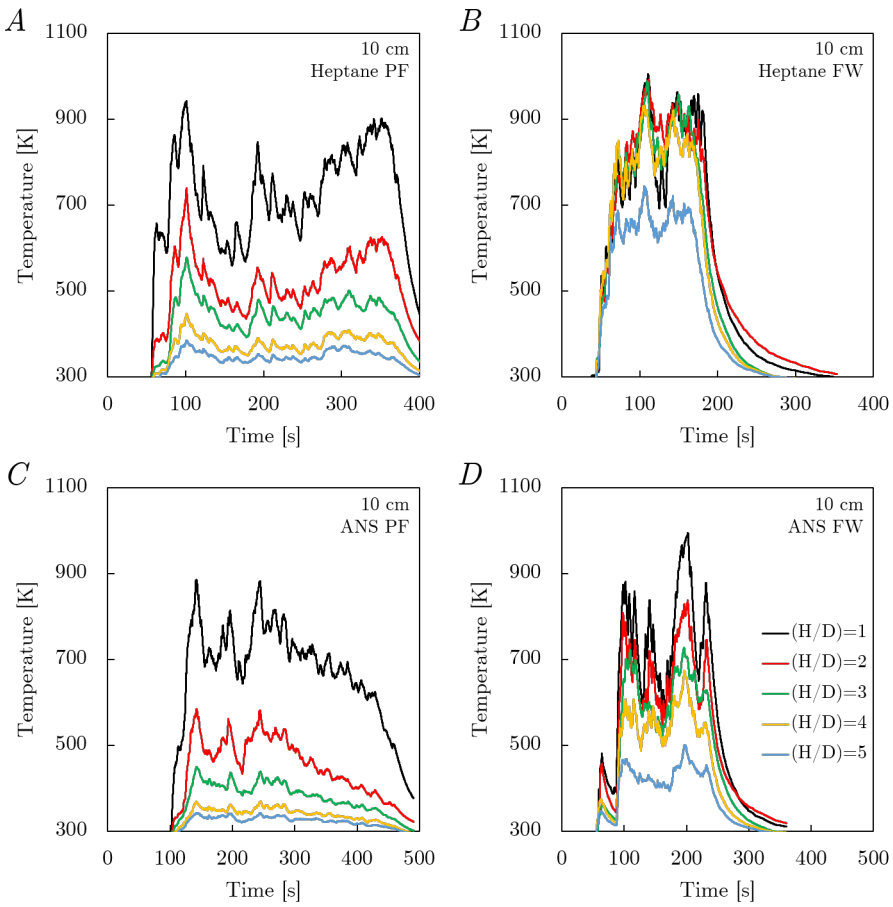

Figure 3.22: Flame temperatures at different axial locations (H) above the fuel surface, for PFs and FWs formed using heptane and crude oil, at $D = 10$ cm. Here, data from a single experiment is shown so that there is no smearing of trends due to averaging.

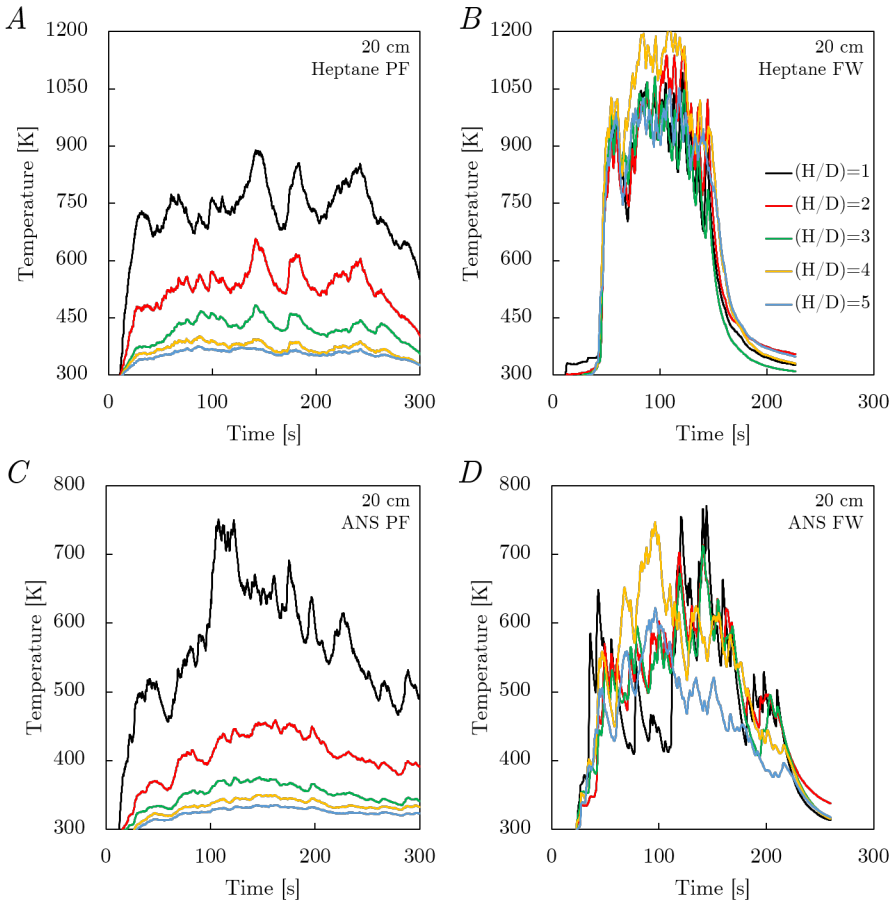

Figure 3.23: Temperature measurements for fires formed at $D = 20$ cm.

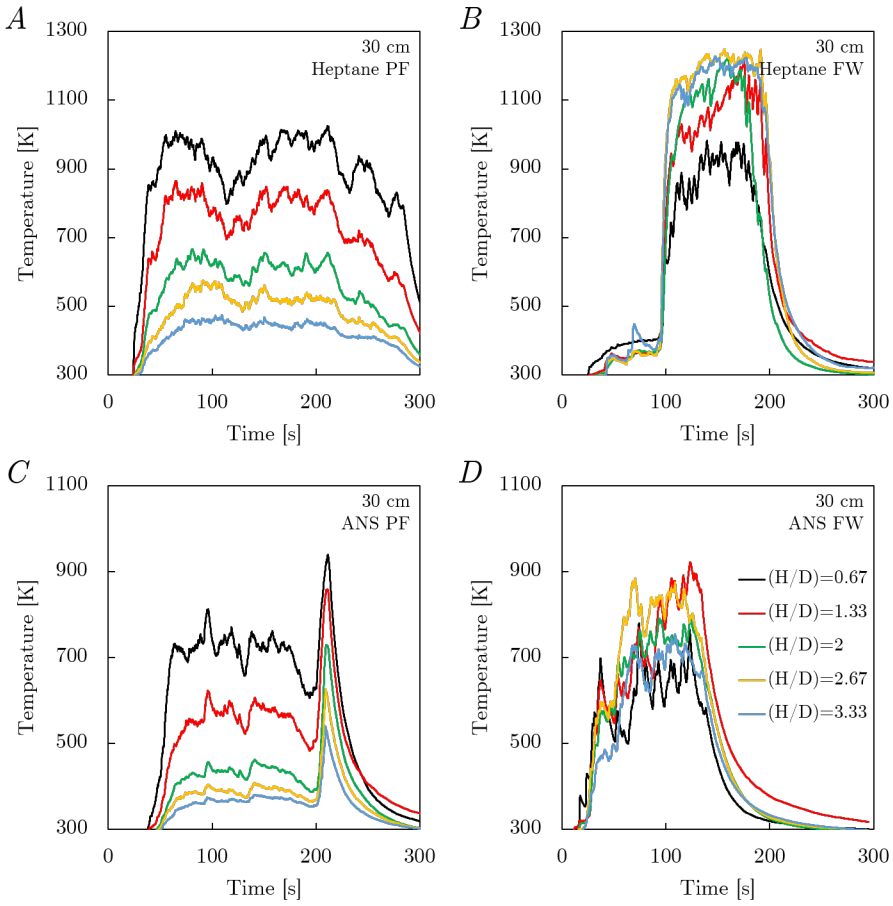

Figure 3.24: Temperature measurements for fires formed at $D = 30$ cm.

3.3.6 Air-Entrainment Velocity

The configuration used here for forming FWs is termed as a fixed-frame apparatus with natural air entrainment. Air entrainment to the fire is controlled by the buoyancy generated within the enclosure and the gap size of the inlets. Air-entrainment (inlet) velocity measurements using either a hot-wire or vane anemometer are reported here. The ambient circulation, Γ, was estimated as $\Gamma = 4\,S\,U_\theta$, where U_θ is the average tangential inlet velocity measured using the anemometer. The values of U_θ and Γ for the different cases are shown in 3.25.

Values for U_θ were averaged over time and between several repetitions, with one standard deviation measurements shown as error bars in Figure 3.25 A,B. U_θ was measured at only one H for FWs at $D = [20, 30]$ cm, shown in panels C and D. At all values of D, U_θ for heptane FWs was higher than that for ANS FWs. The inlet velocity decreases with height (see panels A and E). For $D = 70$ cm, a constant gap size of $W = 45$ cm was used, and U_θ was measured using a combination of hot-wire and vane anemometers. The average U_θ for heptane FWs was between 0.7 and 0.8 m/s, and showed a slight decrease with H. U_θ for ANS FWs decreased from about 0.76 m/s (at $H = 20$ cm) to 0.45 m/s (at $H = 100$ cm).

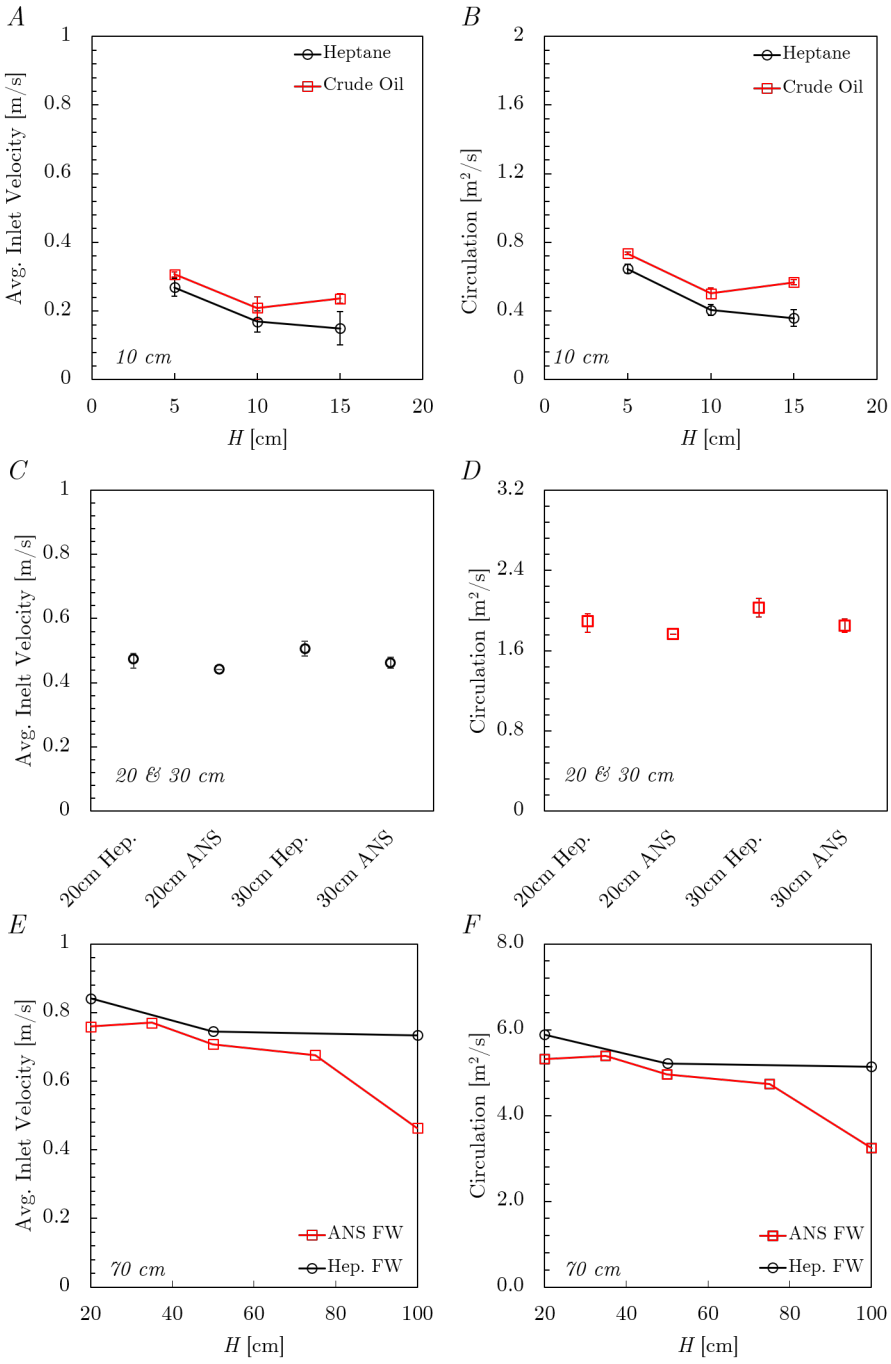

Figure 3.25: Measurements of U_θ and estimates of Γ for FWs formed using heptane and ANS at different D.

3.4 Discussion of Results

To compare the emissions from the two flame regimes formed at different D, the total mass of each emissions species emitted (or consumed, in the case of O_2) was calculated according to Equation 3.3. For PM, CO_2, CO, the emission factor (EF) was defined as

$$\mathrm{EF}_{\mathrm{species}} = \frac{\text{mass of emission species } \ [\mathrm{g}]}{\text{mass of fuel burned } \ [\mathrm{kg}]} \tag{3.4}$$

Similarly, a consumption factor (CF) of O_2 by each fire was defined as

$$\mathrm{CF}_{\mathrm{O2}} = \frac{\text{Total } O_2 \text{ consumed } \ [\mathrm{g}]}{\text{Mass of fuel consumed } \ [\mathrm{kg}]} \tag{3.5}$$

The above definitions are based on the total mass of each species and the mass of fuel burned. A similar definition based on only the carbon content is presented in Chapter 4. The calculation of emission factors at $D = [10, 20, 30]$ cm does not include experiments that showed boilover. The EFs and CF for the different fires are presented in Figure 3.26. In general, the $\mathrm{EF}_{\mathrm{PM}}$ of the FW regime is lower than that of the PF regime, for both fuels and all D. For both fuels and flame regimes, $\mathrm{EF}_{\mathrm{PM}}$ reduces from $D = 10$ cm to $D = 30$ cm, then increases again at $D = 70$ cm. The rise in $\mathrm{EF}_{\mathrm{PM}}$ at $D = 70$ cm cannot be attributed only to boilover since it is observed even for heptane.

In the case of heptane fires, $\mathrm{EF}_{\mathrm{CO_2}}$ and $\mathrm{CF}_{\mathrm{O_2}}$ are similar for PFs and FWs. $\mathrm{EF}_{\mathrm{CO}}$ from PFs is slightly higher for FWs. $\mathrm{EF}_{\mathrm{CO}}$ for heptane fires are on the order

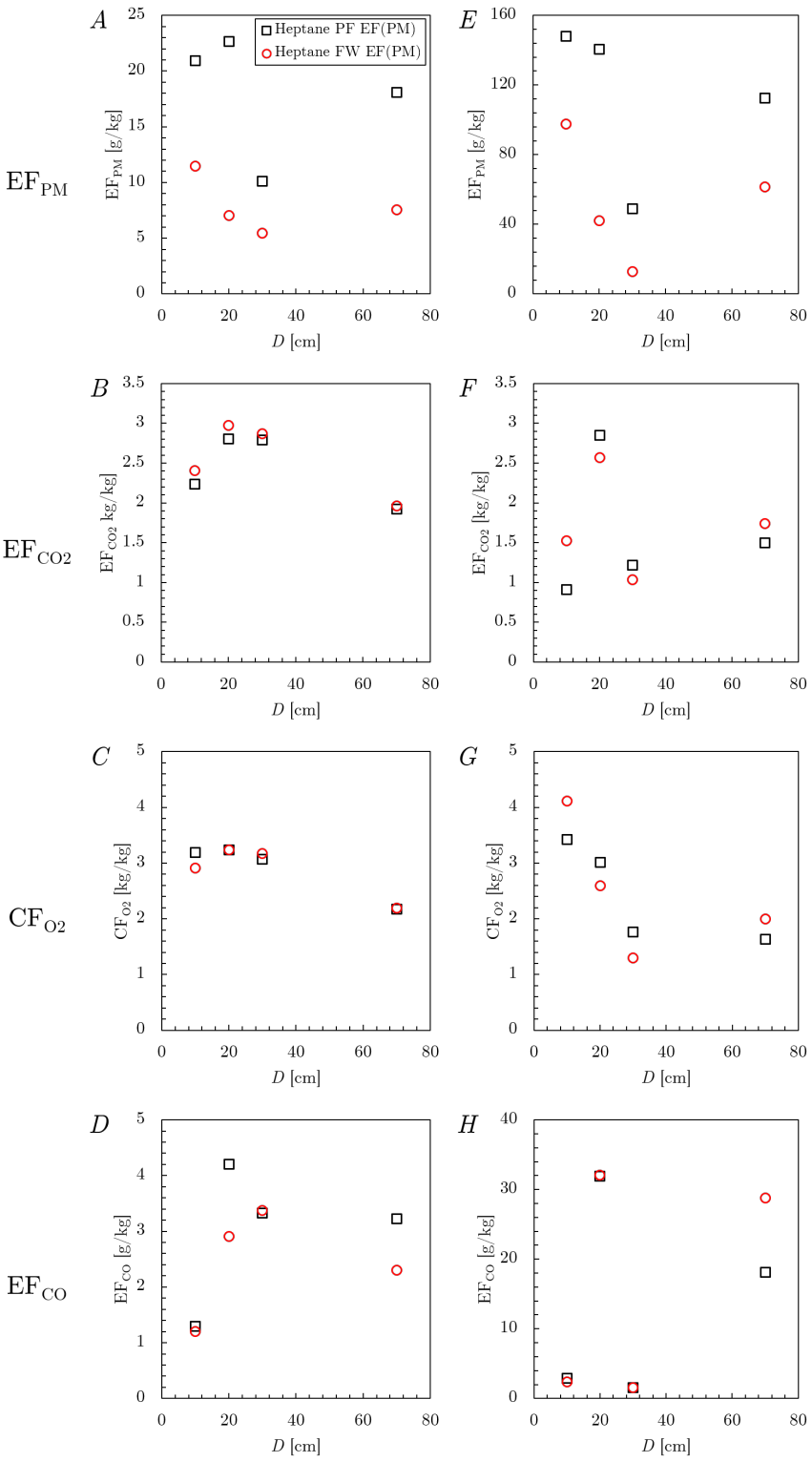

Figure 3.26: EFs and CF (fuel-mass based) for heptane and ANS crude oil fires at different D. Panels (A–D) show results for heptane, and panels (E–H) for ANS crude oil fires. The black square markers denote results for PFs and the red circles denote those for FWs.

of 1 g/kg-of-fuel, which is 3 orders of magnitude below that of EF_{O_2} and EF_{CO_2}. While the same amount of O_2 is consumed by both PFs and FWs, the total amount of PM and CO emitted by FWs is lower. In the case of ANS crude oil, the amount of O_2 used for combustion by FWs is higher, and consequently the amount of CO_2 emitted is also higher. EF_{CO} for ANS fires are on the order of 10 g/kg-of-fuel, and EF_{CO} for FWs is higher than for PFs.

The difference in PM emissions behavior between PFs and FWs stems from multiple factors including fluid dynamics of air entrainment to these fires, the global equivalence ratio (determined by oxygen consumption), effect of D on turbulence and mixing, flame temperature, radiation heat transfer, and the nature of the fuel. These factors are intrinsically coupled and constitute a complex heat-feedback loop. For instance, radial air entrainment increases oxidizer concentration, and reduces flame standoff distance [87] causing convective heat transfer to increase due to higher velocity gradients in the boundary layer [5]. This causes an increase in $\dot{m}$, $\dot{Q}$ and ΔT, increasing the buoyancy within the enclosure, in turn sustaining high values of U_θ.

The above mechanism need to be studied in detail at small scales to understand the dynamics of mixing. A general explanation of PM reduction in fire whirls may be approached by analyzing the increase of average plume temperatures in the presence of additional oxygen (see section 3.3.5), potentially causing partial re-oxidation of carbon in the soot into CO. Higher temperatures potentially contribute to lower PM emissions in two ways:

(i) increasing radiative feedback from soot incandescence. This is visible in Figure 3.21 where the peak heat flux feedback from fire whirls is higher than that in pool fires. The difference is especially high in case of ANS fires which have a higher soot concentrations than heptane fires. The higher values of $\dot{q}''$ leads to higher $\dot{m}$.

(ii) enabling partial oxidation of soot formed in the lower part of the fire whirl. While the mechanism of the soot oxidation or mixing cannot be established from the data presented here, it is clear that a simultaneous reduction in EF_{PM} and an increase in EF_{CO} for fire whirls is the result of higher EF_{O_2} and ΔT. These higher temperatures exist over a longer length scale, which potentially provides sufficient time for mixing and soot oxidation.

The combinations of $\dot{Q}$ and Γ for the different FWs in this study are shown in 3.27A. The range of $\dot{Q}$ in the study spans three orders of magnitude, and $\dot{q}$ increases linearly with $\dot{Q}$ (Figure 3.27B). Parameters such as $\dot{m}$ and $\dot{q}''$ are expected to stabilize beyond 70 cm [217] and the results at $D = 70$ cm may be used to determine applicability to field trials (Figure 3.28).

Chemical-kinetic mechanisms that control soot formation and destruction have not been explored in this work. Parameters such as residence time, flame surface area, turbulence intensity at the different regions of the FW and PF structures determine the emissions of PM. These details of these parameters, however, have not been addressed in this work. The hypothesis that FWs indeed result in lower PM emissions has been confirmed, and predicting the reduction in PM emissions requires

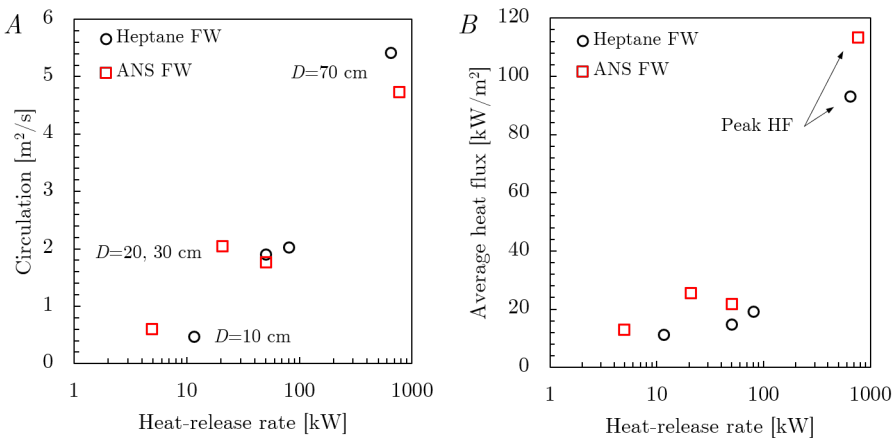

Figure 3.27: (A) Combination of peak $\dot{Q}$, and Γ for the different FWs in this study. (B) Variation of $\dot{q}$ with D.

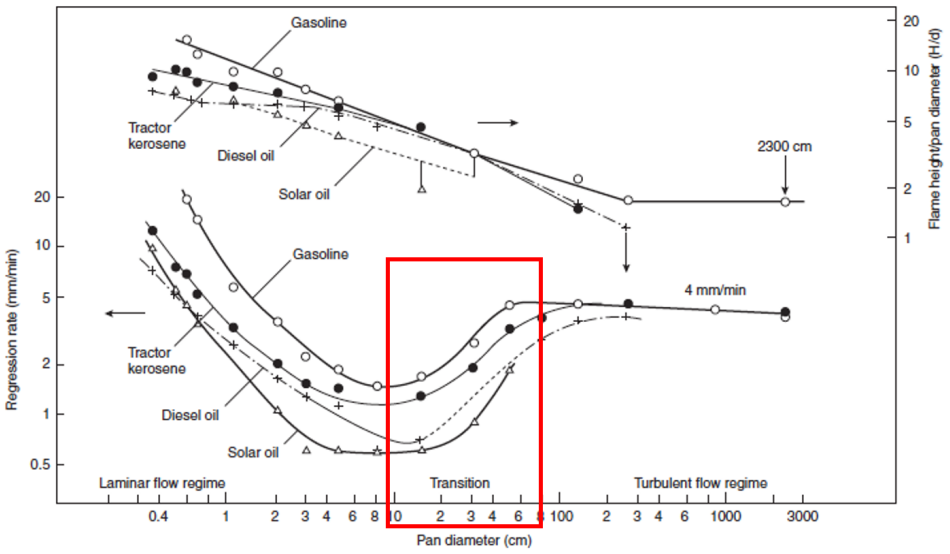

Figure 3.28: Burning rate and flame height for pool fires formed using various liquid fuels. As radiative feedback begins to dominate in large fires, burning rate tends to flatten with pool diameter. Figure adapted from [30].

establishing relationships between the EF_{PM} factor and parameters such as Γ, $\dot{Q}$ and $\dot{q}''$. These global variables define the structure of a FW, and they parameters vary significantly with D (Figure 3.27). Thus, the explanation of the reduction in emissions across length scales can be based on a phenomenological approach, using scaling analysis to relatE EF_{PM} to nondimensional circulation, heat-release rate and heat-flux feedback. This is explored in Chapter 4.

3.5 Summary

Experiments were performed at different length scales, defined by fuel-pool diameter, to quantify emissions from liquid-fueled pool fires and fire whirls. Two fuels were used – heptane, a single-component hydrocarbon, and ANS crude oil, a multi-component mixture of hydrocarbons with large differences in molecular weight and boiling point among the components.

Results show that at all pool diameters, FWs have higher burning rate and lower PM emission factor compared to corresponding PFs, confirming the original hypothesis. PM emission factors from ANS crude oil fires were an order of magnitude higher than those from heptane fires. In the case of ANS crude oil fires, fire whirls also had higher fuel consumption efficiency, although the difference between pool fires and fire whirls was negligible when boilover occurred.

Preliminary explanations for this reduction in PM emissions are based on a feedback mechanism between heat-flux feedback, heat-release rate, entrainment and gas temperature. A scaling approach is necessary to relate the different fire parameters to emissions. Further, the effect of boilover needs to be investigated further using data from the 70 cm ANS crude oil experiments. These aspects are discussed in detail in Chapter 4.

3.6 Acknowledgments

This chapter, in part, was published as report *1094AA, "Efficient Remediation of Oil Spills over Water Using Fire Whirls,"* Bureau of Safety and Environmental Enforcement (BSEE) in the *In Situ Burn Research* category in May 2019 [218]. The final report can be accessed at https://www.bsee.gov/research-record/efficient-remediation-of-oil-spills-over-water-using-fire-whirls.

Experimental results were also included in the proceedings of the *42nd AMOP Technical Seminar, Halifax, Canada, June 2019* [219]; the *11th US National Combustion Meeting, Pasadena, California, March, 2019* [220]; and in a manuscript titled "Comparison of Particulate Emissions from Liquid-Fueled Pool Fires and Fire Whirls at Different Length Scales," by S.B. Hariharan, H.F. Farahani, A.S. Rangwala, J. Dowling, E.S. Oran, M.J. Gollner, in preparation for submision and peer review in August 2020.

Chapter 4

Effect of Circulation and Heat-Release Rate on Particulate-Matter Emissions

4.1 Overview

The addition of swirling flow in a combustor improves flame stability, enhances combustion efficiency and reduces emissions [57]. In most swirl combustors, reduction in emissions typically depends on increasing mixing by increasing turbulence intensity [59, 60]. While there are similarities between swirl combustion and fire whirls, they differ in the manner of air entrainment. In swirl combustion, air is typically premixed with fuel, or injected with considerable axial momentum around a central fuel port or spray injector. There is negligible axial momentum from air entrainment at the bottom surface boundary over which fire whirls are formed, and combustion occurs in a structure that is defined by the Burger's vortex [4]. Compared to pool fires (PF), fire whirls (FW) show higher fuel consumption rates [88]

and burn at higher temperatures [109]. In contrast to swirl combustion, turbulence is generally suppressed in FWs [95]. A fundamental question needs to be answered to evaluate the potential for using FWs in ISBs – when compared to PFs, do FWs emit lower quantities of airborne soot? The experimental data in Chapter 3 showed that the PM emission factor (EF_{PM}) was lower for FWs at a given pool diameter.

In this chapter, the effect of length scale (pool diameter) on burning rate, fuel-consumption efficiency, emissions of PM, unburned hydrocarbons (UHC), CO_2, heat-flux feedback to the fuel pool, and emission factors for each species are explored in detail. Then, two scaling parameters relevant to FW behavior are defined – inverse Rossby number (Ro^{-1}), which represents the effect of ambient circulation, and nondimensional heat-release rate ($\dot{Q}^*$), the effect of buoyancy. EF_{PM} of ANS FWs decreases linearly with the ratio ($Ro^{-1}/\dot{Q}^*$), which quantifies the competition between tangential momentum and axial buoyant momentum. Finally, for ANS fires, boilover was found to cause most of the fuel to be burned in the post-boilover period, although the overall EF_{PM} was not affected significantly by boilover.

4.2 Methods

4.2.1 Emission Factors

The raw experimental data from Chapter 3 is used as the basis for analysis. The instantaneous concentration measured for each species and the total volumetric flow rate through the duct were used to calculate the emission rate in units of [mass/time]. The total mass, M, of each species was measured as an integral over time,

$$M\left[mg\right] = \dot{V}\left[\frac{m^3}{s}\right]\int_0^{t_b} C\left[\frac{mg}{m^3}\right]dt\left[s\right] \tag{4.1}$$

where $\dot{V}$ is the volumetric flow rate measured in the exhaust duct, C is the concentration measured by either the gas analyzer or PM sensor, and t_b is the burn duration.

The concentration of unburned hydrocarbons (UHC) was not directly measured, but was estimated using the carbon mass balance approach [116], assuming the different emissions to be composed of four species, CO_2, CO, PM and UHC. The carbon mass emitted as UHC was estimated as the difference between carbon mass in the fuel consumed and the total carbon mass measured as CO_2, CO and PM. The carbon mass in heptane and ANS crude oil was 84% and 85.9% [221], respectively. For each of the emitted species, an emission factor was defined as

$$\mathrm{EF}_{\mathrm{species}} = \frac{\text{Mass of carbon in emission species [g or kg]}}{\text{Mass of carbon in fuel consumed [kg]}} \tag{4.2}$$

based on the carbon mass in the species and carbon mass in burned fuel, similar to previous work [116, 222]. The burning efficiency (η_b) was defined as

$$\eta_b = \frac{\text{Mass of carbon emitted as } CO_2}{\text{Total mass of carbon in } CO_2\text{, CO, PM, UHC}} \tag{4.3}$$

to compare the relative amount of C emitted as CO_2 to the total mass of C emitted from the fuel as CO_2, CO, UHC and PM. In this way, both η_b and EF are bounded between 0 and 1, and also cause η_b to be numerically equal to EF_{CO_2}. Finally, oxidation factor (OF) is defined for each case as

$$\text{OF} = \frac{\text{Mass of } O_2 \text{ emitted as } CO_2}{\text{Total mass of } O_2 \text{ consumed}} \tag{4.4}$$

which quantifies the fraction of total oxygen consumed that is emitted as CO_2. An oxidation factor of 1 implies all the O_2 consumed is emitted in the form of CO_2.

4.3 Results

4.3.1 Effects of D on Fire Behavior

The variation of burning rate ($\dot{m}$) with D is shown in Figure 4.1. For both heptane and ANS crude oil, $\dot{m}$ is higher for FWs. The experimental variability in the measurement of $\dot{m}$ was negligible, evidenced by the very small error bars in Figure 4.1. For fires formed using each fuel at $D = [10, 30]$ cm, the ratio of $\dot{m}$ of FWs to PFs is about 2, and at $D = 70$, the ratio is 1.3. Comparing each flame regime individually for the $D = [10, 20, 30]$ cm, $\dot{m}$ for heptane fires is larger than that for ANS fires. This trend, however, reverses at $D = 70$ cm, where $\dot{m}$ of ANS is higher than that of heptane. This is also evident in Figure 4.2A, which shows the variation of fuel mass flux ($\dot{m}''$). For heptane FWs, $\dot{m}''$ declines with scale, while for heptane PFs, $\dot{m}''$ decreases from $10 - 30$ cm and then increases at the 70 cm scale. For ANS fires, however, $\dot{m}''$ increases linearly in the $10 - 30$ cm scales, but increases sharply between the 30 and 70 cm scales. The characteristics described above were also tabulated in Table 3.3.

Upon extinction of an ANS crude oil fires, some residue remained over the water surface. This residue is primarily composed of heavier hydrocarbons and tars in the fuel [221]. Measurable residues were not observed with heptane fuel. For ANS fires, fuel-consumption efficiency (η_{fuel}) was defined as

$$\eta_{fuel} = \frac{\text{mass of fuel burned}}{\text{initial mass of fuel}}$$

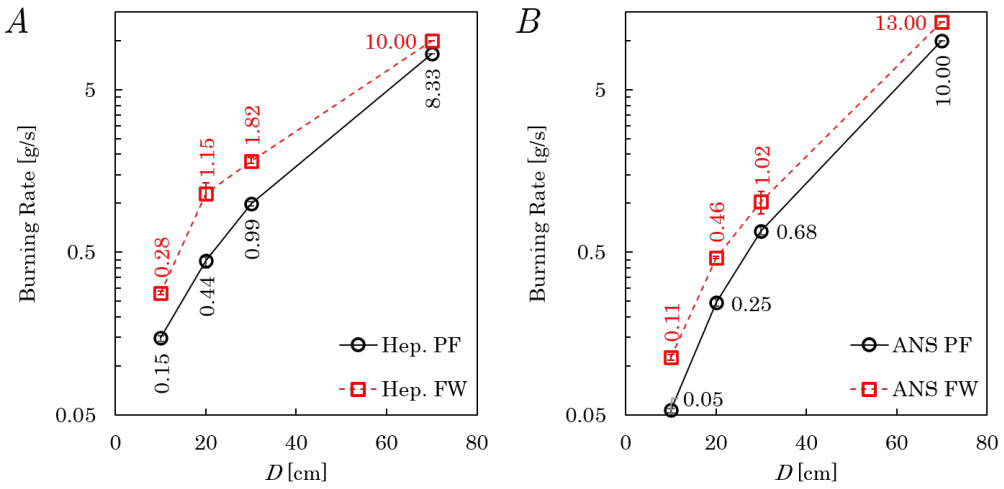

Figure 4.1: Comparison of $\dot{m}$ for PFs and FWs formed using (A) heptane and (B) ANS crude oil.

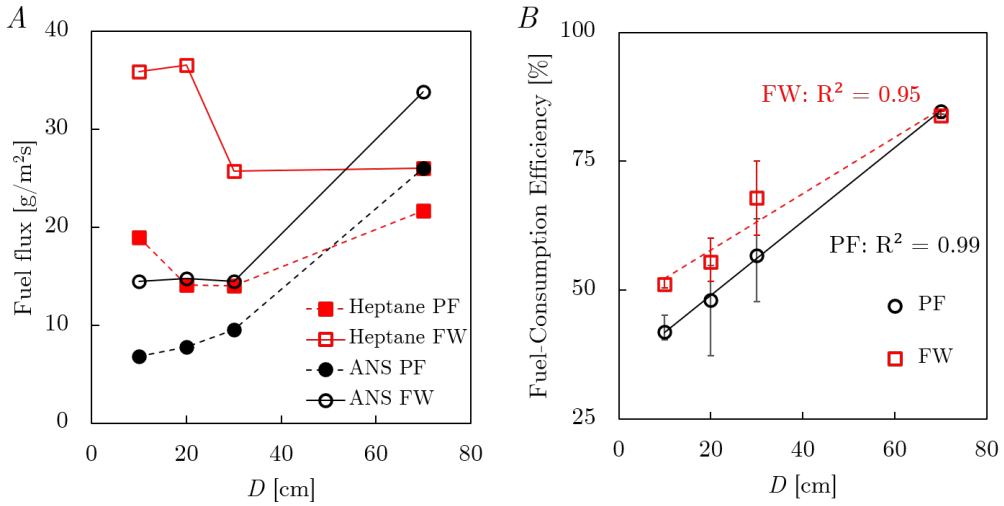

Figure 4.2: Variation of (C) $\dot{m}''$ for heptane and ANS fires, and (D) η_{fuel} with D for ANS fires.

and is shown in Figure 4.2B. In experiments at $D = 10$ cm, η_{fuel} of FWs about 53%, while that of PFs was just over 40%. At $D = 70$ cm, efficiencies above 80% were observed for both PFs and FWs. Removal efficiencies above 90% have been reported in field trials [208]. η_{fuel} is higher for FWs at $D = [10, 20, 30]$ cm, but this difference is negligible at $D = 70$ cm. The sharp rise in both $\dot{m}''$ and the negligible difference in η_{fuel} between for ANS PFs and FWs at $D = 70$ cm is attributed to boilover (section 4.4.2).

4.3.2 Circulation and Heat Feedback

The combination of circulation (Γ) and heat-release rate ($\dot{Q}$) defines the state and shape of a FW [92]. Values of Γ and $\dot{Q}$ for the FWs in this study are shown in Figure 4.3. The $\dot{Q}$ was estimated as $\dot{Q} = \dot{m}\,\Delta h_c$, where Δh_c is the lower heating value of the fuel, and Γ was estimated as $\Gamma = 4\,S\,U_\theta$. The $\dot{Q}$ of the FWs in this study spans three orders of magnitude, wider than most previous studies. According to previous definitions by Lei et al. [92], the shapes of the FWs observed in this study may generally be classified as cylindrical FWs.

The Γ calculated for the FWs in this study is compared to the inverse of the Rossby number in Figure 4.4A. The quantity Ro^{-1} describes the ratio of azimuthal (tangential) momentum from circulation to the buoyant (axial) momentum from heat release. Following [9], Ro^{-1} was estimated as $(\Gamma D)/(\dot{m}''/\rho_b)$, where ρ_b is the air density at $T = 1300$ K. While Γ increases continuously with pool diameter, Ro^{-1} increases from the $10-30$ cm scales, but is relatively unchanged between the 30 and

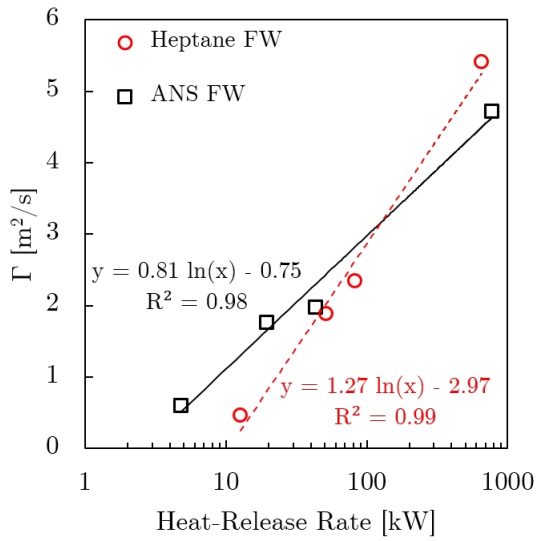

Figure 4.3: Combinations of $\dot{Q}$ and Γ for the FWs in this study, showing a logarithmic relationship for both heptane and ANS FWs.

70 cm scales. Both Γ and Ro^{-1} are generally higher for FWs formed using heptane when compared to those formed using ANS crude oil.

The variation of average heat-flux feedback, $\dot{q}''$, with D is shown in Figure 4.4B. $\dot{q}''$ is higher for FWs at all scales, although the difference is very small in the $10 - 30$ cm scales. At the 70 cm scale, however, $\dot{q}''$ for FWs is more thna twice that for PFs. Also, for the two flame regimes, the value of $\dot{q}''$ for is higher for fires formed with ANS crude oil than those formed with heptane, partly due to the higher concentration of soot particles in the flame. This is discussed in section 4.3.3. For FWs, since Γ increases linearly with D, $\dot{q}''$ also increases roughly linearly with Γ (Figure 4.4C). For each case, nondimensional heat flux was estimated from [223] as $q_f^* = \dot{q}'' / (\rho_0 \, c_p \, \Delta T \, \sqrt{gD})$ and its variation with Γ is shown in Figure 4.4D. In general, an increase in circulation corresponds to an increase in heat flux feedback to the pool, similar to previous studies [87, 224]. The experimental variation is

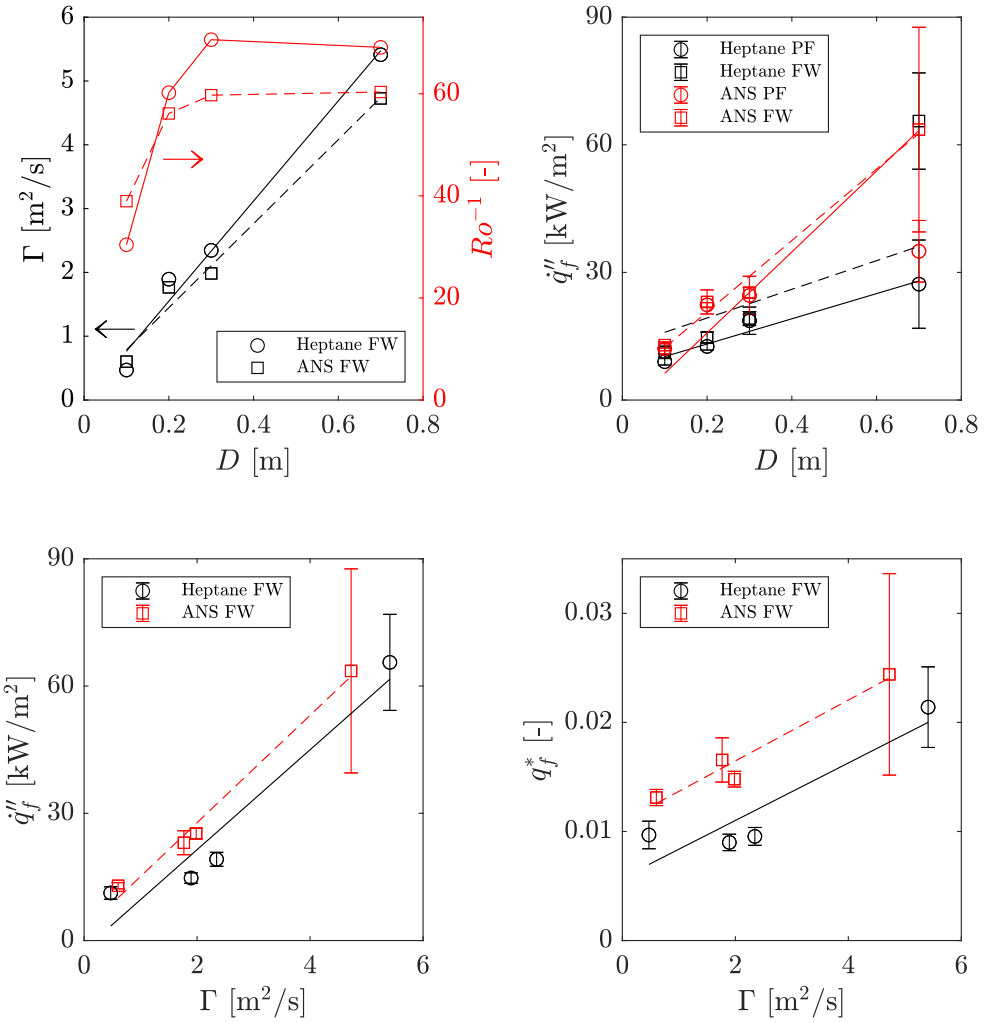

Figure 4.4: Variation of (A) Γ and Ro^{-1} with D, (B) $\dot{q}''_f$ with D. Panels (C) and (D) show the linear increase in $\dot{q}''_f$ and q^*_f with Γ for FWs. Solid lines indicate linear fits for heptane FWs, and dashed lines indicate those for ANS FWs.

higher for fires at $D = 70$ cm since these measurements were made directly using a Schmidt-Boelter gauge, whereas experiments in the smaller scales are averaged temporally and spatially, and instantaneous fluctuations are not apparent.

4.3.3 PM Emissions

The PM-emission rate for fires at $D = 70$ cm is shown in 4.5. Panels (A) and (B) compare heptane fires, and panels (C) and (D) compare ANS fires, with the different line colors indicating individual experiments. As FWs have a higher burning rate as compared to PFs, the duration of PM emission is lower. The peak emission rate of PM is higher for PFs (250 mg/s for heptane PF, 3000 mg/s for ANS PF) than for FWs (175 mg/s for heptane FW, 2300 mg/s for ANS FW). The instantaneous PM emission rate from ANS fires is an order magnitude higher than that from the heptane fires. For heptane fires, the peak emission rate is observed roughly around the middle of the burn duration. For ANS fires, however, there is an initial linear increase in the emission rate from ignition, with a sudden spike in the rate, followed by a quick drop towards extinction. The sharp spike in the emission rate (at ∼65 s for ANS FWs, ∼110 s for ANS PFs) is caused by the onset of boilover. Boilover was seen only with ANS crude oil at $D = 70$ cm, and hence the sharp rise in PM emission rate was not seen in ANS fires for $D = [10, 20, 30]$ cm (refer to Figures 3.11−3.13).

The PM emission factor, $\mathrm{EF_{PM}}$, calculated according to Equation 4.2 is presented in Figure 4.6. The definition of EF based on carbon content of the fuel also

shows that a lower fraction of carbon in the fuel is emitted as soot by FWs. For PFs and FWs formed with both heptane and ANS crude oil, the lowest EF_{PM} is at the 30 cm scale. For PFs and FWs formed using ANS crude oil, the value of EF_{PM} in the pre-boilover and post-boilover periods are similar to the overall EF (Figure 4.5B).

The EFs of UHC (EF_{UHC}) and of CO_2 (EF_{CO_2}) are shown in Figure 4.7. The lowest EF_{UHC} is seen at $D = 20$ cm for both heptane and ANS crude oil. For heptane fires (Figure 4.7A), EF_{UHC} for FWs is slightly lower than from PFs, and this simultaneously corresponds to slightly higher EF_{CO_2} (Figure 4.7C). For ANS fires at $D = [10, 70]$ cm, EF_{UHC} is slightly lower for FWs, along with slightly higher EF_{CO_2}. At $D = [20, 30]$ cm, however, FWs show slightly higher EF_{UHC} but lower EF_{CO_2} (Figure 4.7D). Compared to CO_2 and UHC, CO is found only in trace amounts. EF_{CO} is shown in Figure 4.7 (E) and (F). For heptane, fires, FWs show lower EF_{CO} than PFs. This is reversed for ANS fires, with FWs showing higher EF_{CO} than PFs. The EFs discussed above were calculated based on the mass of carbon in the fuel. The EFs determined on the basis of the total fuel mass burned are tabulated for all species in Table 4.1. EFs calculated by the two methods vary numerically, but show the same trend with D. The mass of UHC emitted was calculated as the product of the molecular weight of propane (C_3H_8) and the estimate of carbon emitted as UHC.

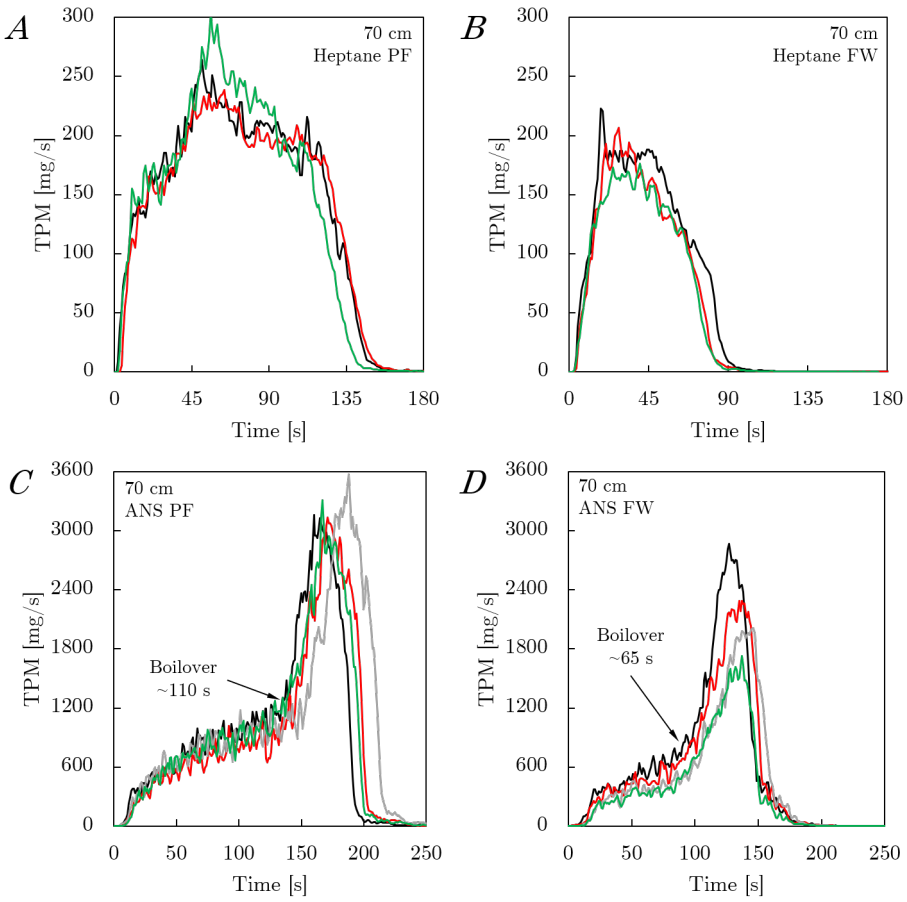

Figure 4.5: PM emission rate, measured at 1 Hz, as a function of time for 70 cm heptane PFs and FWs are shown in panels (A) and (B). Data for 70 cm ANS PFs and FWs are shown in panels (C) and (D). Boilover is evident in the PM emission rate for both ANS PFs and FWs.

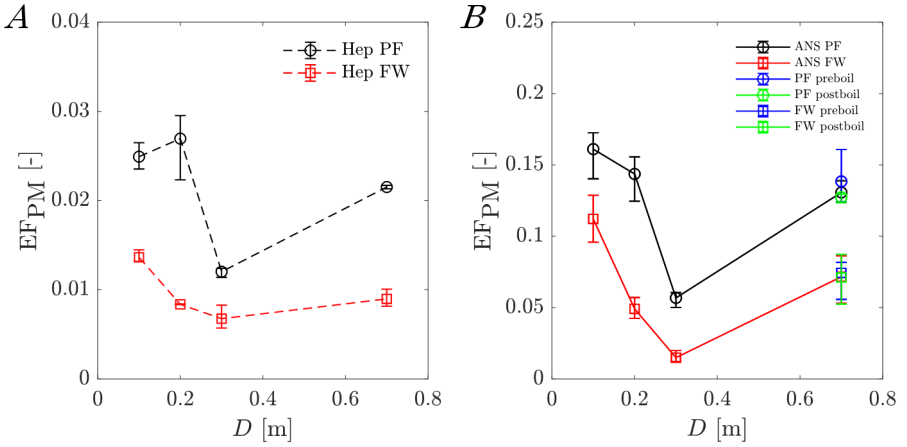

Figure 4.6: EF_{PM} for the different values of D is shown for fires formed using heptane and ANS crude oil in panels (A) and (B). Panel (B) shows markers for overall EF_{PM}, and those calculated for the pre- and post-boilover periods.

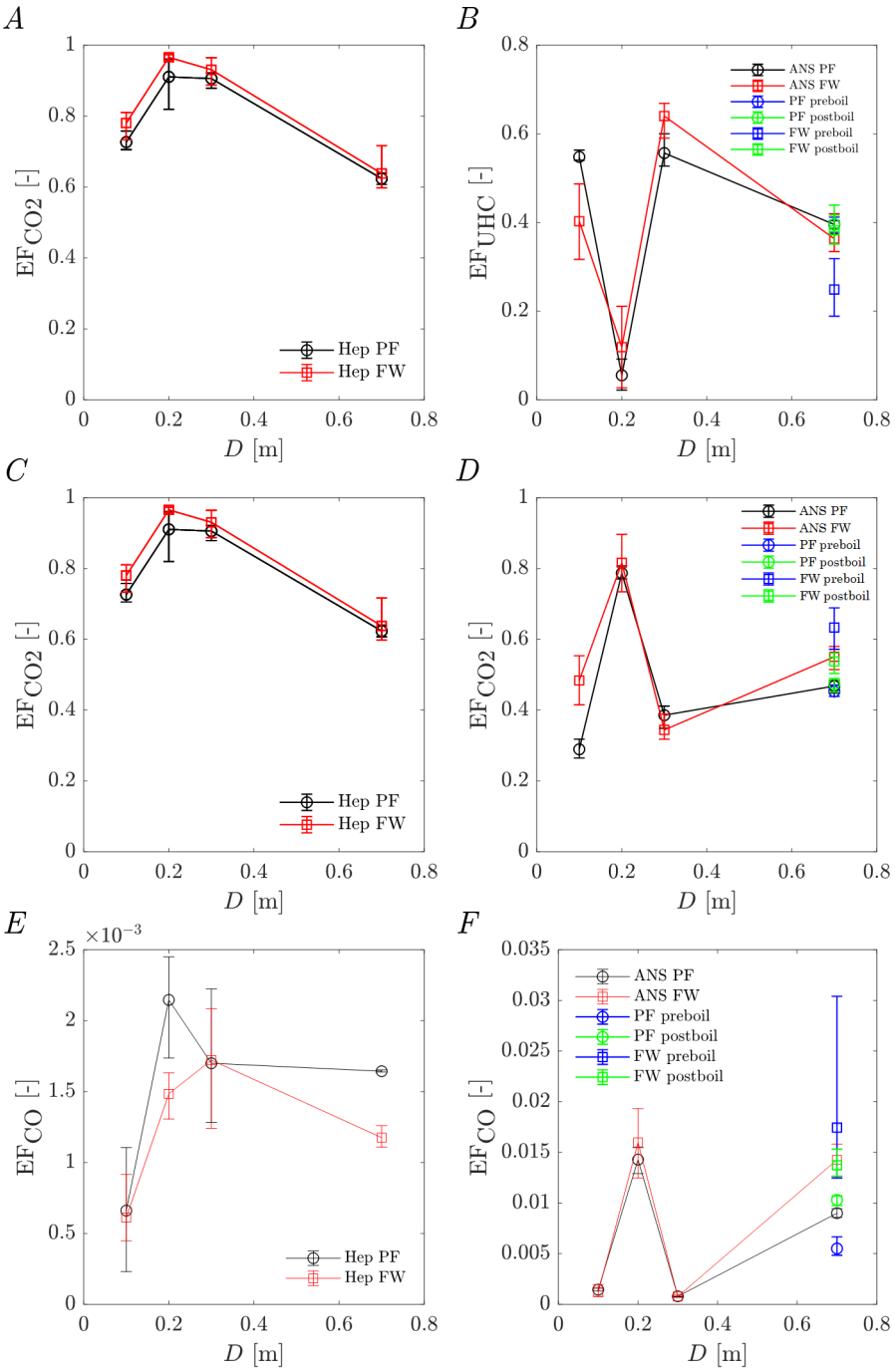

Figure 4.7: Variation of different EFs with D. EF_{UHC} is shown in panels (A) and (B), EF_{CO_2} in panels (C) and (D), and EF_{CO} in panels (E) and (F). Data for 70 cm ANS fires also shows markers for the pre- and post-boilover periods.

Table 4.1: Tabulated values of EF for the different species from PFs and FWs in this study. For each parameter, the mean of three experiments is shown for both fuel-mass based and fuel carbon-mass based estimation methods.

		Emission Factor based on total fuel mass					Emission Factor based on carbon mass in fuel				
	Scale [cm]	EF_{PM} [kg/kg]	EF_{CO_2} [kg/k]g	EF_{CO} [kg/kg]	CF_{O_2} [kg/kg]	EF_{UHC} [kg/kg]	EF_{PM} [kg/kg]	EF_{CO_2} [kg/kg]	EF_{CO} [kg/kg]	CF_{O_2} [kg/kg]	EF_{UHC} [kg/kg]
Heptane PF	10	0.021	2.238	0.001	3.193	0.254	0.025	0.727	0.001	3.801	0.248
	20	0.023	2.805	0.004	3.236	0.062	0.027	0.911	0.002	3.853	0.060
	30	0.010	2.790	0.003	3.067	0.083	0.012	0.906	0.002	3.651	0.080
	70	0.018	1.921	0.003	2.178	0.364	0.022	0.624	0.002	2.593	0.354
Heptane FW	10	0.011	2.403	0.001	2.909	0.211	0.014	0.780	0.001	3.464	0.205
	20	0.007	2.975	0.003	3.237	0.025	0.008	0.966	0.001	3.854	0.024
	30	0.005	2.867	0.003	3.168	0.062	0.007	0.931	0.002	3.772	0.061
	70	0.008	1.965	0.002	2.196	0.369	0.009	0.638	0.001	2.615	0.359
ANS PF	10	0.148	0.912	0.003	3.426	0.575	0.161	0.290	0.001	3.989	0.548
	20	0.141	2.851	0.032	3.016	0.058	0.144	0.787	0.014	3.511	0.055
	30	0.049	1.215	0.002	1.764	0.584	0.057	0.386	0.001	2.054	0.557
	70	0.113	1.501	0.018	1.629	0.415	0.131	0.468	0.009	1.874	0.395
Pre-boilover	70	0.119	1.426	0.011	0.910	0.416	0.138	0.453	0.006	1.874	0.396
Post-boilover		0.109	1.492	0.021	2.419	0.484	0.127	0.474	0.010	1.874	0.396
ANS FW	10	0.097	1.524	0.002	4.112	0.423	0.112	0.484	0.001	4.787	0.403
	20	0.042	2.571	0.032	2.590	0.125	0.049	0.816	0.016	3.016	0.119
	30	0.013	1.037	0.002	1.299	0.672	0.015	0.344	0.001	1.512	0.640
	70	0.062	1.741	0.029	1.997	0.381	0.072	0.551	0.014	2.290	0.363
Pre-boilover	70	0.064	1.995	0.035	0.550	0.261	0.074	0.633	0.017	2.290	0.249
Post-boilover		0.061	1.693	0.028	3.379	0.467	0.071	0.538	0.014	2.290	0.382

4.4 Discussion

The experimental results presented above show that a pool of liquid fuel when burned as a FW, in comparison to a PF, has a higher burning rate and emits lower peak concentrations of airborne PM. These factors together result in a lower EF_{PM} for FWs. Additionally, when ANS crude oil is used as the fuel, FWs had a higher η_{fuel} since the residual mass upon extinction was lower. A minimum slick thickness of $2 - 2.5$ mm is required to sustain burning over water surfaces [121, 208] due to heat loss to the water surface beneath the fuel. Consequently, the consumption efficiency for a given flame regime and pool diameter is directly proportional to the initial slick thickness, since all fires will eventually burn down to the minimum slick thickness.

The behavior of EF_{PM} also shows significant dependence on the fuel type. The EF_{PM} for ANS fires is an order of magnitude higher than those for heptane. Lighter fuels are known to have lower EFs than fuels that are contain high-molecular weight, complex components [16, 116]. For a given flame regime, higher values of EF_{PM} are seen for crude oil, a multi-component fuel with long-chain hydrocarbons with complex structures [221].

The addition of swirl to jet flames results in the reduction of emissions from swirl burners [60]. In swirl burners, the reduction in emissions is enabled by enhancing mixing caused by increased levels of turbulence intensity, which causes combustion to approach premixed conditions. Turbulence, however, is suppressed in FWs, and is one of the reasons for elongation of the flame as compared to a PF formed

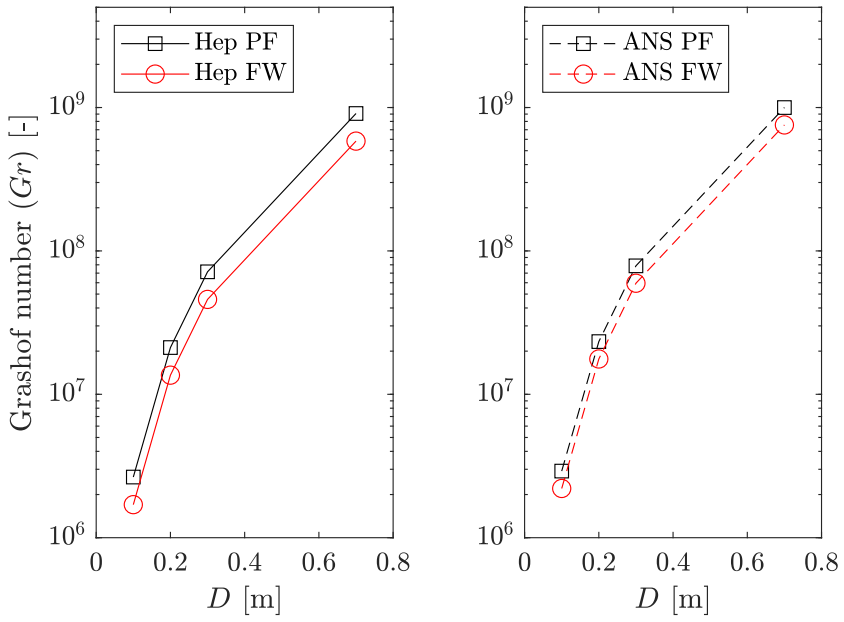

Figure 4.8: Grashof number (Gr) at different values of D.

over a pool at the same D [8,95]. The reduced effect of turbulence is evident in the lower values of the Grashof number (Gr) for PFs in Figure 4.8. Gr was estimated as $Gr = g\beta\Delta T D^3/\nu^2$, where g is gravitational acceleration, β is the ideal-gas expansion coefficient, ΔT is the excess temperature, and ν is the kinematic viscosity. Gr increases significantly with D, but only the fires at $D = 70$ cm approach the turbulent regime ($Gr > 10^9$) [225]. Thus, the lower value for EF_{PM} for FWs is not explicable based on turbulence or mixing effects.

The values of EF_{UHC} and EF_{CO_2} are at least an order of magnitude higher than EF_{PM}, showing that a majority of the carbon in the fuel is emitted in the form of gaseous components, and that only a small fraction is emitted as particulate soot. So, small differences in the values of EF_{UHC} and EF_{CO_2} between the PF and FW regimes can cause significant differences in EF_{PM}. This is evident when comparing

Figure 4.5 (C,D) with Figure 4.7 – the value of EF_{PM} for FWs is roughly half that of PFs, but the values of EF_{UHC} and EF_{CO_2} are within 10% of each other for the different cases.

In the following section, the behavior of EF_{PM} with FW-scaling parameters is analyzed to provide preliminary explanations of the differences between PFs and FWs that lead to reduced emissions.

4.4.1 Scaling

In a FW setup with natural entrainment, Γ is intrinsically coupled with $\dot{Q}$ [24]. This is because the buoyancy, that stems from $\dot{Q}$, controls the strength of air entrainment into the enclosure, U_θ, which in turn determines Γ. The effect of circulation on FWs is represented by either the Froude number ($Fr = U_\theta^2/gD$), which is analogous to the Richardson number ($Ri = g\beta\Delta T D/U_\theta^2$). Both Fr and Ri represent the competing effects of tangential momentum from ambient circulation and buoyant momentum from heat release. While Ri has previously been used to describe H_f [93], Chuah et al. [9] showed that the effect of circulation on FWs and H_f was better represented by the Rossby number (Ro), a nondimensional quantity that is equivalent to Ri^{-1}. The effect of buoyancy on the FW is represented in the form of a nondimensional heat-release rate, $\dot{Q}^*$, defined for FWs as [5]

$$\dot{Q}^* = \frac{\dot{Q}}{\rho_0 \, \Delta T \sqrt{g D^5}} \tag{4.5}$$

where ρ_0 is the ambient air density [17], $\dot{Q}$ is the average heat-release rate. The variation of $\dot{Q}^*$ with D is shown in Figure 4.9A. We now define the ratio $(Ro^{-1}/\dot{Q}^*)$ to compare the effects of buoyancy and circulation for FWs formed at different length scales. The effect of this ratio on EF_{PM} for heptane and ANS FWs is shown in Figure 4.9B.

For ANS FWs, Figure 4.9A shows a linear relationship between EF_{PM} and $(Ro^{-1}/\dot{Q}^*)$. EF_{PM} decreases as $(Ro^{-1}/\dot{Q}^*)$ increases, indicating that as the effect of circulation increases relative to buoyancy, conditions are favorable for lower PM emissions. The ratio $(Ro^{-1}/\dot{Q}^*)$ has a similar effect on EF_{PM} from heptane fires, with the lowest emissions seen at $(Ro^{-1}/\dot{Q}^*) \approx 150$. Beyond this value, however, there is an increase in EF_{PM} for heptane FWs.

For a given fuel and D, with the increasing effect of circulation, EF_{PM} reduces linearly with $(Ro^{-1}/\dot{Q}^*)$, but there exists an upper limit beyond which EF_{PM} rises again. The increase in EF_{PM} for heptane fires beyond this threshold value agrees with previous observations of FW behavior under high values of Γ – above a certain value of ambient Γ, FWs show reduced H_f, increased w_f, and increased soot emissions that are visible as black smoke [61, 92, 226]. Recent experiments conducted by Lei et al. [92] showed that as Γ is increased at a constant value of $\dot{Q}$, H_f first increases, then decreases. This change in H_f and w_f resulting from high Γ is referred to as "over-rotation" [226]. Above $(Ro^{-1}/\dot{Q}^*) \approx 150$, the increase in EF_{PM} may be attributed to over-rotation in heptane FWs. It appears that there may be a different value of this threshold for different fuels, since over-rotation is not observed for ANS FWs in Figure 4.9B.

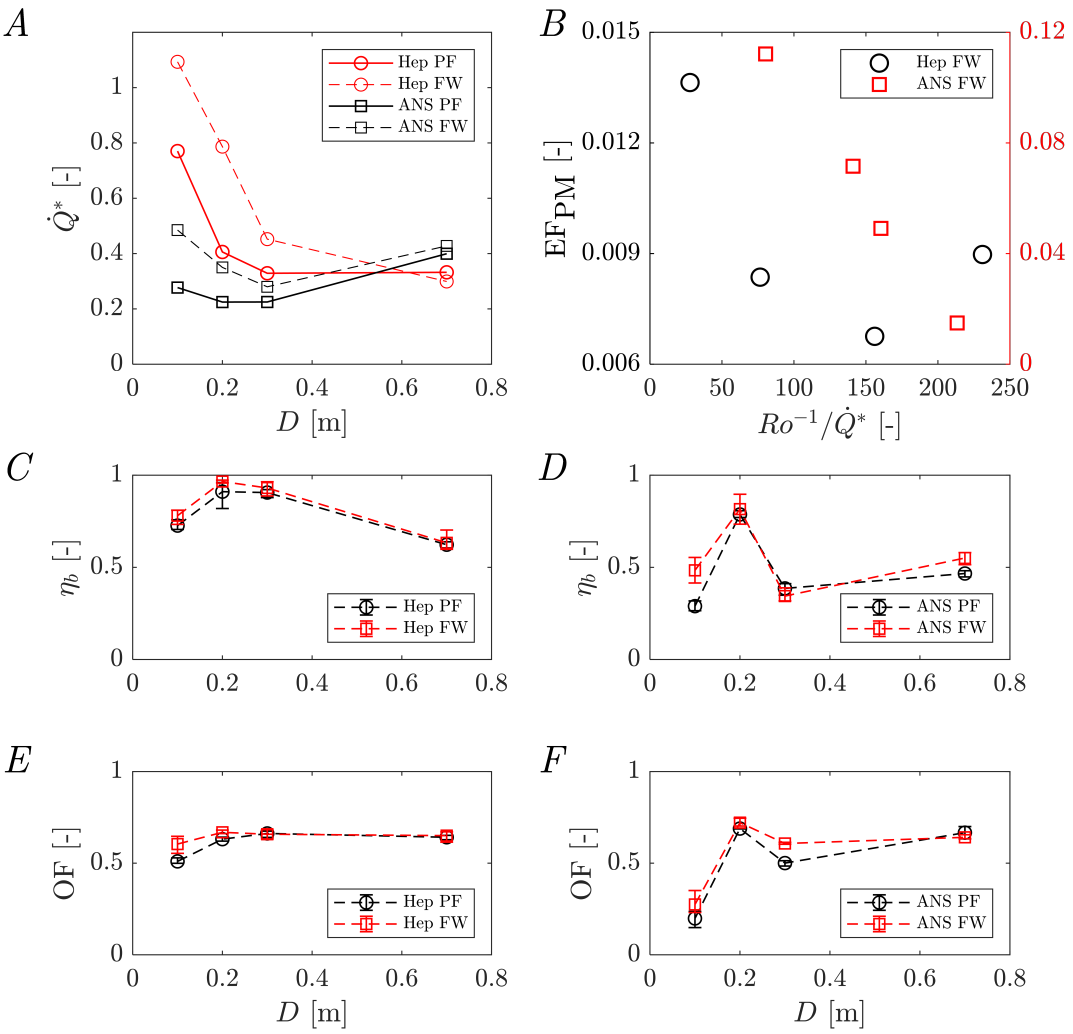

Figure 4.9: (A) Variation of $\dot{Q}^*$ with D. (B) Variation of $\mathrm{EF_{PM}}$ with $(Ro^{-1}/\dot{Q}^*)$. Burning efficiency for (C) heptane and (D) ANS fires. Oxidation factor for (E) heptane and (F) ANS fires.

For ANS FWs, the highest value of the ratio $(Ro^{-1}/\dot{Q}^*)$ is found for $D = 30$ cm. Going from the 30 to 70 cm scales, the value of Ro^{-1} remains relatively unchanged (see Figure 4.4A), but $\dot{Q}^*$ increases (Figure 4.9A), causing $(Ro^{-1}/\dot{Q}^*)$ to decrease from 213 to 141. The increase in $\dot{Q}^*$ at 70 cm is a direct consequence of the steep rise in $\dot{m}''$ caused by boilover. In contrast, for heptane FWs, the largest value of the ratio $(Ro^{-1}/\dot{Q}^*)$ is 231, occurring at $D = 70$ cm. Similar to ANS FWs, heptane FWs at $D = 30, 70$ cm have similar values for Ro^{-1}, but Figure 4.9A shows that heptane FWs have the lowest value of $\dot{Q}^*$ for fires at $D = 70$ cm. The significant reduction in $\dot{Q}^*$ from the $D = 30$ to 70 cm is the major contributing factor to increasing the effect of buoyancy (Figure 4.9B) on the FW and leads to an increase in the value of the ratio $Ro^{-1}/\dot{Q}^*$. Thus, over-rotation in heptane FWs at $D = 70$ cm is a consequence of a decline in $\dot{Q}^*$ rather than an increase in Ro^{-1}. It is hypothesized that if boilover did not occur, the value of $\dot{Q}^*$ would have been lower, causing the value of the ratio $(Ro^{-1}/\dot{Q}^*)$ at $D = 70$ cm to be higher than that at $D = 30$ cm, potentially presenting the opportunity for over-rotation to occur. This may not, however, be a preferred FW state for practical applications since it leads to an increase in $\mathrm{EF_{PM}}$. The variation of $(Ro^{-1}/\dot{Q}^*)$ with D is shown in Figure 4.10.

The variation of η_b and OF, calculated according to Equations 4.3 and 4.4, with D are shown in Figure 4.9 (C−E) for the all the different cases. Generally, FWs have higher values for both η_b and OF as compared to PFs, showing that a higher fraction of carbon from the fuel is oxidized to CO_2, causing EF_{PM} to be lower for FWs than for PFs. Based on the expressions in Equations 4.2 and 4.3, η_b is numerically equivalent to $\mathrm{EF_{CO_2}}$. Again, the metrics η_b and OF are calculated

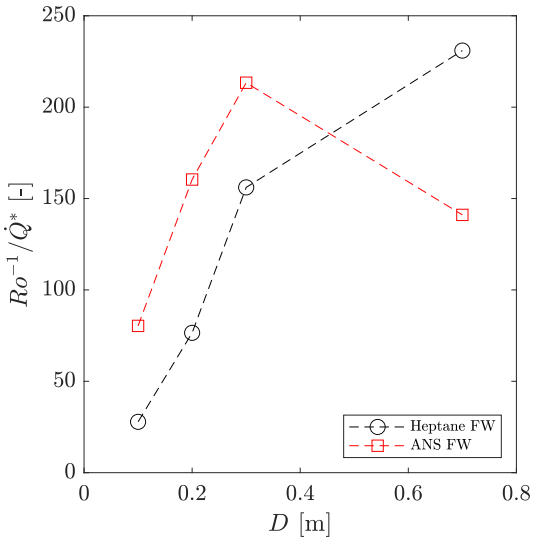

Figure 4.10: Variation of the value of $(Ro^{-1}/\dot{Q}^*)$ with D for heptane and ANS FWs. The ratio un

based on gaseous components, which are primarily composed of CO_2. So even slight improvements in converting carbon in the fuel to CO_2 can result in significant reduction in soot (PM) emissions. Both these parameters are generally higher for heptane fires than for ANS fires. The high values for η_b and OF for ANS fires at the 20 cm scale leads to lower EF_{PM} at these scales for both fuels (see Figure 4.6).

4.4.2 Boilover

The violent burning of thin layers of oil over water is referred to as boilover [215]. Figure 4.11A shows a comparison of normal burning (panel A) and boilover burning (panel B). This regime of burning is caused by a sudden expansion of superheated water-vapor bubbles that nucleate at the fuel-water interface. Characteristics such as burning rate and flame height in this regime depend on many factors including slick thickness, D, fuel type and vaporization order, weathering,

$\dot{q}''$, etc. [121, 227]. Generally, boilover causes a significant increase in both H_f and $\dot{m}$.

In this work, boilover was observed only with ANS crude oil, and was actively avoided in the $10 - 30$ cm experiments by using a magnetic stirrer to continuously mix the water sublayer. This ensured that the water bulk temperature increased only about $10 - 30$ K, depending on D and the flame regime. This prevented the fuel-water interface temperature from reaching boiling point, avoiding any bubble nucleation. At the 70 cm scale, however, a stirrer could not be used. Instead, a recirculating pump system was installed to recirculate the water from the water-fuel interface to the bottom of the sublayer. However, the recirculation system could not completely prevent boilover due to the large value of D, but could delay the onset. For ANS experiments at $D = 70$ cm, a slick thickness of 7 mm was used instead of the 5 mm that was used at the smaller scales. The recirculation system and increased slick thickness delayed boilover onset by about 40 s, allowing sufficient time for capturing data in both normal burning and boilover burning regimes.

During boilover, the bubbles shoot through the fuel-water interface, ejecting oil droplets into the flame [215]. Streaks of these evaporating fuel droplets are visible in Figure 4.11B, significantly increasing the effective surface area for combustion. This results in the large value of both $\dot{m}''$ (Figure 4.2B) and η_{fuel} (Figure 4.2C) for ANS fires at the 70 cm scale when compared to the smaller scales. Boilover burning is also responsible for increased $\dot{q}''$ (Figure 4.4), partially through enhanced radiative feedback, which in turn sustains a high temperature at the fuel-water interface.

The onset of boilover can be determined visually, but was also determined by

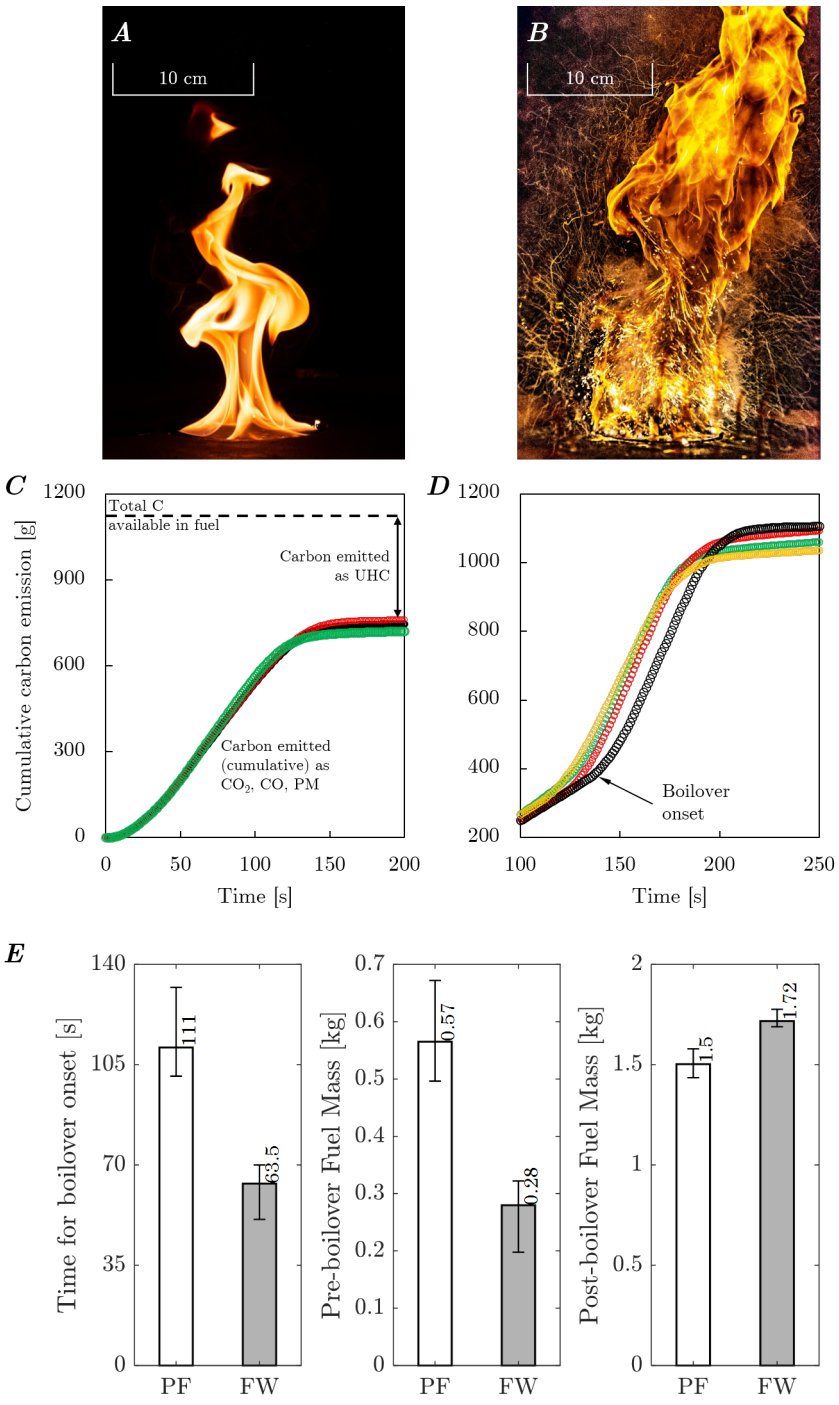

Figure 4.11: Images of a PF under (A) normal and (B) boilover burning, formed using a 5 mm slick of ANS crude oil. The streaks seen in (B) are formed by the fuel droplets emanating from the fuel pool. Variation of carbon-emission rate with time ($D = 70$ cm) for (C) heptane PF and (D) ANS PF. (D) Bar graphs showing the difference between PFs and FWs ($D = 70$ cm) on the basis of time for onset of boilover, fuel mass consumed before boilover onset, and fuel mass consumed during boilover.

the rate of emission of carbon emitted by the fire. This was determined from the cumulative measurements of the carbon emission from CO_2, CO and PM. Carbon-emission rate is almost constant during the normal burning, shown in Figure 4.11C for heptane PFs (D = 70 cm). When boilover occurs, however, the slope of this curve changes during the burning period, seen in Figure 4.11D, showing the carbon-emission rate for ANS PFs. The time at which the slope of the carbon-emission increases to a new value is denoted as the onset of boilover. For the 7 mm slicks used in these experiments, the mean boilover-onset time for PFs and FWs was 111 s and 63.5 s, respectively.

The carbon-emission rate is higher during the boilover phase, resulting in the higher overall value of $\dot{m}$ and $\dot{m}''$ for ANS fires (Figure 4.2 A and B). The mass of fuel consumed in each phase was calculated using the boilover onset time, the fraction of O_2 consumed in the pre-boilover regime, and then extrapolating the fraction to the total fuel mass consumed. For FWs, only 14% of the fuel is burned prior to boilover onset, compared to 25% for PFs (Figure 4.11E). Thus, a majority of the fuel consumed by the FW is during the boilover phase, resulting in the steeper carbon-emission rate in Figure 4.11D.

Figure 4.6 and Table 4.1 show that the value of EF_{PM} for the pre- and post-boilover periods is very similar to the overall EF_{PM}, meaning that the fraction of total carbon in the fuel that is emitted as soot is similar in these periods. This suggests that in terms of soot emissions, the effectiveness of the FW regime is rather similar during normal burning and boilover burning. Present understanding of ISBs suggests that boilover does not occur over open water [208]. Given some of the

benefits of boilover over normal burning such as increased $\dot{m}''$, η_b, radiative feedback, and an EF_{PM} similar to normal burning, it may be advantageous to purposely induce boilover during open-water ISBs.

4.4.3 Factors influencing PM emissions

A preliminary analysis of the differentiating factors between PFs and FWs, and their relation to EF_{PM} is discussed briefly. First, the higher oxygen consumption (and OF) for FWs suggests that their global equivalence ratio is leaner than that of PFs. This causes higher average temperatures in the FW structure, which has a larger surface area as compared to PFs. The high temperatures and improved view factor results in higher radiative heat feedback to the fuel pool [87]. The radiative feedback is higher in ANS fires than heptane fires (Figure 4.4) due to the higher concentration of soot particles in the flame. The convective heat feedback is also enhanced by the strong radial inflow at the bottom boundary layer [88]. When compared to PFs, increased heat feedback ($\dot{q}''$) leads to higher fuel-evaporation rate ($\dot{m}$) and thus, higher heat-release rates ($\dot{Q}$). In a FW apparatus with natural air entrainment, increased $\dot{Q}$ corresponds to increased U_θ and Γ, which in turn contribute to decreasing overall equivalence ratio, increasing OF, ΔT and $\dot{q}''$, completing the feedback loop. The increase in q_f^* with Γ, and the higher η_{fuel} values for ANS FWs indicate that the high-molecular-weight components in ANS crude oil require higher heat feedback to evaporate [227]. Overall, the lower EF_{PM} from FWs is a consequence of higher burning efficiency as compared to PFs.

The detailed mechanisms leading to a reduction of EF_{PM}, when a pool of fuel is burned as a FW rather than a PF, are not immediately apparent from the data presented here. The complex feedback mechanism between the fluid dynamics of air entrainment and combustion in the whirling flames need to be investigated further. More detailed experiments at small length scales will shed light on the role of the vortex structure, turbulence and mixing characteristics, and their interplay with chemical kinetics of soot formation and destruction. Additionally, the effects of boilover are not fully understood in the context of emissions and is dependent on the flame regime. For instance, considering EF_{CO} from PFs, post-boilover emissions are higher than pre-boilover, but this is reversed for FWs. Still, boilover has only a minimal effect on the overall EF_{PM}. The data presented here serves as a platform for more detailed investigations in the future by incorporating the effects of chemical kinetics and soot formation using a combination of non-intrusive diagnostics, scaling methods and numerical simulations.

Another parameter of that influences burning efficiency is the flame surface area, which determined by w_f and H_f. With increasing Γ and Ro^{-1}, H_f increases and w_f decreases, and the overall flame area increases [92]. PFs have the lowest flame area since Ro^{-1} for PFs is 0. As the ratio $(Ro^{-1}/\dot{Q}^*)$ increases above 0, flame surface area increases as FWs are formed, combustion efficiency increases, resulting in the lowering of EF_{PM}. Beyond a certain upper limit of Γ, however, H_f begins to decrease. Apart from Ro^{-1}, H_f is also controlled $\dot{m}$. For the FWs in this study, although $\dot{m}$ increases continuously with D, but H_f does not change linearly with D. This is a consequence of Gr; as D increases from 10 to 70 cm, the values of Gr fall

within the laminar-turbulent transition regime, which exists between $D = 10$ cm and $D = 100$ cm [30,217]. Two effects cause this – (i) the nonlinear in increase in Gr with D causes improved mixing, leading to H_f values being lower than expected. This is similar to the stabilization of the flame height of jet diffusion flames at the onset of turbulence (*Fig. 5.10* in [81]); (ii) more importantly, the height of the enclosure walls also impact H_f. The value of H_f is only slightly higher than the wall height because $\Gamma = 0$ above the limits of the enclosure walls. When the effect of ambient circulation is lost, the flame-lengthening process ceases, eliminating vortex concentration, and eventually the turbulence suppression that is necessary for flame lengthening. This enables buoyant momentum to dominate the fire, causing a transition to turbulence, and the resulting mixing ensures that the flame height ends immediately above the height of the enclosure walls. The higher the wall height, the higher the maximum value of H_f can be.

η_b also depends on the the flame surface area, which in turn depends on the height of the enclosure, which must be capable of supporting the maximum value of H_f possible for a given combination of $\dot{m}$ and D. For instance, Figures 2.3 and 3.7G were both formed at $D = 30$ cm using heptane. But H_f is different because of the height of the enclosure walls and the effect of suction used in the case of Figure 2.3, enabling a strong vortex to be formed.

4.5 Summary

An experimental investigation of airborne emissions from pool fires and fire whirls was conducted at fuel-pool diameters of 10, 20, 30 and 70 cm. Two liquid fuels were used, heptane and ANS crude oil. Free-buoyant pool fires were formed in a quiescent background, and fire whirls were formed in a fixed-frame setup that allowed natural entrainment of air towards the fire. Attributes such as burning rate, burning efficiency, emissions of particulate matter, carbon dioxide, carbon monoxide, and oxygen consumption were measured for the different pool diameters and flame regimes. Results showed that for both fuels, as compared to pool fires, fire whirls burned fuel at higher rates. When burning ANS crude oil, the mass of unburned residue was lower for fire whirls, showing that the fuel consumption efficiency of fire whirls was also higher.

Although the burning rate was higher for FWs, the peak emission rate of particulate matter (soot) form FWs was lower than from PFs. The emission factor of particulate matter emissions from fire whirls was $\sim 50\%$ lower than that from pool fires. This was true for both heptane and ANS crude oil, across all of the pool diameters. For pool fires and fire whirls, the emissions behavior of the two fuels was significantly different. The PM emission factor for ANS crude oil fires was an order magnitude higher than that for heptane fires. The burning efficiency also showed that a over half of the carbon in the crude oil was emitted as unburned hydrocarbons. This is attributed to the significant differences in the composition of the fuels and the fires they supported.

For the fire whirls in the study, a ratio of the inverse of the Rossby number and nondimensional heat-release rate, $Ro^{-1}/\dot{Q}^*$, was defined to compare the effects of buoyancy and circulation on the fire. As the value of $Ro^{-1}/\dot{Q}^*$ increased, the emission factor of particulate matter decreased linearly for ANS fire whirls. For heptane fire whirls, the linear relationship existed for diameters between 10 and 30 cm. The emission factor increased again at 70 cm due to a phenomenon called "over-rotation". Generally, the flame height of a fire whirl increases with Ro^{-1}. But beyond an upper limit, the flame height reduces and flame width begins to increase, a state referred to as over-rotation, which also corresponds to an increase in particulate emissions. While over-rotation has been reported qualitatively in the literature [61], the ratio $Ro^{-1}/\dot{Q}^*$ quantifies the phenomenon and helps explain the increase in emissions as a consequence of the decrease in flame surface area.

Over-rotation was not observed in fire whirls formed using ANS crude oil at the 70 cm scale. This is attributed to the phenomenon of boilover, which occurs during burning of thin films of dense hydrocarbon fuels floating over a water surface. Boilover caused a rapid increase in burning rate, which resulted in an increase in heat-release rate and buoyancy. This was reflected in a significant decrease in the ratio $Ro^{-1}/\dot{Q}^*$, corresponding to an increase in the buoyant momentum relative to tangential momentum, ensuring that over-rotation does not occur. The high burning rate during boilover also resulted in significant increase in the flame height and fuel-consumption efficiency. The onset-time of boilover was lower for fire whirls, and fire whirls also consumed a higher fraction of the initial fuel during the boilover period. Additionally, the overall particulate emission factor was similar to that in

the pre-boilover and post-boilover periods, showing that it may be advantageous to induce boilover during *in-situ* burns.

The reduction in particulate-matter emissions from fire whirls is attributed to the following factors. Compared to pool fires, fire whirls consume more oxygen per unit mass of fuel, leading to a lower global equivalence ratio. They also have higher burning efficiency, and a higher fraction of the oxygen consumed was converted to carbon dioxide. Collectively, these result in higher temperatures in the fire whirl structure, leading to the higher heat feedback to the fuel surface. Heat feedback increased linearly with pool diameter and circulation, and led to higher burning rate, which in turn resulted in higher air-entrainment velocities, which in turn leads to higher oxygen supply to the fire whirl, completing the feedback loop.

A number of open questions regarding the emissions from fire whirls remain to be answered before practical applications are considered. While soot-free whirling flames such as the "blue whirl" are known in the literature [22, 64], they form at very small length scales [24] and are highly sensitive to experimental conditions [66]. Fire whirls, on the other hand, can be formed more robustly across a large range of length scales. While fire whirls do emit some quantities of soot, the results in this work demonstrated that they can still offer opportunities to significantly reduce the environmental impact of ISBs, which are currently burned as pool fires. The range of heat-release rates and circulation for fire whirls in this study is wider than those in the literature, although these factors were not varied independently in this study and only natural-entrainment configurations were used. To understand the independent effect of these parameters on emissions, systematically varying these

quantities by controlling air entrainment could help isolate the effects. The effect of boilover on emissions needs to be investigated further since its onset does not seem to significantly affect the particulate matter emission factor. The metrics presented here provide a global explanation for the reduction in particulate emissions compared to pool fires, and future work will focus on the exact mechanisms leading to efficient combustion.

4.6 Acknowledgments

Data from this chapter, in part, is included in a manuscript titled "Comparison of Particulate Emissions from Liquid-Fueled Pool Fires and Fire Whirls at Different Length Scales," by S.B. Hariharan, H.F. Farahani, A.S. Rangwala, J. Dowling, E.S. Oran, M.J. Gollner, in preparation for submission and peer review in August 2020.

Chapter 5

Quantifying the Effects of Circulation and Buoyancy on the Transition from a Fire Whirl to a Blue Whirl

As demonstrated in Chapters 3 and 4, the addition of circulation (or, a swirling flow field) to a free-buoyant pool fire can lead to an increase in combustion efficiency, reducing the emission of particulate matter (soot). The most ideal case is when no soot is emitted from the flame. There exist two possibilities for the scenario to occur: (i) soot is formed in the flame, but is completely oxidized; this is the case with a non-sooting candle flame [131], where soot nucleates on the rich side, but is consumed on the lean side of the flame, and the products of combustion are gaseous; (ii) soot nucleation does not occur; this is a possibility even in nonpremixed flames, under some specific configurations such as flame strain rate, low pressure, etc. [143, 145]. The blue whirl is a regime where soot does not nucleate, and this is attributed to a combination of partial premixing and strain rate [64, 65]. This chapter discusses the fluid dynamics of transition from a fire whirl to a blue whirl.

5.1 Overview

The relative influence of circulation and buoyancy on fire whirls (FW), blue whirls (BW), and the transition between these regimes of a whirling flame is investigated using a combination of experimental data and scaling analyses. FWs are whirling, turbulent, cylindrical yellow (sooting) flame structures that form naturally in fires and are here created in laboratory experiments. In contrast, a BW is a laminar, blue flame (non-sooting) with an inverted conical shape. Prior measurements of the circulation and heat-release rate are now combined with additional measurements of the flame geometry, particularly the width and height, to provide characteristic length scales for these flames. Using these, a nondimensional circulation (Γ_f^*) and heat-release rate ($\dot{Q}_f^*$) were defined and shown to correspond to azimuthal (buoyancy driven) and axial momenta, respectively. The ratio $\mathcal{W}^* = \Gamma_f^*/\dot{Q}_f^*$, a quantity analogous to the swirl number used to characterize swirling jets, was evaluated for FWs and BWs. For FWs, $\mathcal{W}^* < 1$, so that axial momentum is greater than azimuthal momentum and the flame is dominated by buoyant momentum. For BWs, $\mathcal{W}^* > 1$, so that the flame is circulation dominated. This is argued to be consistent with vortex breakdown being an important part of the transition of FWs to BWs. This work presents a basis for predicting when a BW will form and remain a stable regime.

5.2 Introduction

The interaction of reacting buoyant plumes and swirling flow fields gives rise to structures called fire whirls. The formation and dynamics of fire whirls are important because of the devastating effects they can have in urban and wildland fires [8,47,48]. Both the structure and the dynamic behavior of fire whirls are dominated by the effects of buoyancy, which arises from heat release, and by circulation, determined by the level of ambient swirl. In laboratory-scale experimental investigations, the combination of heat-release rate ($\dot{Q}$) and circulation (Γ) can be controlled to determine the shapes of fire whirls, which have been classified into a number of regimes [92].

The blue whirl is a small, soot-free flame that was first observed in an experimental study of fire whirls formed on a water surface [64]. The transition to the blue whirl occurred naturally, as air was entrained through tangential inlets and without the aid of externally forced air entrainment. The fire whirls that exist before blue-whirl formation are much larger in height than the blue whirl and exist at the laminar-turbulent transition flame regime, evidenced by wrinkled laminar flames at the flame base. In contrast, the blue whirl regime is characterized by a much smaller length scale (see Figure 5.1) and is a laminar flame with no visual or aural indications of turbulence [64]. The unexpected transition from a fire whirl to a blue whirl involves laminarization of the flow, which suggests that the interplay between $\dot{Q}$ and Γ is different from that in fire whirls.

Lei et al. [92] showed the influence of $\dot{Q}$ and Γ on the shape of fire whirls formed

Figure 5.1: Images of fire whirl regimes formed at a gap size of $S = 35$ mm. The experimental configuration is shown in Figure 5.4. The fuel burning rate, $\dot{V}$, varies from (A) to (I) as 0.5, 1.1, 1.5, 2, 3, 4.5, 6, 8 and 10 ml/min. Panels (A)−(B) show BWs, (C)−(E) show TBWs, and (F)−(I) show FWs.

in an Emmons-type [8] fire-whirl apparatus where swirl is generated by a spinning mesh around a central flame. Their $\dot{Q} - \Gamma$ map showed the strong influence of Γ on the overall shape of fire whirls, especially on the flame shape at the base. This map showed an "extinction limit jump," a sharp increase in the threshold $\dot{Q}$ below which fire whirls were extinguished for all values of Γ. In recent work, the $\dot{Q} - \Gamma$ map was extended to include the blue whirl regime [24]. This extended map showed that the combinations of $\dot{Q}$ and Γ that led to blue-whirl formation was within the extinction limit defined in [92]. The formation of blue whirls in this region also requires experimental apparatus to satisfy surface-boundary conditions [66] that were absent in previous work.

In the literature, scaling analyses have often been used to identify parameters and quantities to describe the occurrence of fire whirls [5, 11, 12, 228]. The recent extension of this analysis to blue whirls [24] showed that blue whirls exist in a regime distinct from traditional fire whirls. The transition from the fire whirl to the blue whirl was previously hypothesized to be the result of the onset of vortex breakdown [23, 64], which is characterized by the presence of a recirculation zone (RZ) [229]. Subsequently, the presence of a RZ was shown to exist in the blue whirl [66], qualitatively confirming these suggestions. The presence of the RZ was observed using streaks of incandescent soot within the conical region of the flame. Since soot particles are not present in a stable blue whirl, the RZ is visible fleetingly during the transition process.

The onset of vortex breakdown is driven by the relative magnitude of local momenta in the axial and azimuthal directions. Different types of vortex breakdown

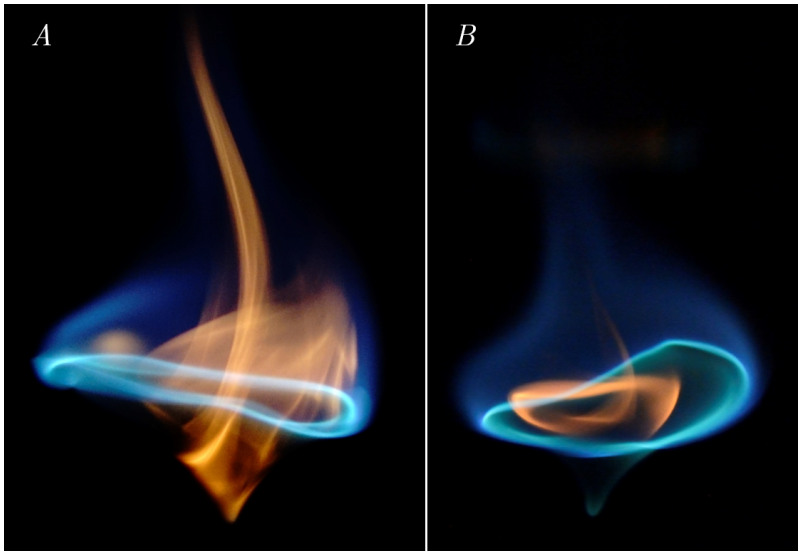

Figure 5.2: Images of the blue whirl where the RZ is visualized by streaks of incandescent soot particles. Images (A) and (B) were captured with exposure times of 1/60 s and 1/100 s, respectively.

can occur in both nonreacting [230,231] and reacting flows [57,59]. The momenta in these directions were compared using a scalar quantity, called the swirl number, $\mathcal{S}$, defined as the ratio of axial flux of azimuthal momentum to the axial flux of axial momentum [232]

$$\mathcal{S} = \frac{\int_0^R u_z\, u_\theta\, r^2\, dr}{R \int_0^R u_z^2\, r\, dr}$$

where u_z and u_θ are the axial and azimuthal velocities, and R is the radius of the vortex core. For an experimental apparatus, however, the definition is simplified and defined based on the geometry of the swirler, with different expressions for axial and radial swirlers [59]. In swirl burners, the RZ develops at a threshold value of $\mathcal{S} \approx 0.6$ [232].

In fire whirls, the axial and azimuthal momenta are represented by buoyancy

and circulation, respectively. The purpose of this work is to test this hypothesis: The flow field of the blue whirl is a state of vortex breakdown, that occurs when the local azimuthal momentum becomes higher than the axial momentum, and this blue whirl retains properties of the bubble mode. We approach this from the experimental point of view by reinvestigating the scaling, which helps us quantitatively distinguish between the fire- and blue-whirl regimes. Through this approach, the entrainment conditions required to generate the blue whirl at other length scales are also explored.

Here, we use the raw data for $\dot{Q}$ and Γ, taken from previous experiments, and define new nondimensional quantities to quantify the role played by buoyancy and circulation in whirling-flames. These quantities are of the same order of magnitude and can be used to differentiate between buoyancy- and circulation-dominated regimes. A nondimensional ratio analogous to $\mathcal{S}$ is used to establish a threshold value for the onset of vortex breakdown in whirling flames, corresponding to formation of the blue whirl. We find that when the flow field is dominated by buoyancy, the traditional fire whirl develops, and when circulation dominates, there is a transition to the blue whirl. The scaling analysis is used to reinterpret fire whirl data in the literature to give an explanation of why this unique transition was not discovered in previous fire whirl experiments.

5.2.1 Background

To date, formation of a blue whirl has always been preceded by a fire whirl. In addition, a blue whirl can be formed from a variety of different liquid hydrocarbon

fuels. Experimental measurements show that it has peak temperatures of about 2000 K [22, 31, 72] and can also be formed on other types of smooth surfaces such as metals [66]. There is intense combustion in the bright blue ring, as evidenced by high concentrations of OH, OH* and CH* radicals in this region [31, 66].

Recent experiments [24] allow us to extend previous scaling analyses to include the blue whirl, providing useful context to the material in the current article. In [24], the experimental setup was a fixed-frame fire-whirl apparatus formed by two semi-cylindrical quartz segments. The semi-cylinders form an enclosure within which combustion occurs, and the offset distance between the pieces creates a gap that allows air entrainment into the enclosure. Various combinations of fuel flow rate ($\dot{V}$) and gap size (S) were used to generate fire whirls and blue whirls. The flow velocity into the enclosure was measured at selected axial (vertical) locations using a DANTEC 54T42 Mini CTA anemometer attached to a DANTEC 55P16 hot-wire probe, which was positioned at the center of one gap. These velocity measurements were used to find an approximate circulation for each flame regime according to $\Gamma = \pi U_\theta D_C$, where U_θ is the tangential velocity measured at the inlet, and D_C is the diameter of the enclosure. Assuming complete combustion of the supplied fuel, the heat-release rate was calculated as $\dot{Q} = \dot{V}\,\Delta h_c\,\rho_f$, where Δh_c is the lower heating value (LHV) and ρ_f is the density of liquid n-heptane.

The combination of S and $\dot{V}$ influences the shape of the flame, and three flame regimes were identified: the blue whirl (BW), the stable fire whirl (FW), and the transitional blue whirl (TBW). Images of the different regimes for $S = 35$ mm are shown in Figure 5.1, and the full data set from [24] is summarized graphically

in Figure 5.3. For high values of $\dot{V}$, unsteady FWs were formed with very large diameters, termed as Large Fire Whirls (LFWs). These impeded safe operation of the hot-wire anemometer and were thus avoided in experiments. These raw data were used in a scaling analysis to determine nondimensional quantities for global scaling using the apparatus diameter (D_C) as the characteristic length scale. Although the apparatus diameter or gap size are not intrinsic properties of the FW itself, they have been used in the literature [11, 12] for scaling purposes since they influence ambient circulation in FW apparatus with natural air entrainment.

This analysis showed that the BW was close to the extinction limit defined previously [92]. The BW formation limits, defined on the basis of $\dot{Q}$ and Γ, as well as the relationship between nondimensional heat-release rate ($\dot{Q}^*_D$) and nondimensional circulation (Γ^*_D), were both sensitive to the gap size between the half-cylinders. The extinction limit for FW regimes was extended by the presence of the BW, and this was attributed to the experimental conditions at the bottom surface over which they formed [66].

Using fixed length scales (such as apparatus or burner diameter) in scaling analyses [92, 97] results in quantities that denote general large-scale effects. For instance, the predictions of flame height of FWs for known values of Γ and $\dot{Q}$. The use of characteristic length scales derived from flame geometry represent effects of the local flow field. In the present work, the raw data for Γ and $\dot{Q}$ is combined with new data on flame geometry. To understand the local effects and the controlling factors in the transition to the BW, flame height, H, and flame width, w_f, are used as characteristic length scales to normalize Γ and $\dot{Q}$.

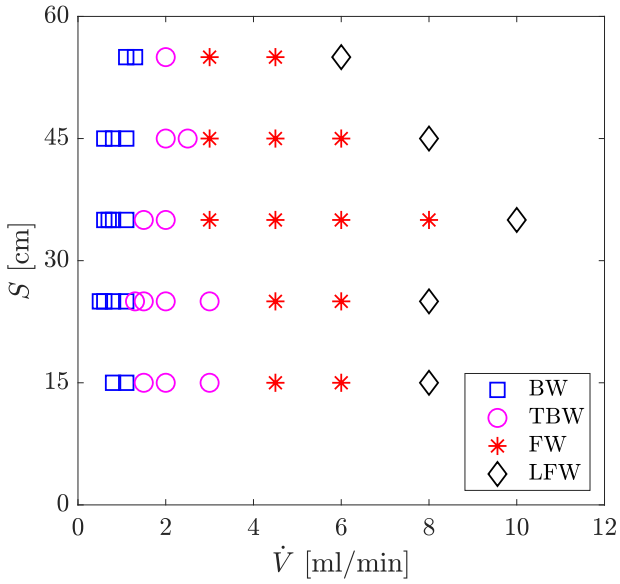

Figure 5.3: Influence of S and $\dot{V}$ on the fire whirl regime, adapted from [24].

The approach presented in this article was taken to help quantify the effects of the primary competing forces in whirling flames, buoyancy and circulation. By incorporating H and w_f into Γ and $\dot{Q}$, local buoyancy and circulation in the flame are represented by their respective nondimensional quantities, $\dot{Q}_f^*$ and Γ_f^*. Their ratio then present a basis for distinguishing buoyancy- and circulation-dominated regimes in whirling flames.

5.3 Experimental Methods

The experimental apparatus (Figure 5.4), similar to that used in previous work [22,24,64,66], consisted of two quartz half-cylinders (310 mm diameter, 600 mm height) suspended on an aluminum frame. The two quartz pieces were positioned over a water pan and offset from each other, forming gaps for natural entrainment of air. Liquid fuel, here n-heptane, was supplied to the water surface using a syringe pump at a constant volumetric flow rate. Upon ignition of the fuel, the buoyant flow due to heat release within the enclosure draws air into the enclosure through the two gaps. For all experiments, a short "overlap" region was constructed from thin sheets of aluminum to form a channel at each inlet (see Figure 5.4). The effect of this inlet channel is discussed in section 5.4. All data were obtained with these overlapping inlet channels.

A typical experiment involved the injection of 10 ml of fuel onto the water surface, followed by ignition using a propane torch. Initially, a pool fire was formed and lasted for a few seconds before evolving to a FW. Upon transition to a fire whirl, fuel was supplied at a constant rate using the syringe pump. After about 60 s, the rate of fuel supply (from the syringe pump) and consumption (by the FW) were nearly equal, and a stable FW or BW formed, depending on the gap size and fuel supply rate. For a given gap size, S, the regime of the FW depended on the fuel supply rate, $\dot{V}$, which was varied in the range of [0.5, 10.0] ml/min. S was varied in the range [15.0, 55.0] mm. Due to the natural-entrainment configuration, the only regimes that formed resulted from a balance between these parameters.

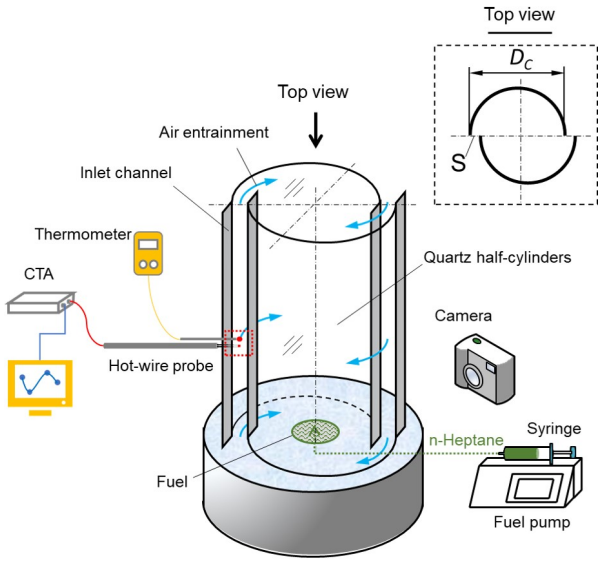

Figure 5.4: Schematic of experimental apparatus.

Measurements were made of flame geometry for each regime. Videos (1280 x 720 pixel resolution) of each experiment were recorded at 60 fps for 60 s using a Sony RX10II, with an aperture of $f/5.6$. The flame width (w_f) and flame height (H) were obtained by averaging the flame contour on multiple frames. From each 60 s video, three separate periods of 0–12 s, 24–36 s and 48–60 s were chosen, and 720 individual frames were extracted from each period. The resulting 2160 RGB images for each experimental condition were converted into grayscale images, which were then converted to a binary format in *ImageJ* [233] using Otsu's method [234] to determine a binarization threshold. This method was reliable since exposure in the videos was set such that there was a dark background in contrast to the bright flame, resulting in maximum intensity separation at the edge of the flame sheet. The mean binary value for each pixel was obtained by stacking all 720 binary images for each time period. Dividing the mean binary value by 256 (the range of intensity values in gray scale), the probability of the flame appearance for each pixel was

determined, giving the probability contours of the flame. The mean flame contour was defined by a probability of 0.5 based on previous literature [235].

Based on this mean contour, the flame width measured at the widest cross-section, was found ∼10 mm above the water surface for FWs, and the width of the bright blue ring (also called vortex rim in [22]) was used as the flame width for both the BW and TBW. The flame height was measured at the highest position of the continuous flame region above the water surface. For each time period, one set of w_f and H was obtained, and an overall average was obtained by calculating a mean from the values for the three time periods recorded and binarized.

5.4 Flame Geometry

Figures 5.5 and 5.6 shows the variation of the flame geometry parameters, w_f and H with both Γ and $\dot{Q}$. The narrow error bars for the FW and BW regimes reflects the relative stability of their flame geometry during the 60 s period analyzed (Figures 5.5A and 5.6A). TBWs, on the other hand, show significant changes in flame geometry parameters due to their repeated transitions between the FW and BW regimes. The FW shows the highest values of w_f, which is not a strong function of Γ or $\dot{Q}$. The dashed line in Figure 5.5B shows a slight decrease from the BW to the TBW, followed by an increase for FWs.

The value of H, however, varies with both Γ and $\dot{Q}$. The increase in H with Γ is shown in Figure 5.6A. The curve is approximated by the fit in Equation 5.1, which has a R^2 value of 0.55. The fit in Equation 5.1 does not include data points for $S = 15$ mm in Figure 5.6A. The data points for $S = 15$ mm (solid square markers) follow a trend different from the other conditions. This bifurcation behavior was discussed in previous work [24]. The relationship between H and $\dot{Q}$, shown in Figure 5.6B, is given by Equation 5.2, which has a R^2 (coefficient of determination) value of 0.96.

$$H = 52.03\ \Gamma^{3.89} \tag{5.1}$$

$$H = 2.91\ \dot{Q}^{1.19} \tag{5.2}$$

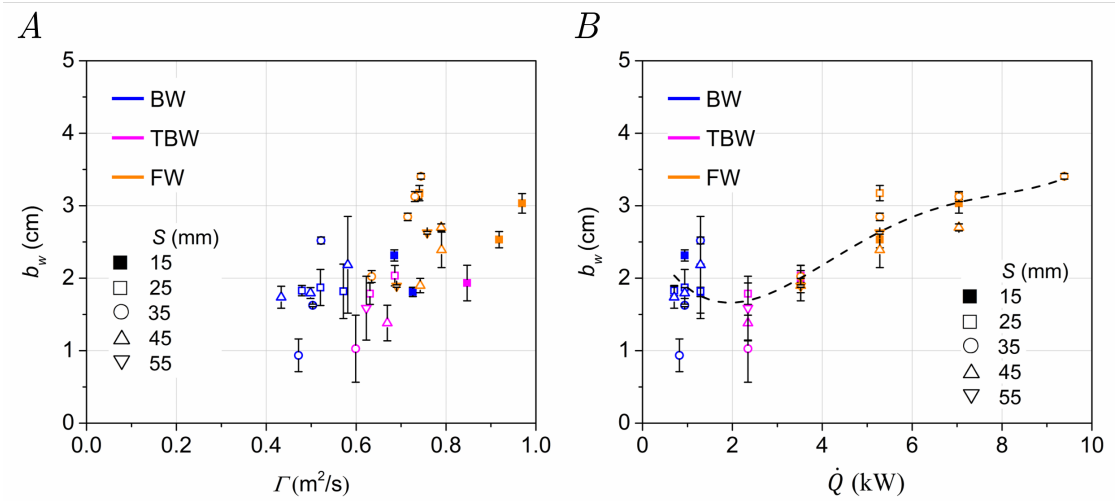

Figure 5.5: Variation of w_f(or b_w) with Γ and $\dot{Q}$. Only a very minimal increase in w_f is seen with $\dot{Q}$.

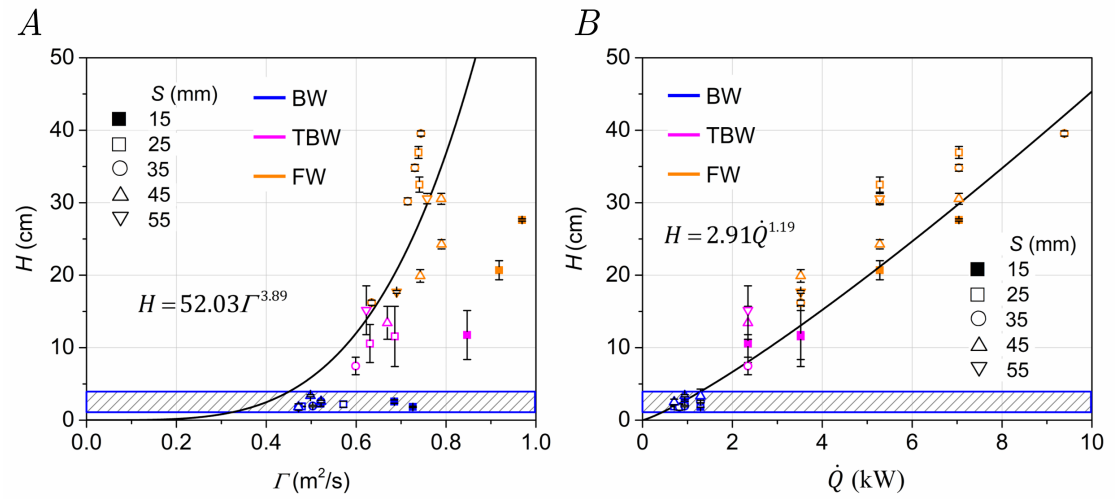

Figure 5.6: Variation of H with Γ and $\dot{Q}$. The hashed section in panels B and D indicates the limited variation in H for the BW. In panel B, flame regimes at $S = 15$ mm are not considered for the curve-fit shown and follow a different trend. This difference at low S^* is discussed in [24].

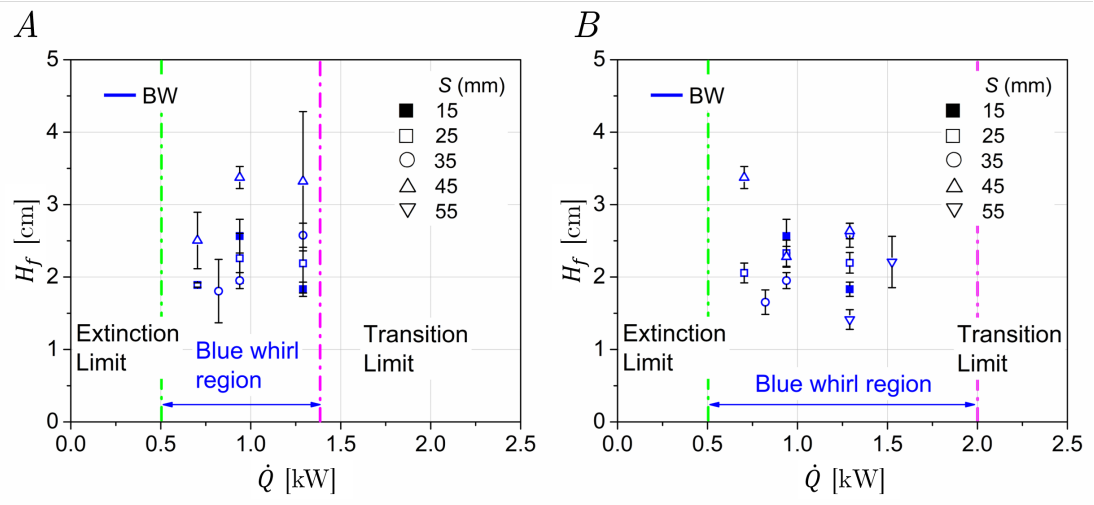

Figure 5.7: Variation of H with $\dot{Q}$, shown for cases without (A) and with (B) the added inlet channels for the BW. The vertical dashed lines, green (left) and magenta (right), indicate limits of extinction and transition, respectively.

The effect of the inlet channels (see Figure 5.4) on the fluctuation in H for BWs is shown in Figure 5.7. The BW is particularly sensitive to ambient perturbations, which cause H to fluctuate significantly when the inlet channel is not present. This results in the large variations in H, seen in Figure 5.7A, particularly near the extinction and transition limits. When the inlet channel was present, the variation in H for BWs decreased even in conditions close to the extinction and transition limits (Figure 5.7B). Furthermore, the BW formation limits were also extended when the inlet channels are present. The differences between panels (A) and (B) in Figure 5.7 reflect the role of the inlet channels in stabilizing the BW. The experimental data obtained *with* the inlet channel was used below in the scaling analysis since they correspond to more stable experimental conditions.

5.5 Dimensional Analysis

Based on a review of previous scaling methods used for FWs [5], the parameters governing circulation (Γ) of a FW in a fixed-frame type apparatus are

$$\Gamma = f_1\ \left(\dot{Q}, S, w_f, H, D_C, T_0, \rho_0, \Delta T, \Delta\rho, C_{p,0}, g\right) \tag{5.3}$$

where Γ, $\dot{Q}$, S, w_f, H and D_C are as defined previously. The quantities T_0, ρ_0, ΔT, $\Delta\rho_0$, $C_{p,0}$ and g are ambient temperature, ambient density, specific heat of air at T_0, and gravitational acceleration. Equation 5.3 assumes that (i) circulation is independent of axial location of the FW, (ii) viscosity is negligible relative to inertial and buoyant forces, (iii) heat conduction and mass diffusion terms are negligible, and (iv) combustion is infinitely fast and steady.

As shown in Figure 5.1, the geometry of the flame may be used to distinguish among the different flame regimes. Specifically, H strongly depends on Γ and $\dot{Q}$ (Figure 5.6). Using H and w_f as characteristic length scales, D_C, T_0, ρ_0 and g were chosen as the basic physical parameters to apply the Buckingham–Π theorem [236] on Equation 5.3, yielding 8 nondimensional Π terms shown below.

$$\left(\Gamma_f^*, H^*, \frac{w_f}{D_C}\right) = f_2\ \left(\dot{Q}_f^*, S^*, \frac{\Delta T}{T_0}, \frac{\Delta\rho}{\rho_0}, \frac{g\, w_f}{C_{p,0}\Delta T}\right) \tag{5.4}$$

The dimensionless circulation is defined as $\Gamma_f^* = \Gamma\,/(D_C\,\sqrt{gH}) = (\pi U_\theta/\sqrt{gH})$, which is analogous to the Froude number, defined as $Fr = (U^2/gd)$. The quantity $\dot{Q}_f^*$= $\dot{Q}/(C_{p,0}\Delta T\rho_0\ w_f^2\ \sqrt{gH})$ is the dimensionless heat-release rate, representing the ratio of the actual heat-release to a reference combustion enthalpy $(\dot{V}/(w_f^2\sqrt{gH}))$, where the subscript '$f$' denotes normalization by a flame dimension. In the quantity $\dot{Q}_f^*$, the denominator $(C_{p,0}\,\Delta T\,\rho_0\,w_f^2\,\sqrt{gH})$ denotes the volumetric distribution of the heat-release rate for a non-swirling diffusion flame of width w_f and height H. Thus, $\dot{Q}_f^*$ reflects an enhancement in combustion intensity due to the presence of swirl, and also represents the buoyancy due to heat release. This is discussed further in section 5.6.

The ratio $S^* = S/D_C$ is the dimensionless gap size, a geometric feature of the setup. The quantity (w_f/D_C) is nearly constant for a given regime (see Figure 5.5). The quantities $(\Delta T/T_0)$ and $(\Delta\rho/\rho_0)$ can be assumed to be nearly constant for most fires [9], and $(g\,w_f/C_{p,0}\,\Delta T)$ indicates the ratio of potential energy to thermal energy, which is small enough to be neglected here. Hence, Equation 5.4 reduces to

$$\left(\Gamma_f^*, H^*\right) = f_3\ \left(\dot{Q}_f^*, S^*\right) \tag{5.5}$$

$$H^* = f_4\ \left(\Gamma_f^*, \dot{Q}_f^*, S^*\right) \tag{5.6}$$

where H^*=H/w_f. The different experimental data and nondimensional quantities for each flame regime are shown in Table 5.1.

According to Equation 5.6, H^* depends on Γ_f^*, $\dot{Q}_f^*$ and S^*. Figure 5.8A shows

Table 5.1: Experimental data and nondimensional quantities for the BW, TBW, FW and LFW regimes.

S [mm]	Flame Regime	D_C [m]	S^* [-]	Γ [m^2/s]	$\dot{Q}$ [kW]	w_f [cm]	H [cm]	Γ_f^* [-]	$\dot{Q}_f^*$ [-]
15	BW	0.333	0.05	0.685	0.436	2.314	2.56	4.1	1.21
	BW			0.726	0.599	1.81	1.83	5.15	3.22
	TBW			0.847	1.634	1.934	11.74	2.37	3.04
	FW			0.918	2.451	2.532	20.69	1.94	2.73
	FW			0.969	3.268	3.033	27.62	1.77	2.19
25	BW	0.343	0.073	0.479	0.327	2.345	2.056	3.11	0.99
	BW			0.521	0.436	2.037	2.329	3.18	1.64
	TBW			0.631	1.003	1.786	10.574	1.81	2.3
	TBW			0.686	1.091	2.035	11.554	1.88	1.85
	FW			0.741	1.178	3.174	32.495	1.21	0.67
	FW			0.739	1.175	3.142	36.943	1.31	0.64
35	BW	0.353	0.1	0.503	0.436	1.625	1.951	3.26	2.81
	FW			0.635	1.634	2.024	16.197	1.43	3.22
	FW			0.715	2.451	2.846	30.198	1.18	1.79
	FW			0.731	3.268	3.126	34.813	1.12	1.84
	FW			0.744	4.357	3.405	39.551	1.07	1.94
45	BW	0.363	0.124	0.433	0.327	2.609	2.28	2.52	0.76
	BW			0.581	0.599	2.762	2.635	3.15	1.15
	TBW			0.669	1.089	1.382	13.43	1.61	3.71
	FW			0.743	1.634	1.899	19.9	1.46	3.3
	FW			0.79	2.451	2.391	24.265	1.41	2.83
	FW			0.789	3.268	2.701	30.543	1.26	2.63
55	BW	0.373	0.15	0.593	0.599	1.611	1.413	4.27	4.62
	BW			0.636	0.708	2.596	2.208	3.67	1.68
	TBW			0.623	1.089	1.586	15.172	1.37	2.65
	FW			0.69	1.634	1.892	17.692	1.41	3.52
	FW			0.758	2.451	2.627	30.561	1.17	2.09
30 [7]	LFW	1.8	0.111	2.62	25	5.6	117	0.43	2.39
				3.22	50	7.6	201	0.4	1.98
				4.12	100	9.4	316	0.41	2.07
				4.9	150	10.4	419	0.42	2.2
				5.87	200	11.1	500	0.47	2.36
				6.27	250	12	543	0.48	2.42
				6.6	300	12.7	553	0.5	2.57

that $\dot{Q}_f^*$ has minimal influence on H^*, in that $H*$ varies only when the flame regime changes. Also, for each flame regime, the influence of $\dot{Q}_f^*$ is limited, particularly for the BW regime. For a given flame regime, H^* does not show any trend with S^*.

The quantity H^*, however, does depend on Γ_f^*, as shown in Figure 5.8B. Figure 5.8A shows that there is a difference of an order magnitude in H^* between the BW and FW regimes. The solid line in Figure 5.8B shows the power-law relationship between H^* and Γ_f^*, approximated by Equation 5.7 with an R^2 of 0.9.

$$H^* = 15.49/{\Gamma_f^*}^2 \tag{5.7}$$

When compared to FWs, BWs form in a region of relatively high Γ_f^* and low H^* (Figure 5.8B). BW formation occurs for $\Gamma_f^* \in [2.4, 5.2]$, while FWs generally form in a much narrower region where $\Gamma_f^* \in [1.0, 1.4]$. The FWs for $S^* = 0.045$ deviate slightly from this trend and occur closer to $\Gamma_f^* \approx 2$. Below $\Gamma_f^* = 2.4$, which is the BW transition limit in Figure 5.8B, H^* begins to increase rapidly. Generally, these results show that the dimensionless circulation, Γ_f^*, has a significant impact on H^*, and appears in this analysis as an important parameter to understand the transition between the FW and BW flame regimes.

The LFW limit is near $\Gamma_f^* = 1$. The LFW was unsteady and its diameter was comparable to that of the enclosure, which did not permit any measurements. Consequently, below we use data for LFWs from the literature to calculate the required nondimensional quantities. In the following section, we will focus on the relationship between Γ_f^* and $\dot{Q}_f^*$, both of which are $\mathcal{O}(1)$.

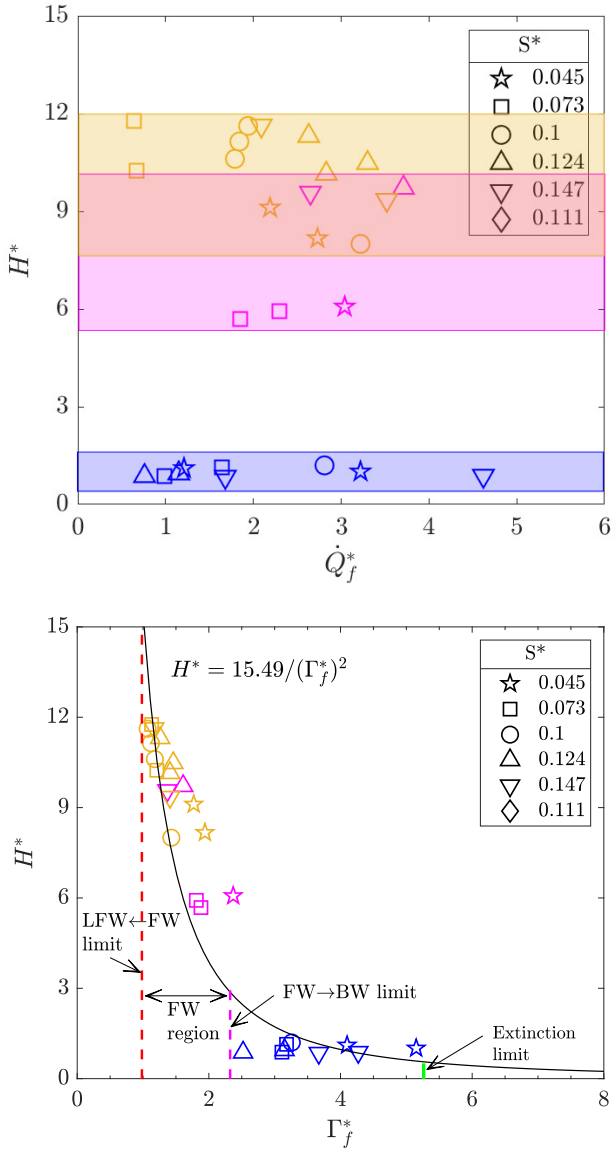

Figure 5.8: (*Top*) Variation of H^* with $\dot{Q}_f^*$. The range of H^* for the BW and FW do not overlap, showing that it varies only when the regime changes. The colored stripes denote the range of H^* for each regime. S^* does not influence H^*, particularly in the BW regime. (*Bottom*) Variation of Γ_f^* with H^*, with the different transition limits shown as dotted lines.

5.6 Discussion

The three nondimensional quantities, Γ_f^*, $\dot{Q}_f^*$ and H^* have different relationships for the FW and BW regimes and may be used to provide insight on the local effects governing the transition from FWs to BWs. Going from the BW to the FW, while w_f is relatively constant with $\dot{V}$, H increases continuously. Thus, H and H^* distinguish these regimes. The near-linear increase in H with $\dot{V}$ is similar in behavior to laminar jet diffusion flames [81]. Within the BW regime, however, H varies little with $\dot{V}$. Figures 5.5B and 5.6B show that the BW forms in a region of low $\dot{Q}$. Since entrainment velocity is directly proportional to $\dot{Q}$ (see *Fig.*5 in [24]), this leads to low Γ for BWs. $\dot{Q}_f^*$, however, lies in the same range for both FWs and BWs (Figure 5.8A).

Figure 5.6A indicates that the BW forms in a region where Γ_f^* is relatively high. As Γ_f^* decreases, there is a steep increase in H^*, leading to the FW. With further decrease in Γ_f^*, the effect of circulation on the buoyant plume reduces. LFWs are formed when $\Gamma_f^* \in (0, 1)$ and flame height varies roughly linearly with circulation [12, 92]. Eventually, when $\Gamma_f^* = 0$, a free-convection pool-fire is formed [80, 102]. Here, H^* depends on other factors such as $\dot{Q}$ and the pool diameter [105, 237].

Plotting $\dot{Q}_f^*$ vs. Γ_f^* allows for the different regimes to be more clearly distinguished, presented in Figure 5.9. Since measurements of the LFW (at $\Gamma_f^* < 1$) are not available from this work, data of LFWs from the literature are used for comparison. Fire whirls similar to the LFW were investigated by Lei et al. [7] using a propane burner in a square fixed-frame setup. The LFWs in their experiments form

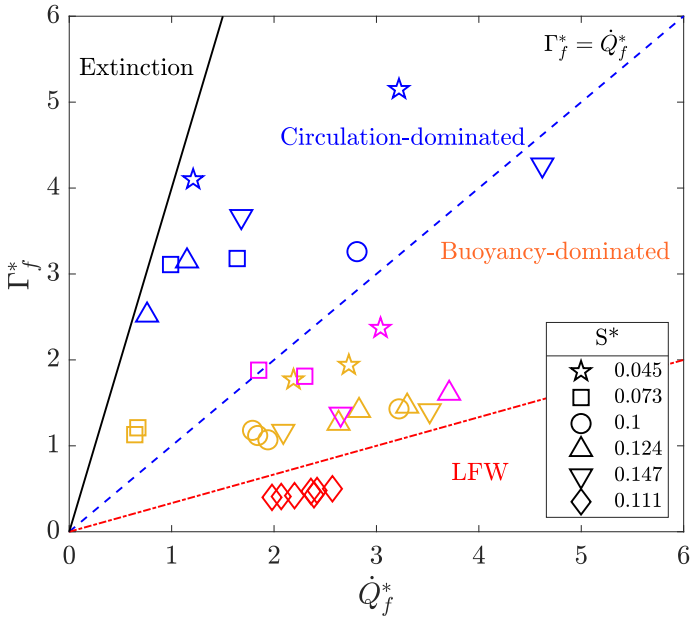

Figure 5.9: Γ_f^* as a function of $\dot{Q}_f^*$ for the different regimes in this study. The blue markers correspond to BWs, magenta to TBWs, yellow to FWs, and black to LFWs. The dotted blue line represents $\Gamma_f^* = \dot{Q}_f^*$, roughly the region where the FW→BW occurs. Quantities for LFWs were calculated from raw data in *Table 1* of [7], whose experiments used a propane burner within a square cross-section setup, with natural air entrainment at $S^* = 0.111$ (calculated based on the definition in this study) and $\dot{Q} \in [25, 300]$ kW. Extinction occurs in the region where $\Gamma_f^* > 4\dot{Q}_f^*$, and FW→LFW transition occurs when $\dot{Q}_f^* > 3\Gamma_f^*$, represented by the red line.

in a narrow range of Γ_f^*, lower than the FWs in this study, and are also included for comparison in Figures 5.9 and 5.10.

The quantities $\dot{Q}_f^*$ and Γ_f^* are of the same order and represent buoyancy and circulation, respectively. The dashed line in Figure 5.9 represents $\Gamma_f^* = \dot{Q}_f^*$, where the influence of circulation and buoyancy is roughly balanced. For the flame regimes above this line, circulation dominates (i.e., $\Gamma_f^* > \dot{Q}_f^*$), and for those below, buoyancy dominates (i.e., $\Gamma_f^* < \dot{Q}_f^*$). In general, the BW lies above the $\Gamma_f^* = \dot{Q}_f^*$ line, and FWs in the region below. Data points for LFWs are well within the buoyancy-dominated region. Figure 5.10A and Table 5.2 show that for naturally-entrained FWs, with

increasing scale, buoyancy tends to dominate circulation (see markers for LFW). This is a consequence of larger $\dot{Q}$, which for liquid-fueled FWs is partially controlled by the fuel pool diameter.

Of the five data points available for the TBW regime, three lie between the FW and BW regimes. This transition regime is expected to occur in the neighborhood of $\Gamma_f^* = \dot{Q}_f^*$, although Figure 5.9 shows two instances deviating more towards the FW side (these deviations are observed for one instance of the BW at $S^* = 0.147$ and two FWs at $S^* = 0.073$). This spread in TBW data is expected from the large fluctuations in H in this regime (see Figures 5.5 and 5.6). Additionally, only five data points exist for the TBW regime in our work, and the trend may become more apparent when there is more data available.

The quantity $(\Gamma_f^*)^2$ is the Froude number, Fr. While Fr represents the competition between buoyant and external momentum, it does not fully represent the effect of circulation on H. Chuah et al. [9] pointed out that the value of Ro (Rossby number) in relation to Fr was important for quantifying the effect of circulation on burning rate in whirling flames. This is especially applicable to configurations with natural air entrainment where Γ and $\dot{Q}$ are not independent.

While Γ_f^* varies significantly for the BW and FW regimes, it does not help in comparing the local relationship between axial and buoyant momenta. Thus for whirling flames, it is more useful to represent the competition between circulation (tangential component) and buoyancy (axial component) in the form of the ratio, $\mathcal{W}^* = (\Gamma_f^*/\dot{Q}_f^*)$, the *whirl number*. The value of the whirl number for the different regimes is shown in Table 5.2. Figure 5.10(B) shows the relationship between H^*

with ($\mathcal{W}^*$) for all the regimes. The relationship is approximated by a least-squares fit as $H^* = 4.14/(\mathcal{W}^*)^{1.32}$. This graph shows that transition to the BW occurs in the neighborhood of $\mathcal{W}^* = 1$, when circulation begins to dominate buoyancy. In other reacting or nonreacting swirl flows, this condition leads to the formation of a recirculation zone (RZ), and to vortex breakdown [57, 232]. In swirl burners, the threshold value for RZ formation is $\mathcal{S} = 0.6$ [59].

Earlier work showed the presence of a RZ within the BW and suggested that the shape of the BW regime may be governed by the bubble mode of vortex breakdown [22, 181]. While the RZ is visible during the transition process, it is not visible in a stable BW due to the absence of soot tracers [66]. Assuming that the development of a RZ is necessary for BW formation [23], $\mathcal{W}^*$ is analogous to $\mathcal{S}$ in predicting the onset of vortex breakdown in whirling flames, and may therefore represent an appropriate nondimensional scale to distinguish whirling flames. Table 5.2 shows that the threshold value of $\mathcal{W}^*$ leading to vortex breakdown and BW formation is ≈ 1.

The large difference in the values of $\mathcal{W}^*$ for FWs and BWs provides hints as to why the BW regime was not observed in previous FW experiments. In addition to the smooth bottom boundary without obstructions to the incoming radial flow [66], a circulation-dominated regime ($\Gamma_f^* > \dot{Q}_f^*$) is required for transition to the BW. FWs subject to strong vorticity have been studied previously [9, 10] and it was found that elongation in FW flame length, when compared to a pool fire, cannot be fully attributed to increasing burning rates. This suggests that that the vortex structure, within which fuel fractions are high, plays a significant role in the increased flame

Table 5.2: Values of $\mathcal{W}^* = (\Gamma_f^* \ / \ \dot{Q}_f^*)$ for the BW, TBW, FW and LFW regimes.

S^*	$\mathcal{W}^* = \Gamma_f^*/\dot{Q}_f^*$			
	BW	TBW	FW	LFW
0.045	3.39	0.78	0.71	
($S = 15$ mm)	1.6		0.81	
0.073	3.15	0.78	1.82	
($S = 25$ mm)	1.94	1.02	1.78	
0.099	1.16		0.44	
($S = 35$ mm)			0.66	
			0.61	
			0.55	
0.124	3.33	0.43	0.44	
($S = 45$ mm)	2.73		0.5	
			0.48	
0.147	0.92	0.52	0.4	
($S = 55$ mm)	2.18		0.56	
0.111				0.18
($S = 300$ mm)				0.2
From [7]				0.2
				0.19
				0.2
				0.2
				0.19

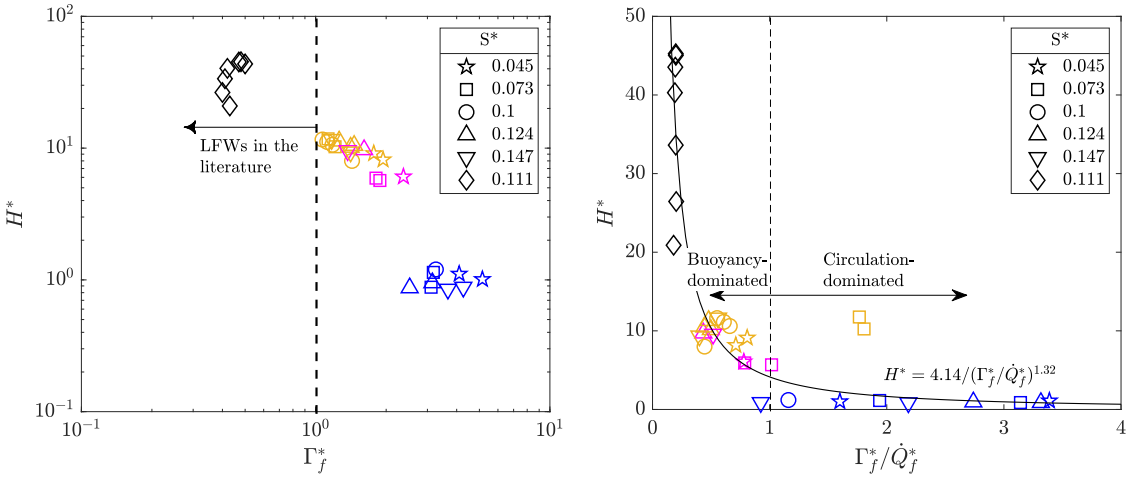

Figure 5.10: Comparison of experimental data in this work with those for LFWs in the literature [7]. (*Top*) The LFW regime occurs when $\Gamma_f^* \in (0, 1)$. The value of H^* for LFWs in the literature are many times that of the FWs in this study, and an order magnitude higher than the BWs. (*Bottom*) The FW-to-BW transition occurs around $\mathcal{W}^* \approx 1$, in the circulation-dominated regime.

height.

In the case of transition from FWs to BWs, increasing Γ_f^* results in suppression of H^*, eventually leading to BW formation (Figures 5.8B and 5.10). The BW does not show much variation in H^* (see Figure 5.8A), which may be attributed to the existence of a RZ upon vortex breakdown. The RZ potentially aids in better mixing, leading to a smaller volume required for the reaction to occur and causing suppression of H^*. This is similar to the reduction in flame height of laminar jet diffusion flames upon transition to turbulence [81].

Coenen et al. [23] noted that for a given fuel pool diameter, BW formation required evaporation of fuel from a fraction of the total pool area such that $\dot{Q}$ and H decrease simultaneously. The contraction in evaporation area is a consequence of intensification in vorticity as the width of the FW vortex core reduces. This behavior

agrees with the data from the present work, where decreasing H^* and $\dot{Q}_f^*$ is enabled by increasing Γ_f^*. Since circulation is conserved radially [8], a reduced vortex core diameter allows tangential momentum to overcome axial momentum locally, resulting in the conditions required for a vortex breakdown bubble to form and results in the BW. The limits presented in this work are determined from experiments on regimes formed by natural air entrainment. Controlling the transition process or further expanding the envelope of BW formation conditions, if possible by means of external forced entrainment, will require independent control of $\dot{Q}$, Γ and the fuel pool area to ensure $\Gamma_f^* > \dot{Q}_f^*$.

For all of the flame regimes, the influence of Γ and $\dot{Q}$ is weak on w_f but strong on H. The flame dimensions are determined by the axial flux of fuel vapor, which is determined by $\dot{V}$, and thus the diameter of the fuel pool over the water surface. For a given flame regime, the fuel mass flux upon evaporation is nearly constant, and the increase in specific volume upon combustion of the fuel vapors shows a near-linear growth in H rather than w_f. This is similar to the behavior of jet diffusion flames, for which the flame height in the laminar regime depends on the volumetric flow rate of fuel from the fuel port, before a transition to turbulence reduces the flame height (see *Fig. 5.10* in [81]).

5.7 Summary

The transition from fire whirls to blue whirls was studied by a scaling approach. Using raw data from previous work and new measurements of flame geometry, an investigation of the scaling parameters now allows us to understand the relative influences of circulation and buoyancy in determining the different fire whirl regimes. In addition to data from previous work, new measurements of the flame geometry (height, H, and width, w_f) were obtained from videos.

The flame width did not vary significantly with circulation (Γ) or heat-release rate ($\dot{Q}$) for the different flame regimes. The relationship between H and Γ was exponential, and between H and $\dot{Q}$ was nearly linear. Using H and w_f as the characteristic length scales, two primary nondimensional quantities were defined: dimensionless heat-release rate, $\dot{Q}^*_f$, and dimensionless circulation, Γ^*_f. These quantities were of the same order of magnitude, and represent the role of buoyancy and circulation in each regime.

The ratio of these quantities, $\mathcal{W}^* = (\Gamma^*_f/\dot{Q}^*_f)$, the ***whirl number***, represents the relative influences of circulation and buoyancy on the flame. This is analogous to the swirl number for swirling jets, where the relative magnitudes of axial Reynolds number and azimuthal swirl determine the flame regime. The influence of this ratio on the tranistion may be summarized as

$$\mathcal{W}^* = \left\{ \begin{array}{ll} < 1, & \text{buoyancy dominated; FW} \\ \approx 1, & \text{transitional; TBW} \\ > 1, & \text{circulation dominated; BW} \end{array} \right\}$$

A value of $\mathcal{W}^* < 1$ represents a flow field dominated by buoyancy, and most fire whirls belong to this regime, with values in the range [0.4, 0.8]. Two instances of fire whirls (referred to as "conical fire whirls" in [92]) showed an average value of 1.8. The value of this ratio was calculated to be ∼0.2 for large fire whirls in the literature, placing them well within the buoyancy-dominated regime.

For the blue whirls in this study, $\mathcal{W}^* \in [0.9, 3.4]$, and generally $\mathcal{W}^* > 1$. This indicates a flow regime where circulation dominates over the buoyancy locally. The transitional blue whirl is defined as a regime that continuously switches between the blue and fire whirl, and may theoretically be expected to occur when the ratio is in the neighborhood of 1, where the effects of buoyancy and circulation are roughly equal. The number of data points for transitional blue whirls was limited and calculated to be in the range of [0.43, 1]. This range extends more towards the buoyancy-dominated side, and is attributed to the large fluctuations in H, caused by repeated alternation between the fire whirl and blue whirl regimes.

The transition from the fire whirl to the blue whirl occurs at a threshold value of $\mathcal{W}^* = 1$, roughly where circulation begins to dominate buoyancy. This favors the formation of a recirculation zone, leading to the onset of vortex breakdown. This is one reason why the blue whirl was not discovered in previous apparatus. Previous fire whirl apparatus generated only buoyancy-dominated regimes by design, and did

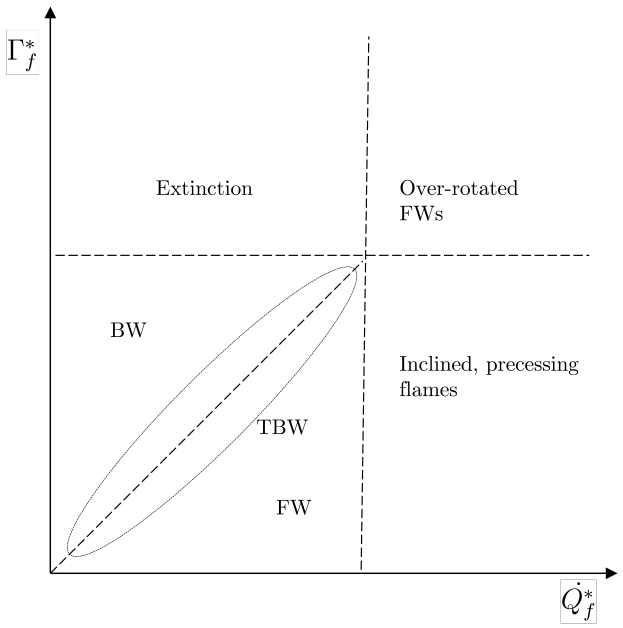

Figure 5.11: Proposed map of some whirling flames regimes as functions of nondimensional circulation and heat-release rate, as defined in this chapter.

not provide the strong radial inflow at the bottom boundary surface [66]. The right combination of low $\dot{Q}$ and natural entrainment at the right length scale provided the optimal conditions for its discovery in the experiments performed by Xiao et al. [64]. With the results presented here, future experiments of the blue whirl can be designed with forced entrainment apparatus to control $\dot{Q}$ and Γ independently at different length scales to directly hone in on the BW regime.

This work provides a quantitative basis to explain the factors controlling the transition from the fire whirl to the blue whirl and lays the foundation for future experimental and numerical efforts on fire whirls and blue whirls. Open questions still remain regarding the flow structure within the recirculation zone and the mixing conditions that stabilize the flame at the bright blue ring. Future measurements using non-intrusive laser diagnostics of the flow-field in the vicinity of the flame

and the distribution of radical species will be helpful in further understanding these better. Finally, the nondimensional quantities presented here may be used to obtain a complete map of all whirling flame regimes as shown in Figure 5.11.

5.8 Acknowledgments

This chapter, in part, was submitted as a research manuscript to *Physical Review Fluids*, titled "Effects of circulation and buoyancy on the transition from a fire whirl to a blue whirl," by S.B. Hariharan, Y. Hu, M.J. Gollner and E.S. Oran, and was accepted for publication in July 2020. The thesis author is the primary author in this publication.

Chapter 6

Understanding the Blue Whirl using Optical Diagnostics

6.1 Overview

The blue whirl (BW) regime of whirling flames shows suppressed soot formation. Observed as a regime that develops from a traditional fire whirl (FW), it stabilizes over a pool of liquid fuel, it is a near-limit flame that occurs at low heat-release rates. Initial studies focused on the general experimental conditions leading to BW formation, the thermal structure, and the range of circulation and heat-release rates leading to BW formation. The results in Chapter 5 showed that the transition from the FW to the BW was dependent on the magnitudes of tangential and axial momentum; a circulation-dominated regime explained the occurrence of a recirculation zone necessary for stabilizing the blue-whirl regime. It is also understood that the reaction front is a ring-like structure, observed as a bright, blue ring, which is lifted from the fuel surface and shows poloidal motion in the same sense of the ambient swirl. Open questions regarding the flame structure and mixing still

remain, and a partially-premixed triple flame has been proposed [23, 64].

In this chapter, these open questions are approached by studying the flame using non-intrusive optical diagnostics. BWs were formed with iso-octane and probed using planar laser-induced fluoresecence (PLIF) and chemiluminescence. First, the distribution of OH and PAH radicals was obtained using PLIF, which showed that the highest concentration of ground-state OH existed in a conical structure above the ring. The highest concentration of OH was at the ring, and diminished continuously in the axial direction. Negligible presence of OH was found towards the conical region below the ring. PAH was observed surrounding the lower conical region, with maximum intensity immediately upstream of the blue ring.

Next, chemiluminescence images of spontaneous emission from OH* and CH* in the BW were captured at 1 kHz. The intensity ratio of OH*/CH* around the blue ring was computed using Abel inversion. A radial map of the intensity ratio shows possibility for the existence of a triple flame anchored at the blue ring. The results presented here are largely qualitative, since an exact relationship between intensity ratio and equivalence could not be obtained. Such a calibration is necessary to identify distinct rich and lean fronts, quantify the mixture fraction around the ring and determine the exact location of the stoichiometric region. A method to determine this relationship is presented using OH* and CH* images of adiabatic methane-air flames stabilized over a 3.81$\times$ cm^2 Hencken burner.

These results indicate that there is potential for the blue ring to be a triple flames, no reaction occurs within the recirculation zone, and that mixing occurs primarily near the blue ring. Future investigations using simultaneous imaging

are necessary to further understand the structure and the dynamics of the mixing process.

6.2 Background

The BW is a regime of the fire whirl, first observed by Xiao et al. [64] while studying the behavior of FWs formed in a fixed-frame setup that allowed natural entrainment of air into the enclosure. The laminar flame structure forms directly over a liquid fuel pool and transitions from the fire whirl when specific conditions of buoyancy and vorticity exist (Chapter 5 and [238]). The conical shape of the flame has been attributed to the bubble mode of vortex breakdown in reacting flow [64], supported by visual observations of a recirculation zone within the flame [66]. Current understanding of the BW includes the experimental conditions required for its formation [66], temperature maps across a radial cross-section of the flame [22], and the combination of nondimensional heat-release rate and circulation that are required for the transition to occur [24]. Open questions remain regarding the exact nature of combustion and the importance of the blue ring region of the flame.

The nature of combustion in the BW is of interest because of negligible emissions of particulate matter (soot) from the flame. Mechanisms of flame stabilization using swirling flow fields have been studied for many decades because of their importance in jet engines and industrial combustors, particularly for stabilization when operating lean [57, 59]. These flames typically operate in a turbulent regime, where reduction in emissions is caused by enhanced mixing between light gaseous fuels and air that are injected as jets into the combustor [60, 84]. In FWs, however, the effect of circulation is to suppresses turbulence [8, 61, 95], which causes the flame height to increase with the level of ambient circulation [8, 10, 11, 92]. In this context, the BW

emits negligible soot even while burning directly above a pool of liquid fuels that traditionally form considerable amounts of soot. It is of interest, therefore, to study the flame structure that leads to negligible soot emissions, and the mechanisms that permit optimal mixing between air and fuel evaporating from a liquid-fuel pool.

For FWs formed over a liquid-fuel pool, the flame diameter above the fuel surface depends on the flow conditions immediately surrounding the fuel pool [66]. If any vertical projections are in the immediate vicinity of the fuel pool, the flame is stabilized at the edge of the fuel pool and the FW diameter at the base is the same as the pool diameter. If the radial boundary layer is uninterrupted and the circulation is sufficiently high, FW diameter can be smaller than the fuel-pool diameter [47]. In the case of the BW, it is stabilized at the blue ring.

In the transition from a FW to a BW, the blue ring lifts off the fuel surface. This is suggested to be caused by a combination of finite-rate chemistry and the large axial momentum at the base of the flame generated by the radial collision in the Ekman layer [23, 86]. The shape of the bottom blue conical region and the upper purple haze are likely a consequence of the recirculation zone setup by vortex breakdown, with the strain rates at the stagnation zone being low enough to support a weak, inverted conical flame. Based on temperature maps and OH* chemiluminescence, it is clear that a large fraction of the heat release occurs at the ring [22, 66]. It has also been suggested that the ring is a rotating triple flame, with the the lower blue cone forming the rich front, the purple haze the lean front, and the ring being stoichiometric [23, 65].

6.2.1 Scope

While the techniques used in previous studies provide global measurements of the flame, measurements of chemical species require non-intrusive diagnostics since the blue whirl is very sensitive to the flow perturbations caused by probes positioned in the vicinity of the flame [22]. In this chapter, non-intrusive optical diagnostics are used to image the distribution of important combustion species. Using PLIF measurements of OH and PAH, rich and lean regions around the reaction front are identified; chemiluminescence imaging of spontaneous emission from OH* and CH* radicals presents a qualitative picture of the triple-flame structure of the ring. A framework for quantitatively determining equivalence ratio around the ring using the emission intensity of OH* and CH* radicals is also presented. These results agree with previous measurements in the literature as well as recent postulations about the partially-premixed nature of the flame.

6.3 Experimental Methods

First, OH-PLIF was used to visualize ground-state OH radical distribution in a radial cross-section of the flame. In this technique, single-photon radiation at 282.750 nm was used to excite OH radical in the Q1(5) rotational line of the OH $A^2\Sigma^+ - X^2\Pi(1,0)$ band, followed by fluorescence emission detection in the OH $A^2\Sigma^+ - X^2\Pi(0,0)+(1,1)$ bands. The nature of the reaction zone is compared for regular conical FWs and BWs using OH-PLIF. To locate the mixing region with respect to the reaction zone, PAH-PLIF was also performed to identify polycyclic aromatic hydrocarbons (PAH). Since iso-octane does not fluoresce, the addition of a dopant such as toluene in small quantities is necessary to visualize fuel [239].

OH* and CH* radicals can be used to locate the reaction front, sometimes even in the visible range [240]. Excited radicals such as OH*, CH*, C_2*, CO_2* contribute the most to visible and UV radiation in hydrocarbon-air flames [187, 189]. The concentration of these radicals and the corresponding intensity of spectral emission are a function of pressure [190], local equivalence ratio, strain rate [191], nature of the fuel [32, 192] etc. Local flame properties such as equivalence ratio or heat-release rate in non-sooting flames may be calculated by evaluating the ratio of the relative intensities of spontaneous chemiluminescence signals from the different radicals [32, 187, 190, 192–194]. In this work, the intensity ratio of OH* and CH* were chosen to determine the equivalence ratio in the region around the blue ring.

6.3.1 Apparatus

BWs were formed using iso-octane fuel in a fixed frame, self-entraining fire whirl apparatus, similar to that used in previous work [22, 24, 64, 66]. In place of a water layer, a flat steel surface (45×45 cm^2) was used as the bottom boundary surface over which FWs and BWs were formed. It was shown by Hariharan et al. [66] that the presence of a water surface was not critical to cause transition from the FW to the BW. The metallic surface was part of a hollow steel cuboid (45×45×2.5 cm^3), which allowed cooling water to be passed below the surface and maintain a constant temperature over the surface. A constant temperature reservoir was setup using a recirculating water chiller (Fisher Scientific Recirculating Heater Isotemp 4100 H7) set to operate at a constant temperature of 36 °C. Two half cylinders (30 cm diameter, 60 cm height) were positioned over the surface and offset such that the gap width was 25 mm. Fuel was supplied at 0.65 ml/min to the center of the metal surface through a threaded stainless-steel tube (3 mm inner diameter) using a syringe pump (NE-300 JustInfusion™ Syringe Pump). The water reservoir and the quartz half-cylinders were positioned over an optical table, and a schematic of the setup is shown in Figure 6.1A.

The setup for optical diagnostics is shown in Figure 6.1B. For PLIF, the laser system consisted of a 10 Hz nanosecond duration Nd:YAG laser (Continuum Powerlite 8000) operating at 532 nm, and used to pump a dye laser (Continuum ND6000) with circulating Rhodamine-590 dye diluted in pure methanol. The output beam of the dye laser was frequency doubled in a beta-barium borate (BBO) crystal to

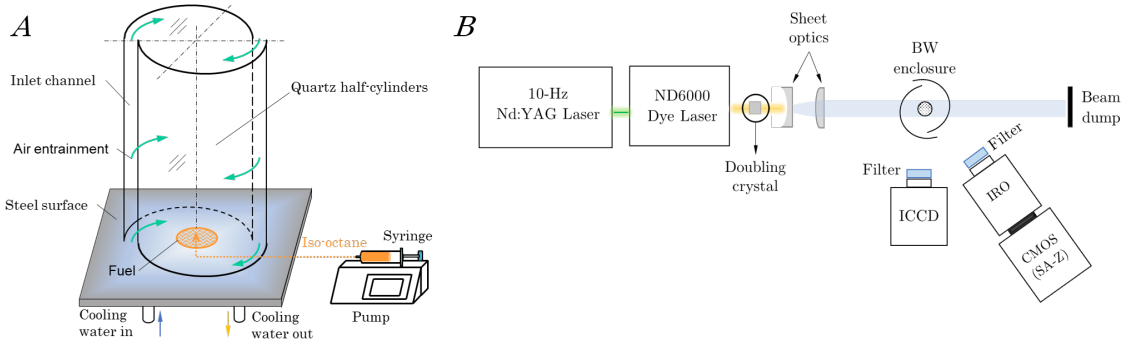

Figure 6.1: (A) Schematic of a fixed-frame fire whirl apparatus formed using two half-cylinders. These were positioned slightly offset to create gaps to allow natural entrainment of air into the enclosure. (B) Schematic of the imaging setups for chemiluminescence intensity and PLIF measurements. These techniques were performed separately for each species of interest. Figure adapted from [31].

generate a UV beam at 282.750 nm with an energy of 4 mJ/pulse. The UV beam was then guided to the blue whirl flame region using several 45° dielectric mirrors (LEO TWB-275-285-45-UF-1025). A plano-concave cylindrical lens (−25 mm focal length) coupled with a +400 mm focal length plano-convex lens was used to generate a laser sheet. The central portion of the laser sheet (uniform within 80%) with dimensions of 53 mm × 0.15 mm was used to image the distribution of OH radicals. The emitted fluorescence was collected at a 90° angle with respect to the beam path using an intensified CCD (ICCD) camera (Princeton Instruments PI-MAX4) fitted with the same UV camera lens fitted with an OH bandpass filter. The ICCD detection gate width was fixed at 100 ns to mitigate flame luminosity.

6.3.2 PLIF experiments

For OH-PLIF experiments, pure iso-octane was used as the fuel. For comparison of FWs and BWs, OH-PLIF was also performed on traditional cylindrical

FWs [8, 47]. Fire whirls formed using iso-octane form soot, which results in their yellow color, and the blackbody radiation can interfere OH fluorescence [66]. Thus, liquid methanol was used as the fuel to avoid soot formation. For PAH-PLIF, a 50%-50% mixture (by volume) of iso-octane and biacetyl was supplied at the same flow rate. Addition of this dopant was necessary since pure iso-octane does not show significant PAH fluorescence [239, 241, 242]. Smaller volume concentrations of biacetyl were tested, but even with very high laser power, a concentration of at least 40% was needed to obtain strong fluorescence signals. The PLIF images obtained from the PI-MAX4 were 14-bit, with intensity values ranging between 0 and 16383. For both OH- and PAH-PLIF, background images were obtained. An average of the background was then subtracted from each frame of interest to ensure sufficient dynamic range.

6.3.3 Chemiluminescence experiments

High-speed OH* and CH* chemiluminescence imaging was performed using a complementary metal-oxide semiconductor (CMOS) camera (Photron SA-Z) coupled to a high-speed intensifier (LaVision HS-IRO). A UV camera lens (+100 mm focal length, f/2, B. Halle Nachfl) was used for focusing chemiluminescence signals onto the detection system. Bandpass filters, 50.8 mm in diameter, for OH* (315 nm, Semrock FF01-315/15-50) and CH* (434 nm, Semrock FF01-434/17-50) were mounted at the front end of camera lens, allowing greater than 90% transmission of the respective signals and blocking all other interferences. The data acquisition

rate was fixed at 1 kHz, with an exposure time and gain of 6 ms and 38% for OH*, and 9 ms and 45% for CH*, respectively.

To obtain calibration images for the OH*/CH* intensity ratio, the BW apparatus was replaced by a standard 38.1×38.1 mm^2 Hencken burner [243]. CH_4-air flames were stabilized over the burner with the flow rate of dry air maintained at 14.28 slpm and varying the CH_4 flow rate between 1.2 to 1.95 slpm to obtain equivalence ratios (ϕ) between 0.8 and 1.3. Each flame was imaged for 0.2 s with the settings described above. Obtaining the correlation between the OH*/CH* intensity ratio and local equivalence ratio [32] is discussed in the rest of this section.

The relationship between chemiluminescence intensity ratio ($I^* = OH^*/CH^*$) and local equivalence ratio (ϕ) for methane and iso-octane was experimentally determined using Cassegrain optics and spectroscopic detection by Hardalupas et al. [192] and Orain et al. [32]. The resulting expressions are given by

$$I^*_{Oct,ref} = \left(\frac{OH^*}{CH^*}\right)_{Oct,ref} = 0.344 + 0.999\, e^{\frac{-(\phi-0.6)}{0.314}} \tag{6.1}$$

$$I^*_{Meth,ref} = \left(\frac{OH^*}{CH^*}\right)_{Meth,ref} = 0.597 + 2.107\, e^{\frac{-(\phi-0.7)}{0.26}} \tag{6.2}$$

While the blue whirls in this work were formed using iso-octane, methane was used in the calibration Hencken burner. The relationship needed is that between I^* and ϕ for iso-octane using the optics used in this study. First, OH* and CH* measurements of methane-air flames over the Hencken burner were obtained to calculate $I^*_{Meth,cal}$ at different values of ϕ, given as

$$I^*_{Meth,cal} = \left(\frac{OH^*}{CH^*}\right)_{Meth,cal} \tag{6.3}$$

The quantity I^*_{ref} is defined as

$$I^*_{ref} = \frac{I^*_{Oct,ref}}{I^*_{Meth,ref}} \tag{6.4}$$

and represents the behavior of the imaging system to methane-air and iso-octane-air flames. Combining the measured response $I^*_{Meth,cal}$ with the reference response I^*_{ref}, we obtain the relationship

$$I^*_{Oct,cal} = I^*_{ref} I^*_{Meth,cal} \tag{6.5}$$

where $I^*_{Oct,cal}$ is the required relationship between intensity ratio and ϕ in the imaging system described above. Now, by capturing images of OH* and CH* in the BW, this function can be used to obtain local ϕ in the blue whirl from $I^*_{Oct,cal}$ by extrapolation.

To calculate $I^*_{Meth,cal}$, a set of 200 images of the Hencken-burner flame were captured using the OH* and CH* filters for each value of $\phi \in [0.8, 1.3]$. An average was obtained using the 200 images, shown in Figure 6.2 for $\phi = 1$. For each value of ϕ, the maximum intensity in the streamwise direction (in the flow direction) was obtained to determine the pixel location of the center of the flame in the image frame. Using this center, an average of the intensity values was calculated for an area of 200 pixels in the transverse direction and 7 pixels in the streamwise direction. The sensitivity of the intensity to the streamwise pixel count is discussed in Figure

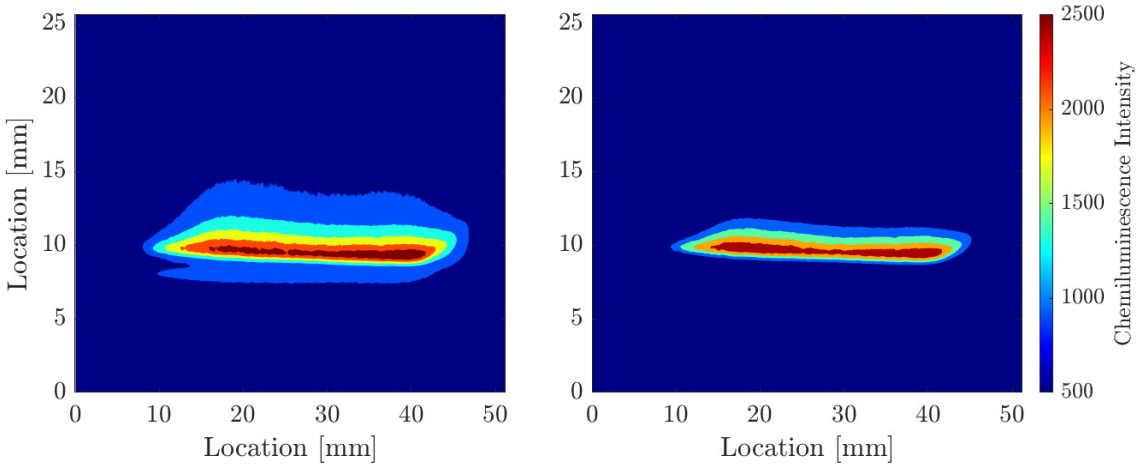

Figure 6.2: Contour plots of 200-frame averages of (A) OH* and (B) CH*, in methane-air flames at $\phi = 1$ stabilized over a 3.81 cm Hencken burner.

6.6.

The average intensity values of each species for every equivalence ratio was then normalized by the total flow rate of the air-fuel mixture and the intensifier gain values used for each species. The relationship between $I^*_{Oct,cal}$ and ϕ depended significantly on the normalization method, and the details are discussed in section 6.4.2.

6.4 Results

6.4.1 PLIF: OH and PAH

The distribution of ground-state OH in the BW is shown in Figure 6.3A. The radial cross section through the center of the flame shows the highest signal intensity at the edge of the blue ring, the anchoring point of the flame. OH exists in a hollow, conical region above the blue ring, and the concentration diminishes continuously in the axial post-flame direction. Previous chemiluminescence measurements of OH* in the BW showed significant intensity only near the blue ring, and not in the post-flame region [66]. The absence of excited-state OH* in the post-flame region is attributed to the lower temperatures. In contrast, the higher temperatures in the intense reaction zone near the blue ring permit the presence of OH* radicals. As the temperature falls in the axial direction in the post-flame region [22], the excited state OH* radicals are not present in sufficient concentration to show chemiluminescence, but the ground-state OH is still present. The approximate width of the ring, estimated as the peak-to-peak distance in this map, is about 12.5 mm. The lift-off distance of the ring from the fuel surface is about $10 - 15$ mm.

In contrast to the BW, ground-state OH is present in a cylindrical structure in the traditional FW. Figure 6.3B shows the lower portion of a tall FW formed with methanol. The FW forms immediately over the fuel surface, showing negligible flame lift-off distance. This cylindrical burning structure agrees with previous measurements of temperature in the FW [7,8,91,93,97]. Previously, chemiluminescence

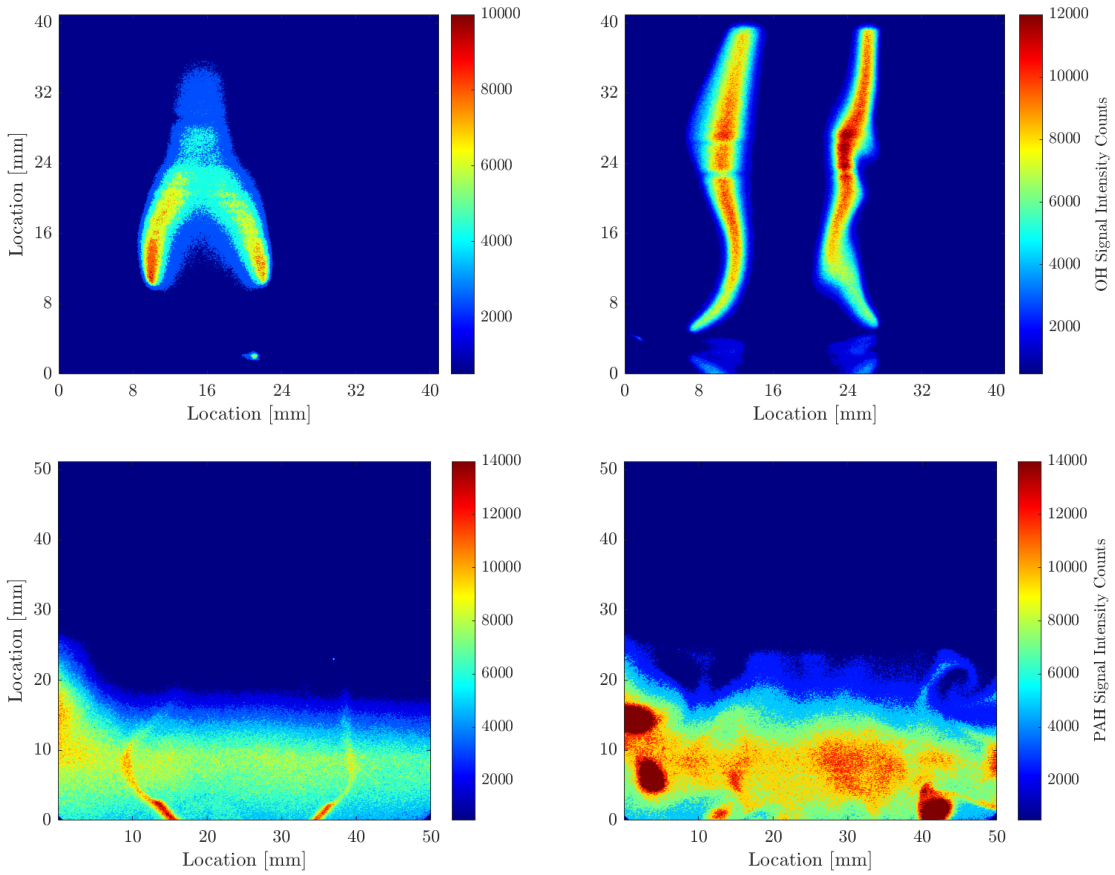

Figure 6.3: Contour maps of ground-state OH in a radial plane of the (A) BW formed with iso-octane, and (B) FW formed with methanol. (C) PAH signals in the BW formed using a mixture of iso-octane and biacetyl. (D) Background signals of PAH after extinction of the BW,caused by scattering of evaporating droplets of fuel-dopant mixture. Additional figures for each species are presented in Appendix C.

measurements of sooty fire whirls suggested a similar structure [66], but the data presented here eliminates any interference from broadband soot incandescence, reinforcing previous hypotheses that relied only on temperature measurements. Emmons and Ying [8] suggested that the interior of the FW was a fuel-rich region consisting of mostly fuel vapor, with a nonpremixed flame forming the flame sheet in a cylindrical structure. Lei et al. [97] also measured tangential velocity in the fire whirl, which showed that the peak values were at this flame sheet.

PAH signals from the blue whirl are shown in Figure 6.3C. The bottom of the image frame is ∼10 mm above the fuel surface. The peak-to-peak distance of PAH signals at the bottom of the frame is ∼18 mm, showing that the two streaks with high signal intensity are in the region immediately outside the blue conical region. In these streaks, higher concentrations are found closer the fuel surface, upto a height of ∼15 mm from the fuel surface (∼5 mm from the bottom of the image frame). This is expected to be the the approximate location of the blue ring, with high fuel concentrations below the ring and low concentrations above it. Between 15 and 25 mm from the bottom of the frame, the signals drop progressively to background levels. The shape of the PAH signals shows that the fuel vapors are distributed in a contour that is similar that of the BW, surrounding it. Background PAH signals were quite high due to substantial scattering from droplets above the fuel pool. This was visible even after blue whirl extinction as shown in Figure 6.3D. It is supposed that this experimental challenge was not encountered in previous work [242] where the fuel-dopant mixture was injected as a spray.

6.4.2 Chemiluminescence

Individual frames of OH* and CH* chemiluminescence in the BW are shown in Figure 6.4. Since the imaging rate is 1000 Hz, a sufficiently large number of images exist for both OH* and CH* where the blue ring is captured as a straight, horizontal line. The straight line represents the intensity observed as integrated along the line-of-sight.

A number of such images were averaged, and Abel inversion was performed to deconvolve the intensity data to the (r, θ, z) coordinate system (see *Fig. 2 in* [194]). The deconvolved data was used to calculate the intensity ratio $I^* = (CH^*/OH^*)$ at each $r - \theta$ location. A map of I^* for the BW is shown in Figure 6.5. Detailed descriptions of the image processing methods including criteria for image selection, averaging, deconvolution, alignment of OH* and CH* images, and background subtraction are discussed in a forthcoming publication [244].

The map of I^* around the blue ring shows that, qualitatively, there exists the possibility of a triple-structure along the ring. At the outer edge of the ring, the values of I^* suggest that the rich branch is above the ring, and the lean branch below it. On the inner edge, however, the location of the rich and lean branches are reversed. The ring may be considered an edge flame since it shows poloidal motion, propagating continuously in the azimuthal direction due to the effect of ambient circulation.

The goal is to use the ratio I^* to determine the local equivalence ratio (ϕ) around the blue ring. This necessitates a calibrated relationship between the quan-

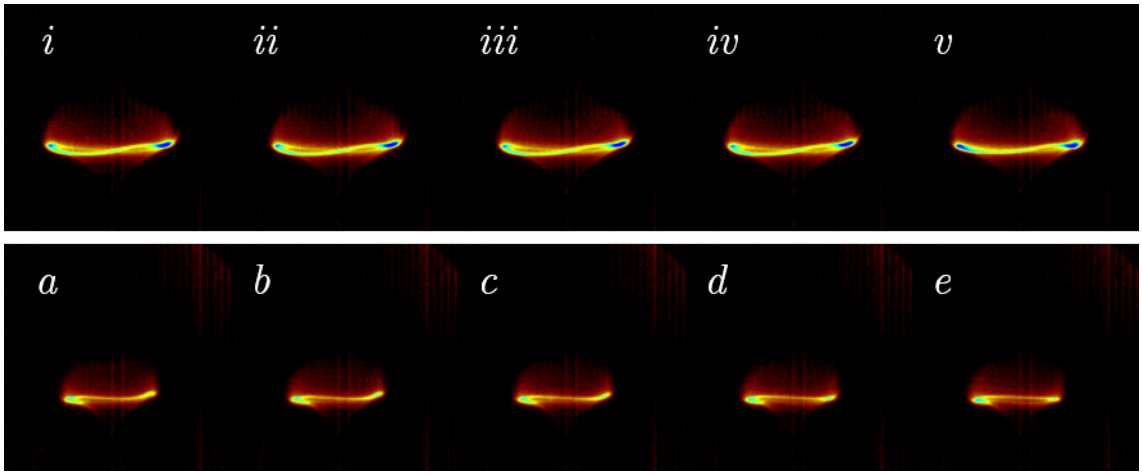

Figure 6.4: Sequence of chemiluminescence images obtained at 1000 Hz, shown in false color. Panels ($i-v$) show CH*, and panels ($a-e$) show OH*. Processed images with intensity values are shown in Figures C.5 and C.6.

tities I^* and ϕ. The calibration process using premixed methane-air flames stabilized over a Hencken burner was described in section 6.3.3. $I^* = (CH^*/OH^*)$ and $I^*_{Oct,cal}$ are related as

$$\left(\frac{CH^*}{OH^*}\right) \propto f(I^*_{Oct,cal})^{-1}$$

where $I^*_{Oct,cal}$ is as defined in section 6.3.3.

The variation of OH* and CH* signal intensity at different values of ϕ is shown in Figure 6.6. As shown in Figure 6.2, the methane-air flames formed over the Hencken burner are quite thin in the streamwise direction. Five different averaging methods were evaluated for their sensitivity on the value of chemiluminescence intensity. For each method, averaging in the transverse direction was done over 200 pixels around the center of the frame. The five methods are

(i) The maximum signal intensity of each species in the streamwise direction

(ii) 1-pixel average, centered at the pixel with maximum transverse intensity at

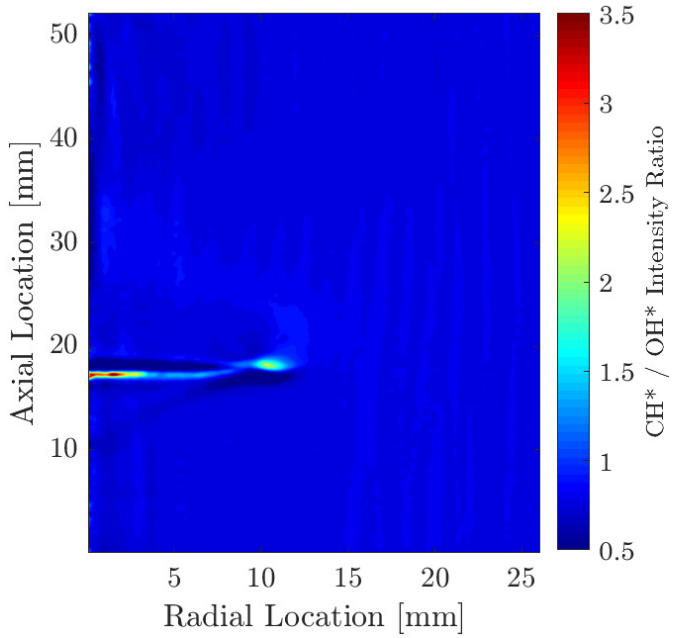

Figure 6.5: Contour map of (CH^*/OH^*) in the BW. A radial location of $r = 0$ signifies a cross sectional plane through the center of the BW.

the center of the frame (area of 1×200 px^2)

(iii) 3-pixel average, with an area of 3×200 px^2

(iv) 5-pixel average, with an area of 5×200 px^2

(v) 7-pixel average, with an area of 7×200 px^2

As evident in Figure 6.6, the line-of-sight intensity values are weak functions of the area over which the intensity data was averaged. The 7-pixel average was used to calculate $I^*_{Meth,cal}$.

The relationship between I^*_{ref} and ϕ, calculated from Equations 6.1, 6.1 [32], is shown in Figure 6.7A. The overall relationships between the (OH^*/CH^*) intensity ratio in iso-octane and ϕ is shown in Figure 6.7B. The three curves represent the three methods of normalization of the OH* and CH* intensity values ($\mathcal{I}$, depicted

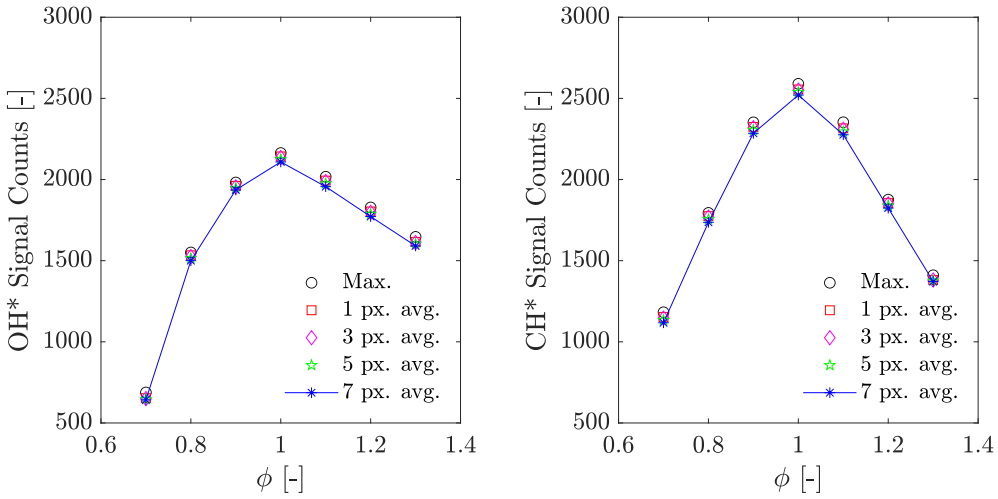

Figure 6.6: Effect of the different averaging methods on the OH* and CH* intensity counts. The 7-pixel average was chosen for determining $I^*_{Meth,cal}$ and thus, $I^*_{Oct,cal}$.

in Figure 6.6. Normalization is required to take into account the two variables in the imaging process: intensifier gain values (G) used for each species, and the total mass flow rate ($\dot{m}_H$) of the fuel-air mixture flowing through the Hencken burner at each value of ϕ. Additionally, normalization by the maximum value measured was recommended by Jeong et al. [194], which helps bounds intensity ratio between 0 and 1. The maximum intensity measured ($\mathcal{I}_{max}$) for both species was at $\phi = 1$ (Figure 6.6). $\mathcal{I}$ was normalized by three methods:

Method A:

$$\frac{\mathcal{I}}{\mathcal{I}_{max}\ \dot{m}_H}$$

Method B:

$$\frac{\mathcal{I}}{\mathcal{I}_{max}\ \dot{m}_H\ G}$$

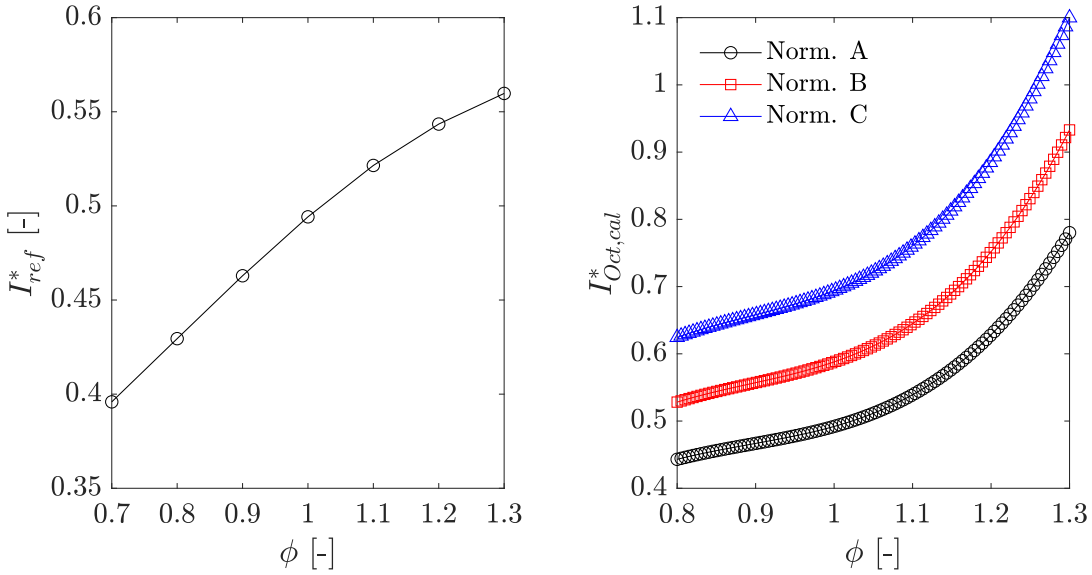

Figure 6.7: (*Left*) Variation of I^*_{ref} with ϕ, obtained using system responses for methane and iso-octane in [32]. (*Right*) Calibration curve showing the overall relationship between $I^*_{Oct,cal}$ and $\phi \in [0.8, 1.3]$ for the three different normalization methods.

where $G_{OH} = 38$ and $G_{CH} = 45$, and

Method C:

$$\frac{\mathcal{I}}{\mathcal{I}_{max}\ \dot{m}_H\ G^2}$$

The three methods resulted in the three curves shown in Figure 6.7. The curve fit for each normalization method is a third-order polynomial of the form

$$I^*_{Oct,cal}(\phi) = a\phi^3 + b\phi^2 + c\phi + d \tag{6.6}$$

The values of a, b, c and d are shown in Table 6.1. The normalization methods result in similar shapes of the polynomial functions, and may be considered to be just displaced in the ordinate direction, with differences in the $I^*_{Oct,cal}$ intercept. Dif-

Table 6.1: Coefficients for the third-order polynomial functions relating $I^*_{Oct,cal}$ and ϕ, shown for the three methods used to normalize $\mathcal{I}$.

Normalization method	a	b	c	d	R^2
A	3.383	-9.056	8.291	-2.126	1
B	4.007	-10.72	9.818	-2.517	1
C	4.745	-12.7	11.63	-2.981	1

ferences in response between different normalization procedures has been previously been shown to significantly affect the calibration curve (see *Fig. 9* in [245]).

In spite of the similar shape for each of the calibration curves for the different normalization methods, the calibration curve cannot be directly used to determine ϕ in the BW. This is because the normalization methods necessitate normalization by the total mass-flow rate to account for the population density of the reactive species, *and* an arbitrary maximum, which was found at $\phi = 1$ for both OH* and CH*. Determining the local flow rate around the blue whirl and the arbitrary maximum are challenges since they present an open ended problem − no assumptions can be made about either of these parameters since doing so will fix either the global equivalence ratio or the stoichiometric conditions ($\phi = 1$) at some arbitrary value of $I^*_{Oct,cal}$.

One potential solution is to use data from numerical simulations of the BW [33,72] to first determine an iso-surface of $\phi = 1$ near the blue ring, then identify the corresponding region in the map of I^*. The value of $I^*_{Oct,cal}$ at that radial location in the BW will represent the known value of $\phi = 1$, which then provides a way to quantify the distribution of ϕ around the blue ring. This is outside of the scope of

this work and requires additional experiments with simultaneous imaging to verify the results.

6.5 Discussion

OH-PLIF images show that ground-state OH concentration is highest at the blue ring, where the flame is anchored. The concentration diminishes continuously in the post-flame region, forming a hollow conical structure. The high concentration of OH at the ring supports previous observations of high OH* concentration there – the high temperatures enable the existence of OH* at the ring, but as the temperature reduces in the post-flame region (termed "purple haze" [23, 65]), only ground-state OH exists. Heat release is expected to occur in the haze region, but at much lower rates than at the ring. Measurements of HCO, or simultaneous imaging of OH and HCHO, are required to quantify the heat-release rates in the different regions.

The concentration of fuel vapor increased with axial distance and peaked at the region immediately upstream of the blue ring. PAH-PLIF images also showed that no fuel was present within the recirculation zone. The absence of OH and PAH fluorescence signals in the recirculation zone indicates that the region is dominated by products, potentially aiding the ignition process and stabilizing the flame by acting as a flame holder.

Occasionally, small particles of soot emanating from the ring are observable due to faint incandescence (see Appendix C, and *Supplementary Figures, Figures S.1 and S.2*). They generally accelerate in the axial direction due to buoyancy, and the visible incandescence reduces as the particles move through the purple haze. The reduction in incandescence is postulated to be because of the availability of OH to, at least partially, oxidize the soot particles. This leads to a situation similar to a

perfect candle flame, where soot is formed in the flame, but is completely oxidized in the leaner regions of the flame [131, 132]. Of course, the production of soot is not continuous in the BW, owing to the partially-premixed nature of the flame.

Traditional triple flames are typically studied using opposed flow burners [246–248], and chemiluminescence measurements of the BW suggest that the blue ring is likely to be a propagating triple (edge) flame formed under the influence of ambient circulation and within the radial boundary layer of the whirling flame. The locations of the rich and lean branches depend on the radial location. A major portion of the ring shows the rich branch located below (in the axial direction) the ring, with the lean branch above it. The lower blue cone is then expected to be a partially-premixed rich front, as postulated by Coenen et al. [23]. Numerical simulations by Chung [33] generally agree with this structure, although a nonpremixed (diffusion) flame was proposed to exist in the fuel-lean post-flame region with heat-release rates comparable to that at the blue ring. Experimental data does not show significant presence of OH* or PAH to support a separate reaction front in the purple haze. A "wing-like" lean front is more likely, visible when imaging total chemiluminescence (*Supplementary Figures, Figures S.1 and S.2*). Numerical simulations of the blue whirl (Figure 6.8) show significant heat release in the purple haze region, which agrees with measurements of OH, but not with OH*. Finally, the location of the rich and lean branches seem to reverse at the very edge of the ring, possibly a part of the "wing" seen in the numerical simulations and total chemiluminescence mesaurements. This aspect needs to be investigated further in future work.

Quantities of less than 5% by volume of biacetyl were recommended in previous

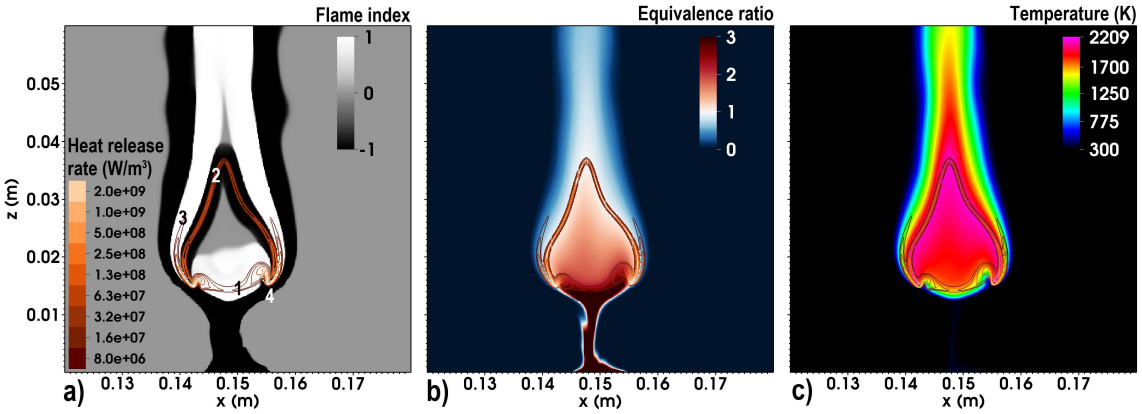

Figure 6.8: Contours of flame index (indicating level of premixing), equivalence ratio and temperature heat-release rate in the blue whirl, obtained using numerical simulations. Figure adapted from [33].

work [239], but sufficient signal levels were not observed for these small quantities when used in the blue whirl. The fraction had to be increased to 50% biacetyl in the fuel mixture for PAH-PLIF – this affects both evaporative characteristics of the fuel and chemical kinetics in the blue whirl. A significant fraction of the biacetyl was not consumed by the flame and remained over the metallic surface over which the fuel was supplied. The results presented here are sufficient to make conjectures that the lower blue cone is the rich front and the purple haze is the lean front, but probing mixing dynamics will require a technique to visualize fuel evaporation without the dopant interfering with either the diagnostic technique or combustion chemistry. Additionally, since PAH is basically a precursor to soot, and no soot is eventually formed in the blue whirl, the measurements are only qualitative. Determining density counts will require the utilization of other optical techniques.

Using these results, a 2-D representation of fuel and air flow around the blue whirl is represented in Figure 6.9. The blue ring is the widest part of the flame, and the diameter is always smaller than the fuel pool over which the flame stabilizes

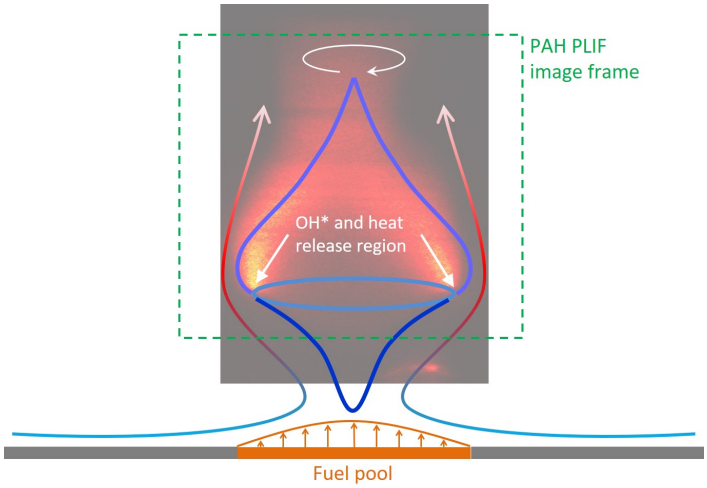

Figure 6.9: A simplified schematic of the flame structure of the blue whirl, based on measurements of OH, PAH, OH* and CH*.

[22, 23]. The strong radial entrainment at the bottom surface helps concentrate the evaporating fuel into a small region above the fuel pool. The strong radial boundary layer influences the conical shape of the lower part of the flame and the lift-off of the ring [23], which stabilizes at the region where the fuel-air mixture has the highest reactivity. Mixing begins in the region outside the lower blue cone, and the highest concentration is seen immediately below the ring. Some fuel vapor may react in the lean flame of the purple haze, although there is a possibility that some vapors are not entrained towards any of the reaction zones. This is postulated from PAH-PLIF signals that peak near the ring, but decrease in intensity in the axial direction (Figure 6.9). The shape of the vortex-breakdown bubble and the recirculation zone determines the flow path around the bubble towards the blue ring region. The lower blue cone, in addition to being the rich branch, may support heat release in the form of low-temperature hydrocarbon cracking, causing low-intensity visible radiation. The details of the recirculation zone are not depicted in Figure 6.9 since

the dynamics are not evident from the diagnostics used in this study.

The composition of the region within the conical region is still unclear, and previous work on vortex breakdown in both reacting [59,232] and non-reacting [229, 231] bubble modes of vortex breakdown suggest that the interior of the bubble may be composed mostly of combustion products. This may also be diluted by additional entrainment by flow in the reverse axial direction. This needs to be verified by imaging CO_2^* or H_2O. The proposed structure is for a stable blue whirl and detailed diagnostics are required to study the mixing dynamics during a transition from a fire whirl to a blue whirl, as well as the lift-off of the ring from the surface of the fuel pool.

6.6 Summary

An experimental investigation of the blue whirl was performed to identify the distribution of different radicals in the flame. PLIF was used to identify OH and PAH, and chemiluminescence to image OH* and CH*. The results present qualitative insight to the flame structure, which is expected to be a lifted triple-flame under ambient circulation. The flame is stabilized at the blue ring, with the rich branch formed by the lower blue cone, and the lean branch formed by the purple haze region. A large fraction of the heat release occurs at the ring, due to the high concentration of OH in the region, with the possibility of some heat release in the post-flame (purple haze) region where OH concentration diminished continuously in the axial direction. Quantifying the relative rates of heat release in these regions requires either HCO imaging, or simlutaneous measurements of OH and HCHO.

The ratio of OH* and CH* signal intensities used to determine the rich and lean edges are as yet uncalibrated due to the effects of data normalization. Data normalization could be performed for standard, premixed, methane-air flames, but the procedure could not be extended to images of the blue whirl due to the necessity of knowing the local flow rates in the blue whirl and the requirement of an arbitrary maximum value. Previous studies that used the chemiluminescence-intensity ratios of different radical species to determine heat-release rate or equivalence ratio typically use the calibration process that is validated by numerical modeling [187] or limit the procedure to observing only the calibration flame [194]. Calibration using premixed flames to extrapolate properties to partially-premixed flames has

also not been attempted earlier. This approach needs to be investigated further to determine applicability to complex flames such as the blue whirl. Additionally, the subtraction of chemiluminescence from CO_2* also needs to be accounted for in future simultaneous OH*/CH* experiments [249].

The absence of OH or PAH signals in the recirculation zone indicates that it is composed of combustion products, which act as a flame holder, stabilizing the blue ring, enabling thermal cracking of the fuel at the edge of the lower blue cone, which exhibits visible faint blue signals. CO_2 and H_2O imaging could be performed, possibly in the IR range, to confirm this. The dynamics of the mixing process outside the blue cone are still unclear, and certain experimental challenges need to be overcome to probe this. For instance, the wandering of the flame needs to be suppressed such that simultaneous imaging of OH/PAH-PLIF can be performed for a sufficient period of time at high speed to track the flow of fuel towards the reaction zone.

The qualitative results obtained in this work present explanations for the thermal structure previously established in the literature. They also present sufficient qualitative understanding of the flame structure and mixing that can be supplemented by concurrent efforts in numerical simulations, and also a foundation for future quantitative, simultaneous, multi-species measurements.

6.7 Acknowledgments

The contents of this chapter, in part, were presented as a talk titled "Understanding Combustion in the Blue Whirl using Optical Diagnostics", by S.B. Hariharan, Y. Wang, P.M. Anderson, M.J. Gollner, W.D. Kulatilaka, E.S. Oran at the *72nd Annual Meeting of the APS Division of Fluid Dynamics, Seattle, Washington, November 2019*. Some data is also included in a manuscript in preparation for submission to *Combustion and Flame* by the same authors.

Chapter 7

Conclusions and Future Directions

Whirling flames have been a subject of academic interest for many decades as they present a phenomenon involving complex interactions between combustion, heat transfer and fluid instabilities. Experimental, theoretical and numerical approaches have focused on each of the above aspects with the aim of understanding the mechanisms that lead to their formation. Early studies were devoted to predicting fire-whirl occurrence during urban or wildland fires, and although progress has been made in this front, limitations still exist in extending the knowledge to real-world scenarios.

In contrast to whirling flames, the field of swirl combustion is quite mature, given the extensive relevance to applications in propulsion and energy conversion. One crucial difference between these fields is the difference between length scales of *experimental* investigations in the laboratory and that of the real-world applications; in swirl combustion, the length scales of laboratory study are very close to that in actual applications: in the case of fire whirls, however, laboratory studies can

sometimes be orders of magnitude smaller than the real-world scenarios they seek to understand and explain. Despite this, substantial progress has been made in the understanding of fire whirls.

Emissions from fire whirls

This dissertation explored aspects of whirling flames that were not considered previously in the literature and is motivated by potential applications in environments that are relatively controlled when compared to wildfires. First, the emissions of particulate matter (soot) were measured for fire whirls and compared to those from free-buoyant pool fires to evaluate the potential for fire whirls to reduce the impact of airborne emissions during in-situ burning of spilled oil. Measurements were performed for pool fires and fire whirls formed with two liquid fuels, n-heptane and ANS crude oil. The length scales chosen ranged from typical typical laboratory scale pools (10, 20, 30 cm in diameter) to length scales that can represent characteristics of field trials (70 cm).

Fire whirls had higher burning rate and fuel-consumption efficiency, and lower emission rates of particulate matter, all of which led to lower emission factors. This was consistent at the four pool diameters and for both fuels. Phenomenological relationships between global scaling parameters such as Rossby number and nondimensional heat-release rate showed that the emission factor of particulate matter from a whirling flame decreases as the effect of ambient circulation on the fire increases. These relationships do not provide a predictive methodology for estimating

the reduction in emissions by burning a pool of liquid fuel as a fire whirl rather than a pool fire, but present a foundation for further improving developing these approaches by studying the effects of circulation and heat-release rate on emissions. Further, challenges in the domain of engineering and implementation were not explored; rather, a fundamental hypothesis has been tested and confirmed, providing strong justification to subsequently consider more detailed research.

Studies on the blue whirl

Next, the blue whirl, an ideal state of a whirling flame producing no particulate emissions was analyzed. The transition from the traditional fire-whirl regime to the blue whirl was explored using a scaling analysis to quantify the roles of local buoyant and tangential momenta. The transition from a buoyancy-dominated regime to a circulation-dominated regime correlated to the establishment of a recirculation zone and the onset of the bubble mode of vortex breakdown. Here, dependent variables based on flame geometry were used as characteristic length scales for normalization of heat-release rate and circulation. At this stage, this limits the potential to predict transition to the blue whirl at length scales larger than those tested. Still, the results presented help definitively answer why the transition occurs, and to quantitatively differentiate between different regimes of whirling flames, with scope to improve the deterministic capabilities by developing simple empirical relationships between fixed dimensions of the experimental apparatus and those of flame geometry. Finally, the distribution of OH, PAH, OH* and CH* radicals in the flame indicate potential for

the blue ring to be a triple-flame, with the lower blue cone forming the rich branch and the purple haze forming the lean branch.

7.1 Future Work

Fire-whirl formation and emissions

Emissions from fire whirls were consistently lower for all pool diameters. But, as mentioned above, the formation conditions where not the same for fire whirls formed at the different length scales. This affects the geometry of fire whirls, and consequently their burning characteristics and efficiency. One aspect that may be standardized in future investigations is the area ratio, defined as

$$A_{ratio} = \frac{A_{pool}}{A_{enclosure}}$$

The values of A_{ratio} for the different values of D in this study are shown in Figure 7.1. A_{ratio} needs to be constant for fire whirls formed at different values of D to ensure that the entrainment conditions are similar. Since flame area is important parameter influencing burning efficiency, ensuring the maximum flame height at each length scale will permit evaluation of the maximum possible value of burning efficiency at each scale.

From this work, it is evident that FWs have higher flame surface area as compared to PFs. But the data at the different scales are vastly different in terms of the effects of Gr and external Re. So, experiments in a given regime, preferably the laminar regime with pool diameters below 10 cm, are required to study the influence of circulation on emission factor.

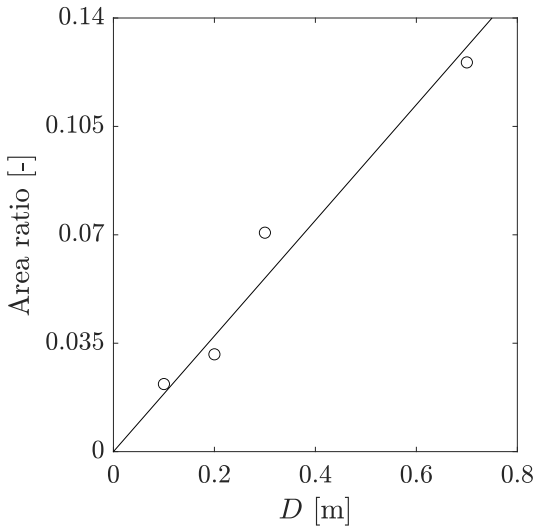

Figure 7.1: Variation of A_{ratio} with D. Lineat fit shown has a R^2 value of 0.96.

Secondly, the effects of circulation and buoyancy need to be investigated independently. In the literature, flame geometry data for pool fires and fire whirls formed at similar values of $\dot{Q}$ are available [106], but the experimental apparatus can vary significantly. Particularly, the bottom boundary over which the fires are formed are important − the presence of a *lip* can cause large differences in $\dot{m}$ (see *Fig. 5* in [8]). Independent control over Γ and $\dot{Q}$ requires a setup with forced entrainment, enabled by a spinning mesh or a bank of fans to control entrainment velocity, thus fixing the value of Γ. Results from preliminary experiments comparing the effects of natural and forced entrainment on liquid-fueled fire whirls are included in Appendix A. $\dot{Q}$ can be controlled separately by the use of a gaseous burner. While experiments with such arrangements have been performed in the past, emissions data for these conditions do not exist. Experiments with a spinning mesh can also help study the effects of flame stretch and residence time on soot formation.

More generally for fire whirls, the linear relation between heat-release rate and

circulation exists only up to a certain point in natural entrainment configurations. Additionally, the linear relationship between flame height and circulation exists only if $\Gamma_f^* \in (0, 1)$. Over-rotated FWs reduce in height, with corresponding increase in flame width. For all these cases, the relationship between heat-release rate and flame area needs to be investigated. A systematic study of pool fires, and fire whirls formed over a range of externally-controlled circulation, are needed over a wide range of heat-release rates to observe the effect of flame area on emissions.

Other gaseous species such as SO_x and NO_x need to be measured for comparing pool fires and fire whirls. Given that temperatures are lower than 1800 K, it is unlikely that NO_x formation is a major concern. Unburned hydrocarbons need to be measured directly using methods such as Flame Ionization Detection (FID) rather than estimation using the carbon balance method, which requires assumptions regarding the composition of combustion products. Additionally, an analysis of the post-combustion residue can help understand the effects of high heat feedback on the residue.

Another aspect of this work is to investigate the effect of fuel slick thickness and boilover on emissions. Characteristics such as burning rate can change significantly with time when burning crude oil, and the composition of the emission species is also expected to change over extended periods of time. Boilover can occur in laboratory-scale experiments, but is not observed in field conditions. By varying the fuel layer thickness, regular burning can be sustained over a longer duration, resulting in combustion of a broader range of hydrocarbons from the crude oil.

Increased slick thicknesses can also delay boilover, causing a longer duration

of normal burning, making emissions less dependent on test conditions such as pool diameter. This is a more practical approach to evaluate fire whirl use in ISBs. Other practical concerns also include evaluating the efficacy of fire whirls on crude oil under varying degrees of weathering.

Finally, the exact mechanisms of mixing and combustion in the fire whirl are of immense importance to understanding its emissions behavior. The dynamics at the base of the fire-whirl structure are important since most of the entrainment occurs there, and the mixture fractions and turbulence intensity in that region determine the shape and regime of the fire whirl. These characteristics are best explored using non-intrusive laser diagnostics, both absorption and emission spectroscopy. Such experiments can then serve as a foundation to validate numerical simulations with detailed chemistry.

Future studies of the blue whirl

Similar to the fire whirl, the mixing dynamics and the mechanisms of flame stabilization at the blue ring are important to advancing our understanding the blue whirl. Here too, there is a need for using non-intrusive and high-speed diagnostics to probe multiple reactive species simultaneously. This will help understand the role of the ring, the recirculation zone and the blue conical region. More importantly, visualization of the change in the nature of the flow during the transition from a fire whirl a blue whirl is necessary to understand the development of the recirculation zone and the ring lift-off. The optical-diagnostic results presented in this work

need to be quantified: density counts of HCO, or OH and HCHO, are needed to quantify the local heat-release rate. These can also help validate and calibrate existing numerical models of the blue whirl.

Before such experiments are possible, there is a need to develop a burner that can stably form the blue whirl using a gaseous fuel and eliminates flame wander. Flame wander is intrinsic to whirling flames, but limiting it to within one burner diameter will aid in obtaining a sufficient amount of data to analyze the transition processes.

For the bubble mode to appear, axial momentum must be overcome by tangential momentum [229, 230, 250], and this is more likely to occur when $\Gamma_f^* > \dot{Q}_f^*$ (Chapter 5). Although vortex breakdown is a phenomenon occurring in the vicinity of the flame, the axial profile of tangential velocity at the inlet for the blue whirl [24] is quite different from the typical velocity profile measured for a quasi-steady on-source fire whirl [251]. While the measurements in this study are made at the inlet section, the flow field in the vicinity of the blue whirl is unclear and deserves further study.

Practical applications of the blue whirl are still an open question. The laminar nature of the flame, in addition to high sensitivity to experimental conditions, make it unlikely to be used in applications such as power generation or propulsion. It could, however, potentially serve as a canonical model to study vortex breakdown under the influence of heat release at low Reynolds number (low turbulence intensity). A preliminary study of whirling flames under microgravity was recently performed [83]. Microgravity conditions may offer an alternative method of study-

ing the blue whirl since the effect of buoyancy is suppressed, providing the impetus for vortex breakdown to occur in whirling flames

7.2 Contributions

This work has contributed to whirling-flame literature in three areas not explored previously. First, the potential for practical utilization of whirling flames have been shown, which advances our knowledge of whirling flames beyond traditional considerations of safety during unwanted urban and wildland fires. The lower particulate-matter emissions from whirling flames present a platform to evaluate considerations of practicality and the engineering of devices for remediation or even energy conversion applications. Second, circulation- and buoyancy-dominated regimes were identified in whirling flames, and the transition to a circulation-dominated regime was shown to correspond with the occurrence of the bubble mode of vortex breakdown, resulting in blue-whirl formation. These results, while presented in the context of reacting flows, can be extended to non-reacting flows as well. Finally, the near-limit blue whirl was shown to have a flame structure similar to that of a triple flame, anchored at the blue ring region. The above contributions have been disseminated in the form of project reports, conference presentations and proceedings, and peer-reviewed journal articles, listed below.

1. **S.B. Hariharan**, Y. Hu, M.J. Gollner, E.S. Oran, "Effects of circulation and buoyancy on the transition from a fire whirl to a blue whirl," *Accepted for publication in Physical Review Fluids*

2. **S.B. Hariharan**, H.F. Farahani, A.S. Rangwala, J. Dowling, E.S. Oran, M.J. Gollner, "Comparison of Emissions from Liquid-Fueled Pool Fires and Fire

Whirls at Different Length Scales," In preparation for submission and peer review in August 2020

3. **S.B. Hariharan**, Y. Wang, P.M. Anderson, M.J. Gollner, W.D. Kulatilaka, E.S. Oran, "On the nature of combustion in the blue whirl using optical diagnostics," In preparation for submission to *Combustion and Flame*

4. M.J. Gollner, E.S. Oran, **S.B. Hariharan**, J. Dowling, H.F. Farahani, A.S. Rangwala, "Efficient Remediation of Oil Spills over Water Using Fire Whirls," *BSEE Project Number 1094, Washington, DC, 2019.*

5. **S.B. Hariharan**, Y. Wang, P. Anderson, W.D. Kulatilaka, M.J. Gollner, E.S. Oran, "Understanding Combustion in the Blue Whirl using Optical Diagnostics," *72nd Annual Meeting of the APS Division of Fluid Dynamics, Session C06.3, Seattle, Washington, November 2019.*

6. **S.B. Hariharan**, J. Dowling, M.R. Jones, V.M. Valletta, M.J. Gollner, E.S. Oran, A. Ogorzaly, E.S. Neumann, S. Olson, P. Ferkul, "Fire Whirls in Microgravity," 35th *Annual Meeting, American Society for Gravitational and Space Research, Denver, Colorado, November 2019.*

7. **S.B. Hariharan**, J. Dowling, H.F. Farahani, Y. Hu, A. Tohidi, K. Stone, A. Rangwala, E.S. Oran, M.J. Gollner, "Demonstration of Reduction in Emissions by Fire Whirls through Small Scale Experiments," *42nd AMOP Technical Seminar, Halifax, Nova Scotia, Canada, June 2019.*

8. **S.B. Hariharan**, "Fire Whirls and Blue Whirls: Emissions Reduction and

Vortex Breakdown," *2019 Research Symposium on Environmental and Applied Fluid Dynamics, Johns Hopkins University, May 2019.*

9. **S.B. Hariharan**, J. Dowling, H.F. Farahani, M.J. Gollner, E.S. Oran, "Comparison of emissions from liquid-fueled pool fires and fire whirls," *11^{th} US National Combustion Meeting, Pasadena, California, March 2019.*

10. Y. Hu, **S.B. Hariharan**, H. Qi, M.J. Gollner, E.S. Oran, Conditions for formation of the blue whirl, Combustion and Flame. 205 (2019) 147–153.

11. Y. Hu, **S.B. Hariharan**, M.J. Gollner, E.S. Oran, Conditions for Formation of the Blue Whirl, *Eastern States Section of the Combustion Institute Spring Technical Meeting, The Pennsylvania State University, Abstract 3B08, Pennsylvania, March 2018.*

12. **S.B. Hariharan**, P.M. Anderson, H. Xiao, M.J. Gollner, E.S. Oran, The blue whirl: Boundary layer effects, temperature and OH* measurements, Combust. Flame. 203 (2019) 352–361.

13. **S.B. Hariharan**, E.T. Sluder, M.J. Gollner, E.S. Oran, Thermal structure of the blue whirl, Proc. Combust. Inst. 37 (2019) 4285–4293.

Appendix A: Effect of Entrainment Conditions on PM Emissions from Fire Whirls

A.1 Overview

The experimental results discussed in Chapters 3 and 4 represent conditions where fire whirls were formed under natural entrainment, i.e., circulation is not imposed externally on the fire. Rather, the circulation is intrinsically coupled with the heat-release rate of the fire whirl and depends, to a certain extent on the gap size in a four-walled setup. This means that only one combination of heat-release rate and circulation are permitted for each scale, similar to experiments with the blue whirl discussed in Chapter 5.

To decouple the effect of heat-release rate and circulation, heat-release rate is maintained constant by controlling fuel-flow rate in a gaseous-fuel burner, and externally-controlled air entrainment is be imposed by means of a rotating mesh (such as the early Emmons-type apparatus [8]) or using a bank of fans to control the inlet velocity. Most experimental setups in the literature do not use the fan-based setup, although recent work on micrgravity fire whirls used this setup [83]. In such apparatus with forced entrainment, heat-release rate and circulation remain

coupled if a condensed-phase fuel is used.

For a fuel pool of given diameter, it is of interest to understand the effect of different entrainment conditions on PM emissions from fire whirls such that the ideal level of ventilation may be designed for a practical device. Hence, preliminary experiments were performed with 70 cm pools to determine the effect of enclosure gap size and different levels of forced entrainment. The results discussed here are primarily qualitative since U_θ was not measured, and therefor an estimate of circulation was not possible. Still, these results still help in understanding that an optimum condition exists, and provide insight on how to design future experiments to identify the combinations of circulation and heat-release rate that result in the low values of $\mathrm{EF_{PM}}$ for a given D.

A.2 Experiments

Experiments with diesel fuel were conducted only at the 70 cm scale, and details of the general setup and PM measurements have been presented in sections 3.2 and 4.2. For experiments with heptane and ANS crude oil, gap size in the four-walled configuration was kept constant for all experiments. For the 70 cm fuel pool, the enclosure side was 175 cm with a fixed gap size of 45 cm. The fuel used was automotive-grade diesel due to its low cost and easy accessibility.

The different experimental conditions in this study are shown in Table A.1. Four natural-entrainment (NE) conditions were studied by varying the gap sizes between 35 and 65 cm. Four forced-entrainment (FE) conditions were studied with

Table A.1: Experimental conditions for the different air entrainment conditions for fire whirls formed using diesel fuel.

Air entrainment mechanism	Gap width, W [cm]	Enclosure side length, S [cm]	Enclosure wall height, H [cm]	Fuel volume [ml]
Natural	35	175	240	2000
	45			
	55			
	65			
Natural: Level 0	55	175	240	2000
Forced: Level 1				
Forced: Level 2				
Forced: Level 3				

a fixed gap size of 55 cm and positioning a box fan at each of the four inlets. The box fan (50×50 cm^2, Lasko Model 3733) could be operated at three speeds, although a characterization of the flow profile or outlet velocity are not available at this time. The fans supplied air only to the lower part of the enclosure, and future experiments at smaller scales will be required to design inlets that supply air along the entire height of the enclosure. For comparison, a pool fire experiment was also performed. For all experiments, 2L (5 mm slick) of diesel was used. For each of the conditions listed in Table A.1, only one experiment was performed. Thus, there is no estimation of error, and the results from this preliminary study may be used as a platform to design systematic multi-scale experiments in the future.

A.3 Results and Discussion

Similar to ANS crude oil, pool burning of diesel left behind a residue. This residue, however, could not be collected using the 3M adsorbent pads for mass measurement. Right before extinction, a distinct crackling noise was also audible, similar to boilover, but existed for only a few seconds. The PM emission rate for each of the different conditions in Table A.1 is shown in Figure A.1, and the corresponding PM emission factors are shown in Figure A.2. The burning duration for the NE conditions are slightly higher than for the FE conditions. The peak emission rate under NE occurs at a gap size of 35 cm, and is higher than the peak emission rate from the pool fire. The average emission rate is lowest for a 55 cm gap, and is lower than that for the pool fire, similar to previous results for non-boilover burning of heptane and ANS crude oil. In the case of FE, the peak emission rate increases continuously with fan speed, with the highest concentration being exceeding the DustTrak's measurement limit after ∼100 s.

For the 70 cm pools burning heptane and ANS crude oil, EF_{PM} of fire whirls was around ∼50 % of that of pool fires (Figure 4.5). For diesel, however, the reduction in EF_{PM} by fire whirls is not as significant. EF_{PM} reduces continuously with gap size, and the value levels off after 55 cm. With FE, the lowest EF_{PM} occurs at the lowest inlet velocity, but then increases continuously with fan speed. At the highest fan speed, the EF_{PM} for the FW is higher than that for a pool fire . These results suggest that a unique combination of gap size and inlet velocity (or Γ), that results in the lowest EF_{PM}, exists for a given fuel pool diameter.

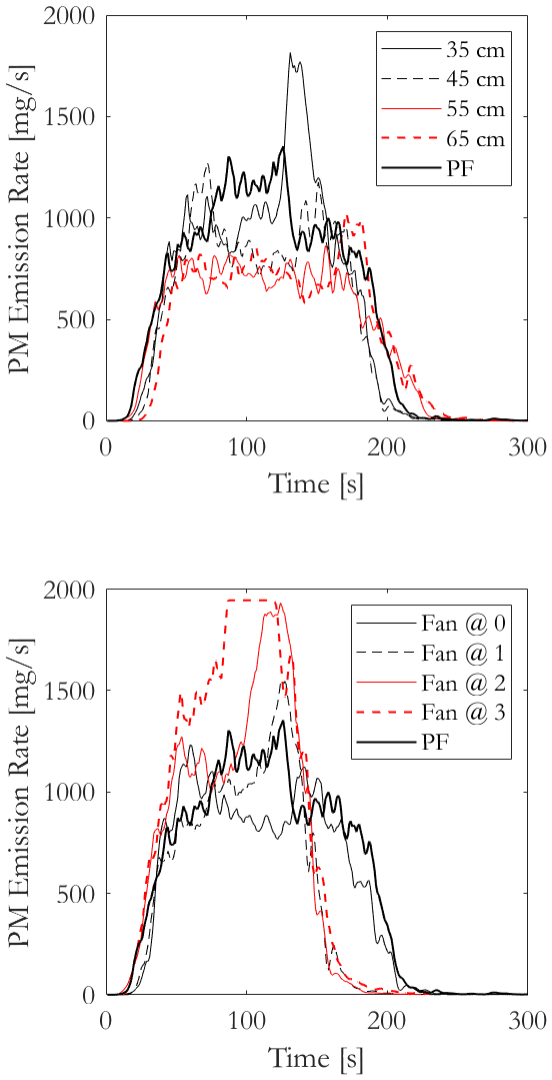

Figure A.1: Dependence of PM emission rate on gap size for the naturally entrainment cases *(top)*, and fan speed on the forced entrainment cases *(bottom)* for fire whirls formed over a 70 cm diesel pool.

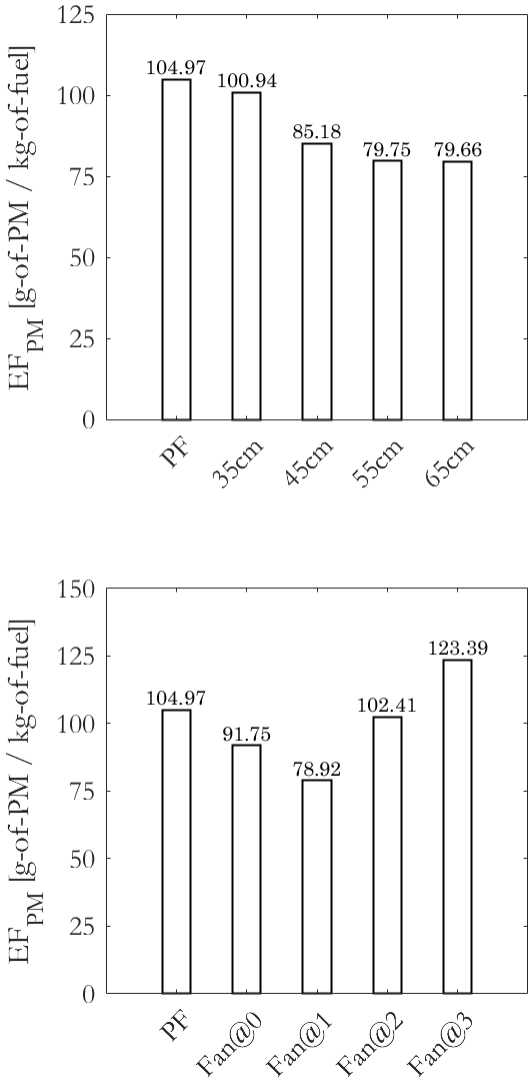

Figure A.2: PM emission factors for fire whirls formed over a 70 cm diesel pool. Dependence on gap size for naturally entrainment cases *(top)*, and dependence on fan speed for forced entrainment cases *(bottom)*.

Results in Chapter 4 showed the importance of the relative influences of buoyancy and circulation on EF_{PM}. The primary effect of changing gap size or adding forced entrainment is to change the level of circulation on the fire. These results show that for a given fuel pool diameter, natural air entrainment does not offer the ideal conditions for lowest PM emissions. Some level of external forcing is required, which increases circulation, and for liquid fuel pools, alters the heat-release rate.

Gabler's work on asymmetrically whirling flames formed using gaseous fuels [252] presents a method to analyze the influence of varying momenta in different directions on NO_x and CO emissions. The nondimensional Damköhler number (Da) was used to explain some of the emissions behavior. The effect of Damköhler number (Da) is typically associated with extinction [253], and has recently been shown to significantly affect the transition from a fire whirl to a blue whirl [82].

Similar to Gabler's approach [60,84,252], it is proposed that the mechanism of soot emission from fire whirls may need to be related to flow characteristics defined based on the relative time scales (derived from local flow velocities) in the two directions of interest - axial, due to buoyancy, and azimuthal, due to air entrainment. These quantities may be used to define a Froude number (Fr) and analyze the effects on EF_{PM}. For this, an estimate both of axial [7] and azimuthal velocity [54] in the vicinity of the flame sheet at different heights. For more global descriptions, a scaling approach still needs to be used by defining nondimensional quantities representing circulation and heat-release rate. Characteristic axial and azimuthal time scales may be determined based on appropriate length scales which may be either the fuel pool diameter, fire whirl height and width, ratio of of gap size to enclosure side etc.,

depending on the type of forced entrainment used in the experiment.

A.4 Conclusions

Circulation controls many properties of the fire whirl including flame height and width, temperature, heat-flux feedback etc. Additionally, for condensed-fuel flames, it also affects burning rate. Lei et al. [92] showed that fire whirl height first increases with Γ, then decreases, while flame width follows the opposite trend. Circulation and heat-release rate are intrinsically coupled in apparatus with natural air entrainment and only one combination of these quantities can form stably for a given set of dimensions such as pool diameter, enclosure side (or diameter), gap width and enclosure height. Preliminary results have shown that this combination of circulation and heat-release rate under natural entrainment does not lead to the lowest possible particulate matter emission factor. Rather, a small level of externally forced entrainment leads to a reduction in the emission factor. This reduction is attributed to some additional air available for combustion at the lower region of the fire whirl, and enhanced mixing.

The preliminary experiments involved only one fuel pool diameter, and only one test for each of the different entrainment conditions. A more systematic approach, similar to those discussed in Chapters 3 and 4 is needed to fully understand the effects of forced entrainment on pollutant emission at different length scales. This would also provide an estimate of the experimental errors associated with the measurements. For this, suitable apparatus need to be designed to identify differ-

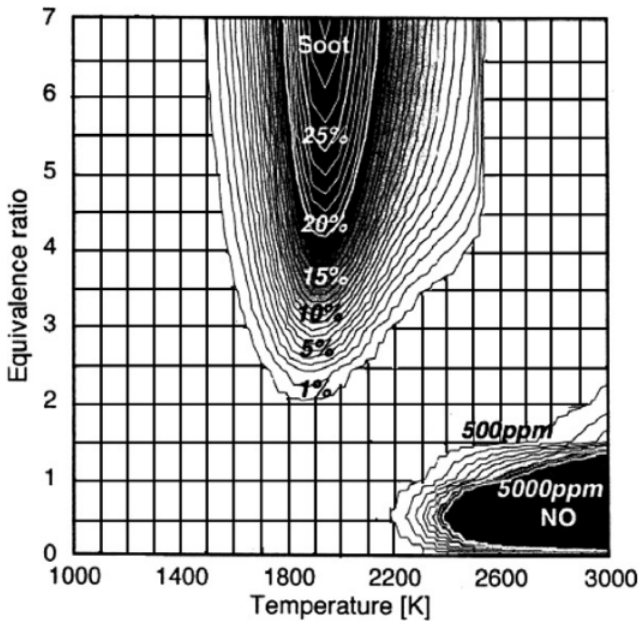

Figure A.3: Influence of equivalence ratio and in-cylinder temperature on soot and NO emissions from an internal combustion reciprocating engine. Figure from [34].

ences between the popular rotating mesh setup and the fan-based setup. This would also help generate a fire-whirl behavior map for liquid-fueled fire whirls, following the approach of Lei et al. [92] for a gas burner.

Effects of Da and Fr could be incorporated into the analysis to include the effects of local flow properties and fuel chemistry to generate a topological map of the influence of important parameters on soot emissions from fire whirls. Similar approaches are used in other fields such as IC engines, for which in-cylinder pollutant production is controlled by local equivalence ratio and temperature [17, 254]. High temperatures and low equivalence ratios favors production of NO, while low temperatures and high equivalence ratios favors production of soot (see Figure A.3, adapted from [34] and pertaining to pressures above atmospheric conditions). For fire whirls and jet flames under swirling flow fields, characteristic Da and Fr num-

bers may be used to explain particulate matter emission by including the effects of chemistry and identifying the right operating conditions that are required for an engineering device. One possibility for field use may be a burner based on a large pilot-ignited spray flame, described in detail by Tuttle et al. [255].

Appendix B: Supplementary Material to Chapters 3 and 4

This appendix contains additional data and figures as supplement to Chapters 3 and 4. The different line colors in Figures B.1−B.9 depict individual experimental trials.

Table B.1: Experimental variability in the estimation of η_{fuel} for ANS fires at $D = 70$ cm.

		Initial mass [g]	Residue [g]	η_{fuel} [%]
ANS PF (7 mm)	Test 1	2400	388	83.8
	Test 2	2450	375	84.7
	Test 3	2550	390	84.7
	Test 4	2400	377	84.3
ANS FW (7 mm)	Test 1	2360	362	84.67
	Test 2	2360	386	83.6
	Test 3	2400	401	83.3
	Test 4	2400	382	83.9
ANS PF (5 mm)	Test 1	1710	284	83.4
	Test 2	1710	304	82.2
	Test 3	1710	315	81.6
ANS FW (5 mm)	Test 1	1710	284	83.4
	Test 2	1710	285	83.3
	Test 3	1710	295	82.7
	Test 4	1710	298	82.6

Table B.2: Experimental variability in the estimation of η_{fuel} for ANS fires at $D = [10, 20, 30]$ cm.

D [m]	Regime		Initial mass [g]	Residue [g]	η_{fuel} [%]
10	PF	Test 1	33	18.1	45.1
		Test 2	33	19.7	40.4
		Test 3	33	61.4	40.4
	FW	Test 1	33	16.35	50.45
		Test 2	33	16.3	50.7
		Test 3	33	15.8	52.2
20	PF	Test 1	132.5	83.1	37.3
		Test 2	128.5	58.1	54.8
		Test 3	129.3	61.4	52.5
	FW	Test 1	132.9	64.2	51.7
		Test 2	132.9	53	60.1
		Test 3	132.9	60.3	54.6
30	PF	Test 1	313.3	163.5	47.8
		Test 2	306.8	126.1	58.7
		Test 3	310	112	63.9
	FW	Test 1	310.4	99.7	67.9
		Test 2	314	182.3	41.9

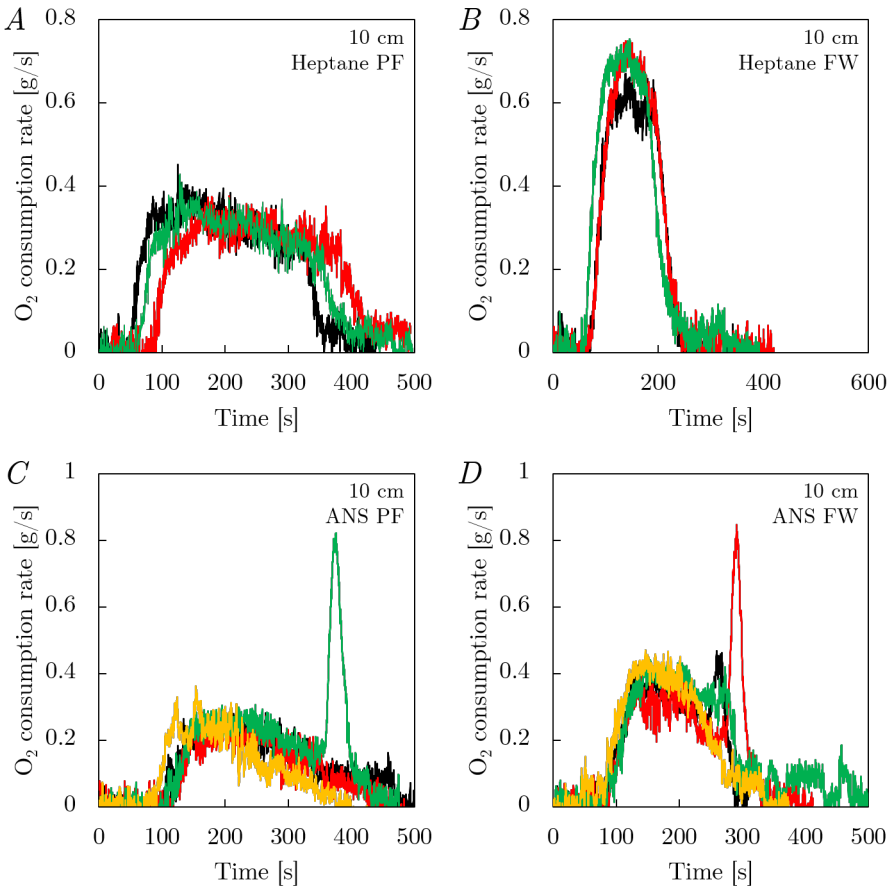

Figure B.1: O_2 consumption, $D = 10$ cm.

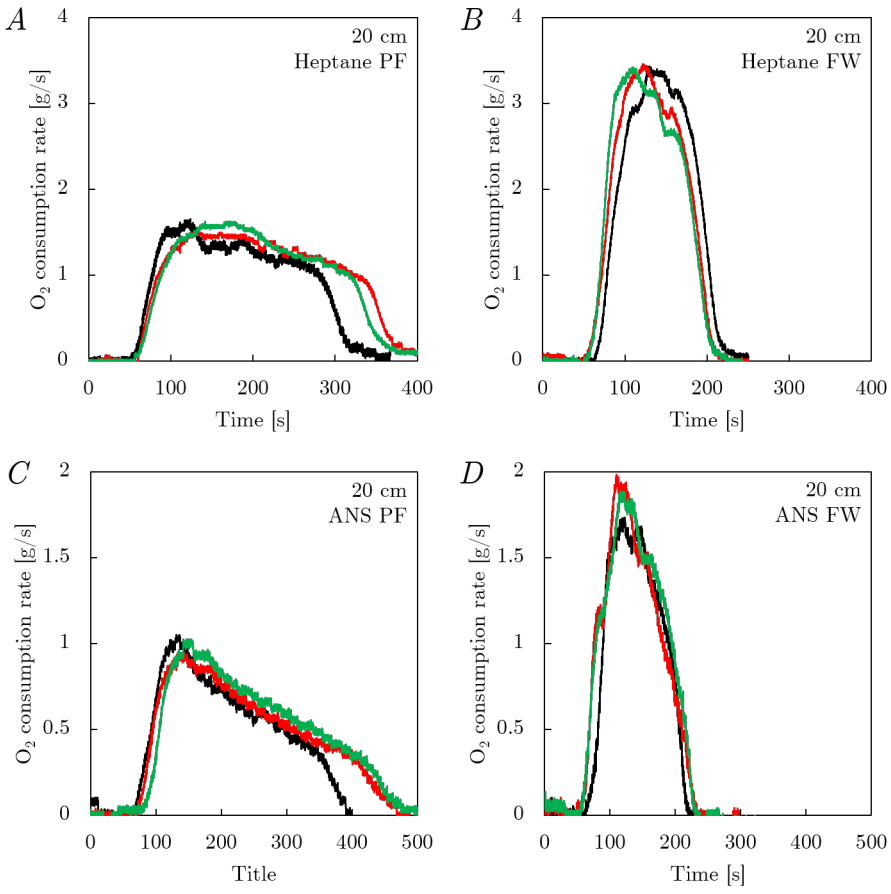

Figure B.2: O_2 consumption, $D = 20$ cm.

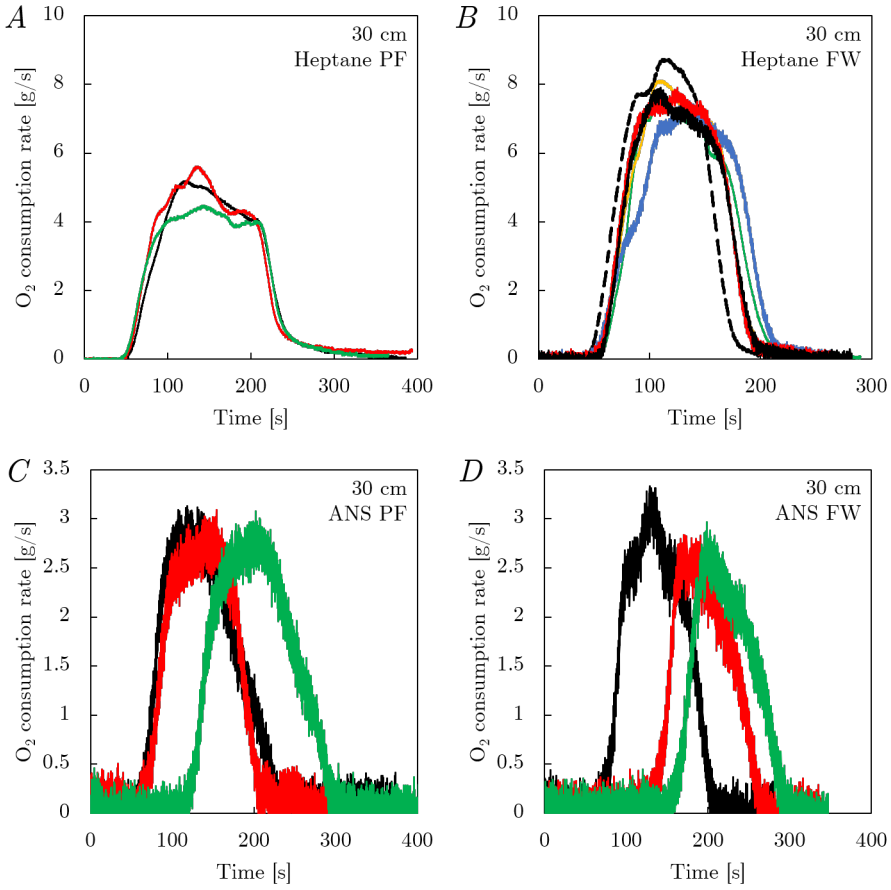

Figure B.3: O_2 consumption, $D = 30$ cm. Panel B shows results from six different experiments.

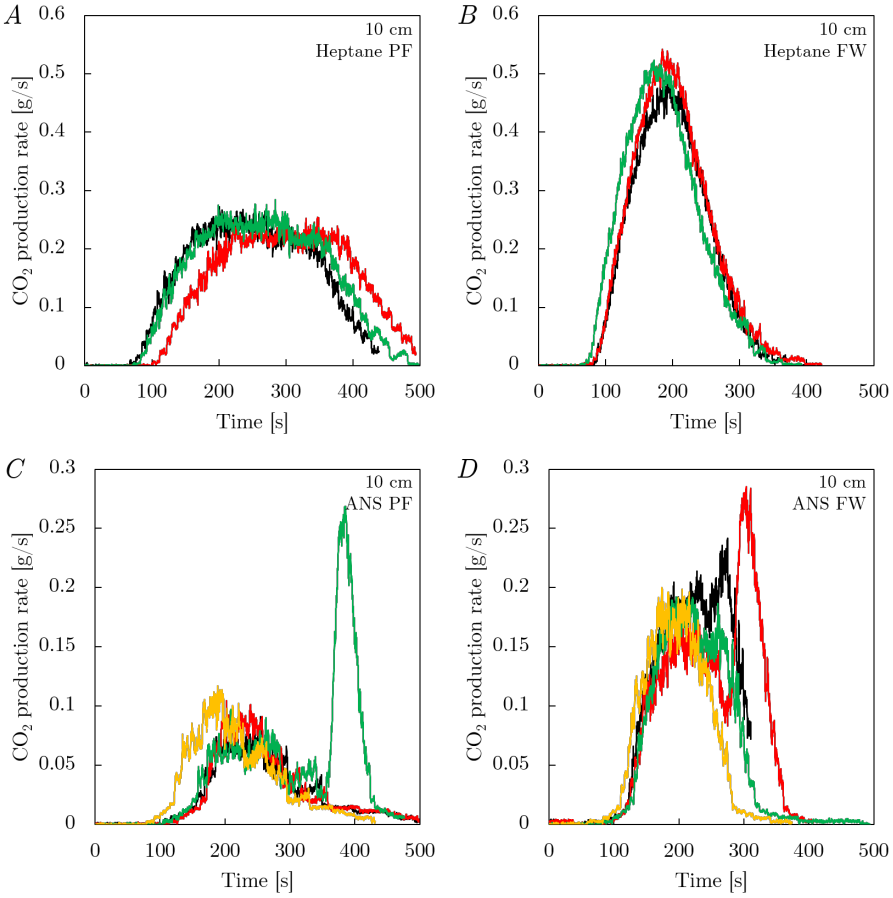

Figure B.4: CO_2 emission rate, $D = 10$ cm.

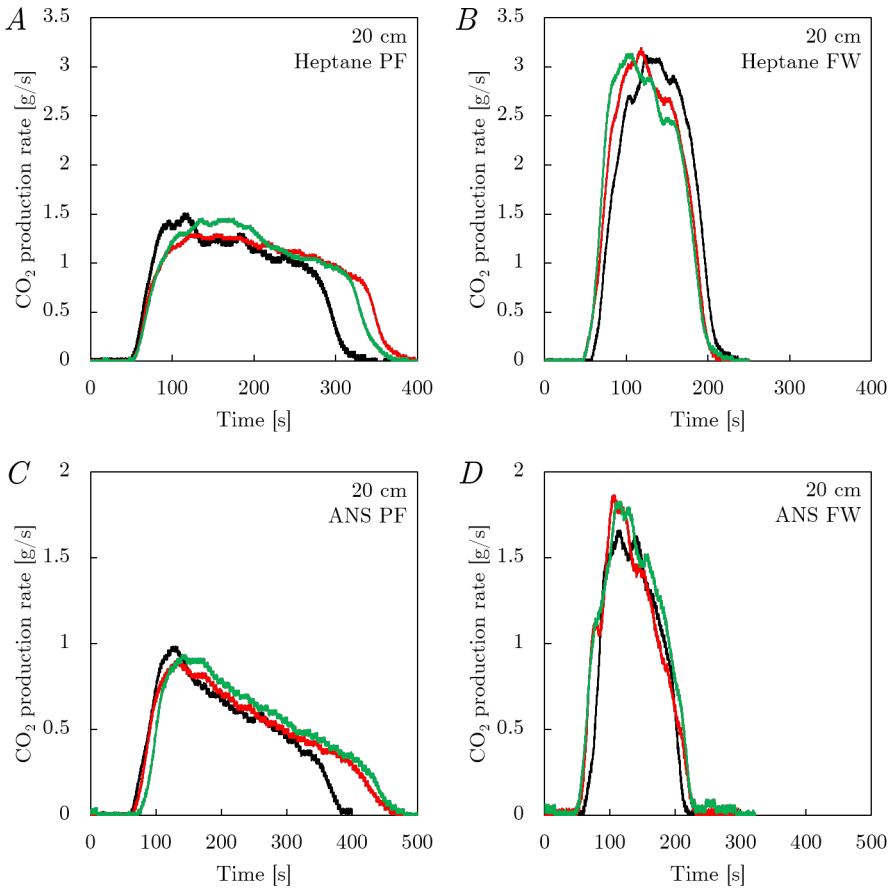

Figure B.5: CO_2 emission rate, $D = 20$ cm.

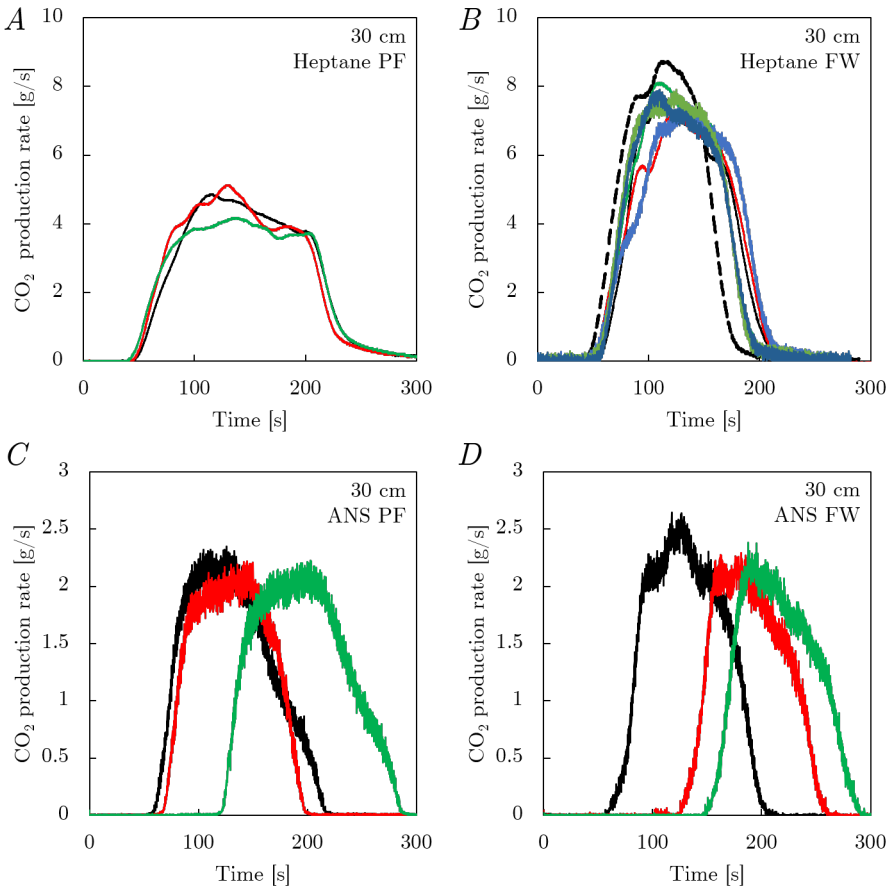

Figure B.6: CO_2 emission rate, $D = 30$ cm.

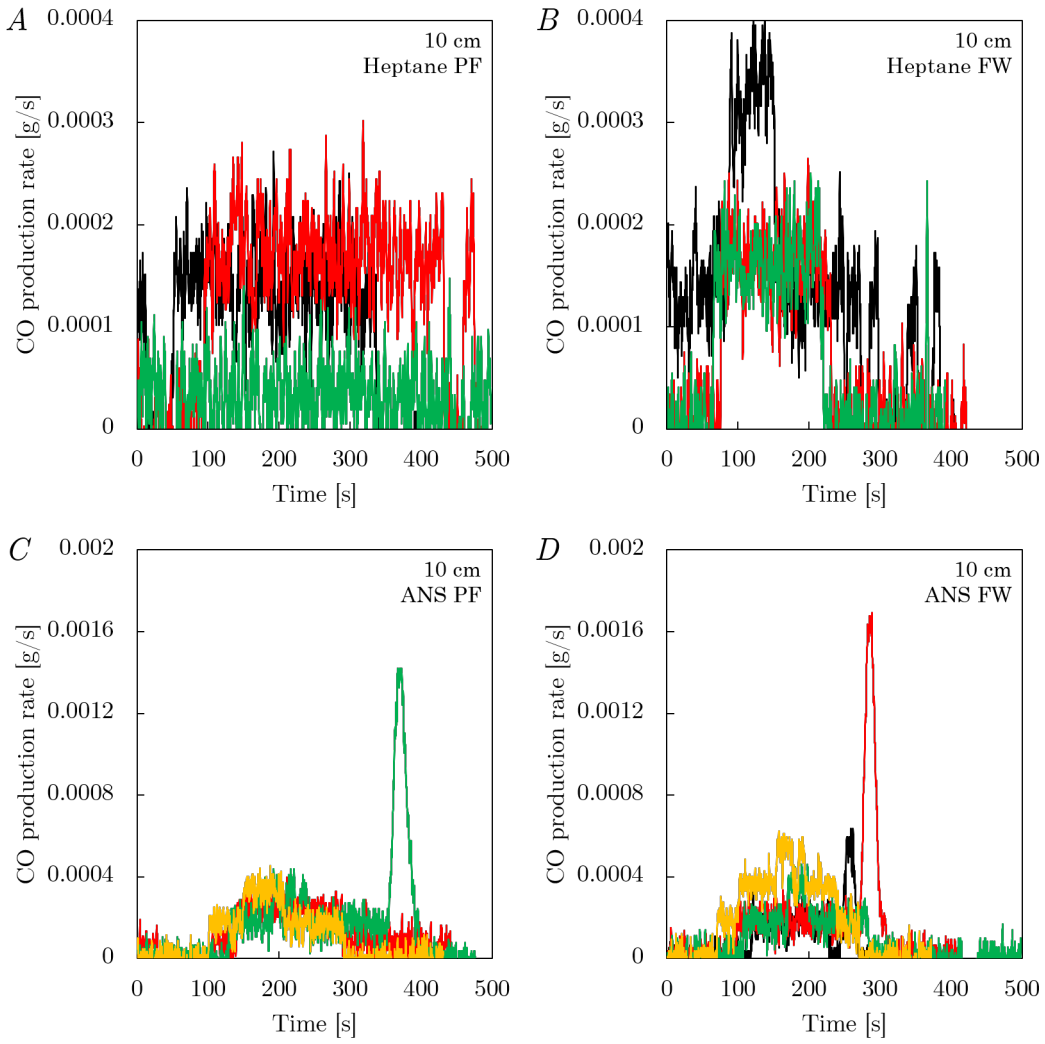

Figure B.7: CO emission rate, $D = 10$ cm.

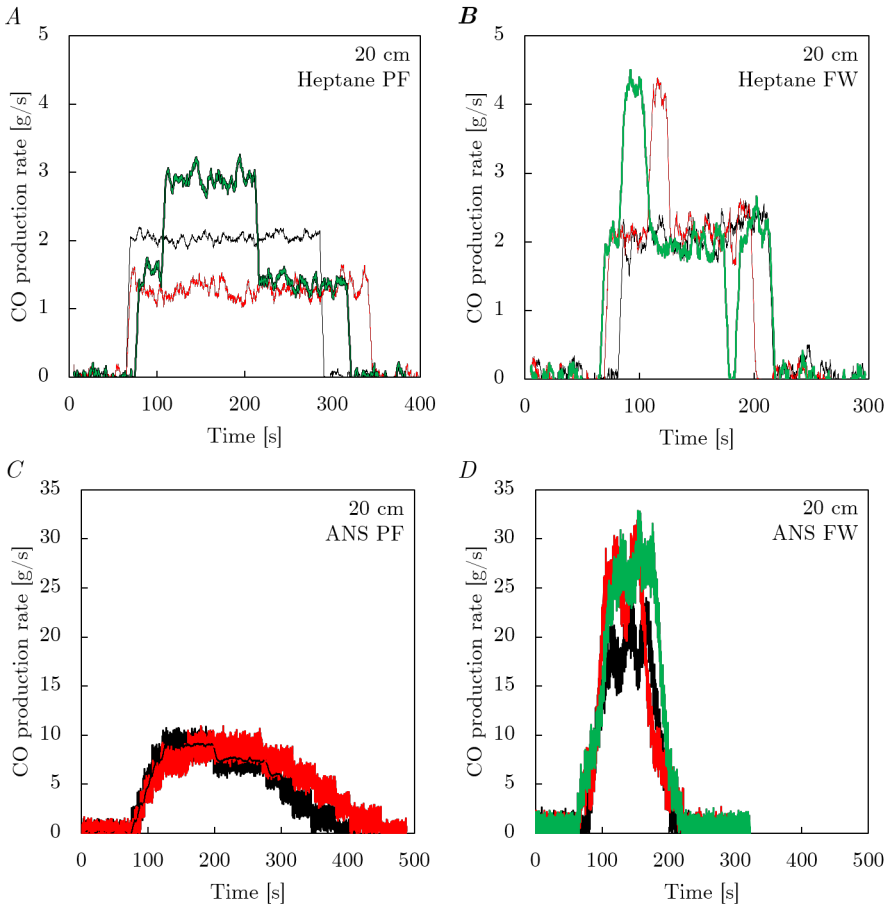

Figure B.8: CO emission rate, $D = 20$ cm.

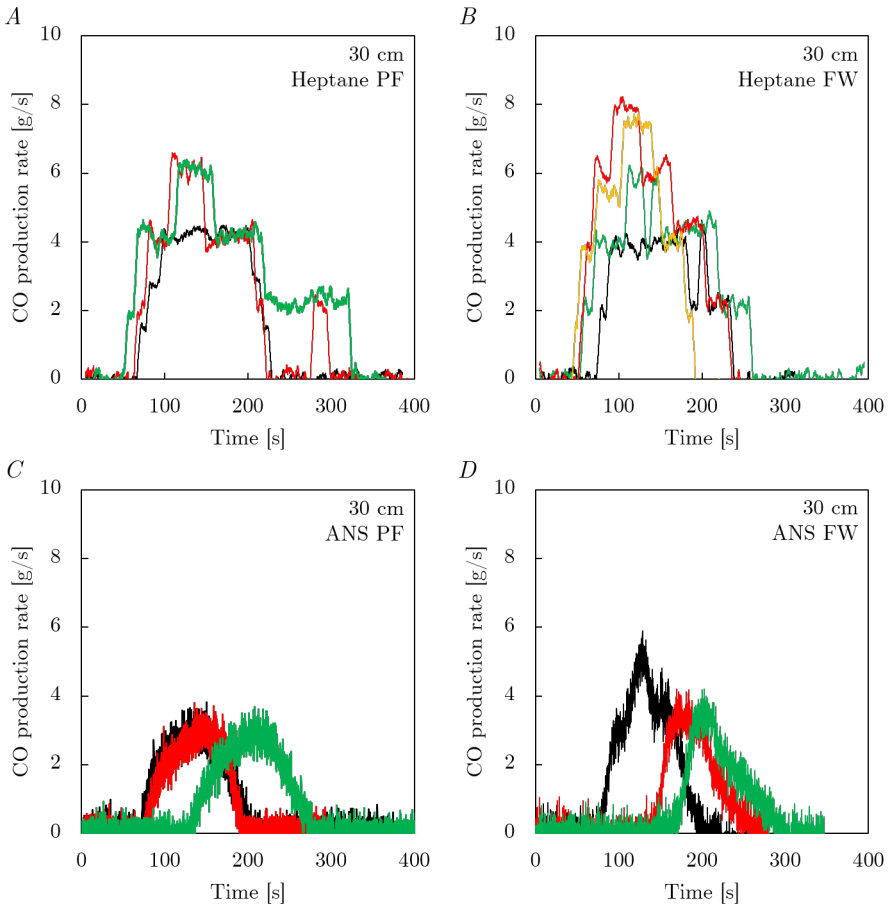

Figure B.9: CO emission rate, $D = 30$ cm.

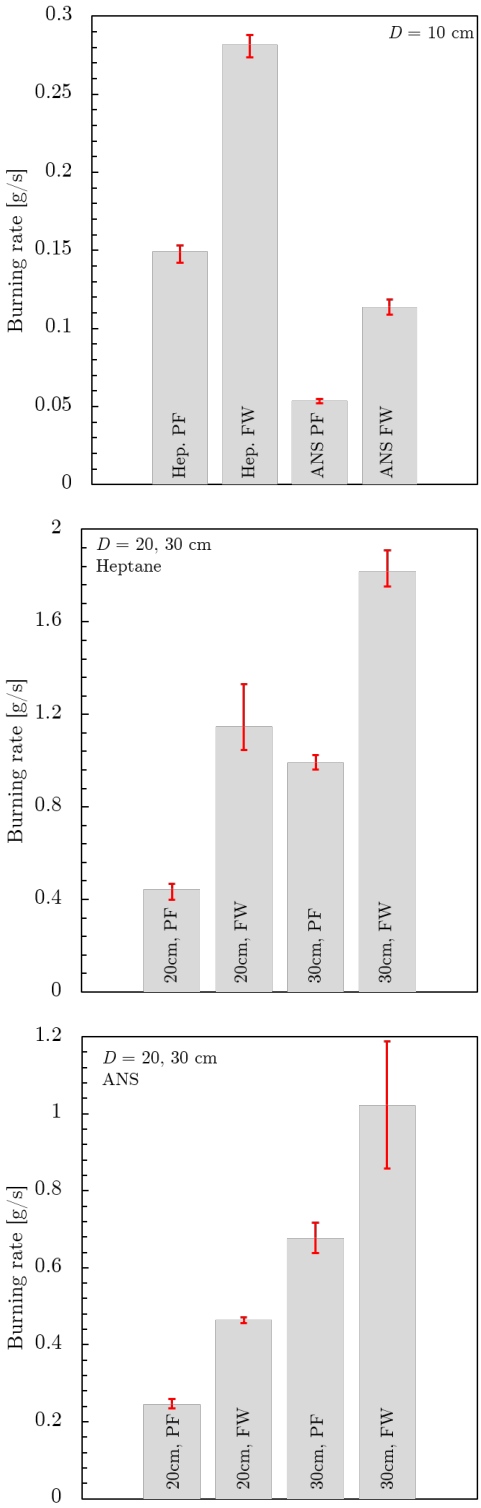

Figure B.10: Experimental variability in the measurement of $\dot{m}$ at $D = [10, 20, 30]$ cm.

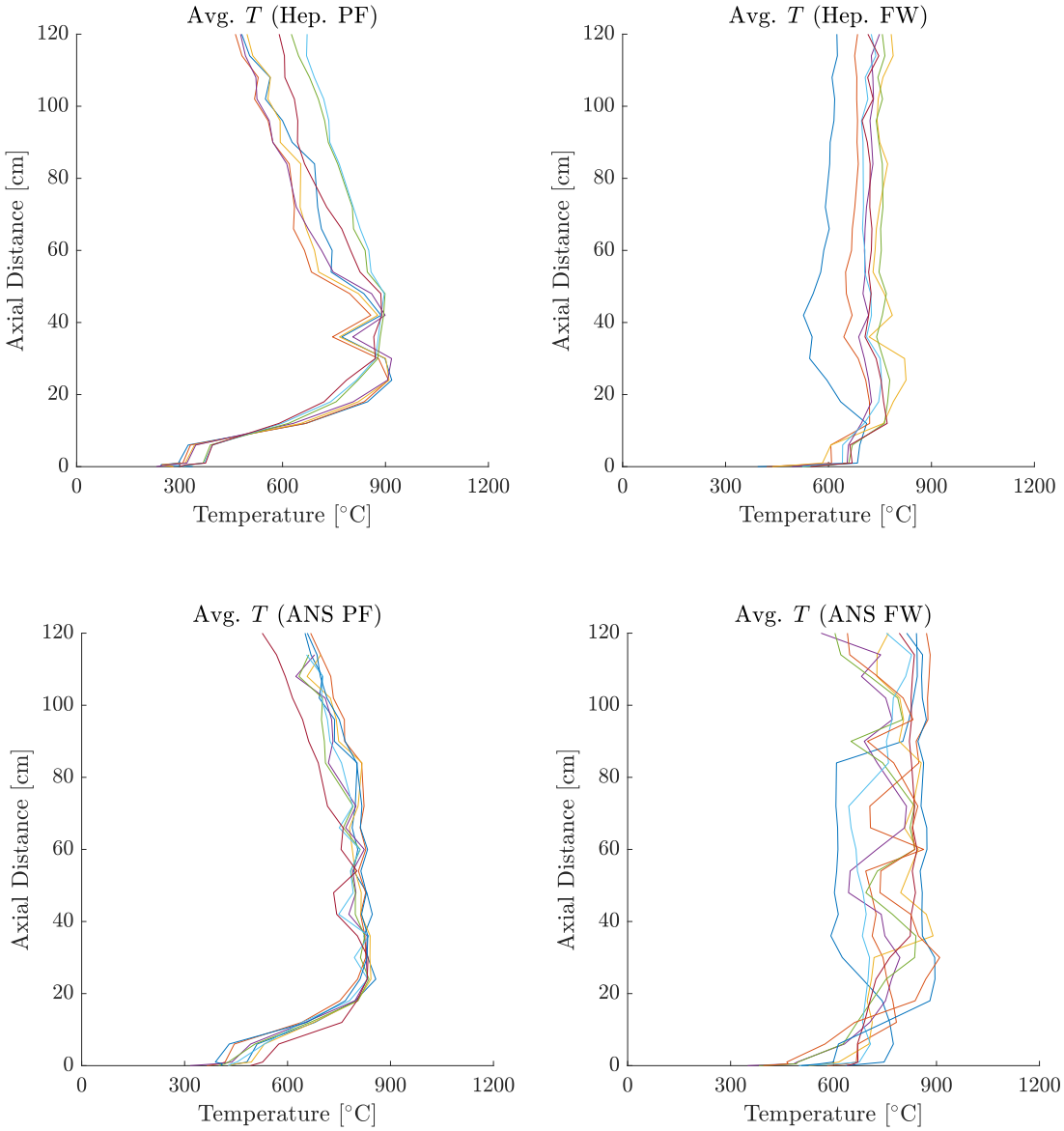

Figure B.11: Average values of centerline temperature measured at different axial distances for PFs and FWs formed with heptane and ANS crude oil.

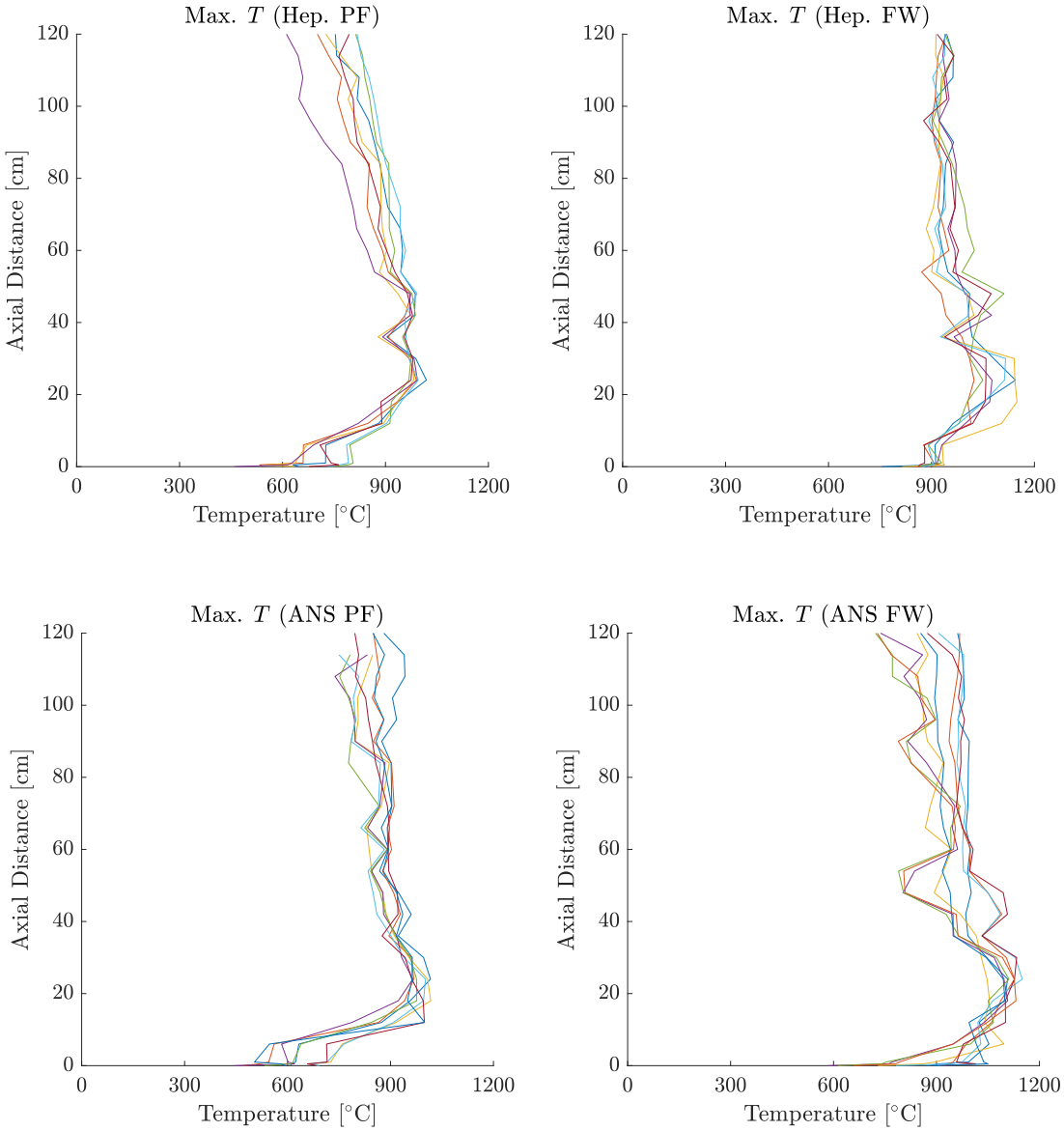

Figure B.12: Maximum values of centerline temperature measured at different axial distances for PFs and FWs formed with heptane and ANS crude oil.

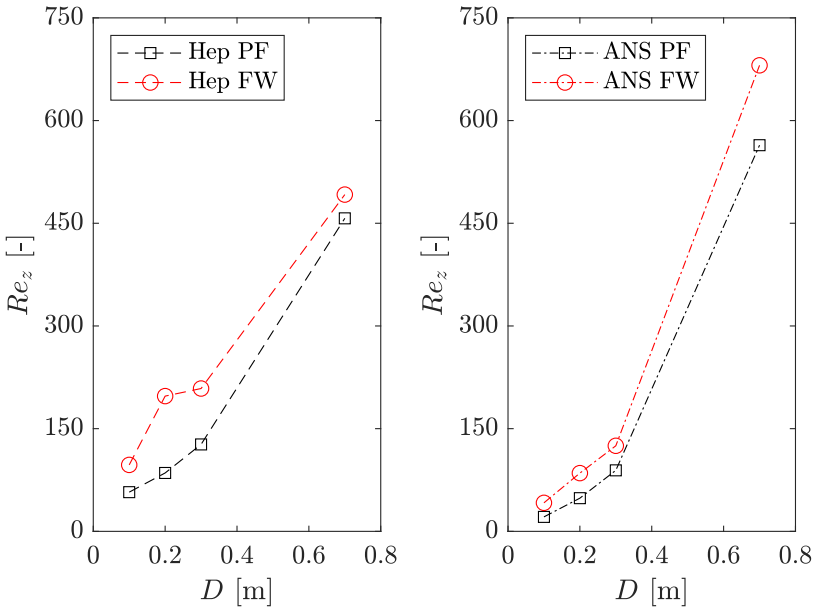

Figure B.13: Re_z, estimated as $(\dot{m}''D/\rho)/\nu$, with ρ and ν evaluated at T_{film}. The values of T_{film} for heptane PF, heptane FW, ANS PF and ANS FW were 675 K, 800 K, 650 K and 725 K, respectively. The ratio $(\dot{m}''/\rho)$ is $U_{z=0}$, the spatially averaged value of fuel evaporation at the fuel surface.

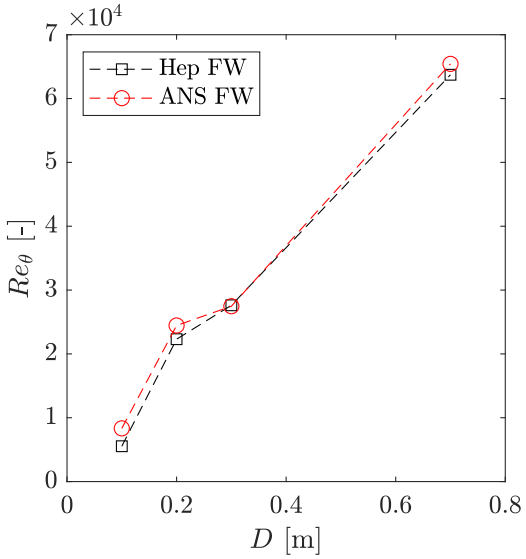

Figure B.14: Re_θ, estimated as Γ/ν.

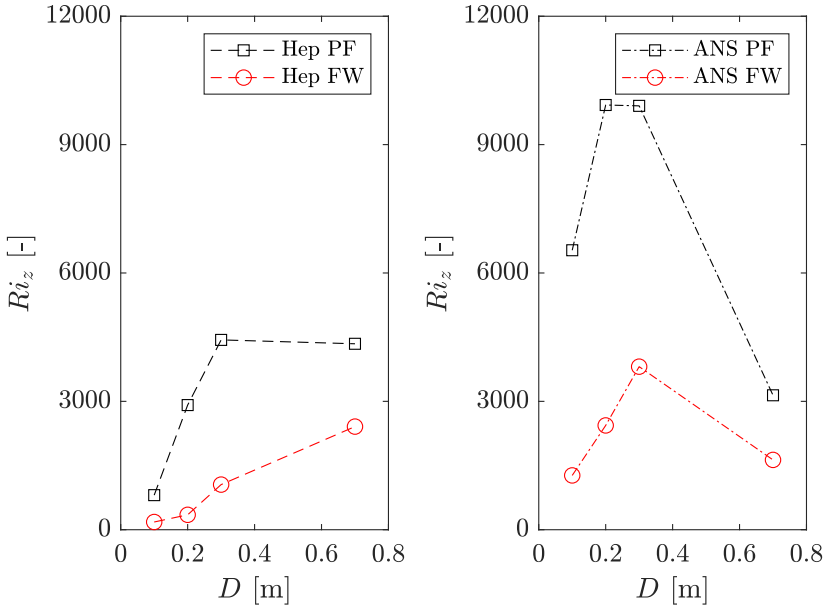

Figure B.15: Ri_z, estimated as Gr/Re_z^2.

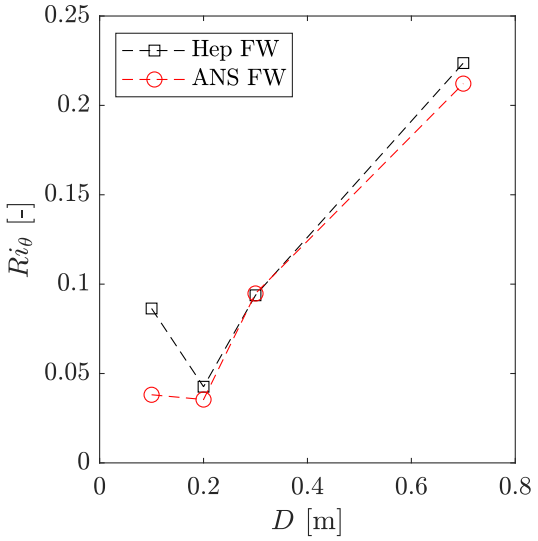

Figure B.16: Ri_θ, estimated as Gr/Re_θ^2.

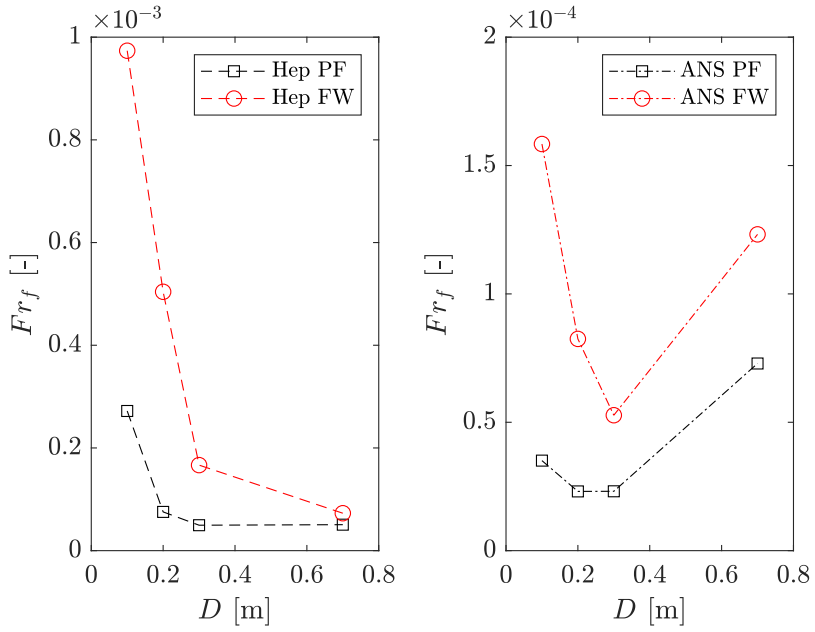

Figure B.17: Fuel Froude number, Fr_f, estimated as $(\dot{m}''^2)/(\rho_0^2 g D)$ [11], with ρ_0 evaluated at $T_0 = 300K$.

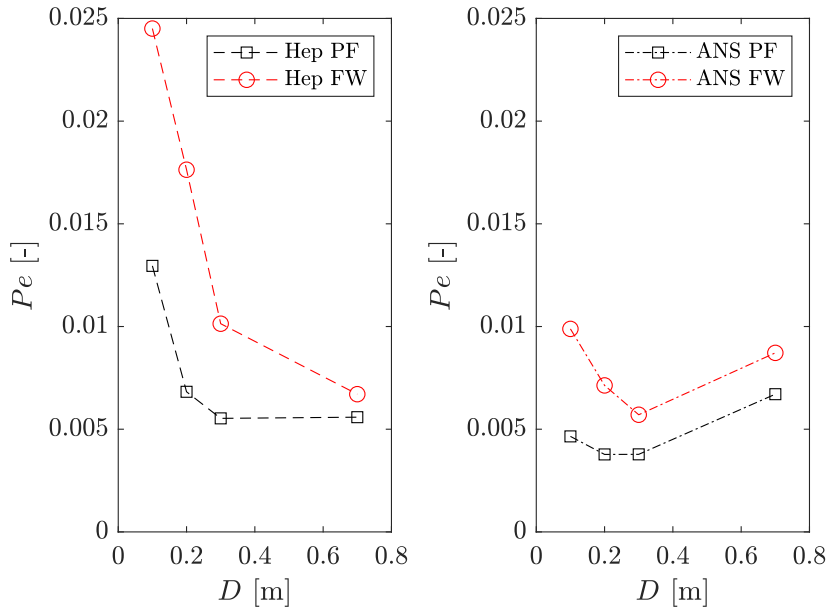

Figure B.18: Modified Peclet number, Pe, evaluated as $(\dot{m})/(\rho\sqrt{gD^5})$ [35].

Appendix C: Supplementary Material to Chapter 6

C.1 Chemiluminescence data of premixed methane-air flames

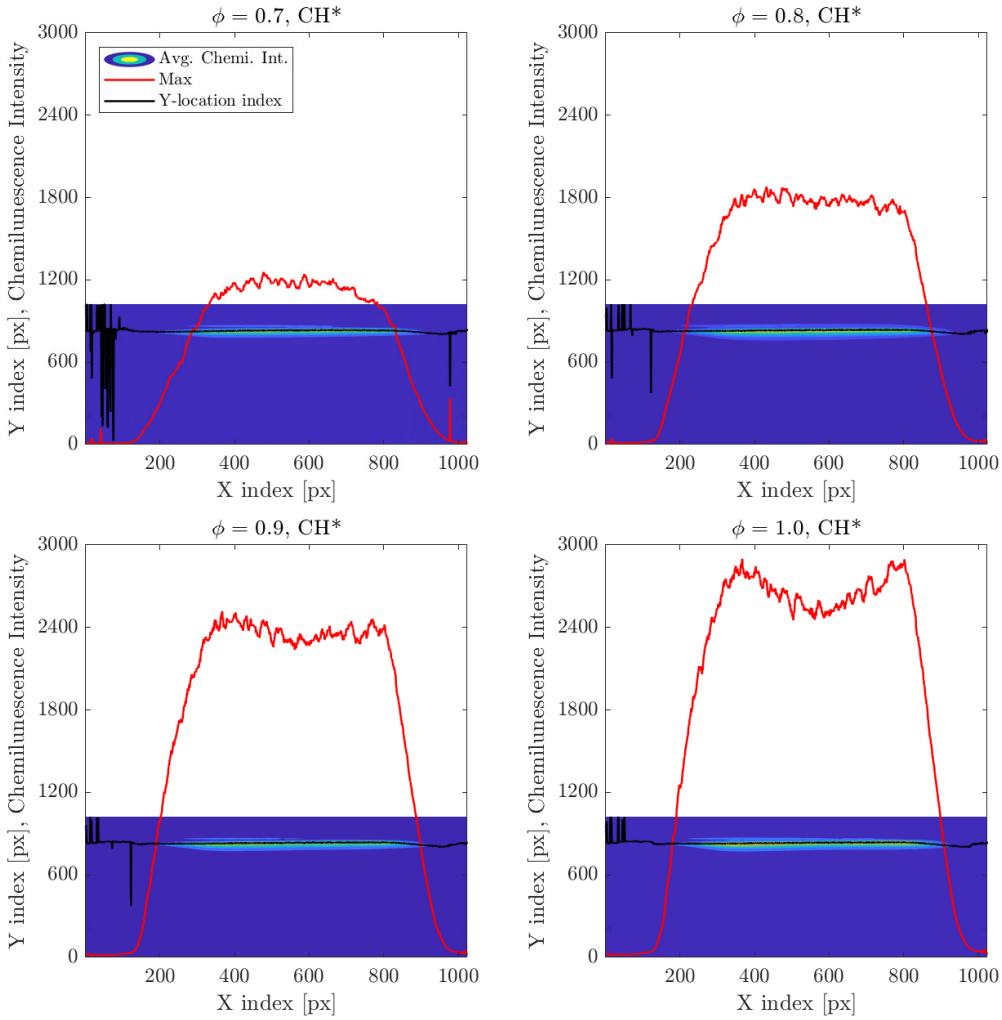

Figure C.1: Average contours of CH* chemiluminescence intensity, maximum intensity and location indices of maximum intensity for $\phi = [0.7, 0.8, 0.9, 1.0]$.

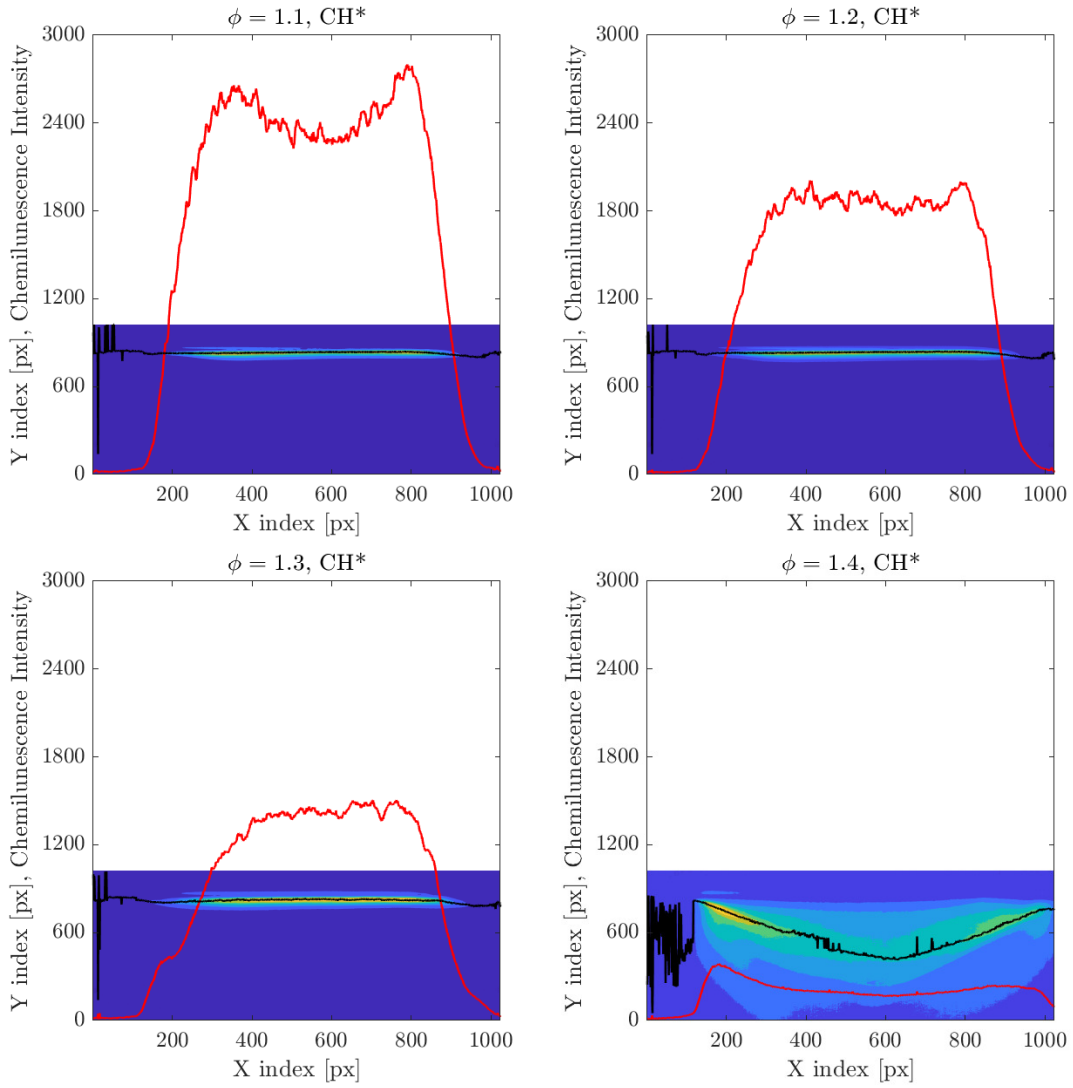

Figure C.2: Average contours of CH* chemiluminescence intensity, maximum intensity and location indices of maximum intensity for $\phi = [1.1, 1.2, 1.3, 1.4]$.

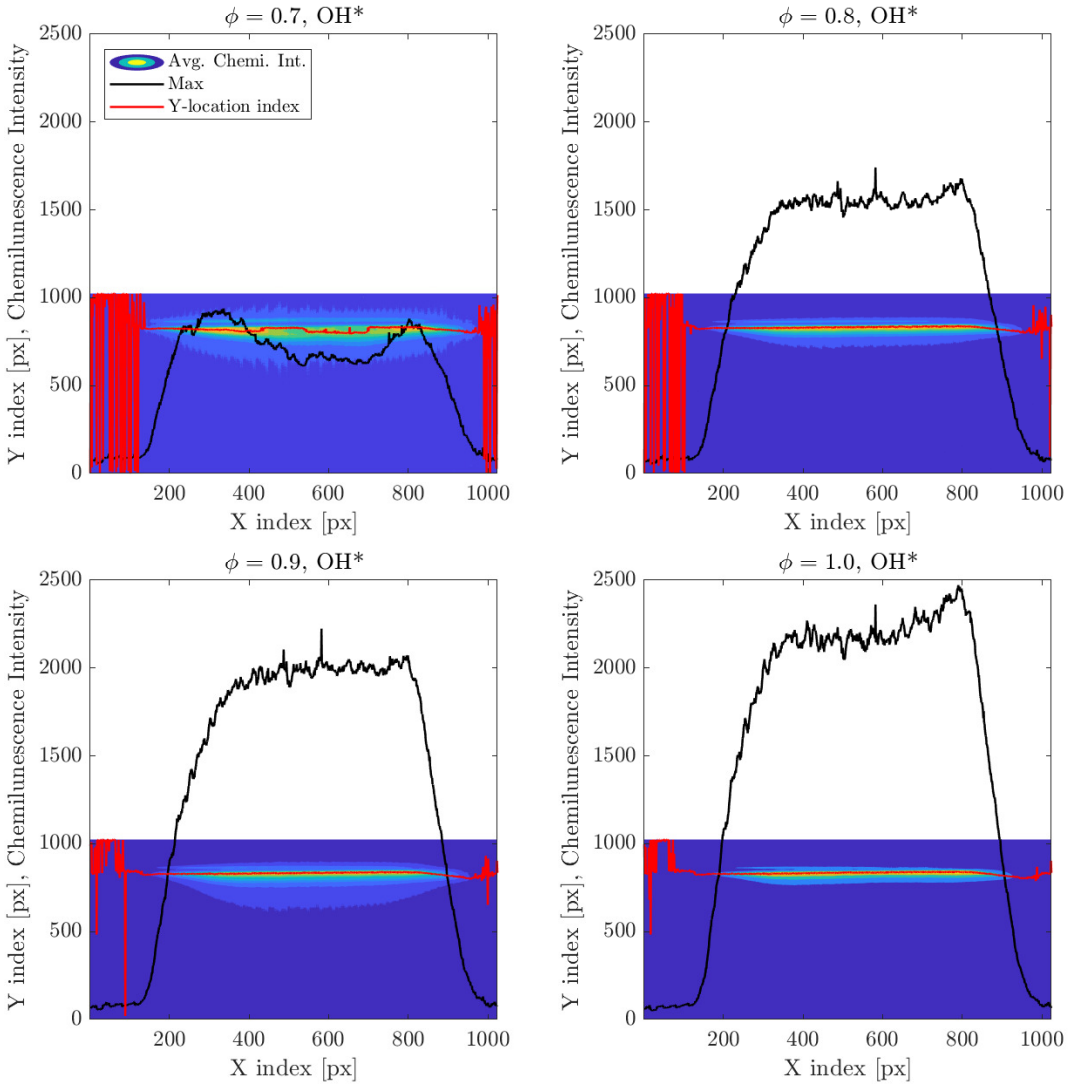

Figure C.3: Average contours of OH* chemiluminescence intensity, maximum intensity and location indices of maximum intensity for $\phi = [0.7, 0.8, 0.9, 1.0]$.

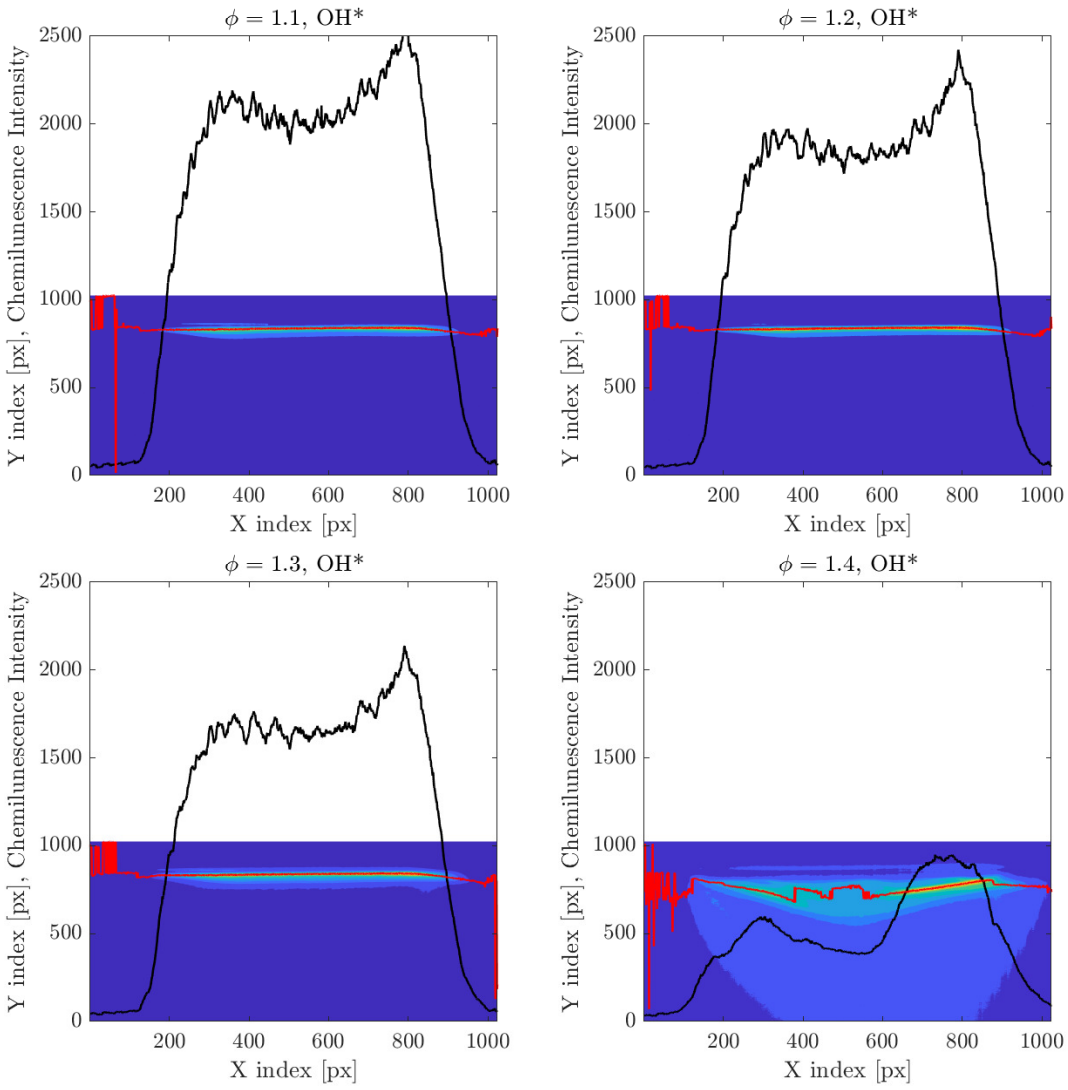

Figure C.4: Average contours of OH* chemiluminescence intensity, maximum intensity and location indices of maximum intensity for $\phi = [1.1, 1.2, 1.3, 1.4]$.

C.2 Chemiluminescence and PLIF: BW

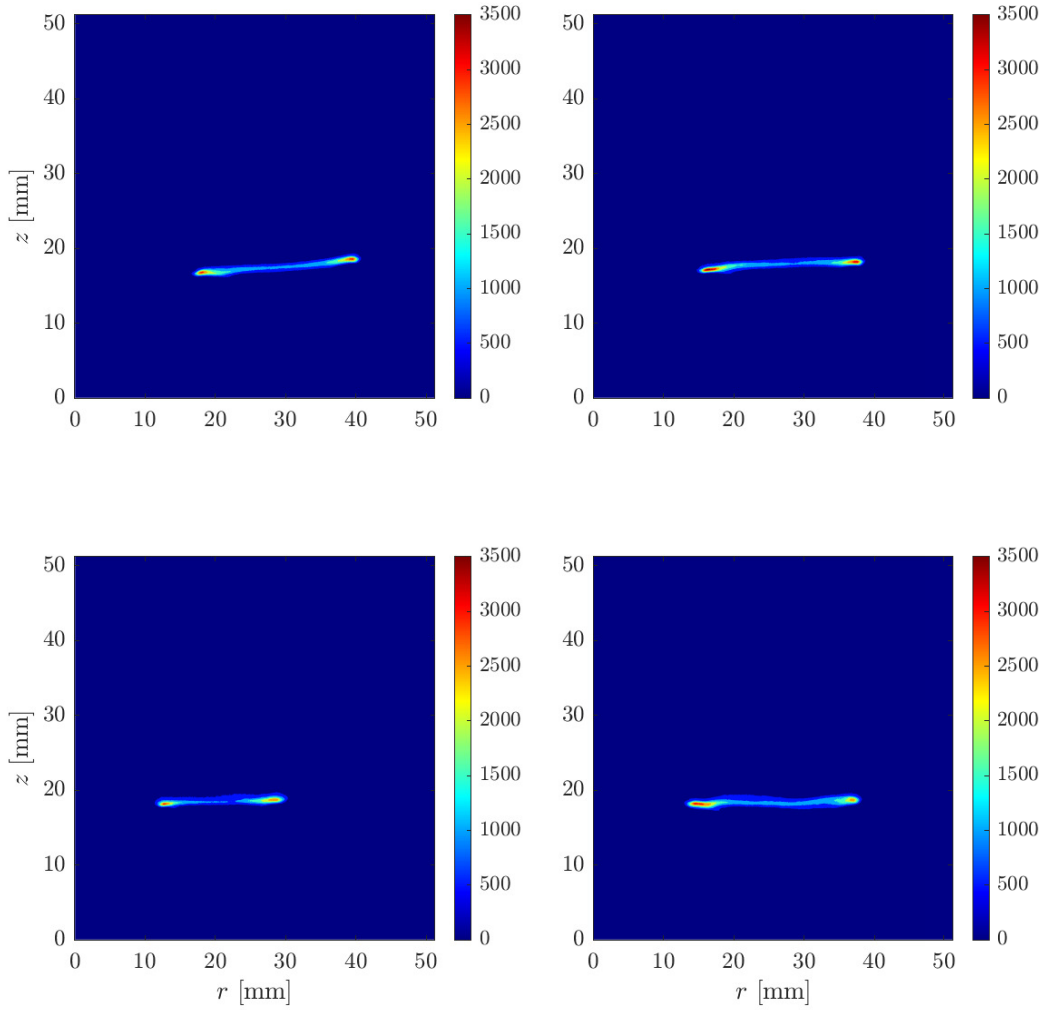

Figure C.5: CH* in the BW.

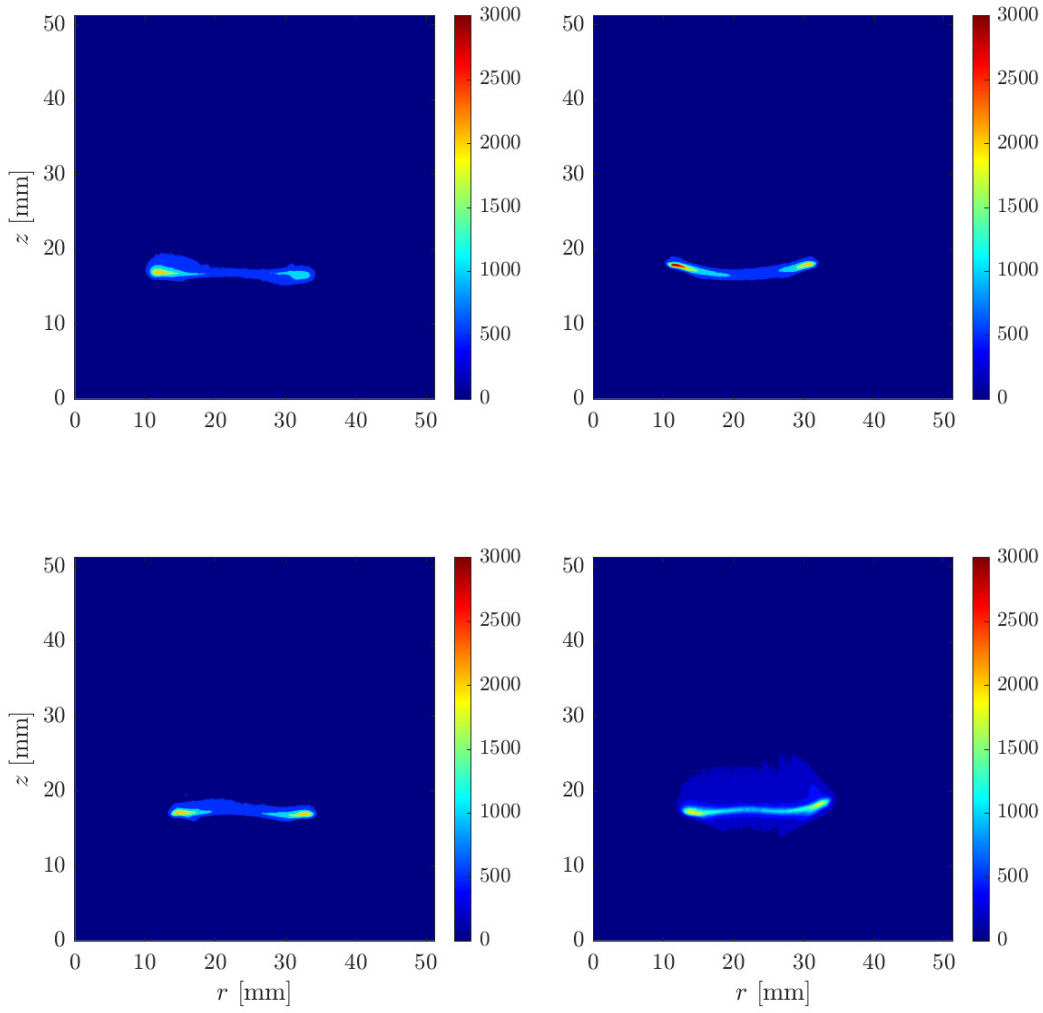

Figure C.6: OH* in the OH.

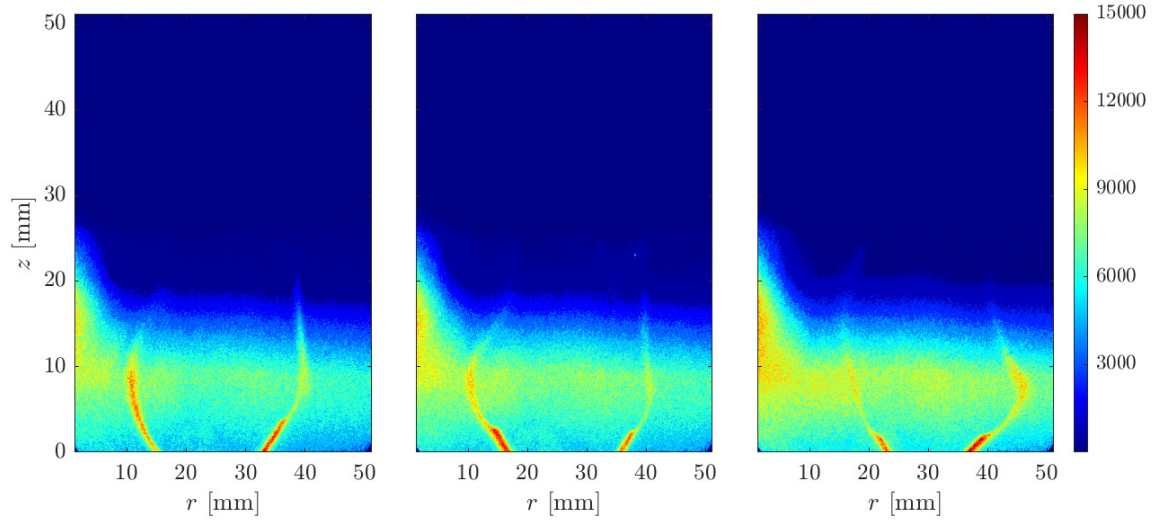

Figure C.7: Individual frames showing PAH in the BW.

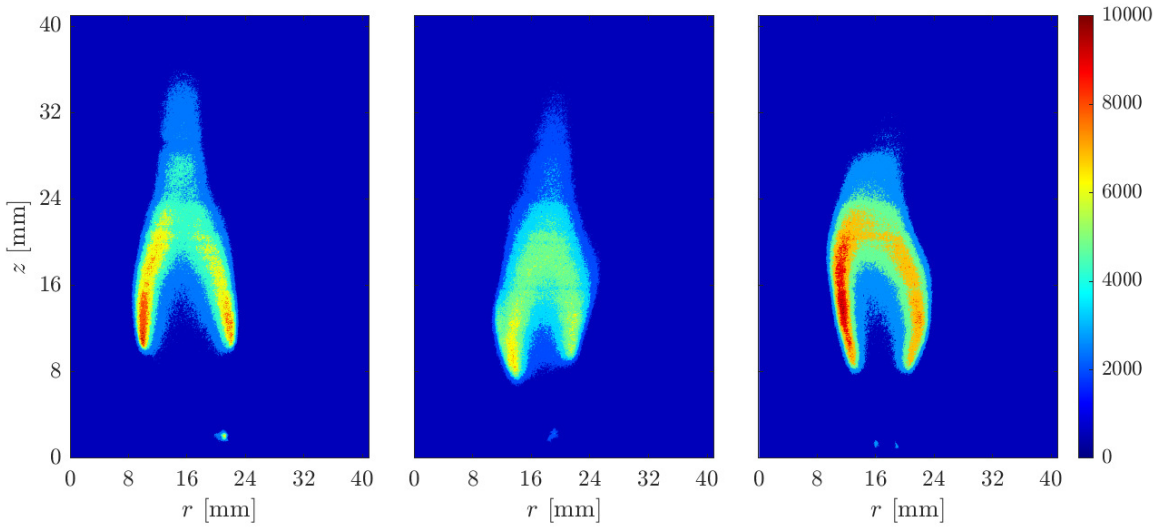

Figure C.8: Individual frames showing OH in the BW.

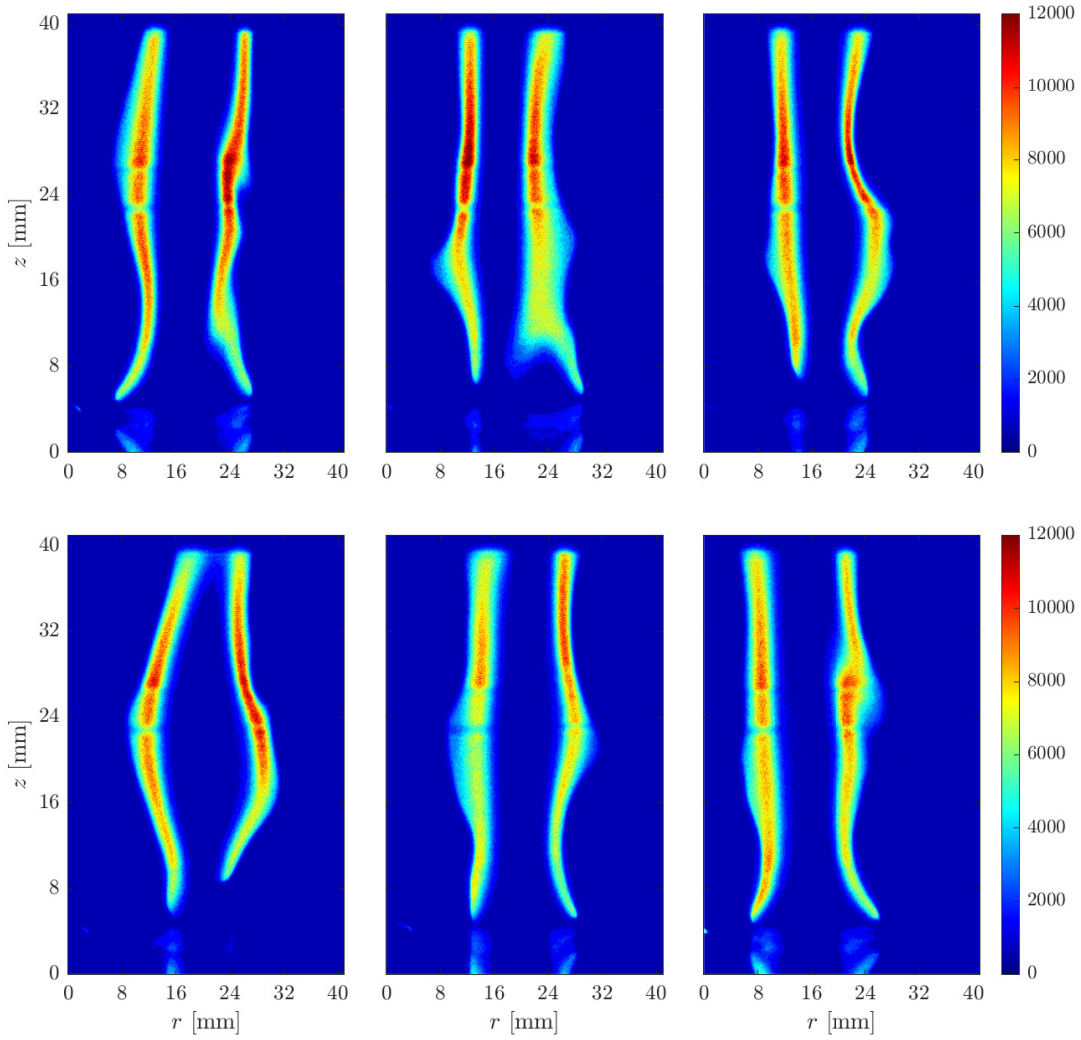

Figure C.9: Sequence of frames showing OH in the FW. Two frames (*top right, bottom left*) show a tendency to transition to the BW, evidenced by the bulging of the flame sheet, but the flame stays in the FW regime in the following frames.

C.3 Flow in the post-flame region of the blue whirl

Close observation of the BW shows the emanation of small, short-lived soot particles from the blue ring. They are visible briefly before being consumed in the post-flame region. The is visible when total chemiluminescence was imaged at high frame rates (see *Supplementary Material, Figures S.1A and S.2A*). These soot traces may be used to estimate roughly the residence time of soot within the post-flame region and the Damköhler number (Da). Since the diameter of each particle cannot be measured from the incandescence, it is assumed here that the Stokes number (Stk) is low enough that it closely follows the local flow path.

The path lines of some soot particles tracked using the *Fiji* version of *ImageJ* [256]. Each instance of soot-particle emanation was tracked using the "ManualTrack" feature in *Fiji*. The overlayed tracks are shown in *Supplementary Material, Figures S.1B and S.2B*). The vectors for some cases are shown in Figure C.10. Most instances involved a particle following a trajectory in the axial direction, but some particles first showed an azimuthal trajectory before eventually exiting the flame in the axial direction. One such instance is shown in Figure C.10B.

Although the motion of the soot particles is in 3 dimensions, the projected velocity of each particle was determined using the tracking-coordinate data and the inter-frame time (0.04 s). The magnitudes of horizontal, vertical and total velocity (u,v, $|\vec{u}|$) are summarized in Table C.1.

The Damköhler number is defined as [17]

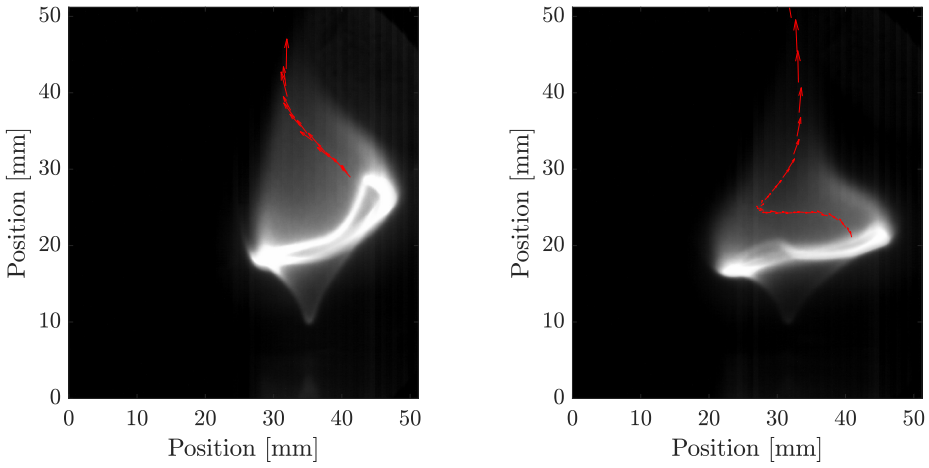

Figure C.10: Vectors showing the instantaneous velocity of two examples of soot particles emanating from the blue ring and passing through the post-flame region.

$$Da = \frac{\tau_{flow}}{\tau_{rxn}} \tag{C.1}$$

where τ_{flow} and τ_{rxn} are the characteritic flow and reaction time scales. The two time scales for the BW are defined as

$$\tau_{flow} = \frac{BW\ diameter}{|\vec{u}|} \tag{C.2}$$

$$\tau_{rxn} = \frac{ring\ thickness}{\mathcal{V}_{f,iso-octane}} \tag{C.3}$$

where τ is the characteristic time scale, $\mathcal{V}_{flame}$ is the laminar flame speed of iso-octane at 1 atm [257]. Using the limits of $|\vec{u}|$ from Table C.1 and an average BW diameter of 20 mm, τ_{flow} was calculated to be in the range $(0.5, 1)$ s. Using values of $\mathcal{V}_{flame}$ from [257] and a ring thickness of 1.5 mm, τ_{rxn} was estimated as

Table C.1: Consolidated velocity data (in [mm/s]) obtained by tracking soot in three individual experiments.

		u	v	$\|\vec{u}\|$
Video 1	Overall Mean	12.6	23	27.3
	Std. deviation	8.1	7.6	8.2
Video 2	Overall Mean	9.6	15.6	19
	Std. deviation	6.6	12.7	12.9
Video 3	Overall Mean	16	27.7	34.5
	Std. deviation	7.8	23.7	21.3

≈ 0.004 s. Thus, the estimate of Da is in the range of $(125, 250)$. The velocity measurements are in the post-flame region, and the upstream flow velocity can be calculated by adjusting for the excess temperature. Assuming the average postflame temperature as 1500 K, the upstream velocity reduces by a factor of $\frac{1500}{300}$, which results in $\tau_{flow} \in (0.1, 0.2)$ and $Da \in (25, 50)$.

Bibliography

[1] NASA/JPL-Caltech/Space-Science-Institute. Basking in Light, 2016.

[2] Cathal Cummins, Madeleine Seale, Alice Macente, Daniele Certini, Enrico Mastropaolo, Ignazio Maria Viola, and Naomi Nakayama. A separated vortex ring underlies the flight of the dandelion. *Nature*, 562(7727):414–418, 2018.

[3] Daniel Durox, Jonas P. Moeck, Jean François Bourgouin, Pascal Morenton, Marc Viallon, Thierry Schuller, and Sébastien Candel. Flame dynamics of a variable swirl number system and instability control. *Combustion and Flame*, 160(9):1729–1742, 2013.

[4] Pengfei Wang, Naian Liu, Katherine Hartl, and Alexander Smits. Measurement of the Flow Field of Fire Whirl. *Fire Technology*, 52(1):263–272, 1 2016.

[5] Ali Tohidi, Michael J. Gollner, and Huahua Xiao. Fire Whirls. *Annual Review of Fluid Mechanics*, 50(1):187–213, 1 2018.

[6] Jiao Lei, Naian Liu, and Kohyu Satoh. Buoyant pool fires under imposed circulations before the formation of fire whirls. *Proceedings of the Combustion Institute*, 35(3):2503–2510, 2015.

[7] Jiao Lei, Naian Liu, Linhe Zhang, and Kohyu Satoh. Temperature, velocity and air entrainment of fire whirl plume: A comprehensive experimental investigation. *Combustion and Flame*, 162(3):745–758, 2015.

[8] Howard W. Emmons and Shuh-Jing Ying. The fire whirl. *Symposium (International) on Combustion*, 11(1):475–488, 1 1967.

[9] Keng Hoo Chuah, Kazunori Kuwana, Kozo Saito, and Forman A. Williams. Inclined fire whirls. *Proceedings of the Combustion Institute*, 33(2):2417–2424, 2011.

[10] A. Y. Klimenko and F. A. Williams. On the flame length in firewhirls with strong vorticity. *Combustion and Flame*, 160(2):335–359, 2013.

[11] Kazunori Kuwana, Kozo Sekimoto, Kozo Saito, and Forman A. Williams. Scaling fire whirls. *Fire Safety Journal*, 43(4):252–257, 5 2008.

[12] K.A. Hartl and A.J. Smits. Scaling of a small scale burner fire whirl. *Combustion and Flame*, 163:202–208, 1 2016.

[13] Kazunori Kuwana, Satoshi Morishita, Ritsu Dobashi, Keng H. Chuah, and Kozo Saito. The burning rate's effect on the flame length of weak fire whirls. *Proceedings of the Combustion Institute*, 33(2):2425–2432, 2011.

[14] A. Hamins, J.C. Yang, and T. Kashiwagi. An experimental investigation of the pulsation frequency of flames. *Symposium (International) on Combustion*, 24(1):1695–1702, 1 1992.

[15] Hiroyuki Sato, Kenji Amagai, and Masataka Arai. Scale Modeling of Puffing Frequencies in Pool Fires Related with Froude Number. In *Progress in Scale Modeling*, pages 133–147. Springer Netherlands, Dordrecht, 2008.

[16] Johanna Aurell, David Hubble, Brian K. Gullett, Amara Holder, Ephraim Washburn, and Dennis Tabor. Characterization of Emissions from Liquid Fuel and Propane Open Burns. *Fire Technology*, 53(6):2023–2038, 11 2017.

[17] Stephen R. Turns. *An Introduction to Combustion: Concepts and Applications*. McGraw-Hill, 3rd edition, 2012.

[18] Hai Wang. Formation of nascent soot and other condensed-phase materials in flames. *Proceedings of the Combustion Institute*, 33(1):41–67, 2011.

[19] K. O. Johansson, M. P. Head-Gordon, P. E. Schrader, K. R. Wilson, and H. A. Michelsen. Resonance-stabilized hydrocarbon-radical chain reactions may explain soot inception and growth. *Science*, 361(6406):997–1000, 9 2018.

[20] Chun Lou, Chen Chen, Yipeng Sun, and Huaichun Zhou. Review of soot measurement in hydrocarbon-air flames. *Science China Technological Sciences*, 53(8):2129–2141, 8 2010.

[21] TSI Incorporated. Theory of Operation - DustTrak DRX Aerosol Monitor. Technical report, TSI Incorporated, 2012.

[22] Sriram Bharath Hariharan, Evan T. Sluder, Michael J. Gollner, and Elaine S. Oran. Thermal structure of the blue whirl. *Proceedings of the Combustion Institute*, 37(3):4285–4293, 2019.

[23] Wilfried Coenen, Erik J. Kolb, Antonio L. Sánchez, and Forman A. Williams. Observed dependence of characteristics of liquid-pool fires on swirl magnitude. *Combustion and Flame*, 205:1–6, 7 2019.

[24] Yu Hu, Sriram Bharath Hariharan, Haiying Qi, Michael J. Gollner, and Elaine S. Oran. Conditions for formation of the blue whirl. *Combustion and Flame*, 205:147–153, 2019.

[25] Ronald K. Hanson, R. Mitchell Spearrin, and Christopher S. Goldenstein. *Spectroscopy and Optical Diagnostics for Gases*. Springer International Publishing, Cham, 2016.

[26] CAI-Instruments. Non-Dispersive Infrared (NDIR) Analyzers.

[27] TSI-Incorporated. DUSTTRAK DRX AEROSOL MONITOR 8534.

[28] W M Thornton. XV. The relation of oxygen to the heat of combustion of organic compounds. *The London, Edinburgh, and Dublin Philosophical Magazine and Journal of Science*, 33(194):196–203, 2 1917.

[29] C. Beyler, P. Croce, C. Dubay, P. Johnson, and M. McNamee. Oxygen consumption calorimetry, William Parker: 2016 DiNenno Prize. *Fire Science Reviews*, 6(1):1–7, 2017.

[30] Morgan J. Hurley, Daniel Gottuk, John R. Hall, Kazunori Harada, Erica Kuligowski, Milosh Puchovsky, José Torero, John M. Watts, and Christopher Wieczorek, editors. *SFPE Handbook of Fire Protection Engineering*. Springer New York, New York, NY, 2016.

[31] Sriram Bharath Hariharan, Yejun Wang, Paul M Anderson, Waruna D. Kulatilaka, Michael J. Gollner, and Elaine S. Oran. Understanding Combustion in the Blue Whirl using Optical Diagnostics. In *72nd Annual Meeting of the APS Division of Fluid Dynamics*, Seattle, Washington, 2019.

[32] Mikaël Orain and Yannis Hardalupas. Effect of fuel type on equivalence ratio measurements using chemiluminescence in premixed flames. *Comptes Rendus Mécanique*, 338(5):241–254, 2010.

[33] Joseph Dongil Chung. *Numerical Simulation of the Blue Whirl: A Reacting Vortex Breakdown Phenomenon*. PhD thesis, University of Maryland, College Park, 2020.

[34] Suyin Gan, Hoon Kiat Ng, and Kar Mun Pang. Homogeneous Charge Compression Ignition (HCCI) combustion: Implementation and effects on pollutants in direct injection diesel engines. *Applied Energy*, 88(3):559–567, 2011.

[35] James G. Quintiere. *Fundamentals of Fire Phenomena*. 2006.

[36] Philip S Marcus. Jupiter's Great Red Spot and Other Vortices. *Annual Review of Astronomy and Astrophysics*, 31(1):523–569, 9 1993.

[37] A. Einstein. Die Ursache der Maanderbildung der FluBlaufe und des sogenannten Baerschen Gesetzes. *Die Naturwissenschaften*, 14(11):223–224, 1926.

[38] C. S. Yogananda and Albert Einstein. The cause of the formation of meanders in the courses of rivers and of the so-called Baer's law. *Resonance*, 5(3):105–108, 2000.

[39] R. D. HEY. Geometry of river meanders. *Nature*, 262(5568):482–484, 8 1976.

[40] H Helmholtz. Über Integrale der hydrodynamischen Gleichungen, welche den Wirbelbewegungen entsprechen. *Journal für die reine und angewandte Mathematik (Crelles Journal)*, 1858(55):25–55, 1 1858.

[41] H Helmholtz. LXIII. On Integrals of the hydrodynamical equations, which express vortex-motion. *The London, Edinburgh, and Dublin Philosophical Magazine and Journal of Science*, 33(226):485–512, 1 1867.

[42] Martin Kemp. Leonardo's laboratory: studies in flow. *Nature*, 571:322–323, 2019.

[43] Vincent Van Gogh. The Starry Night, 1889.

[44] Katherine Wright. Arts & Culture: Turbulence in The Starry Night. *Physics*, 4 2019.

[45] J L Aragón, Gerardo G Naumis, M Bai, M Torres, and P K Maini. Turbulent Luminance in Impassioned van Gogh Paintings. *Journal of Mathematical Imaging and Vision*, 30(3):275–283, 2008.

[46] James Beattie and Neco Kriel. Is The Starry Night Turbulent? (arXiv:1902.03381v2). *arXiv*, (2):1–6, 2 2019.

[47] George M. Byram and Robert E. Martin. Fire Whirlwinds in the Laboratory. *Fire Control Notes*, 23(1):13–17, 1962.

[48] George M. Byram and Robert E. Martin. The Modeling of Fire Whirlwinds. *Forest Science*, 16:386–399, 1970.

[49] Jason M. Forthofer and Scott L. Goodrick. Review of vortices in wildland fire. *Journal of Combustion*, 2011(Figure 1), 2011.

[50] N. P. Lareau, N. J. Nauslar, and J. T. Abatzoglou. The Carr Fire Vortex: A Case of Pyrotornadogenesis? *Geophysical Research Letters*, 45(23):107–13, 2018.

[51] CalFIRE. CalFire Green Sheet: Burn Over Fatalities July 26, 2018, Carr Incident 18-CA-SHU-007808, 18-CA-SHU-007962, California Northern Region. Technical report, CalFire, 2018.

[52] A. Muraszew, J.B. Fedele, and W.C. Kuby. Trajectory of firebrands in and out of fire whirls. *Combustion and Flame*, 30:321–324, 1 1977.

[53] Kazunori Kuwana, Kozo Sekimoto, Kozo Saito, Forman a. Williams, Yoshihiko Hayashi, and Hideaki Masuda. Can We Predict the Occurrence of Extreme Fire Whirls? *AIAA Journal*, 45(1):16–19, 1 2007.

[54] K. A. Hartl and A. J. Smits. Stereo PIV measurements in fire whirls. *Experiments in Fluids*, 60(1):1–16, 2019.

[55] Y. Hayashi, K. Kuwana, and R. Dobashi. Influence of Vortex Structure on Fire Whirl Behavior. *Fire Safety Science*, 10:671–679, 2011.

[56] M. Hassan, Kazunori Kuwana, Kozo Saito, and Fengjuan Wang. Flow Structure Of A Fixed-frame Type Firewhirl. *Fire Safety Science*, 8:951–962, 2005.

[57] N. Syred and J.M. Beér. Combustion in swirling flows: A review. *Combustion and Flame*, 23(2):143–201, 1974.

[58] Randal G. McKinney and James B. Hoke. Aero Gas Turbine Combustion: Metrics, Constraints, and System Interactions. In Timothy C. Lieuwen and Vigor Yang, editors, *Gas Turbine Emissions*, chapter 1, pages 3–23. Cambridge University Press, 2013.

[59] Sébastien Candel, Daniel Durox, Thierry Schuller, Jean-François Bourgouin, and Jonas P. Moeck. Dynamics of Swirling Flames. *Annual Review of Fluid Mechanics*, 46(1):147–173, 1 2014.

[60] Richard A Yetter, Irvin Glassman, and H Clay Gabler. Asymmetric Whirl Combustion: A New Low NOx Approach. *Proceedings of the Combustion Institute*, 28(x):1265–1272, 2000.

[61] N.A. Chigier, J.M. Beér, D. Grecov, and K. Bassindale. Jet flames in rotating flow fields. *Combustion and Flame*, 14(2):171–179, 4 1970.

[62] N. A. Chigier and A. Chervinsky. Aerodynamic study of turbulent burning free jets with swirl. *Symposium (International) on Combustion*, 11(1):489–499, 1967.

[63] Rikiya YAMADA and Kazunori KUWANA. Scaling laws of flow structures around geometrically similar fire whirls. *Journal of Thermal Science and Technology*, 14(1):1–7, 2019.

[64] Huahua Xiao, Michael J. Gollner, and Elaine S. Oran. From fire whirls to blue whirls and combustion with reduced pollution. *Proceedings of the National Academy of Sciences*, 113(34):9457–9462, 8 2016.

[65] Sriram Bharath Hariharan. *The Structure of the Blue Whirl: A Soot-Free Reacting Vortex Phenomenon.* MS thesis, University of Maryland, College Park, 2017.

[66] Sriram Bharath Hariharan, Paul M Anderson, Huahua Xiao, Michael J Gollner, and Elaine S Oran. The blue whirl: Boundary layer effects, temperature and OH* measurements. *Combustion and Flame*, 203:352–361, 5 2019.

[67] Ying Huang and Vigor Yang. Dynamics and stability of lean-premixed swirl-stabilized combustion. *Progress in Energy and Combustion Science*, 35(4):293–364, 2009.

[68] V. Tangirala, R. H. Chen, and J. F. Driscoll. Effect of heat release and swirl on the recirculation within swirl-stabilized flames. *Combustion Science and Technology*, 51(1-3):75–95, 1987.

[69] Sandipan Chatterjee and Ömer L. Gülder. Soot concentration and primary particle size in swirl-stabilized non-premixed turbulent flames of ethylene and air. *Experimental Thermal and Fluid Science*, 95(January):73–80, 2018.

[70] P. Palies, D. Durox, T. Schuller, and S. Candel. Experimental study on the effect of swirler geometry and swirl number on flame describing functions. *Combustion Science and Technology*, 183(7):704–717, 2011.

[71] David G. Lilley. Swirl Flows in Combustion: A Review. *AIAA Journal*, 15(8):1063–1078, 1977.

[72] Joseph Chung, Xiao Zhang, Carolyn Kaplan, and Elaine S. Oran. Blue whirl structure revelead. In *72nd Annual Meeting of the APS Division of Fluid Dynamics*, Seattle, Washington, 2019.

[73] D. D. Evans, G. W. Mulholland, H. R. Baum, W. D. Walton, and K. B. McGrattan. In situ burning of oil spills. *Journal of Research of the National Institute of Standards and Technology*, 106(1):231–278, 2001.

[74] John L Ross, Ronald J. Ferek, and Peter V. Hobbs. Particle and Gas Emissions from an In Situ Burn of Crude Oil on the Ocean. *Journal of the Air & Waste Management Association*, 46(3):251–259, 3 1996.

[75] Alan A Allen and Ronald J Ferek. Advantages and Disadvantages of Burning Spilled Oil. *International Oil Spill Conference Proceedings*, 1993(1):765–772, 3 1993.

[76] David D. Evans and William D. Walton. Burning of Oil Spills. Technical report, National Institute of Standards and Technology, Gaithesburg, MD.

[77] Jan Paul Zock, Gema Rodríguez-Trigo, Francisco Pozo-Rodríguez, Joan A. Barberà, Laura Bouso, Yolanda Torralba, Josep M. Antó, Federico P. Gómez, Carme Fuster, and Héctor Verea. Prolonged respiratory symptoms in clean-up workers of the Prestige oil spill. *American Journal of Respiratory and Critical Care Medicine*, 176(6):610–616, 2007.

[78] Gina M. Solomon and Sarah Janssen. Health effects of the gulf oil spill. *Disaster Medicine and Public Health Preparedness*, 4(4):273–276, 2010.

[79] Olusegun G. Fawole, X. M. Cai, and A. R. Mackenzie. Gas flaring and resultant air pollution: A review focusing on black carbon. *Environmental Pollution*, 216:182–197, 2016.

[80] H.W. Emmons. Fundamental problems of the free burning fire. *Symposium (International) on Combustion*, 10(1):951–964, 1 1965.

[81] Amable Linan and Forman A. Williams. *Fundamental Aspects of Combustion*. Oxford University Press, New York, 1993.

[82] Jaime Carpio, Wilfried Coenen, Antonio L Sanchez, Elaine Oran, and Forman A Williams. Numerical description of blue whirls over liquid-fuel pools (Under Review). *Proceedings of the Combustion Institute*, 2020.

[83] Sriram Bharath Hariharan, Joseph Dowling, Michael R. Jones, Vittorio M. Valletta, Michael J. Gollner, Elaine S. Oran, Anthony Ogorzaly, Eric S. Neumann, Sandra Olson, and Paul Ferkul. Fire Whirls in Microgravity. In *2019 Meeting of the American Society for Gravitational and Space Research*, Denver, Colorado, 2019.

[84] H Clay Gabler, Richard A Yetter, and Irvin Glassman. Asymmetric Whirl Combustion : A New Approach for Non-Premixed Low NOx Gas Turbine Combustor Design. *AIAA Journal*, pages 1–11, 1998.

[85] Aaron Alex Frank. *Effects of Downscaling on the Low Swirl Burner*. PhD thesis, University of California, Berkeley, 2019.

[86] W. Coenen, P. Rajamanickam, A. D. Weiss, A. L. Sánchez, and F. A. Williams. Swirling flow induced by jets and plumes. *Acta Mechanica*, 230(6):2221–2231, 2019.

[87] Ritsu Dobashi, Tetsuya Okura, Ryosuke Nagaoka, Yasuhiro Hayashi, and Toshio Mogi. Experimental Study on Flame Height and Radiant Heat of Fire Whirls. *Fire Technology*, 52(4):1069–1080, 7 2016.

[88] Jiao Lei, Naian Liu, Linhe Zhang, Zhihua Deng, Nelson Kudzo Akafuah, Tianxiang Li, Kozo Saito, and Kohyu Satoh. Burning rates of liquid fuels in fire whirls. *Combustion and Flame*, 159(6):2104–2114, 6 2012.

[89] Hanyuan Yu, Song Guo, Minjun Peng, Quanwei Li, Jifeng Ruan, Wei Wan, and Chen Chen. Study on the influence of air-inlet width on fire whirls combustion characteristic. *Procedia Engineering*, 62:813–820, 2013.

[90] Kuibin Zhou, Naian Liu, and Xieshang Yuan. Effect of Wind on Fire Whirl Over a Line Fire. *Fire Technology*, 52(3):865–875, 2016.

[91] Pengfei Wang, Naian Liu, Linhe Zhang, Yueling Bai, and Kohyu Satoh. Fire Whirl Experimental Facility with No Enclosure of Solid Walls: Design and Validation. *Fire Technology*, 51(4):951–969, 2015.

[92] Jiao Lei, Naian Liu, Yan Jiao, and Shaojie Zhang. Experimental investigation on flame patterns of buoyant diffusion flame in a large range of imposed circulations. *Proceedings of the Combustion Institute*, 36(2):3149–3156, 2017.

[93] Jiao Lei, Congcong Ji, Naian Liu, and Linhe Zhang. Effect of imposed circulation on temperature and velocity in general fire whirl: An experimental investigation. *Proceedings of the Combustion Institute*, 37(3):4295–4302, 2019.

[94] Shao Lin Lee and Charles A. Garris. Formation of multiple fire whirls. *Symposium (International) on Combustion*, 12(1):265–273, 1969.

[95] Jiao Lei, Naian Liu, and Ran Tu. Flame height of turbulent fire whirls: A model study by concept of turbulence suppression. *Proceedings of the Combustion Institute*, 36(2):3131–3138, 2017.

[96] Kuibin Zhou, Naian Liu, Linhe Zhang, and Koyu Satoh. Thermal Radiation from Fire Whirls: Revised Solid Flame Model. *Fire Technology*, 50(6):1573–1587, 2014.

[97] Jiao Lei, Naian Liu, Linhe Zhang, Haixiang Chen, Lifu Shu, Pu Chen, Zhihua Deng, Jiping Zhu, Kohyu Satoh, and John L. De Ris. Experimental research on combustion dynamics of medium-scale fire whirl. *Proceedings of the Combustion Institute*, 33(2):2407–2415, 2011.

[98] A Bouhafid, J.P. Vantelon, P Joulain, and A.C. Fernandez-Pello. On the flame structure at the base of a pool fire. *Symposium (International) on Combustion*, 22(1):1291–1298, 1 1989.

[99] Vytenis Babrauskas. Estimating large pool fire burning rates. *Fire Technology*, 19(4):251–261, 11 1983.

[100] Chen Kuang, Longhua Hu, Xiaolei Zhang, Yujie Lin, and Larry W. Kostiuk. An experimental study on the burning rates of n-heptane pool fires with various lip heights in cross flow. *Combustion and Flame*, 201:93–103, 2019.

[101] E. J. Hopfinger and G J F V Heijst. Vortices in Rotating Fluids. *Annual Review of Fluid Mechanics*, 25(1):241–289, 1 1993.

[102] Jiao Lei and Naian Liu. Reciprocal transitions between buoyant diffusion flame and fire whirl. *Combustion and Flame*, 167:463–471, 5 2016.

[103] Kuibin Zhou, Xiaole Qin, Le Zhang, and Yueqiong Wu. An experimental study of jet fires in rotating flow fields. *Combustion and Flame*, 210:193–203, 2019.

[104] S Soma and K Saito. Reconstruction of fire whirls using scale models. *Combustion and Flame*, 86(3):269–284, 8 1991.

[105] James G. Quintiere. *Fundamentals of Fire Phenomena*. John Wiley & Sons, Ltd, Chichester, UK, 3 2006.

[106] Pierre Joulain. The behavior of pool fires: State of the art and new insights. *Symposium (International) on Combustion*, 27(2):2691–2706, 1998.

[107] Zhigang Wang, Wai Cheong Tam, Ki Yong Lee, and Anthony Hamins. Temperature Field Measurements using Thin Filament Pyrometry in a Medium-Scale Methanol Pool Fire - NIST Technical Note 2031. Technical report, NIST, 2018.

[108] M Klassen and Jay P Gore. Structure and radiation properties of pool fires. Technical report, National Institute of Standards and Technology, Gaithesburg, MD, 1994.

[109] A. Hamins, S. J. Fischer, T. Kashiwagi, M. E. Klassen, and J. P. Gore. Heat Feedback to the Fuel Surface in Pool Fires. *Combustion Science and Technology*, 97(1-3):37–62, 4 1994.

[110] R. I. EMORI and K. SAITO. A Study of Scaling Laws in Pool and Crib Fires. *Combustion Science and Technology*, 31(5-6):217–231, 5 1983.

[111] Longhua Hu. A review of physics and correlations of pool fire behaviour in wind and future challenges. *Fire Safety Journal*, 91:41–55, 2017.

[112] Longhua Hu, Junjun Hu, and John L. de Ris. Flame necking-in and instability characterization in small and medium pool fires with different lip heights. *Combustion and Flame*, 162(4):1095–1103, 2015.

[113] Daniel Moreno-Boza, Wilfried Coenen, Jaime Carpio, Antonio L. Sánchez, and Forman A. Williams. On the critical conditions for pool-fire puffing. *Combustion and Flame*, 192:426–438, 2018.

[114] Baki M. Cetegen and Tarek A. Ahmed. Experiments on the periodic instability of buoyant plumes and pool fires. *Combustion and Flame*, 93(1-2):157–184, 4 1993.

[115] A. Bejan. Predicting the Pool Fire Vortex Shedding Frequency. *Journal of Heat Transfer*, 113(1):261–263, 2 1991.

[116] Johanna Aurell, Brian K. Gullett, and Dirk Yamamoto. Emissions from Open Burning of Simulated Military Waste from Forward Operating Bases. *Environmental Science & Technology*, 46(20):11004–11012, 10 2012.

[117] J.A. Fay. The Spread of Oil Slicks on a Calm Sea. In *Oil on the Sea - Ocean Technology*, chapter The Spread, pages 53–63. Springer, Boston, MA, Boston, MA, 1969.

[118] D P Hoult. Oil Spreading on the Sea. *Annual Review of Fluid Mechanics*, 4(1):341–368, 1 1972.

[119] P. Cooperman. Some criteria for the in situ combustion of crude oil. *Journal of Applied Physics*, 30(9):1376–1380, 1959.

[120] Charles H. Peterson, Stanley D. Rice, Jeffrey W. Short, Daniel Esler, James L. Bodkin, Brenda E. Ballachey, and David B. Irons. Long-Term Ecosystem Response to the Exxon Valdez Oil Spill. *Science*, 302(5653):2082–2086, 2003.

[121] Laurens van Gelderen and Grunde Jomaas. The Parameters Controlling the Burning Efficiency of In-Situ Burning of Crude Oil on Water. In *Proceedings of the 40th AMOP Technical Seminar on Environmental Contamination and Response*, pages 817–832, Calgary, Canada, 2017.

[122] Howard D Ross. Ignition of and flame spread over laboratory-scale pools of pure liquid fuels. *Progress in Energy and Combustion Science*, 20(1):17–63, 1994.

[123] Neil Wu, Michael Baker, Gilles Kolb, and Jose L. Torero. Ignition, flame spread and mass burning characteristics of liquid fuels on a water bed. *Spill Science and Technology Bulletin*, 3(4):209–212, 1996.

[124] Neil Wu, Gilles Kolb, and Jose L. Torero. Piloted ignition of a slick of oil on a water sublayer: The effect of weathering. *Symposium (International) on Combustion*, 27(2):2783–2790, 1998.

[125] Ian Buist. Window-of-opportunity for in situ burning. *Spill Science and Technology Bulletin*, 8(4):341–346, 2003.

[126] J. L. Torero, Stephen M. Olenick, J. P. Garo, and J. P. Vantelon. Determination of the burning characteristics of a slick of oil on water. *Spill Science and Technology Bulletin*, 8(4):379–390, 2003.

[127] A. Y. Walavalkar and A. K. Kulkarni. Combustion of water-in-oil emulsion layers supported on water. *Combustion and Flame*, 125(1-2):1001–1011, 2001.

[128] Nicholas L. Brogaard, Martin X. Sørensen, Janne Fritt-Rasmussen, Ali S. Rangwala, and Grunde Jomaas. A new experimental rig for oil burning on water - Results for crude and pure oils. *Fire Safety Science*, 11:1481–1494, 2014.

[129] Irvin Glassman. Supersonic flight and cooking over wood-burning stoves: Challenges to the combustion community. *Proceedings of the Combustion Institute*, 28(1):1–10, 2000.

[130] I. Glassman and R. A. Yetter. *Combustion*. Elsevier, 4th edition, 2008.

[131] Michael Faraday. *The Chemical History of a Candle*. Chatto and Windus, London, 1908.

[132] Bill Hammack and Don DeCoste. *Michael Faraday's The Chemical History of a Candle (Edited)*. Articulate Noise Books, 2016.

[133] U. Bonne, K. H. Homann, and H. G.G. Wagner. Carbon formation in premixed flames. *Symposium (International) on Combustion*, 10(1):503–512, 1965.

[134] Fang. Xu. *Soot growth in laminar premixed flames*. PhD thesis, University of Michigan, 1999.

[135] W Flower. Optical Measurements of Soot Formation in Premixed Flames. *Combustion Science and Technology*, 33:17–33, 4 2007.

[136] Peter Bradford Sunderland. *Soot formation in laminar jet diffusion flames*. PhD thesis, University of Michigan, Ann Arbor, 1995.

[137] Charles A. Amann and Donald C. Siegla. Diesel particulates—What they are and why. *Aerosol Science and Technology*, 1(1):73–101, 1982.

[138] Jonathan O. Anderson, Josef G. Thundiyil, and Andrew Stolbach. Clearing the Air: A Review of the Effects of Particulate Matter Air Pollution on Human Health. *Journal of Medical Toxicology*, 8(2):166–175, 2012.

[139] EPA. Regulations for Emissions from Vehicles and Engines (https://www.epa.gov/regulations-emissions-vehicles-and-engines).

[140] J. H. Kent. A quantitative relationship between soot yield and smoke point measurements. *Combustion and Flame*, 63(3):349–358, 1986.

[141] J. De Ris and X. Cheng. The Of Role Of Smoke-point In Material Flammability Testing. *Fire Safety Science*, 4:301–312, 1994.

[142] Robert J. Santoro and Thomas F. Richardson. Concentration and Temperature Effects on Soot Formation in Diffusion Flames. In Henning Bockhorn, editor, *Soot Formation in Combustion*, chapter 13, pages 221–238. Springer-Verlag, Berlin, 1994.

[143] K.-C. Lin and G. M. Faeth. Hydrodynamic suppression of soot emissions in laminar diffusion flames. *Journal of Propulsion and Power*, 12(1):10–17, 1996.

[144] K C Lin and G M Faeth. Effects of hydrodynamics on soot formation in laminar opposed-jet diffusion flames. *Journal of Propulsion and Power*, 12(4):691–698, 1996.

[145] K.-C Lin and G M Faeth. State Relationships of Laminar Permanently-Blue Opposed-Jet Hydrocarbon-Fueled Diffusion Flames. *Int. J. Environ. Combust. Tech. Vol I*, pages 53–79, 2000.

[146] S. M. Mahmoud, G. J. Nathan, Z. T. Alwahabi, Z. W. Sun, P. R. Medwell, and B. B. Dally. The effect of exit strain rate on soot volume fraction in turbulent non-premixed jet flames. *Proceedings of the Combustion Institute*, 36(1):889–897, 2017.

[147] B. A. Strayer, D. Dunn-Rankin, and F. Jabbari. A comparison between frequency- and amplitude-modulated adaptive control of a non-premixed flame. *Symposium (International) on Combustion*, 27(1):1247–1254, 1998.

[148] Akshit Markan, Peter B. Sunderland, James G. Quintiere, John L. de Ris, Dennis P. Stocker, and Howard R. Baum. A Burning Rate Emulator (BRE) for study of condensed fuel burning in microgravity. *Combustion and Flame*, 192:272–282, 2018.

[149] M. S. Cha, S. M. Lee, K. T. Kim, and S. H. Chung. Soot suppression by nonthermal plasma in coflow jet diffusion flames using a dielectric barrier discharge. *Combustion and Flame*, 141(4):438–447, 2005.

[150] R. A. Dobbins and C. M. Megaridis. Morphology of Flame-Generated Soot As Determined by Thermophoretic Sampling. *Langmuir*, 3(2):254–259, 1987.

[151] Irvin Glassman. Soot formation in combustion processes. *Symposium (International) on Combustion*, 22(1):295–311, 1 1989.

[152] J. Du and R. L. Axelbaum. The effect of flame structure on soot-particle inception in diffusion flames. *Combustion and Flame*, 100(3):367–375, 1995.

[153] K H Homann and H G Wagner. Chemistry of Carbon Formation in Flames. *Proceedings of the Royal Society of London. Series A, Mathematical and Physical Sciences*, 307(1489):141–152, 3 1968.

[154] B. S. Haynes and H. Gg Wagner. Soot formation. *Progress in Energy and Combustion Science*, 7(4):229–273, 1981.

[155] M. Bachmann, W. Wiese, and K. H. Homann. PAH and aromers: Precursors of fullerenes and soot. *Symposium (International) on Combustion*, 26(2):2259–2267, 1996.

[156] Charles S. McEnally, Ümit Ö Köylü, Lisa D. Pfefferle, and Daniel E. Rosner. Soot volume fraction and temperature measurements in laminar nonpremixed flames using thermocouples. *Combustion and Flame*, 109(4):701–720, 1997.

[157] Samuel L. Manzello, David B. Lenhert, Ahmet Yozgatligil, Michael T. Donovan, George W. Mulholland, Michael R. Zachariah, and Wing Tsang. Soot particle size distributions in a well-stirred reactor/plug flow reactor. *Proceedings of the Combustion Institute*, 31 I(1):675–683, 2007.

[158] Ü Ö Köylü, C. S. Mcenally, D. E. Rosner, and L. D. Pfefferle. Simultaneous measurements of soot volume fraction and particle size / microstructure in flames using a thermophoretic sampling technique. *Combustion and Flame*, 110(4):494–507, 1997.

[159] Chiara Saggese, Alberto Cuoci, Alessio Frassoldati, Sara Ferrario, Joaquin Camacho, Hai Wang, and Tiziano Faravelli. Probe effects in soot sampling from a burner-stabilized stagnation flame. *Combustion and Flame*, 167:184–197, 2016.

[160] Nathan J. Kempema, Bin Ma, and Marshall B. Long. Investigation of in-flame soot optical properties in laminar coflow diffusion flames using thermophoretic particle sampling and spectral light extinction. *Applied Physics B: Lasers and Optics*, 122(9):1–13, 2016.

[161] Alex M. Vargas and Ömer L. Gülder. A multi-probe thermophoretic soot sampling system for high-pressure diffusion flames. *Review of Scientific Instruments*, 87(5), 2016.

[162] Randall L. Vander Wal. A TEM Methodology for the Study of Soot Particle Structure. *Combustion Science and Technology*, 126(1-6):333–351, 7 1997.

[163] Paul M. Anderson, Haiqing Guo, and Peter B. Sunderland. Repeatability and reproducibility of TEM soot primary particle size measurements and comparison of automated methods. *Journal of Aerosol Science*, 114(October):317–326, 2017.

[164] Haiqing Guo, Jose A. Castillo, and Peter B. Sunderland. Digital camera measurements of soot temperature and soot volume fraction in axisymmetric flames. *Applied Optics*, 52(33):8040–8047, 2013.

[165] Catherine Hamel, Fernando Raffan-Montoya, and Stanislav I. Stoliarov. A method for measurement of spatially resolved radiation intensity and radiative fraction of laminar flames of gaseous and solid fuels. *Experimental Thermal and Fluid Science*, 104:153–163, 6 2019.

[166] Peter B. Kuhn, Bin Ma, Blair C. Connelly, Mitchell D. Smooke, and Marshall B. Long. Soot and thin-filament pyrometry using a color digital camera. *Proceedings of the Combustion Institute*, 33(1):743–750, 2011.

[167] Dennis K. Kim and Peter B. Sunderland. Fire ember pyrometry using a color camera. *Fire Safety Journal*, 106(February):88–93, 2019.

[168] H. A. Michelsen, C. Schulz, G. J. Smallwood, and S. Will. Laser-induced incandescence: Particulate diagnostics for combustion, atmospheric, and industrial applications. *Progress in Energy and Combustion Science*, 51:2–48, 2015.

[169] R. L. Vander Wal and K. J. Weiland. Laser-induced incandescence: Development and characterization towards a measurement of soot-volume fraction. *Applied Physics B Laser and Optics*, 59(4):445–452, 1994.

[170] Seong Young Lee, Stephen R. Turns, and Robert J. Santoro. Measurements of soot, OH, and PAH concentrations in turbulent ethylene/air jet flames. *Combustion and Flame*, 156(12):2264–2275, 2009.

[171] Chen Gu, He Lin, Joaquin Camacho, Baiyang Lin, Can Shao, Ruoxin Li, Hao Gu, Bin Guan, Zhen Huang, and Hai Wang. Particle size distribution of nascent soot in lightly and heavily sooting premixed ethylene flames. *Combustion and Flame*, 165:177–187, 2016.

[172] R.J. Santoro, H.G. Semerjian, and R.A. Dobbins. Soot particle measurements in diffusion flames. *Combustion and Flame*, 51(3):203–218, 1 1983.

[173] M. Y. Choi, G. W. Mulholland, A. Hamins, and T. Kashiwagi. Comparisons of the soot volume fraction using gravimetric and light extinction techniques. *Combustion and Flame*, 102(1-2):161–169, 1995.

[174] Simone Amaral, João de Carvalho, Maria Costa, and Cleverson Pinheiro. An Overview of Particulate Matter Measurement Instruments. *Atmosphere*, 6(9):1327–1345, 9 2015.

[175] J. H. Sun and S. H. Chan. A time-resolved measurement technique for particulate number density in diesel exhaust using a fast-response flame ionization detector. *Measurement Science and Technology*, 8(3):279–286, 1997.

[176] Florentin M.J. Bulot, Steven J. Johnston, Philip J. Basford, Natasha H.C. Easton, Mihaela Apetroaie-Cristea, Gavin L. Foster, Andrew K.R. Morris, Simon J. Cox, and Matthew Loxham. Long-term field comparison of multiple low-cost particulate matter sensors in an outdoor urban environment. *Scientific Reports*, 9(1):1–13, 2019.

[177] Nathaniel May, Evan Ellicott, and Michael Gollner. An examination of fuel moisture, energy release and emissions during laboratory burning of live wildland fuels. *International Journal of Wildland Fire*, 28(3):187–197, 2019.

[178] Andreas Petzold, Richard Marsh, Mark Johnson, Michael Miller, Yura Sevcenco, David Delhaye, Amir Ibrahim, Paul Williams, Heidi Bauer, Andrew Crayford, William D. Bachalo, and David Raper. Evaluation of methods for measuring particulate matter emissions from gas turbines. *Environmental Science and Technology*, 45(8):3562–3568, 2011.

[179] Jerzy Merkisz and Jacek Pielecha. *Nanoparticle Emissions From Combustion Engines*, volume 8 of *Springer Tracts on Transportation and Traffic*. Springer International Publishing, Cham, 2015.

[180] Hans Grimm and Delbert J. Eatough. Aerosol measurement: The use of optical light scattering for the determination of particulate size distribution, and particulate mass, including the semi-volatile fraction. *Journal of the Air and Waste Management Association*, 59(1):101–107, 2009.

[181] S.B. Hariharan, Y. Hu, H. Xiao, M.J. Gollner, and Elaine S. Oran. The Structure of the Blue Whirl. In *70th Annual Meeting of the APS Division of Fluid Dynamics*, Denver, Colorado, 2017.

[182] J. Warnatz, Ulrich Maas, and Robert W. Dibble. *Combustion*. Springer, 4th edition, 2006.

[183] A C Eckbreth. Laser Diagnostics for Temperature and Species in Unsteady Combustion. In F Culick, M V Heitor, and J H Whitelaw, editors, *Unsteady Combustion*, pages 393–410. Springer Netherlands, Dordrecht, 1996.

[184] Christof Schulz, Andreas Dreizler, Volker Ebert, and Jürgen Wolfrum. Combustion Diagnostics BT - Springer Handbook of Experimental Fluid Mechanics. In Cameron Tropea, Alexander L Yarin, and John F Foss, editors, *Springer Handbook of Experimental Fluid Mechanics*, pages 1241–1315. Springer Berlin Heidelberg, Berlin, Heidelberg, 2007.

[185] T. Kathrotia, M. Fikri, M. Bozkurt, M. Hartmann, U. Riedel, and C. Schulz. Study of the H+O+M reaction forming OH*: Kinetics of OH* chemiluminescence in hydrogen combustion systems. *Combustion and Flame*, 157(7):1261–1273, 2010.

[186] Jun Kojima, Yuji Ikeda, and Tsuyoshi Nakajima. Basic aspects of OH(A), CH(A), and C2(d) chemiluminescence in the reaction zone of laminar methane-air premixed flames. *Combustion and Flame*, 140(1-2):34–45, 2005.

[187] Venkata Nori and Jerry Seitzman. Evaluation of Chemiluminescence as a Combustion Diagnostic Under Varying Operating Conditions. In *46th AIAA Aerospace Sciences Meeting and Exhibit*, number January, pages 1–14, Reston, Virigina, 1 2008. American Institute of Aeronautics and Astronautics.

[188] C. S. Panoutsos, Y. Hardalupas, and A. M K P Taylor. Numerical evaluation of equivalence ratio measurement using OH* and CH* chemiluminescence in premixed and non-premixed methane-air flames. *Combustion and Flame*, 156(2):273–291, 2009.

[189] Thomas P Clark. Studies of OH, CO, CH, and C(sub 2) Radiation from Laminar and Turbulent Propane-air and Ethylene-air Flames. Technical report, National Advisory Committee for Aeronautics. Lewis Flight Propulsion Lab, Cleveland, Ohio, 1958.

[190] Yuji Ikeda, Jun Kojima, and Hideki Hashimoto. Local chemiluminescence spectra measurements in a high-pressure laminar methane/air premixed flame. *Proceedings of the Combustion Institute*, 29(2):1495–1501, 2002.

[191] B. Higgins, M. Q. McQuay, F. Lacas, and S. Candel. An experimental study on the effect of pressure and strain rate on CH chemiluminescence of premixed fuel-lean methane/air flames. *Fuel*, 80(11):1583–1591, 2001.

[192] Y. Hardalupas and M. Orain. Local measurements of the time-dependent heat release rate and equivalence ratio using chemiluminescent emission from a flame. *Combustion and Flame*, 139(3):188–207, 2004.

[193] Jun Kojima, Yuji Ikeda, and Tsuyoshi Nakajima. Spatially resolved measurement of OH, CH, and C2 chemiluminescence in the reaction zone of laminar methane/air premixed flames. *Proceedings of the Combustion Institute*, 28(2):1757–1764, 2000.

[194] Yong Ki Jeong, Chung Hwan Jeon, and Young June Chang. Evaluation of the equivalence ratio of the reacting mixture using intensity ratio of chemiluminescence in laminar partially premixed CH4-air flames. *Experimental Thermal and Fluid Science*, 30(7):663–673, 2006.

[195] T. M. Muruganandam, B. H. Kim, M. R. Morrell, V. Nori, M. Patel, B. W. Romig, and J. M. Seitzman. Optical equivalence ratio sensors for gas turbine combustors. *Proceedings of the Combustion Institute*, 30(1):1601–1608, 2005.

[196] Chadwick C. Rasmussen, Sulabh K. Dhanuka, and James F. Driscoll. Visualization of flameholding mechanisms in a supersonic combustor using PLIF. *Proceedings of the Combustion Institute*, 31 II:2505–2512, 2007.

[197] Z. S. Li, B. Li, Z. W. Sun, X. S. Bai, and M. Aldén. Turbulence and combustion interaction: High resolution local flame front structure visualization using simultaneous single-shot PLIF imaging of CH, OH, and CH2O in a piloted premixed jet flame. *Combustion and Flame*, 157(6):1087–1096, 2010.

[198] Mamoru Tanahashi, Shinichirou Murakami, Gyung Min Choi, Yuichi Fukuchi, and Toshio Miyauchi. Simultaneous CH-OH PLIF and stereoscopic PIV measurements of turbulent premixed flames. *Proceedings of the Combustion Institute*, 30(1):1665–1672, 2005.

[199] Mingfa Yao, Zhaolei Zheng, and Haifeng Liu. Progress and recent trends in homogeneous charge compression ignition (HCCI) engines. *Progress in Energy and Combustion Science*, 35(5):398–437, 2009.

[200] Swetaprovo Chaudhuri, Stanislav Kostka, Michael W. Renfro, and Baki M. Cetegen. Blowoff dynamics of bluff body stabilized turbulent premixed flames. *Combustion and Flame*, 157(4):790–802, 2010.

[201] Bikram R. Chowdhury and Baki M. Cetegen. Effects of free stream flow turbulence on blowoff characteristics of bluff-body stabilized premixed flames. *Combustion and Flame*, 190:302–316, 2018.

[202] S. Böckle, J. Kazenwadel, T. Kunzelmann, and C. Schulz. Laser-diagnostic multi-species imaging in strongly swirling natural gas flames. *Applied Physics B: Lasers and Optics*, 71(5):741–746, 2000.

[203] S. R. Pezeshki, M. W. Hester, Q. Lin, and J. A. Nyman. The effects of oil spill and clean-up on dominant US Gulf coast marsh macrophytes: A review. *Environmental Pollution*, 108(2):129–139, 2000.

[204] Robin J Law and Jocelyne Hellou. Contamination of fish and shellfish following oil spill incidents. *Environmental Geosciences*, 6(2):90–98, 6 1999.

[205] Michael J. Moran and Howard N. Shapiro. *Engineering Thermodynamics*. John Wiley & Sons, Inc., 5th edition, 2006.

[206] National-Response-Team. Guidance on Burning Spilled Oil in Situ. Technical Report December 1995, Office of Response and Restoration, 1995.

[207] Michael A. Peters. Oil geopolitics and eco-nightmares. *Educational Philosophy and Theory*, 49(5):435–438, 2017.

[208] Mervin F Fingas, Greg Halley, Francine Ackerman, Robert Nelson, Martine Bissonnette, Nanci Laroche, Zhendi Wang, Patrick Lambert, Ken Li, Paula Jokuty, Gary Sergy, Edward J Tennyson, Joe Mullin, Larry Hannon, Wayne Halley, John Latour, Roy Galarneau, Bill Ryan, Rod Turpin, Phil Campagna, Don V Aurand, and Robert R Hiltabrand. The Newfoundland Offshore Burn Experiment—NOBE. *International Oil Spill Conference Proceedings*, 1995(1):123–132, 2 1995.

[209] Ian Buist, Ken Trudel, Jake Morrison, and Don Aurand. Laboratory Studies of the Properties of In-Situ Burn Residues. *International Oil Spill Conference Proceedings*, 1997(1):149–156, 4 1997.

[210] Ian Buist, Steve Potter, Tim Nedwed, and Joseph Mullin. Herding surfactants to contract and thicken oil spills in pack ice for in situ burning. *Cold Regions Science and Technology*, 67(1-2):3–23, 2011.

[211] Qianxin Lin, Irving A. Mendelssohn, Kenneth Carney, Scott M. Miles, Nelson P. Bryner, and William D. Walton. In-situ burning of oil in coastal marshes. 2. Oil spill cleanup efficiency as a function of oil type, marsh type, and water depth. *Environmental Science and Technology*, 39(6):1855–1860, 2005.

[212] IPIECA and IOGP. In-Situ Burning of Spilled Oil - Good practice guidelines for incident management and emergency response personnel. Technical report, IPIECA, IOGP, London, UK, 2016.

[213] TSI Incorporated. DustTrak DRX Aerosol Monitor Model 8534 Operation and Service Manual. Technical Report January, TSI Incorporated, 2017.

[214] S. Brohez, C. Delvosalle, and G. Marlair. A two-thermocouples probe for radiation corrections of measured temperatures in compartment fires. *Fire Safety Journal*, 39(5):399–411, 2004.

[215] J. P. Garo, J. P. Vantelon, and A. C. Fernandez-Pello. Boilover burning of oil spilled on water. *Symposium (International) on Combustion*, 25(1):1481–1488, 1994.

[216] C.S. Cragoe. Thermal Properties of Petroleum Products. Technical report, Bureau of Standards, 1933.

[217] Benjamin D. Ditch, John L. de Ris, Thomas K. Blanchat, Marcos Chaos, Robert G. Bill, and Sergey B. Dorofeev. Pool fires - An empirical correlation. *Combustion and Flame*, 160(12):2964–2974, 2013.

[218] Michael J. Gollner, Elaine S. Oran, Sriram Bharath Hariharan, Joseph Dowling, Hamed F. Farahani, and Ali S. Rangwala. Efficient Remediation of Oil Spills over Water using Fire Whirls (Project Number 1094). Technical report, Bureau of Safety and Environmental Enforcement, Washington, DC, 2019.

[219] Sriram Bharath Hariharan, Joseph Dowling, Hamed F. Farahani, Yu Hu, Ali Tohidi, Karen Stone, Ali S. Rangwala, Elaine S. Oran, and Michael J. Gollner. Demonstration of reduction in emissions by fire whirls through small scale experiments. In *2019 AMOP Technical Seminar on Environmental Contamination and Response*, Halifax, Nova Scotia, Canada, 2019.

[220] Sriram B Hariharan, Joseph Dowling, Hamed F Farahani, Michael J Gollner, Elaine S Oran, and Karen Stone. Comparison of emissions from liquid-fueled pool fires and fire whirls. In *11th U.S. National Combustion Meeting*, Pasadena, California, 2019.

[221] ExxonMobil. Alaska North Slope Material Safety Data Sheet, 2018.

[222] R. J. Yokelson, J. G. Goode, D. E. Ward, R. A. Susott, R. E. Babbitt, D. D. Wade, I. Bertschi, D. W. T. Griffith, and W. M. Hao. Emissions of formaldehyde, acetic acid, methanol, and other trace gases from biomass fires in North Carolina measured by airborne Fourier transform infrared spectroscopy. *Journal of Geophysical Research: Atmospheres*, 104(D23):30109–30125, 12 1999.

[223] Wei Tang, Colin H. Miller, and Michael J. Gollner. Local flame attachment and heat fluxes in wind-driven line fires. *Proceedings of the Combustion Institute*, 36(2):3253–3261, 2017.

[224] Kuibin Zhou, Naian Liu, Jesse S. Lozano, Yanlong Shan, Bin Yao, and Kohyu Satoh. Effect of flow circulation on combustion dynamics of fire whirl. *Proceedings of the Combustion Institute*, 34(2):2617–2624, 2013.

[225] Katsuhisa Noto, Kenji Teramoto, and Tsuyoshi Nakajima. Spectra and critical grashof numbers for turbulent transition in a thermal plume. *Journal of Thermophysics and Heat Transfer*, 13(1):82–90, 1999.

[226] RUI ZHOU and ZI-NIU WU. Fire whirls due to surrounding flame sources and the influence of the rotation speed on the flame height. *Journal of Fluid Mechanics*, 583:313–345, 7 2007.

[227] Laurens Van Gelderen, Linus M V Malmquist, and Grunde Jomaas. Vaporization order and burning efficiency of crude oils during in - situ burning on water. *Fuel*, 191:528–537, 2017.

[228] Keng Hoo Chuah, Kazunori Kuwana, and Kozo Saito. Modeling a fire whirl generated over a 5-cm-diameter methanol pool fire. *Combustion and Flame*, 156(9):1828–1833, 2009.

[229] Sidney Leibovich. The Structure of Vortex Breakdown. *Annual Review of Fluid Mechanics*, 10(11):221–246, 1978.

[230] J H Faler and S Leibovich. Disrupted states of vortex flow and vortex breakdown. *Physics of Fluids*, 20(9):1385, 1977.

[231] Turgut Sarpkaya. On stationary and travelling vortex breakdowns. *Journal of Fluid Mechanics*, 45(03):545–559, 1971.

[232] A K Gupta, D G Lilley, and N Syred. *Swirl flows*. Abacus Press, Tunbridge Wells, Kent, 1984.

[233] Michael D. Abràmoff, Paulo J. Magalhães, and Sunanda J. Ram. Image processing with imageJ. *Biophotonics International*, 11(7):36–41, 2004.

[234] Nobuyuki Otsu. A Threshold Selection Method from Gray-Level Histograms. *IEEE Transactions on Systems, Man, and Cybernetics*, 9(1):62–66, 1 1979.

[235] Gunnar Heskestad. Luminous heights of turbulent diffusion flames. *Fire Safety Journal*, 5(2):103–108, 1983.

[236] Bruce R. Munson, Donald F. Young, Theodore H. Okiishi, and Wade W. Huebsch. *Fundamentals Sixth Edition of Fluid Mechanics*. John Wiley & Sons, Inc., 6th edition, 2010.

[237] E. E. Zukoski. Properties of fire plumes. In *Combustion Fundamentals of Fire*, pages 101–219. Academic Press Ltd., 1995.

[238] Sriram Bharath Hariharan, Yu Hu, Michael J. Gollner, and Elaine S. Oran. Conditions for Formation of the Blue Whirl. In *71st Annual Meeting of the APS Division of Fluid Dynamics*, volume 63, Atlanta, Georgia, 2018.

[239] James D. Smith and Volker Sick. High-speed fuel tracer fluorescence and OH radical chemiluminescence imaging in a spark-ignition direct-injection engine. *Applied Optics*, 44(31):6682–6691, 2005.

[240] Zhi Wang, Yunliang Qi, Xin He, Jianxin Wang, Shijing Shuai, and Chung K. Law. Analysis of pre-ignition to super-knock: Hotspot-induced deflagration to detonation. *Fuel*, 144:222–227, 2015.

[241] J. D. Smith and V. Sick. Crank-angle resolved imaging of biacetyl laser-induced fluorescence in an optical internal combustion engine. *Applied Physics B: Lasers and Optics*, 81(5):579–584, 2005.

[242] James D. Smith and Volker Sick. Quantitative, dynamic fuel distribution measurements in combustion-related devices using laser-induced fluorescence imaging of biacetyl in iso-octane. *Proceedings of the Combustion Institute*, 31(1):747–755, 1 2007.

[243] R. S. Barlow, R. W. Dibble, J. Y. Chen, and R. P. Lucht. Effect of Damköhler number on superequilibrium OH concentration in turbulent nonpremixed jet flames. *Combustion and Flame*, 82(3-4):235–251, 1990.

[244] Sriram Bharath Hariharan, Yejun Wang, Paul M. Anderson, Michael J. Gollner, Waruna D. Kulatilaka, and Elaine S. Oran. On the nature of combustion in the blue whirl using optical diagnostics (In preparation). 2020.

[245] P. G. Aleiferis, Y. Hardalupas, A. M.K.P. Taylor, K. Ishii, and Y. Urata. Flame chemiluminescence studies of cyclic combustion variations and air-to-fuel ratio of the reacting mixture in a lean-burn stratified-charge spark-ignition engine. *Combustion and Flame*, 136(1-2):72–90, 2004.

[246] J.W. Dold. Flame propagation in a nonuniform mixture: Analysis of a slowly varying Triple Flame. *Combustion and Flame*, 76(1):71–88, 4 1989.

[247] J. Buckmaster. Edge-flames. *Journal of Engineering Mathematics*, 31(2-3):269–284, 1997.

[248] J. Buckmaster. Edge-flames. *Progress in Energy and Combustion Science*, 28(5):435–475, 2002.

[249] Zhengyang Wang, Peter B. Sunderland, and Richard L. Axelbaum. Double blue zones in inverse and normal laminar jet diffusion flames. *Combustion and Flame*, 211:253–259, 2020.

[250] J. H. Faler and S Leibovich. An experimental map of the internal structure of a vortex breakdown. *Journal of Fluid Mechanics*, 86(1978):313–335, 1978.

[251] Kazunori Kuwana, Kozo Sekimoto, Takeaki Minami, Takahiro Tashiro, and Kozo Saito. Scale-model experiments of moving fire whirl over a line fire. *Proceedings of the Combustion Institute*, 34(2):2625–2631, 2013.

[252] Hampton Clay Gabler. *An Experimental and Numerical Investigation of Asymmetrically-Fueled Whirl Flames*. PhD thesis, Princeton University, 1998.

[253] F. A. Williams. Urban and wildland fire phenomenology. *Progress in Energy and Combustion Science*, 8(4):317–354, 1982.

[254] John B Heywood. *Internal Combustion Engine Fundamentals*, volume 21. McGraw-Hill, 1988.

[255] Steven G. Tuttle, Katherine Hinnant, Thomas N. Loegel, and Brian T. Fisher. Development of a Low-Emission Spray Combustor for Emulsified Crude Oil. Technical report, Bureau of Safety and Environmental Enforcement, Washington, DC, 2017.

[256] Johannes Schindelin, Ignacio Arganda-Carreras, Erwin Frise, Verena Kaynig, Mark Longair, Tobias Pietzsch, Stephan Preibisch, Curtis Rueden, Stephan Saalfeld, Benjamin Schmid, Jean-Yves Tinevez, Daniel James White, Volker Hartenstein, Kevin Eliceiri, Pavel Tomancak, and Albert Cardona. Fiji: an open-source platform for biological-image analysis. *Nature Methods*, 9(7):676–682, 7 2012.

[257] S. G. Davis and C. K. Law. Laminar flame speeds and oxidation kinetics of iso-octane-air and n-heptane-air flames. *Symposium (International) on Combustion*, 27(1):521–527, 1998.